

AD-A257 848



AEOSR-TR- 5-2 05 61

2

DROP/GAS INTERACTIONS IN DENSE SPRAYS

by

L.-P. Hsiang, J.-S. Wu, M. Mizukami and G. M. Faeth
Department of Aerospace Engineering
The University of Michigan
Ann Arbor, Michigan 48109-2140

DTIC
ELECTE
NOV 17, 1992
S B D

College of Engineering

DEPARTMENT OF AEROSPACE ENGINEERING

The University of Michigan
Ann Arbor, Michigan 48109-2140



**BEST
AVAILABLE COPY**

DISTRIBUTION STATEMENT A
Approved for public release
Distribution Unlimited

DROP/GAS INTERACTIONS IN DENSE SPRAYS

by

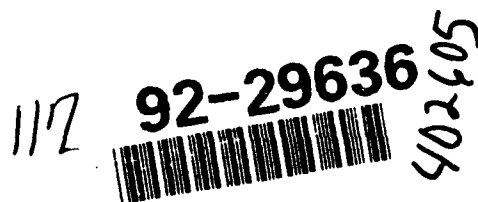
L.-P. Hsiang, J.-S. Wu, M. Mizukami and G. M. Faeth
Department of Aerospace Engineering
The University of Michigan
Ann Arbor, Michigan 48109-2140

Final Report
15 August 1989-14 August 1992

Grant No. AFOSR-89-0516
Air Force Office of Scientific Research Bolling AFB, DC 20332-6448
J. M. Tishkoff, Technical Manager

The views and conclusions contained in this document are those of the authors and should not be interpreted as representing the official policies, or endorsements, either expressed or implied, of the Air Force Office of Scientific Research or the U. S. Government.

30 September 1992



92 11 16 063

REPORT DOCUMENTATION PAGE

Form Approved

OMB No. 0704-0188

Public reporting burden for the collection of information is estimated to average 1 hour per response, including the time for reviewing instructions, searching existing data sources, gathering and maintaining the data needed, and completing and reviewing the collection of information. Send comments regarding this burden estimate or any other aspect of this collection of information, including suggestions for reducing this burden, to Washington Headquarters Services, Directorate for Information Operations and Reports, 1215 Jefferson Davis Highway, Suite 1204, Arlington, VA 22202-4302, and to the Office of Management and Budget, Paperwork Reduction Project (0704-0188), Washington, DC 20503.

1. AGENCY USE ONLY (Leave blank)**2. REPORT DATE**

30 September 1992

3. REPORT TYPE AND DATES COVERED

Final Report, 8/15/89-8/14/92

4. TITLE AND SUBTITLE

(U) Drop/Gas Interactions in Dense Sprays

5. FUNDING NUMBERS

PE - 61102F

PR - 2308

SA - BS

G - AFOSR-89-0516

6. AUTHOR(S)L.-P. Hsiang, J.-S. Wu, M. Mizukami
and G. M. Faeth**7. PERFORMING ORGANIZATION NAME(S) AND ADDRESS(ES)**Department of Aerospace Engineering
The University of Michigan
218 Aerospace Engineering Building
Ann Arbor, MI 48109-2140**8. PERFORMING ORGANIZATION
REPORT NUMBER****9. SPONSORING/MONITORING AGENCY NAME(S) AND ADDRESS(ES)**AFOSR/NA
Building 410
Bolling AFB DC 20332-6448**10. SPONSORING/MONITORING
AGENCY REPORT NUMBER****11. SUPPLEMENTARY NOTES****12a. DISTRIBUTION/AVAILABILITY STATEMENT**Approved for public release; distribution is
unlimited**12b. DISTRIBUTION CODE****13. ABSTRACT (Maximum 200 words)**

This is a final report of research considering three types of drop/gas interactions that are important in the near-injector, dense region of sprays, namely: (1) secondary drop breakup, which is an intrinsic outcome of primary breakup and is the most significant rate process of dense sprays; (2) turbulence generation by dispersed phases, which is the most significant source of turbulence production within dense sprays; and (3) the structure of sphere wakes at moderate Reynolds numbers, which is a fundamental property needed to understand turbulence generation. The properties of secondary breakup were observed for shock wave initiated disturbances in air at normal temperature and pressure, using pulsed shadowgraphy and holography to measure the dynamics and outcome of breakup and phenomenological theories to interpret and correlate the measurements. Particle-generated turbulence was observed using uniform fluxes of spherical particles falling through stagnant (in the mean) air, using phase-discriminating laser velocimetry to measure flow properties and stochastic analysis to interpret and correlate the measurements. The properties of sphere wakes at moderate Reynolds numbers were observed in both nonturbulent and turbulent environments, using laser velocimetry to measure flow properties and similarity theories to interpret and correlate the results.

14. SUBJECT TERMSMultiphase flow
Sprays
Turbulence Generation**15. NUMBER OF PAGES**

116

16. PRICE CODE**17. SECURITY CLASSIFICATION
OF REPORT**

Unclassified

**18. SECURITY CLASSIFICATION
OF THIS PAGE**

Unclassified

**19. SECURITY CLASSIFICATION
OF ABSTRACT**

Unclassified

20. LIMITATION OF ABSTRACT

UL

ACKNOWLEDGMENTS

The authors wish to acknowledge the contributions of D.R. Glass, W.C. Eaton, G. L. Gould, T. L. Griffin, D. Huddleson and T. Larrow for assisting apparatus development; S. C. Bauerle and D. Laird for assisting financial management and publication preparation.

This research was sponsored by the Air Force Office of Scientific Research, Air Force Systems Command, under Grant No. AFOSR-89-0516.

TABLE OF CONTENTS

ABSTRACT	<u>Page</u> ii
ACKNOWLEDGMENTS	iii
LIST OF TABLES	v
LIST OF FIGURES	vi
NOMENCLATURE	vii
1. INTRODUCTION	1
2. SECONDARY BREAKUP	4
2.1 Introduction	4
2.2 Experimental Methods	4
2.3 Results and Discussion	6
2.4 Conclusions	9
3. TURBULENCE GENERATION	11
3.1 Introduction	11
3.2 Experimental Methods	11
3.3 Theoretical Methods	13
3.4 Results and Discussion	13
3.5 Conclusions	14
4. SPHERE WAKES	18
4.1 Introduction	18
4.2 Experimental Methods	18
4.3 Results and Discussion	20
4.4 Conclusions	29
REFERENCES	30
APPENDIX A: FAETH (1990)	33
APPENDIX B: HSIANG AND FAETH (1992)	38
APPENDIX C: PARTHASARATHY AND FAETH (1990a)	48
APPENDIX D: PARTHASARATHY AND FAETH (1990b)	64
APPENDIX E: MIZUKAMI ET AL. (1992)	77
APPENDIX F: WU AND FAETH (1992)	86

LIST OF TABLES

<u>Table</u>	<u>Title</u>	<u>Page</u>
1	Summary of Investigation	1

LIST OF FIGURES

<u>Figure</u>	<u>Caption</u>	<u>Page</u>
1	Sketch of the shock tube apparatus	5
2	Drop deformation and breakup regime map	7
3	Drop breakup times as a function of We and Oh.	8
4	Correlation of SMD after secondary breakup	10
5	Sketch of homogeneous particle/air flow apparatus	12
6	Streamwise and crosstream r.m.s. velocity fluctuations	15
7	Temporal power spectra of crosstream velocity fluctuations	16
8	Streamwise and crosstream spatial integral scales.....	17
9	Sketch of the sphere wake apparatus for a quiescent environment.....	19
10	Sketch of the sphere wake apparatus for a turbulent environment	21
11	Mean streamwise velocities along the wake axis for a quiescent environment	22
12	Radial profiles of mean streamwise velocities in the turbulent wake region for a quiescent environment.....	23
13	Streamwise turbulence intensities along the axis of wakes in a quiescent environment	24
14	Streamwise mean velocities along the axis of wakes in a turbulent environment	26
15	Radial profiles of mean streamwise velocities in wakes in a turbulent environment	27
16	Effective turbulent viscosity for laminar-like wakes in a turbulent environment	28

DTIC QUALITY INSPECTED 4

Accession For	
NTIS GRA&I	<input checked="" type="checkbox"/>
DTIC TAB	<input type="checkbox"/>
Unannounced	<input type="checkbox"/>
Justification.....	
By.....	
Distribution/.....	
Availability Codes	
Dist	Avail and/or Special
A-1	

NOMENCLATURE

a	rate of acceleration
C	constant for turbulent/laminar wake transition
C_D	drag coefficient
C_u, C_v	empirical constants for velocity fluctuations
d	drop or particle diameter
D	pipe diameter
E_o	Eötvös number, $a(\rho_f - \rho_g) d^2/\sigma$
$E_v(f)$	temporal power spectral density of crosstream velocity fluctuations
f	frequency
g	generic wake effect
G	generic property of turbulence generation
l	characteristic wake width
L_{ux}, L_{uy}	spatial integral scales
MMD	mass median diameter
\dot{n}	particle number flux
Oh	Ohnesorge number $\mu_f/(\rho_f d\sigma)^{1/2}$
$PDF(\phi)$	probability density function of ϕ
r	radial distance
Re	Reynolds number, du/v_∞ or dU/v_∞
Re_t	turbulence Reynolds number, $\bar{u}_\infty d/v_t$
Re_w	wake Reynolds number, $l \bar{u}_c / v_\infty$
SMD	Sauter mean diameter
t	time
t_b	breakup time
t^*	characteristic breakup time, $d_o(\rho_L/\rho_G)^{1/2}/u_o$
u	streamwise velocity
U	streamwise relative velocity
$(U_o)_t$	velocity scale for turbulent wake region
v	crosstream velocity
We	Weber number $\rho_G d_o u_o^2/\sigma$
x	streamwise distance
δ	boundary layer thickness
ϵ	rate of dissipation of turbulence kinetic energy
θ	initial momentum thickness of wake

μ	molecular viscosity
ν	kinematic viscosity
ν_t	effective turbulence kinematic viscosity
ρ	density
σ	surface tension
ϕ	generic property, azimuthal angle

Subscripts

c	centerline value
cr	critical value for drop breakup
f	liquid property
g	gas property
G	gas property
rel	relative to ambient conditions
rem	property of drop forming drop
s	streamwise property
t	turbulent wake region property
w	wake property
o	initial conditions, virtual origin
∞	ambient conditions

Superscripts

$(\bar{})$	time-averaged mean property
$(\bar{})'$	root mean squared fluctuating property

1. INTRODUCTION

Sprays and spray processes have been studied extensively due to their many applications (Faeth 1987, 1990). Nevertheless, sprays are complex multiphase turbulent flows and fundamental understanding of their properties is not well developed — particularly those processes relating to the near-injector dense portion of the flow. This is a serious deficiency because the dense-spray region involves the breakup of the liquid to form a dispersed phase, which is crucial to the mixing properties of sprays, and also develops the initial conditions required to analyze the structure of the better understood dilute portion of sprays. Thus, the objective of the present investigation was to study three aspects of dense sprays that involve drop/gas interactions, namely: (1) secondary drop breakup, which is an intrinsic outcome of primary breakup of the liquid, and is the most significant rate process of dense sprays; (2) turbulence generation by dispersed phases, which is the most significant source of turbulence production within dense sprays; and (3) the structure of sphere wakes at moderate Reynolds numbers, which is a fundamental property needed to understand the mechanism of turbulence generation. The research has relevance to air-breathing propulsion systems, liquid rocket engines and internal combustion engines, among others.

The following description of the research is relatively brief. Additional details may be found in articles, papers and theses resulting from the investigation that are summarized in Table 1. This table also provides a summary of participants in the investigation and oral presentations of portions of the research results. Finally, for convenience, several articles resulting from the research are reproduced in appendices, including: Faeth (1990), Hsiang and Faeth (1992), Parthasarathy and Faeth (1990a,b), Mizukami et al. (1992) and Wu and Faeth (1992).

Table 1. Summary of Investigation

Articles, Papers and Theses:

- Faeth, G. M. (1990) Structure and atomization properties of dense turbulent sprays. Twenty-third Symposium (International) on Combustion, The Combustion Institute, Pittsburgh, 1345-1352.
- Faeth, G. M. and Parthasarathy, R. N. (1989) Homogeneous particle-laden flows: 2. turbulent dispersion. Bull. Amer. Phys. Soc. 34, 2312 (abstract only).
- Faeth, G. M. and Wu, J. S. (1991) Structure of the wakes of spheres at moderate Reynolds numbers. Bull. Amer. Phys. Soc. 36, 2625 (abstract only).
- Faeth, G. M., Mizukami, M. and Parthasarathy, R. N. (1990) Particle-generated turbulence in homogeneous dilute dispersed flows. Bull. Amer. Phys. Soc. 35, 2286 (abstract only).
- Hsiang, L.-P. and Faeth, G. M. (1992) Near-limit drop deformation and secondary breakup. Int. J. Multiphase Flow 18, 635-652.
- Hsiang, L.-P. and Faeth, G. M. (1993) Deformation and secondary breakup of drops. AIAA Paper No. 93-0814.

- Mizukami, M., Parthasarathy, R. N. and Faeth, G. M. (1992) Particle-generated turbulence in homogeneous dilute dispersed flows. Int. J. Multiphase Flow 18,397-412.
- Parthasarathy, R. N. (1989) Homogeneous dilute turbulent particle-laden water flows. Ph.D. thesis, The University of Michigan, Ann Arbor, Michigan.
- Parthasarathy, R. N. and Faeth, G. M. (1989) Homogeneous particle-laden flows:1. continuous-phase turbulence properties. Bull. Amer. Phys. Soc. 34, 2312 (abstract only).
- Parthasarathy, R. N. and Faeth, G. M. (1990a) Turbulence modulation in homogeneous dilute particle-laden flows. J. Fluid Mech. 220, 485-514.
- Parthasarathy, R. N. and Faeth, G. M. (1990b) Turbulent dispersion of particles in self-generated homogeneous turbulence. J. Fluid Mech. 220, 515-537.
- Ruff, G. L. (1990) Structure and mixing properties of the near-injector region of nonevaporating pressure-atomized sprays. Ph.D. thesis, The University of Michigan, Ann Arbor, Michigan.
- Ruff, G. A., Bernal, L. P. and Faeth, G. M. (1990) High speed in-line holocinematography for dispersed-phase dynamics. J. Appl. Optics 29, 4544-4546.
- Ruff, G. A., Bernal, L. P. and Faeth, G. M. (1991) Structure of the near-injector region of non-evaporating pressure-atomized sprays. J. Prop. Power 7, 221-230.
- Ruff, G. A., Wu, P.-K., Bernal, L. P. and Faeth, G. M. (1992) Continuous-and dispersed-phase structure of dense nonevaporating pressure-atomized sprays. J. Prop. Power 8, 280-289.
- Wu, J. S. and Faeth, G. M. (1992a) Sphere wakes in still surroundings at intermediate Reynolds numbers. AIAA J. in press.
- Wu, J. S. and Faeth, G. M. (1992b) Sphere wakes in turbulent surroundings at intermediate Reynolds numbers. AIAA J., submitted.

Participants:

Faeth, G. M., Principal Investigator, Professor, The University of Michigan

Hsiang, L.-P., Graduate Student Research Assistant, Doctoral Candidate, The University of Michigan.

Mizukami, M., Graduate Student Research Assistant, The University of Michigan; currently, Research Engineer, Propulsion Systems Division, NASA Lewis Research Center.

Parthasarathy, R. N., Graduate Student Research Assistant, Doctoral Candidate, The University of Michigan; currently Research Scientist, Institute of Hydraulic Research, University of Iowa.

Ruff, G. A., Graduate Student Research Assistant, Doctoral Candidate, The University of Michigan; currently, Assistant Professor, Mechanical Engineering, Drexel University.

Wu, J. S., Graduate Student Research Assistant, Doctoral Candidate, The University of Michigan.

Oral Presentations:

Faeth, G. M., "Separated-flow and breakup phenomena in dense sprays," ASME Workshop on Issues in Spray Systems, Philadelphia, PA, August 1989.

Faeth, G. M., "Structure of dense pressure-atomized sprays," Mechanical Engineering Seminar, Carnegie-Mellon University, Pittsburgh, PA, September 1989.

Faeth, G. M., "Homogeneous particle-laden flows. 2. Turbulent dispersion," 42nd Annual Meeting, American Physical Society, Division of Fluid Dynamics, Palo Alto, CA, November 1989.

Faeth, G. M., "Progress concerning dense spray processes," International Atomization and Spray Systems Conference, Hartford, CT, May 1990.

Faeth, G. M., "Atomization and mixing in dense turbulent sprays," Twenty-Third Symposium (International) on Combustion, Orleans, France, July 1990.

Faeth, G. M., "Turbulence generation in homogeneous dilute particle/liquid or gas flows," Mechanical Engineering Seminar, Wayne State University, Detroit, MI, September 1990.

Faeth, G. M., "Particle-generated turbulence in homogeneous dilute dispersed flows," 43rd Annual Meeting, American Physical Society, Division of Fluid Dynamics, Ithaca, NY, November 1990.

Faeth, G. M., "Structure and breakup processes of dense sprays," Mechanical and Aerospace Engineering Seminar, Princeton, NJ, December 1990.

Faeth, G. M., "Optical diagnostics for combustion studies," NSF Workshop on Particulate Two-Phase Flow Visualization, Washington, DC, March 1991.

Faeth, G. M., "Structure, breakup and turbulence interactions in sprays," NSF Workshop on Atomization and Sprays 2000, Gaithersburg, MD, July 1991.

Faeth, G. M., "Structure of the wakes of spheres at moderate Reynolds numbers," 44th Annual Meeting, American Physical Society, Division of Fluid Dynamics, Tempe, AZ, November 1991.

Faeth, G. M., "Secondary drop breakup in the deformation regime," AIAA 30th Aerospace Sciences Meeting, Reno, NV, January 1992.

Hsiang, L.-P., "Near-limit drop breakup from step velocity changes," International Conference on Liquid Atomization and Spray Systems, Gaithersburg, MD, July 1991.

Hsiang, L.-P., "Secondary drop breakup," Gas Dynamics Seminar, University of Michigan, Ann Arbor, MI, October 1991.

Parthasarathy, R. N., "Homogeneous particle-laden flows: 1. Continuous-phase turbulence properties," 42nd Annual Meeting, American Physical Society, Division of Fluid Dynamics, Palo Alto, CA, November 1989.

Wu, J.-S., "Structure of sphere wakes at moderate Reynolds numbers," Gas Dynamics Seminar, University of Michigan, Ann Arbor, MI, February 1992.

The following report considers secondary breakup, turbulence generation, and sphere wakes, in turn. Each section is written so that it stands alone; therefore, readers can skip to sections of interest.

2. SECONDARY BREAKUP

2.1 Introduction

Secondary breakup of drops is an important fundamental multiphase flow phenomenon with applications to propellant combustion and numerous other natural and engineering processes. In particular, recent studies of dense sprays confirm the conventional view of liquid atomization that primary breakup at a liquid surface yields drops that are intrinsically unstable to secondary breakup; and that secondary breakup tends to control mixing rates in dense sprays much like drop vaporization tends to control mixing rates in dilute sprays, see Ruff et al. (1989a,b, 1991, 1992) and Faeth (1987, 1990) and references cited therein. Motivated by these observations, the objectives of this phase of the investigation were to study drop deformation and breakup for well-defined shock wave disturbances.

Reviews of past work on secondary breakup are reported by Hinze (1955), Krzeczowski (1980), Faeth (1987, 1990) and Hsiang and Faeth (1992). The reviews indicate that the regimes of breakup have been defined reasonably well but analogous deformation regimes are unknown, that effects of liquid viscosity (high Oh) on breakup times have not been examined and that information concerning the outcome of breakup is not available. Thus, these issues were emphasized during the present theoretical and experimental investigation. The present description of the research is brief, see Hsiang and Faeth (1992, 1993) for more details.

2.2 Experimental Methods.

Apparatus. A shock tube with the driven section open to the atmosphere was used to generate shock-wave disturbances, see Fig. 1. The driven section was rectangular (38 × 64 mm) with a 6.7 m length to provide 17-24 ms of uniform flow behind the shock wave for test purposes. A vibrating capillary tube generator provided a stream of drops across the shock tube, with an electrostatic separation system used to vary spacing between drops in order to avoid drop/drop interactions. The interactions between the drop stream and the shock wave flow could be observed through windows in the walls of the driven section (25 mm high × 305 mm long).

Instrumentation. Drops were observed in two ways: pulsed shadowgraph photographs and motion pictures to observe overall breakup dynamics, and single-and double-pulse holography to observe the outcome of breakup. The details of these

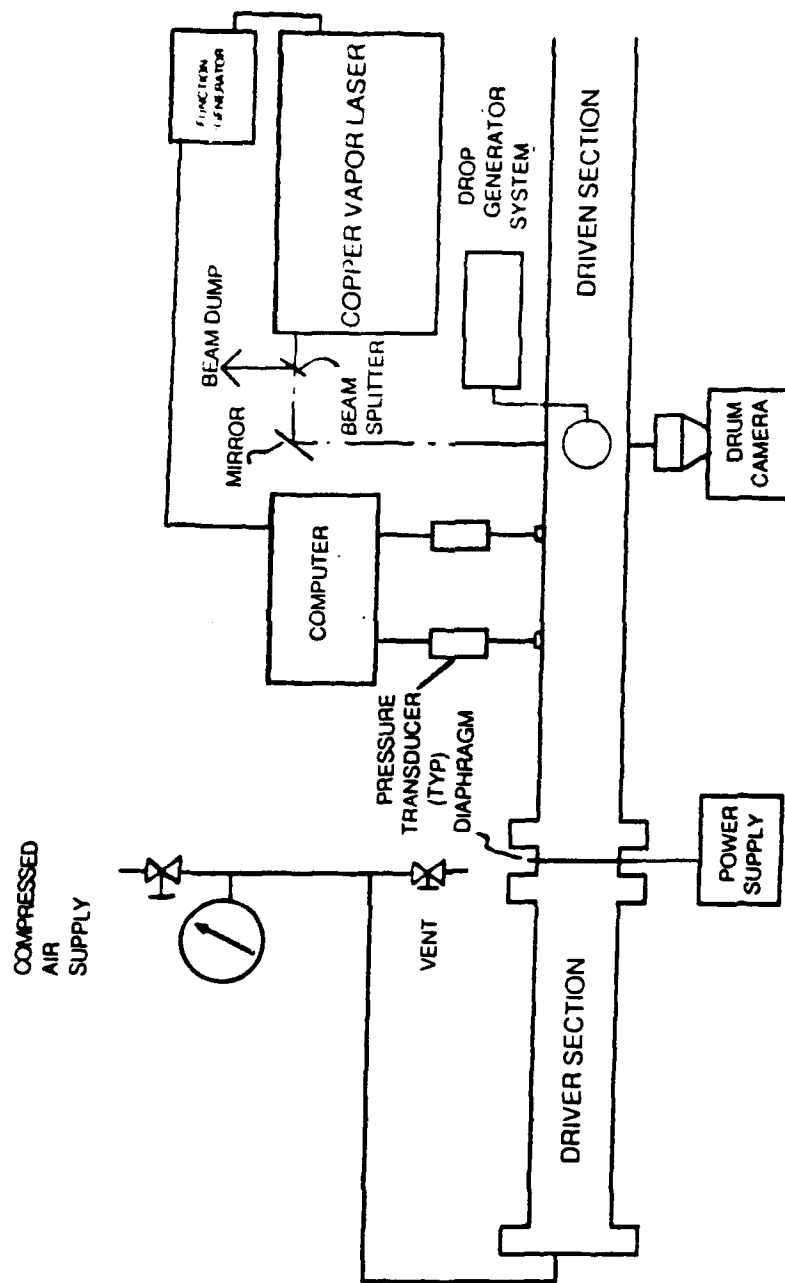


Figure 1. Sketch of the shock tube apparatus

instruments and the resulting uncertainties of the measurements are discussed by Hsiang and Faeth (1992, 1993)

2.3 Results and Discussion

The presentation of results will begin with definition of deformation and breakup regime transitions to help organize the rest of the findings. These transitions are plotted in Fig. 2 as functions of We and Oh , following earlier work (Hinze 1955; Krzeczkowski 1980). Three breakup regimes are delineated: bag breakup, where the center of the drop deforms as a bag in the downstream direction; shear breakup, where drops are stripped from the periphery of the original drop; and multimode breakup, which is a complex combination of the first two modes. In view of the somewhat arbitrary definition of these regimes, the agreement of present results with those of Hinze (1955) and Krzeczkowski (1980) is quite satisfying. The deformation regimes illustrated in Fig. 2 have not been reported before, and involve non oscillatory and oscillatory deformation with the latter regime being relatively limited.

The most striking feature deformation and breakup regime map of Fig. 2 is that progressively higher We numbers are needed for the various transitions as Oh increases. In fact, it appears that breakup might no longer be observed for Oh somewhat greater than 4, which was the highest value observed during the present investigation, with deformation also probably disappearing for somewhat larger values of Oh . This large Oh regime is encountered during spray combustion at high pressures where the surface tension becomes small as the drop approaches thermodynamic critical conditions. Thus, present findings suggest that drops will not shatter into small drops near the thermodynamic critical point, as often thought (Faeth 1990); instead, they will only deform, or simply remain spherical at sufficiently large Oh . This behavior has significant implications concerning spray combustion processes at elevated pressures, however, resolving the issue will require considering liquid/gas density ratios much nearer to unity than the present test conditions.

Drop breakup time is a key parameter needed to understand effects of liquid viscosity through Oh on breakup processes, e.g., as breakup and velocity relaxation times approach one another, the propensity for drop breakup decreases due to reduced relative velocities. Present measurements of breakup times, along with earlier results for shock wave disturbances due to Engel (1958), Simpkins and Bales (1972), Ranger and Nicholls (1969) and Reinecke and coworkers (1969, 1970), are plotted as a function of We in Fig. 3. The breakup times are normalized by the characteristic shear breakup time of Ranger and Nicholls (1969):

$$t^* = d_0 (\rho_L / \rho_G)^{1/2} / u_0 \quad (1)$$

Except for present results, which are grouped according to Oh , the measurements are for $Oh < 0.1$ where effects of liquid viscosity are small. A remarkable feature of the results is that t_b / t^* varies very little even though We varies from 10 to 10^6 for $Oh < 0.1$, yielding $t_b / t^* = 5$. However, t_b progressively increases as Oh increases, yielding the following empirical relationship over the present test range

$$t_b / t^* = 5 / (1 - Oh/7); We < 10^3 \quad (2)$$

This result is consistent with the observation of a limited breakup region as Oh increases but is based on relatively few data with $Oh < 3.5$.

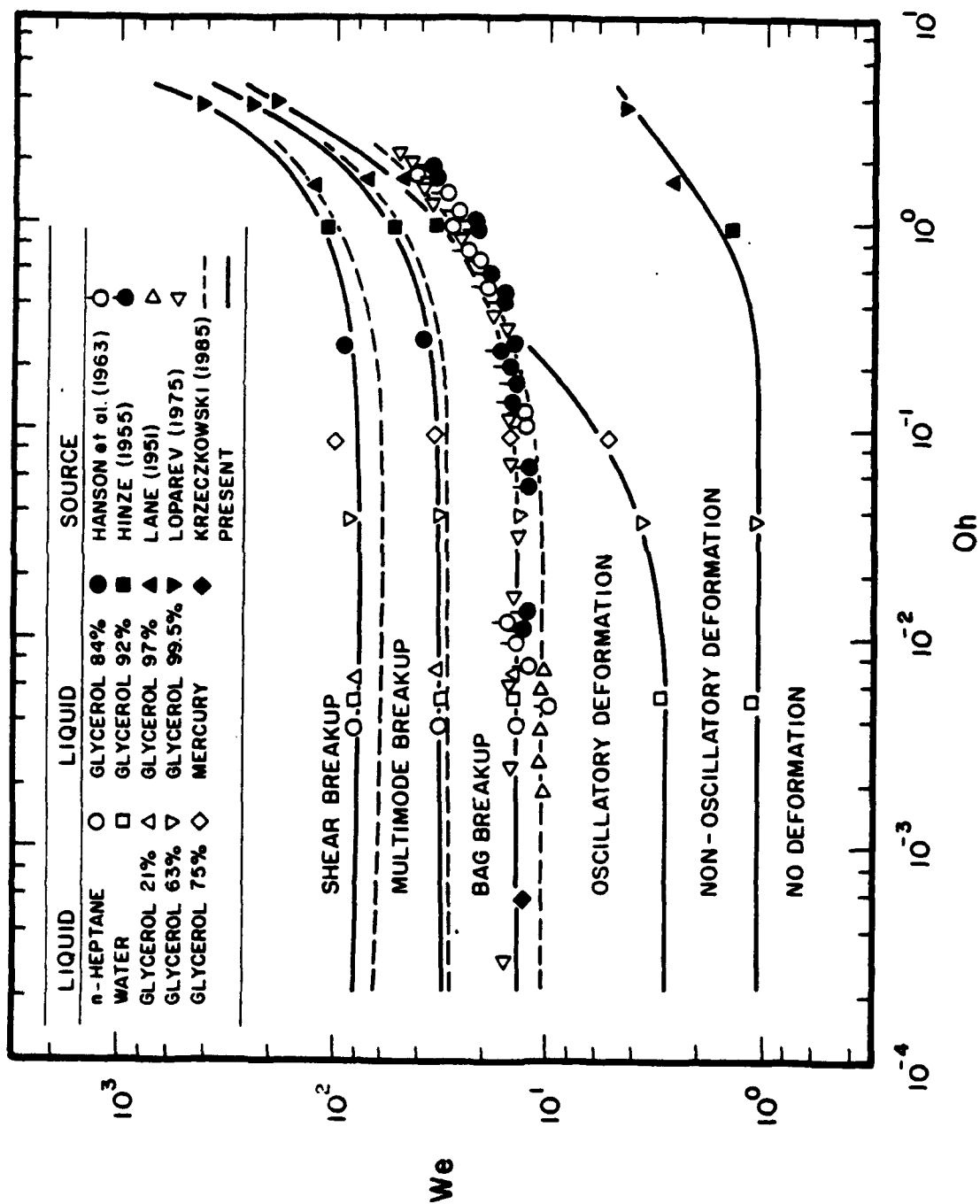


Figure 2. Drop deformation and breakup regime map

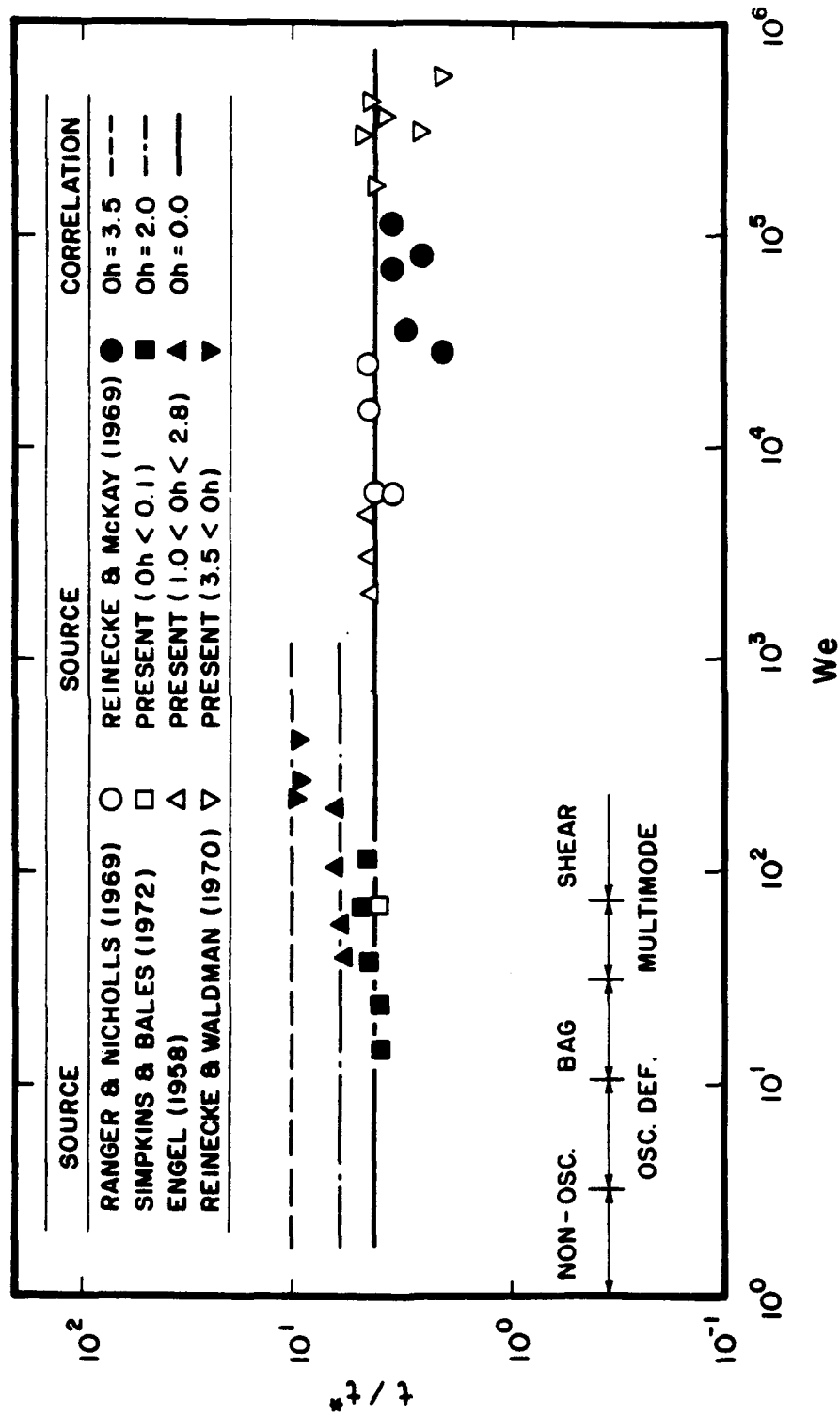


Figure 3. Drop breakup times as a function of We and Oh

Similar to past work on the structure of dense sprays and processes of primary breakup (Ruff et al. 1992; Wu et al. 1992c), drop size distributions after secondary breakup generally satisfied Simmons' (1977) universal root normal distribution with $MMD/SMD = 1.2$. (Hsiang and Faeth 1992). Shear breakup was an exception when the drop-forming drop was considered, however, this deficiency could be eliminated by removing the drop-forming drop from the distribution and treating it separately (Hsiang and Faeth 1993). Thus, the entire drop size distribution can be represented by the SMD alone, which is the practice that will be followed subsequently.

A correlation for the sizes after secondary breakup was developed based on phenomenological analysis of shear breakup that served equally well for the bag and multimode breakup processes (Hsiang and Faeth 1992). Present measurements of drop sizes after secondary breakup are illustrated according to this correlation in Fig. 4. These results are for $Oh < 0.1$ and $We < 10^3$, and yield the following fit:

$$\rho_G SMD u_0^2/\sigma = 6.2 (\rho_L/\rho_G)^{1/4} [\mu_L/(\rho_L d_0 u_0)]^{1/2} We \quad (3)$$

with the overall correlation coefficient of the fit being 0.91. It should be noted, however, that ρ_L/ρ_G does not vary greatly over the present list range and additional measurements are needed to explore density ratio effects. It probably is fortuitous, and certainly surprising, that a single correlation can express the SMD after bag, multimode and shear breakup. However, this behavior is consistent with the observation that their breakup times correlate in the same way, see Fig. 3.

The breakup regimes of Fig. 2 are marked on Fig. 4, assuming that the velocities of the drops after secondary breakup remain at u_0 . If this were the case, drops at initially large We would remain unstable to breakup after the secondary breakup process had occurred, which obviously is not plausible. Recent work has resolved this difficulty by finding drop velocity distributions after secondary breakup and successfully correlating these results using phenomenological theory (Hsiang and Faeth 1993). This shows that variations of drop velocities during secondary breakup are sufficient to reduce We numbers to the stable regime. An exception is the drop forming drop during high We shear breakup, however, in this case, the drop forming drop no longer is subject to shock loading so that it becomes stable even at a large We . These results highlight the fact that We , time and the relative acceleration rates of drops all affect drop breakup, with shock loading only being a convenient limiting process, see Hsiang and Faeth (1993) for additional discussion of this behavior.

2.4 Conclusions

Drop deformation and secondary breakup after shock wave initiated disturbances were studied for a variety of liquids in air at normal temperature and pressure. Major conclusions of the study are as follows:

1. The We for the onset of deformation and breakup regimes increase for increasing Oh , with no breakup observed over the present test range for $Oh > 4$. This suggests that drops do not shatter as they approach their thermodynamic critical point, as generally thought (Faeth 1990); instead, they simply deform or may even remain as spheres for sufficiently large Oh .
2. Unified scaling of breakup times was observed, showing relatively weak effects of We , but increasing breakup times at Oh increased.

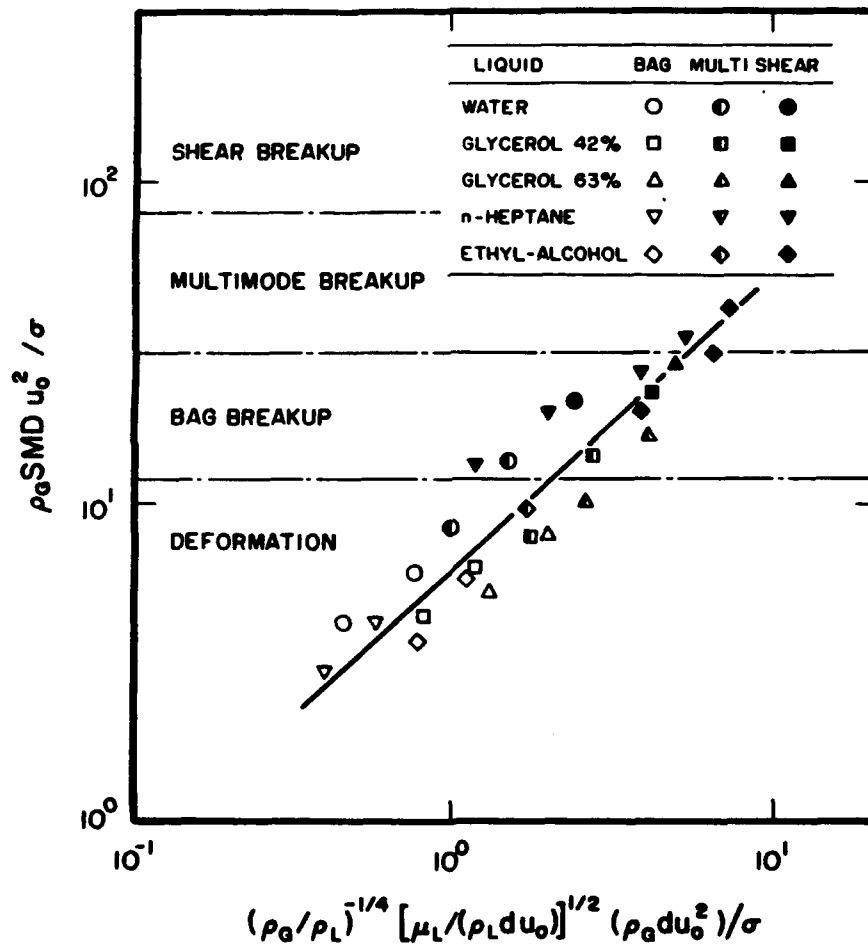


Figure 4. Correlation of SMD after secondary breakup

3. Drop size distributions after secondary breakup satisfied Simmons' (1977) universal root normal distribution with $MMD/SMD = 1.2$. The SMD after secondary breakup could be correlated based on phenomenological analysis of shear breakup for $Oh < 0.1$ and all three breakup regimes.
4. It also was possible to correlate drop velocity distributions after secondary breakup based on phenomenological analysis of the shear breakup regime. These results show that most drops are below stability limits for shock disturbances after secondary breakup while the drop forming drop during shear breakup is stable for its accelerative environment when drop stripping ends.

Most of present test results are for $Oh < 0.1$ and $\rho_L/\rho_G > 500$. Thus, current work is emphasizing test conditions at larger Oh and smaller ρ_L/ρ_G , that are more representative of combusting sprays at the elevated pressures of contemporary propulsion systems.

3. TURBULENCE GENERATION

3.1 Introduction

The objective of this portion of the investigation was to study turbulence generation by the motion of dispersed phases in multiphase flows. Experimental conditions involved uniform fluxes of particles falling in nearly stagnant (in the mean) air, in order to supplement earlier findings for similar particle/water/flows (Parthasarathy and Faeth 1990a,b). A simplified stochastic model of the flow due to Parthasarathy and Faeth (1990a) was used to interpret and correlate both sets of measurements.

Reviews of past work on turbulence generation are reported by Parthasarathy and Faeth (1990a,b) and Mizukami et al. (1992). Based on this status, the objective of the present investigation was to extend the particle/water study of Parthasarathy and Faeth (1990a) to particle/air flows. The main motivation for this step is that rates of dissipation of particle energy in air are orders of magnitude larger than for particles in water at similar conditions so that effects of this important parameter can be resolved. The following description of the research is brief, additional details can be found in Parthasarathy and Faeth (1990a, b) and Mizukami et al. (1992).

3.2 Experimental Methods

Apparatus. A sketch of the particle/air flow apparatus appears in Fig. 5. The tests were conducted using monodisperse spherical glass particles having nominal diameters of 0.5, 1.0 and 2.0 mm. The particles were dispersed by falling through an array of screens and then passed through a windowed test chamber ($410 \times 535 \times 910$ mm) where measurements were made. The particles collected with little rebound at the bottom of the chamber and were removed periodically.

Instrumentation. Measurements involved particle number fluxes, particle velocities and continuous-phase flow properties. Particle number fluxes were measured by collecting particles in containers at the bottom of the test chamber for timed intervals: they were uniform within experimental uncertainties except for the region near the walls of the test chamber. Particle velocities were measured by particle tracking, illuminating the central portion of the tank with a stroboscopic light source and recording the images with an open camera shutter. Continuous-phase mean and fluctuating velocities were measured with a two-point phase discriminating laser velocimeter (LV), identical to Parthasarathy and Faeth (1990a,b). Assessment of flow properties with the LV showed

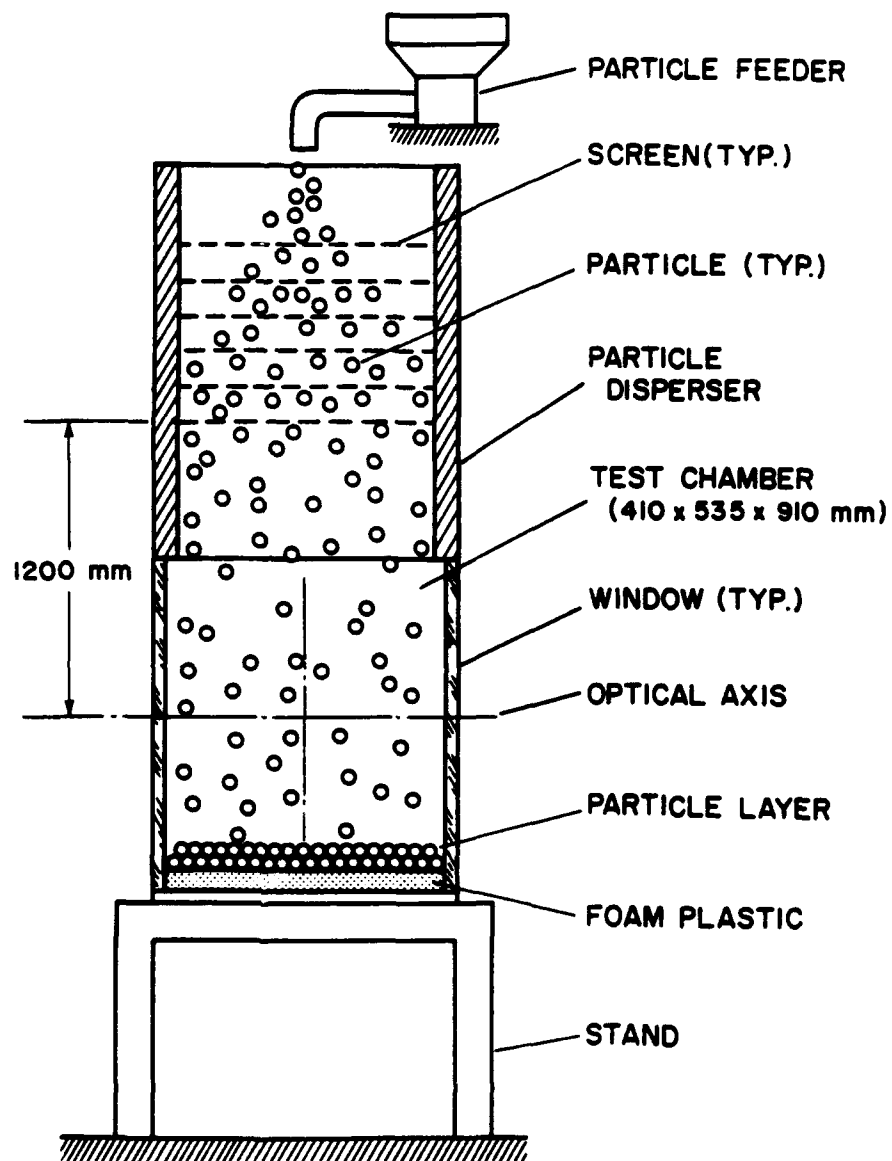


Figure 5. Sketch of homogeneous particle/air flow apparatus

that they were uniform within the central portion of the test chamber (± 120 mm in the cross-stream direction and ± 180 mm in the streamwise direction).

3.3 Theoretical Methods

The simplified analysis of Parthasarathy and Faeth (1990a) was used to help interpret the measurements. The major assumptions of the analysis are as follows: the flows are statistically stationary with uniform particle fluxes and constant continuous-phase properties; particle arrival times are independent of other particle arrival times so that they satisfy Poisson statistics; the flows are infinite in extent, the flows are dilute so that the probability of a test point being within a particle is small; the contribution of flow properties immediately around particles is ignored for the same reason; and because the equations of motion are linear for asymptotic wakes, flow properties are taken to be the result of a linear superposition of particle flow fields (wakes) that have reached a particular position.

Summing flow properties under these assumptions is an extension of methods used to analyze random noise (Rice 1954). Taking the point of observation be the origin of a cylindrical coordinate system and taking the effect of a particle to have mean and turbulent contributions of $\bar{g}(r, \phi, t)$ and $g'(r, \phi, t)$, the resulting mean-squared fluctuation about the average (which is zero for present flows) becomes (Parthasarathy and Faeth 1990a):

$$\bar{G}^2 = \dot{n} \int_{-\infty}^{\infty} dt \int_0^{2\pi} d\phi \int_0^{\infty} [g^2(r, \phi, t) + g'^2(r, \phi, t)] r dr. \quad (4)$$

Equation (4) is for a monodisperse particle or drop flow. Under the assumption of linear superposition, however, if $\phi(d)$ is a generic property for a particular diameter, then the mean value of ϕ becomes:

$$\bar{\phi} = \int_0^{\infty} \phi(d) \text{PDF}(d) dd \quad (5)$$

where PDF(d) is the probability density function of particle diameter.

The main difficulty in applying Eqs. (4) and (5) is that little is known about the properties of particle wakes at modest Reynolds numbers (< 100) in a turbulent environment, as discussed later. Effects of wake turbulence cannot be ruled out because wake Reynolds numbers are greater than unity for the range of interest; therefore, integration to find flow properties used mean turbulent wake properties from existing results for asymptotic turbulent wakes (Uberoi and Freymuth 1970; Tennekes and Lumley 1972). A second problem is that the integrals of Eq. (4) do not converge as $t \rightarrow \infty$. Pending resolution of this difficulty, integrations were terminated at $z/d = 175$, which provides a reasonable fit of the measurements and yields mean wake velocities that are small in comparison to velocity fluctuation levels which would be expected to be lost in the background turbulent field.

3.4 Results and Discussion

Particle-generated turbulence fields are unusual because it is rather simple to find the local rate of dissipation of turbulence kinetic energy, which must be equal to the local loss of particle mechanical energy, e.g.

$$\varepsilon = \pi \dot{n} d^2 C_D U^2/8 \quad (6)$$

Then based on the simplified theory, the following expressions are obtained for the turbulence intensities in the streamwise and crosstream directions (Mizukami et al. 1992):

$$(\bar{u}^2)^{1/2}/(C_u U) = (\bar{v}^2)^{1/2}/(C_v U) = [\epsilon d(\theta/d)^{2/3}/U^3]^{1/2} \quad (7)$$

where $C_u = 6.84$ and $C_v = 4.63$. Results are plotted according to Eq. (7) in Fig. 6, indicating excellent agreement between predictions and measurements for a 1000:1 variation of the independent variable (the dissipation factor) with both air and water as the continuous phase. Relative turbulence intensities from this mechanism are appreciable, approaching 10% for large values of the dissipation factor — which approaches conditions typical of dense sprays.

An interesting feature of particle-generated turbulence is that it exhibits a large range of scales even though the Reynolds numbers of the particles themselves are relatively low (< 1000). This is illustrated in Fig. 7 by the temporal power spectral densities of crosstream velocity fluctuations. These results are for particles in air but results for particles in liquids are similar. The measurements are accompanied by a prediction that ignores the contribution of wake turbulence; this limitation is not significant because wake turbulence only makes a small contribution which is at frequencies higher than could be resolved by the measurements. Additionally, sampling limitations prevent correct measurements of spectra at frequencies higher than the step-noise limit marked on the plot. The unusually broad spectrum is clearly evident; additionally the spectra decay according to $f^{-1.5}$ rather than $f^{-5/3}$ which is characteristic of the inertial range of conventional turbulence. The theory is in excellent agreement with the measurements which helps explain these differences between the spectra; namely, the turbulence properties differ because they result from mean velocity distributions in randomly-arriving particle particles, with the large range of scales involved because flow properties are strongly affected by wake mean velocities.

Other spatial and temporal correlations and spectra were measured and successfully correlated, providing a rather complete description of this novel form of turbulence, see Parthasarathy and Faeth (1990a) and Mizukami et al. (1992). Figure 8 provides measured and predicted streamwise and crosstream spatial integral scales as an example. The results are plotted as suggested by the theory but reoptimized to best fit the measurements. The integral scales exhibit significant anisotropy, with $L_{ux}/L_{uy} = 3.9$, which is typical of shear flows like wakes (Hinze 1975). The range of scales also is unusually large with integral scales being 150-300 times Kolmogorov length scales, which implies effective turbulence Reynolds numbers of 1000-2000 in terms of conventional turbulence properties, even though particle Reynolds numbers generally were ca. 100. This behavior also follows because mean velocities of particle wakes contribute to the turbulence field.

3.5 Conclusions

The present investigation considered the properties of particle-generated turbulence for homogeneous conditions. The major conclusions are as follows:

1. Relative turbulence intensities and integral scales could be correlated as functions of the dissipation factor, $\epsilon d(\theta/d)^{2/3}/U^3$. Relative turbulence intensities from this mechanism can be quite large, approaching 10% for conditions comparable to dense sprays.
2. A number of features of particle-generated turbulence are similar to other homogeneous turbulent flows: probability density functions of velocity fluctuations

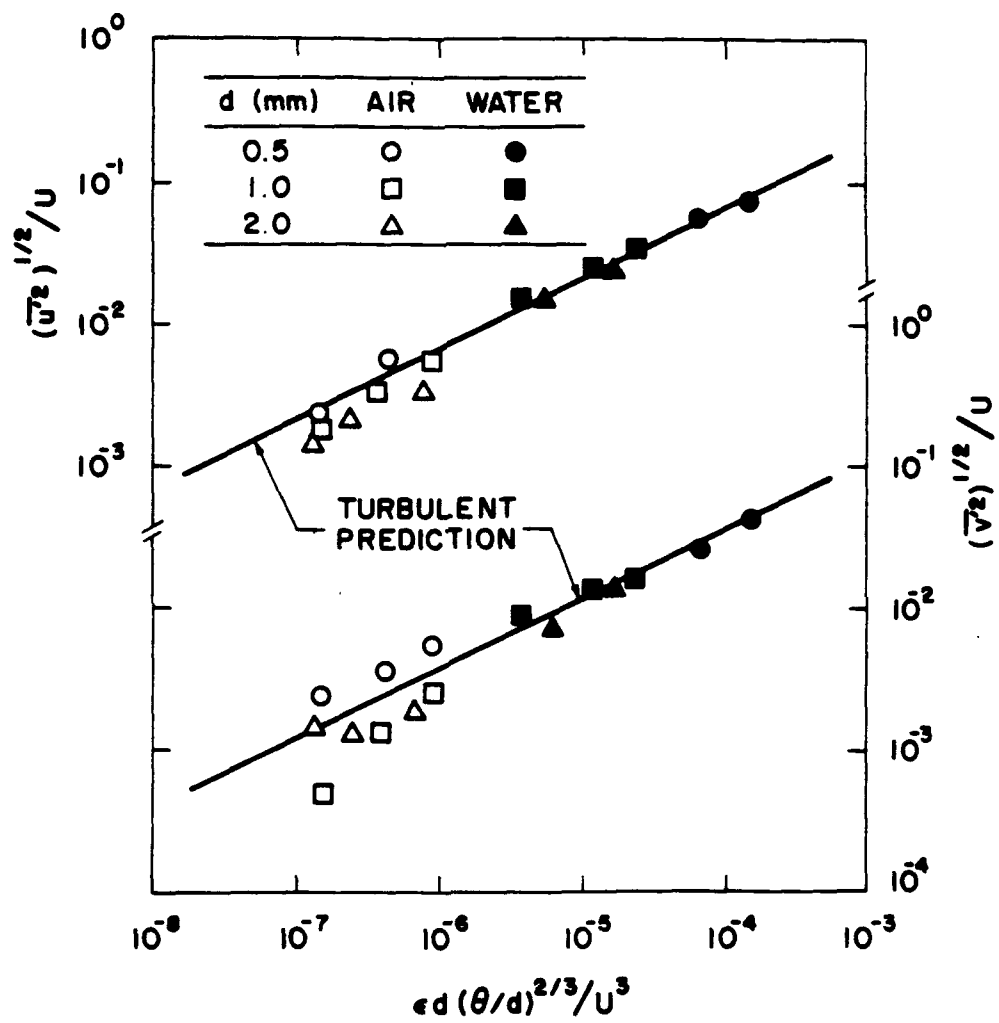


Figure 6. Streamwise and crosstream r.m.s. velocity fluctuations

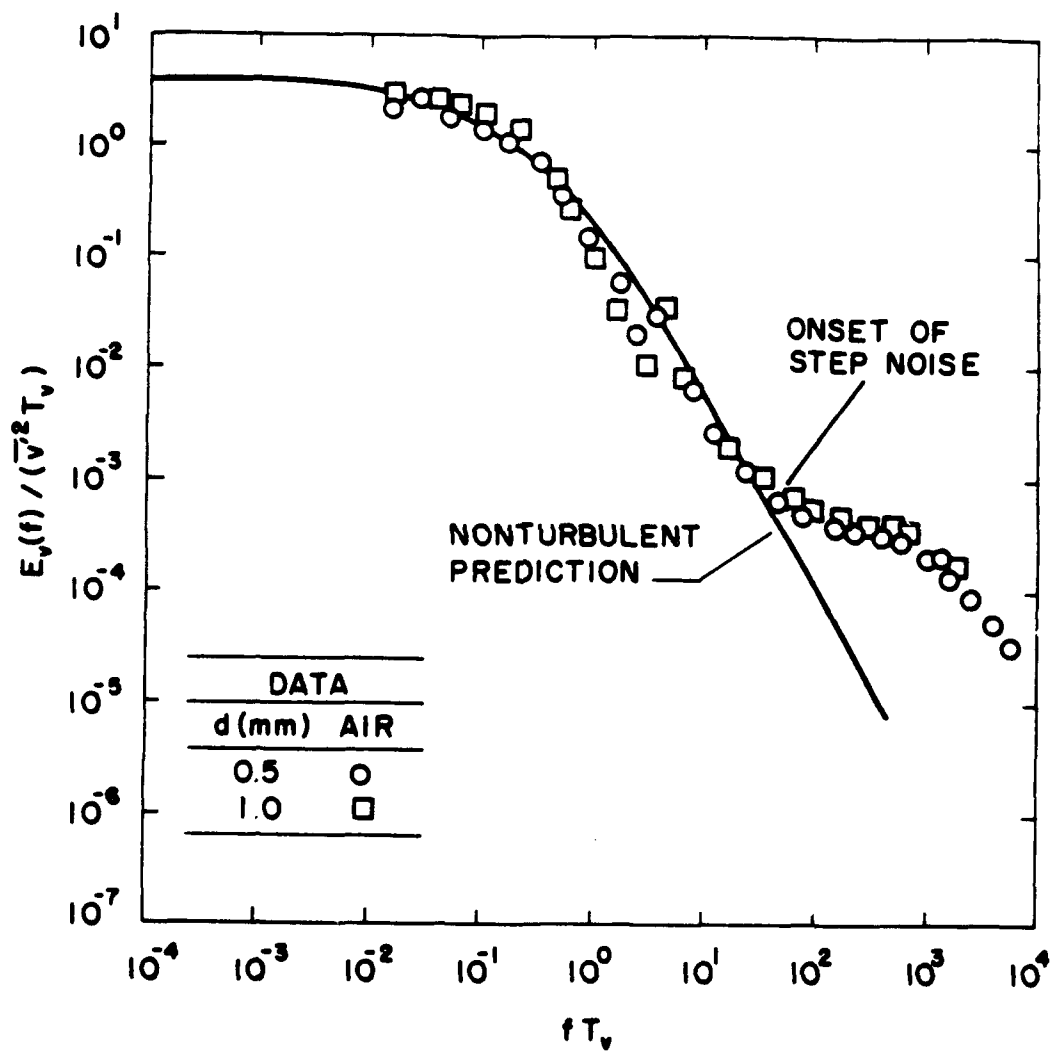


Figure 7. Temporal power spectra of crosstream velocity fluctuations

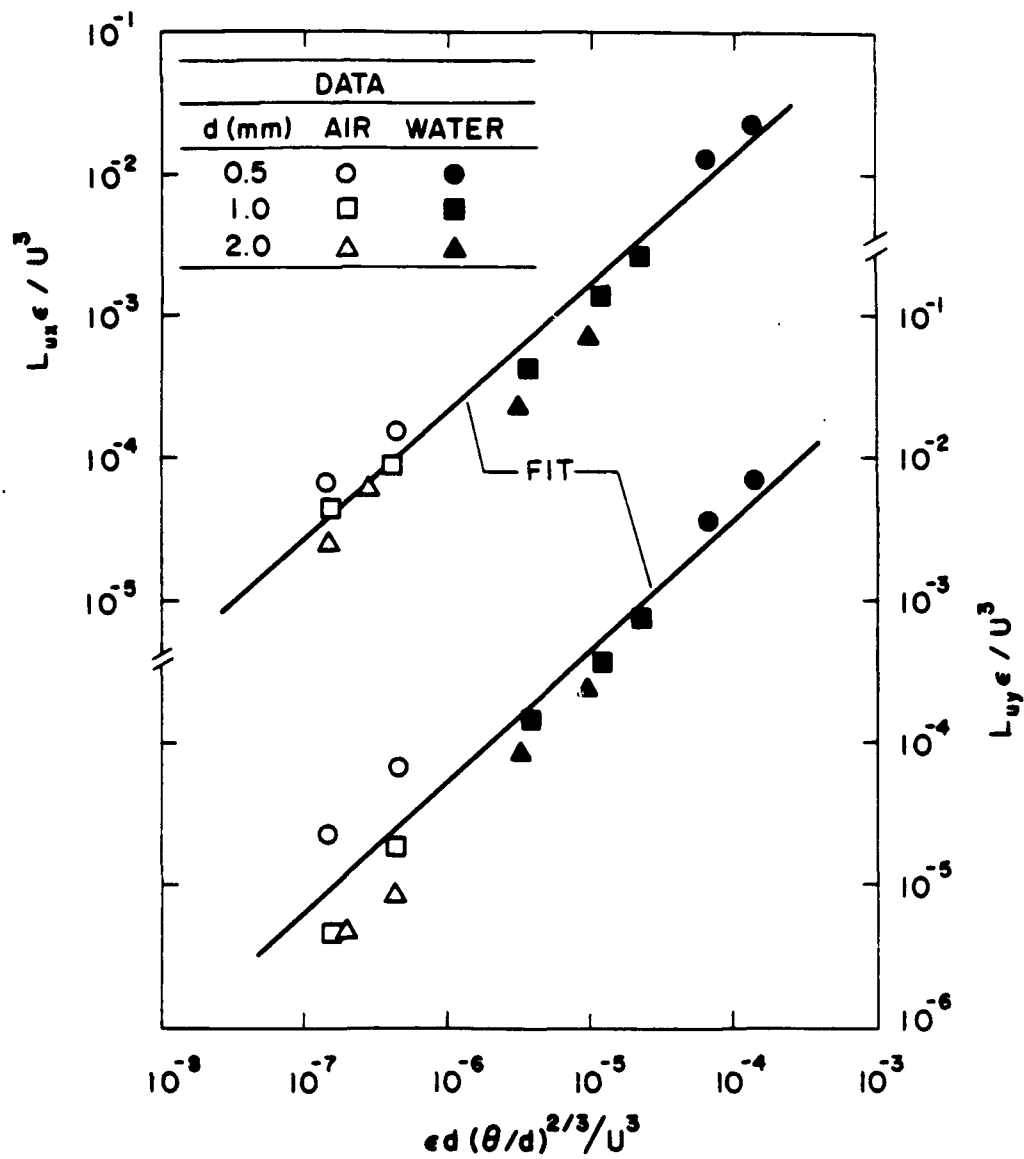


Figure 8. Streamwise and crosstream spatial integral scales

are Gaussian, and normalized spatial correlations and temporal spectra are relatively independent of flow conditions.

3. However, a number of features of particle-generated turbulence are distinctly different from conventional turbulence due to contributions from the mean velocities of randomly-arriving particle wakes: the anisotropy is unusually large with streamwise relative turbulence intensities roughly twice crosstream values, length scales correlate with wake properties and are independent of the average spacing between particles, ranges of length and time scales are unusually large even though particle Reynolds numbers are modest, and spectra decay at rates with respect to frequency at much lower rates than conventional turbulence, e.g., $f^{-1.1}$ and $f^{-1.5}$ rather than $f^{-5/3}$ for crosstream and streamwise temporal spectra.
4. A simplified model, based on linear superposition of randomly-arriving particle velocity fields, was helpful for explaining many features of the flow. However, more information on the character of particle wakes at modest Reynolds numbers in turbulent environments is needed to assess the theory quantitatively — work along these lines will be considered next.

4. SPHERE WAKES

4.1 Introduction

Flow associated with spheres has attracted attention due to numerous applications, e.g., dispersed particle-laden flows, sprays and rainstorms, among others. The work on turbulence generation by dispersed phases discussed in Section 3, however, has shown the need for more information about sphere wakes at the intermediate sphere Reynolds numbers ($10 < Re < 10^3$) typical of drops in sprays. Thus, the objective of this phase of the investigation was to measure flow properties near spheres at intermediate Reynolds numbers, considering both quiescent and turbulent environments.

A review of past work of the flow near spheres is provided by Wu and Faeth (1992). The results of this review indicated that there is relatively little information available about effects of vortex shedding on flow properties, and the properties of wakes at intermediate Reynolds numbers, including even whether these wakes are laminar or turbulent. Thus, the objective of the present study was to seek information to help resolve these issues. Two experimental configurations were considered, involving towed spheres in a quiescent water bath, and spheres mounted near the axis of fully developed turbulent pipe flow in air. The following description of the research is brief, additional details can be found in Wu and Faeth (1992a, b).

4.2 Experimental Methods

Apparatus. A sketch of the test apparatus for sphere flow in a quiescent environment is illustrated in Fig. 9. The approach involved traversing test spheres through a still liquid bath ($415 \times 535 \times 910$ mm) and observing flow properties at the center of the bath. The sides and bottom of the bath were insulated (not shown in the figure) to minimize natural convection disturbances, except for small openings for optical access. The bath liquid was water or various glycerol mixtures to provide a range of sphere Reynolds numbers. The test sphere was a 10 mm diameter plastic ball mounted on taut 125 μ m diameter stainless steel wire. The sphere was traversed at constant velocity for a 700 mm length, nearly symmetric about the measuring location, using a stepping motor driven linear positioner. The position of the sphere could be traversed

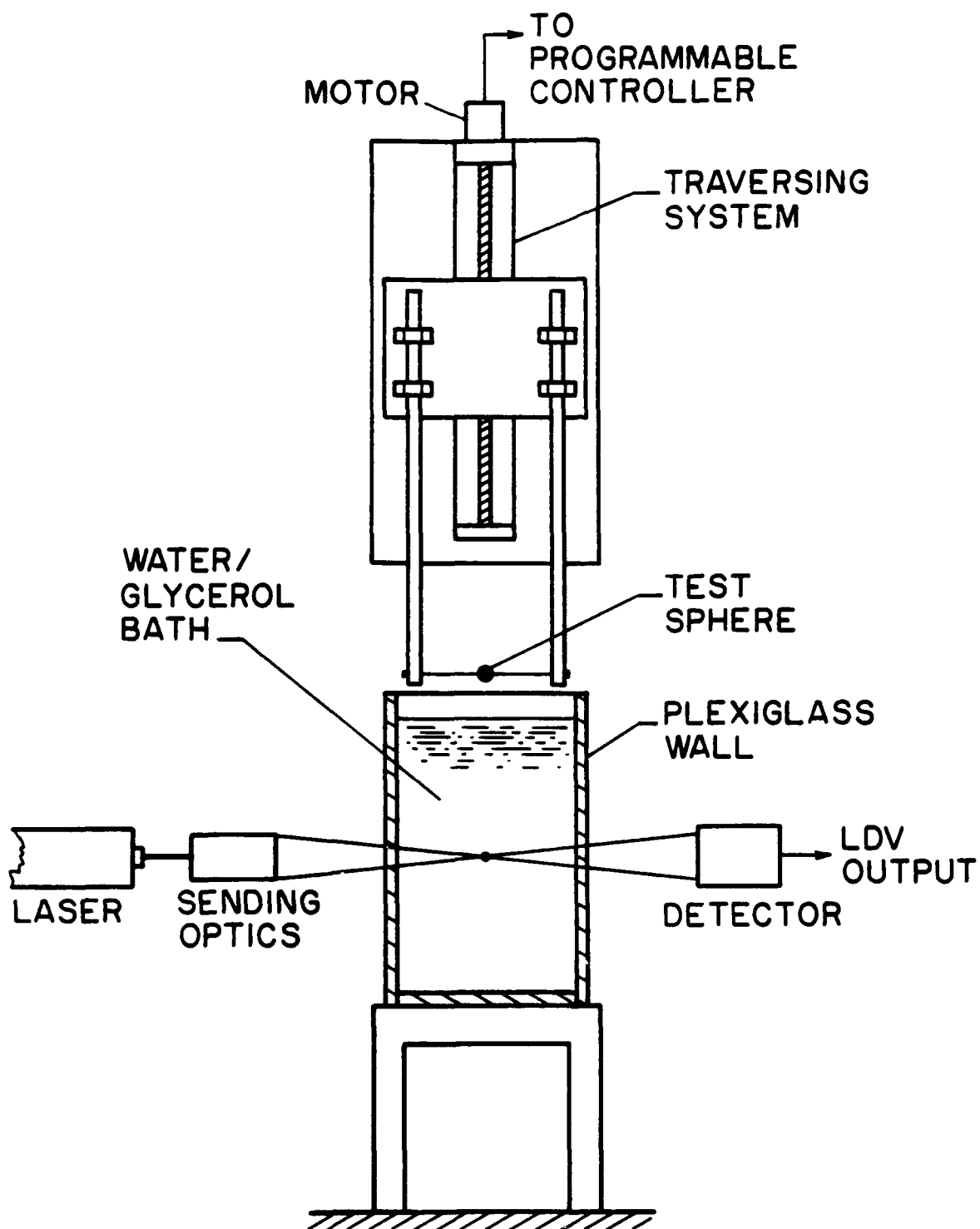


Figure 9. Sketch of the sphere wake apparatus for a quiescent environment

normal to the direction of the wire to access different positions in the flow, with the sphere traverse itself providing access to various streamwise positions.

The test apparatus for spheres in a turbulent environment is illustrated in Fig. 10. In this case, the test sphere was mounted near the axis of a fully developed turbulent pipe flow of air, within a 300 mm diameter duct. The test sphere could be traversed in three directions to accommodate rigidly mounted instrumentation. Small plastic spheres (diameters of 1.2 - 5.6 mm) mounted on fine wires (51 and 127 μm in diameter) in tension were studied. Calibration of flow properties in the pipe indicated rather close correspondence of the turbulence properties to existing results for fully-developed turbulent pipe flow, e.g. Laufer's (1954) results cited in Hinze (1975) for corresponding pipe Reynolds numbers.

Instrumentation. Light sheet illuminated dye traces were used to observe the flow near the spheres in quiescent environments. The resulting dye pattern was photographed with exposure times of 1 - 4 ms to stop the motion of the fluid.

Quantitative measurements in both flows were made using laser velocimetry with an arrangement similar to Parthasarathy and Faeth (1990a). The results for traversing spheres (quiescent environments) were obtained by ensemble averaging measurements from 20 - 120 traverses at a particular position. For spheres in turbulent environments, results were time-averaged in a conventional manner.

4.3 Results and Discussion

Quiescent Environment. Flow visualization showed that the recirculation zone on the downstream side of the sphere was stable and symmetric for $Re < 200$, stable and unsymmetric for $200 < Re < 280$, and unstable with vortex shedding for $Re > 280$. The transition to vortex shedding was similar to earlier findings in the literature, e.g. transition Re in the range 270 - 300.

Streamwise mean velocities along the axis are illustrated in Fig. 11 for Re extending up to vortex shedding conditions. The results show the presence of three wake regions: a fast decay wake region near the sphere when vortex shedding is present (barely visible at $Re = 280$ but more pronounced at higher Re), a turbulent wake region where $\bar{u}_c \sim (x-x_0)^{-2/3}$, and a laminar wake region where $\bar{u}_c \sim (x-x_0)^{-1}$ — the last two regions corresponding to classical similarity behavior for turbulent and laminar wakes, respectively. The fast-decay wake region ends by smoothly transitioning into turbulent wake behavior. Similarly, the transition from turbulent to laminar wake behavior is smooth and occurs at a wake Reynolds number, Re_w , of roughly 10. Thus, for low levels of turbulence generation, where the continuous phase is nearly quiescent, particle wakes largely exhibit turbulent behavior until a final decay to a laminar wake.

Radial profiles of mean velocities in the important turbulent wake region are plotted in terms of classical similarity parameters, see Tennekes and Lumley (1972), in Fig. 12. Results of Uberoi and Freymuth (1970) for a sphere Reynolds number, $Re = 8600$, and Chevray (1968) for $Re = 458,000$ are shown on the plots along with present results at much lower Re . Remarkably, all the results are nearly identical even though present measurements involve rather low wake Reynolds numbers.

The character of the decay of turbulence near transition from a turbulent to a laminar wake is illustrated in Fig. 13. Turbulence intensities at the axis are plotted as a function of wake Reynolds number for present results as well as results from Uberoi and Freymuth (1970) and Carmodey (1964) at generally higher wake Reynolds numbers. For

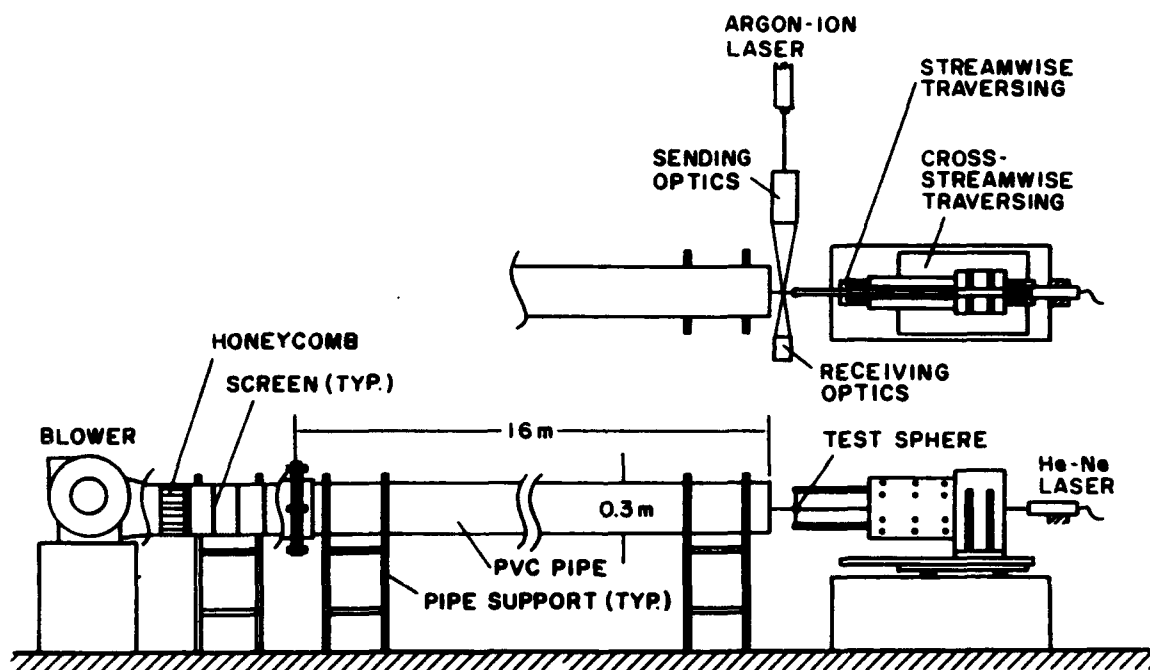


Figure 10. Sketch of the sphere wake apparatus for a turbulent environment

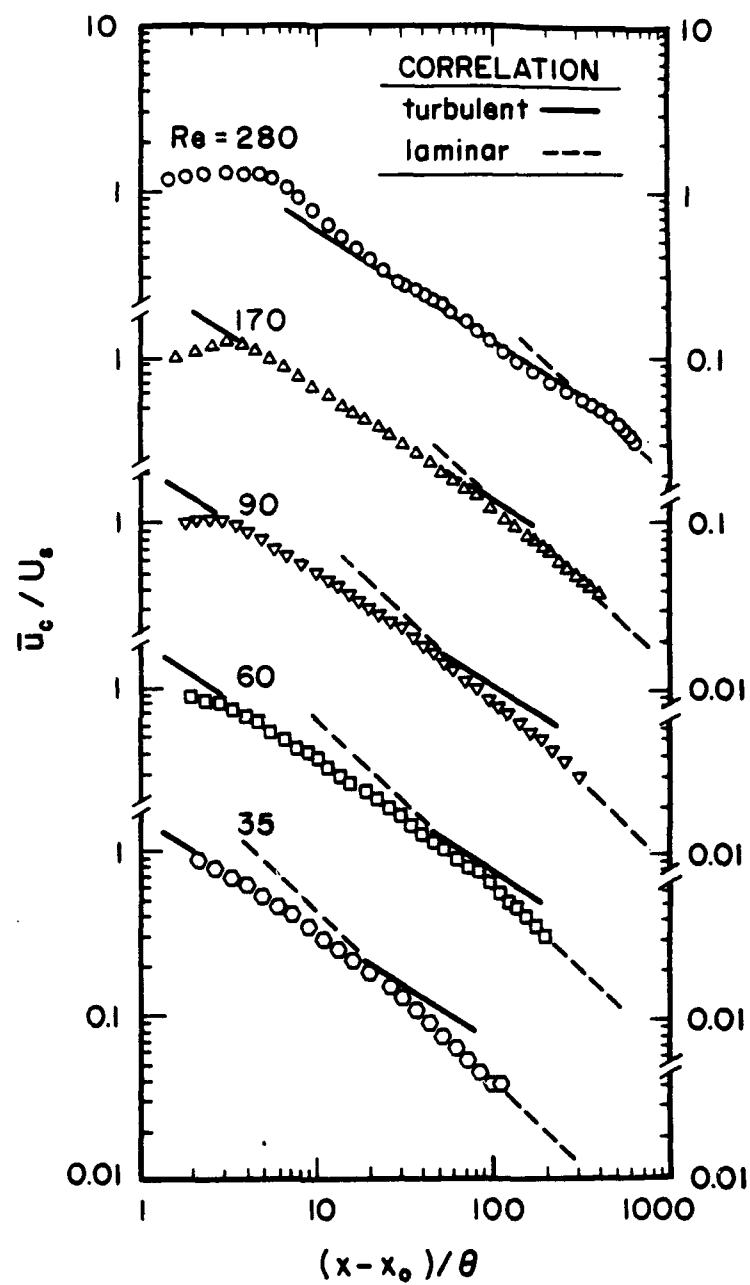


Figure 11. Mean streamwise velocities along the wake axis for a quiescent environment

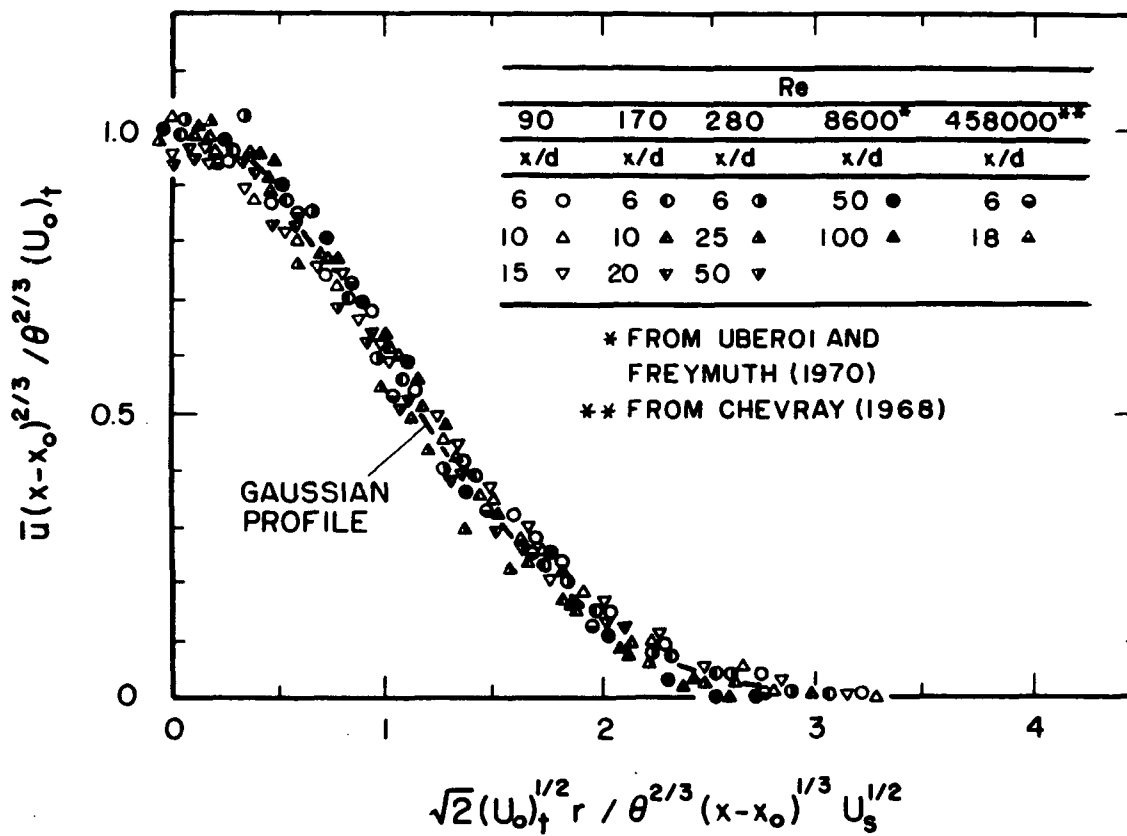


Figure 12. Radial profiles of mean streamwise velocities in the turbulent wake region for a quiescent environment

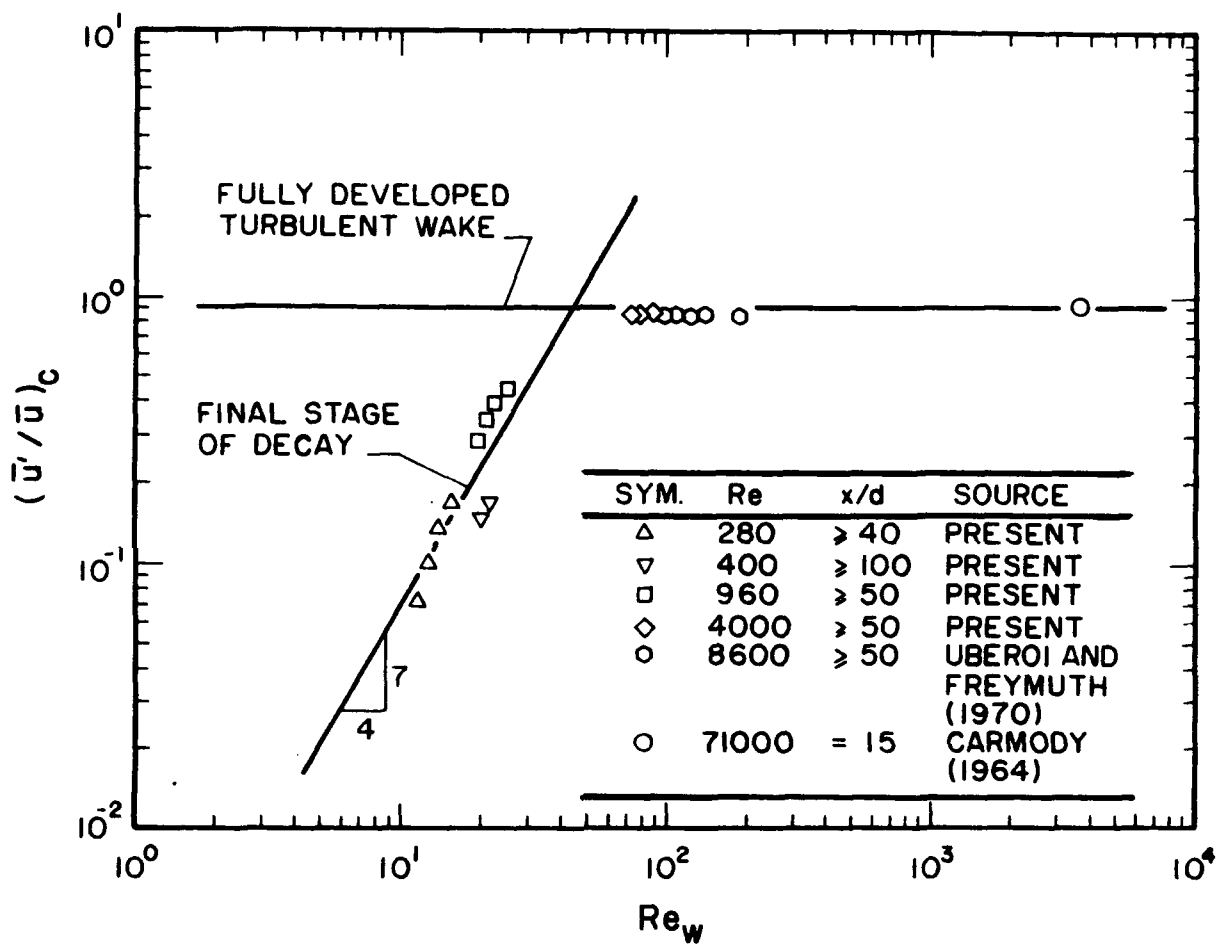


Figure 13. Streamwise turbulence intensities along the axis of wakes in a quiescent environment

$Re_w > 70$, turbulence intensities along the axis are nearly constant with $(\bar{u}'\bar{u})_c$ in the range 0.85 - 0.92. At lower Re_w , however, turbulence intensities rapidly decrease in a final decay period. Based on analysis of the final decay period of axisymmetric wakes (Phillips 1956; Lee and Tan 1967), behavior in this region should be as follows (Wu and Faeth 1992a):

$$(\bar{u}'\bar{u})_c = C Re_w^{7/4} \quad (8)$$

Present results are in excellent agreement with Eq. (8), with $C = 1.3 \times 10^{-3}$ yielding the best fit of the data. In view of the relatively large velocity fluctuations upon transition to the laminar wake region (for $Re_w \sim 10$) it is remarkable that radial profiles of mean velocities in the laminar wake region are in excellent agreement with classical laminar wake scaling (Wu and Faeth 1990a). This can be explained, however, by noting that turbulence in the final decay period is not connected over the crosssection of the wake; instead it involves noninteracting regions of decaying turbulence or turbulence spots (Batchelor and Townsend 1948). Thus, the absence of connectedness prevents mixing or entrainment by large-scale structures so that entrainment follows laminar scaling with mean velocities adjusting to this behavior as well.

Turbulent Environment. Sphere wakes at moderate Reynolds numbers in turbulent environments also exhibited a number of surprising features. The first of these is illustrated in Fig. 14, which is a plot of streamwise velocities along the axis for sphere Reynolds numbers in the range 135 - 1560. In this case, all the results yield scaling satisfying laminar wake similarity even though the flow is clearly turbulent (ambient turbulence intensities are roughly 4% and intensities within the wakes generally are larger). This behavior can best be explained by noting that while the scaling is laminar-like, the effective (turbulent) viscosities generally are 2 - 50 times larger than the molecular viscosity over the test range. Thus, the effect of the ambient turbulence is to provide a turbulent fluid whose effective viscosity is large enough so that global scaling follows laminar scaling laws.

The laminar-like scaling of wakes in turbulent environments is clearly shown by the radial profiles of mean streamwise velocities plotted in Fig. 15. The scaling in both the streamwise and crossstream directions follows conventional laminar wake scaling rules (Schlichting 1977) with the effective turbulent viscosity only varying with the sphere Reynolds number. As might be anticipated from the results of Fig. 14, laminar scaling provides an excellent representation of the measurements, well within experimental uncertainties.

The next important issue is the behavior of the effective turbulent viscosity. First of all, it was found that the effective turbulent viscosity had a single value for a particular sphere Reynolds number. This behavior is illustrated in Fig. 16 for the present range of Re and sphere diameters of 1.2 - 5.6 mm. The ratio ν_t/ν progressively increases with Re but exhibits three ranges: a low Re regime for $Re < 300$, a transition regime for $300 < Re < 600$, and a high Reynolds number regime for $Re > 600$. The ratio, $\nu_t/\nu \sim Re$ in the low and high Reynolds number regimes with a greater variation with Re in the transition regime. Thus, the scaling in the low and high Re regimes is consistent with conventional eddy viscosity ideas (Tennekes and Lumley 1972), even though scaling of the mean velocities themselves is laminar-like. Finally, the transition regime is consistent with an effect of onset of eddy shedding. In particular, temporal spectra in the wake exhibited the appearance of a spike when $Re \approx 300$, very similar to the onset of eddy shedding in quiescent environments. Furthermore, the spike gradually disappeared for $Re > 600$ suggesting evolution into a highly turbulent regime consistent with the high Re branch of ν_t/ν . Finally, it is not surprising that the onset of eddy shedding is not very different for

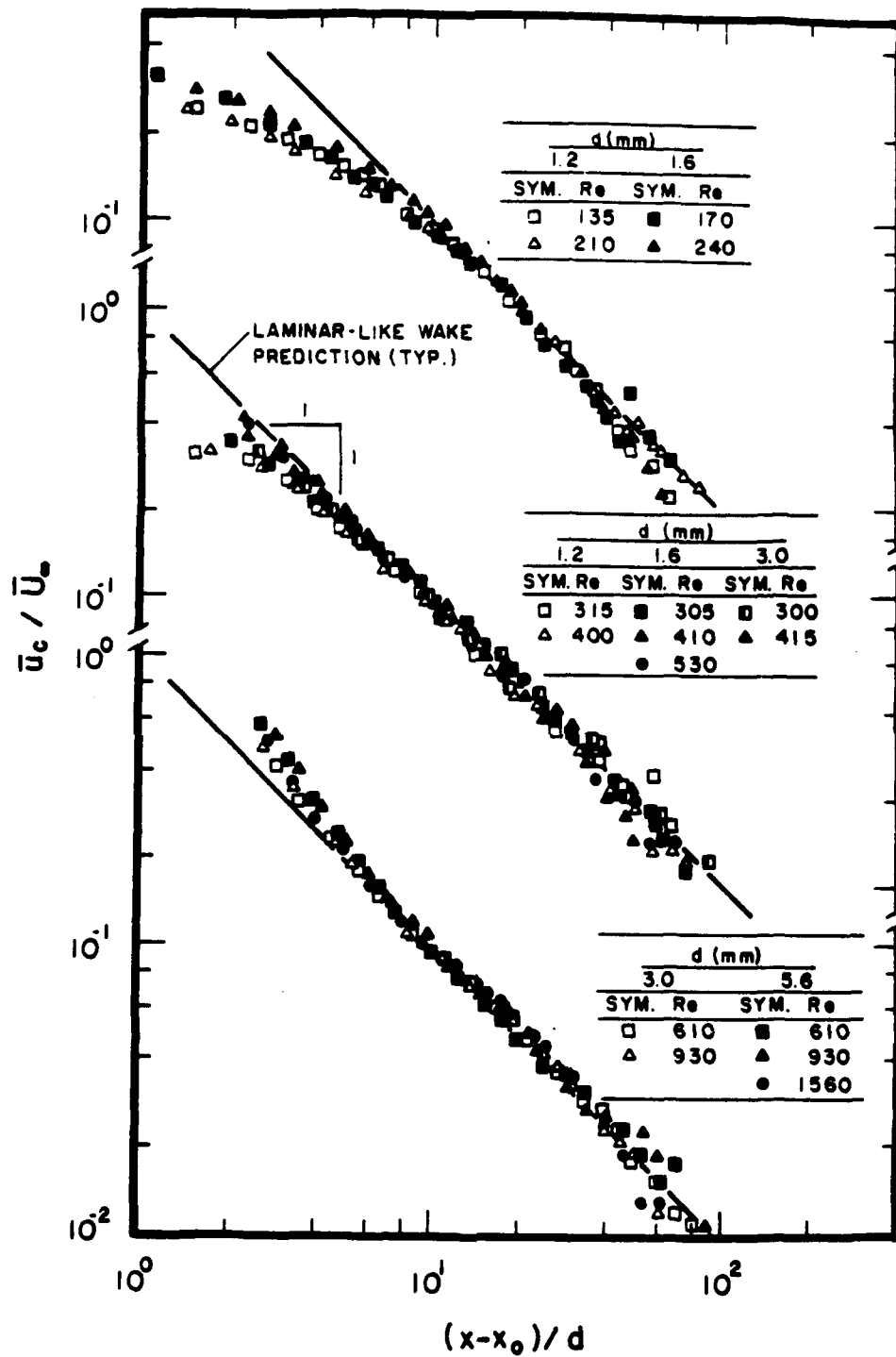


Figure 14. Streamwise mean velocities along the axis of wakes in a turbulent environment

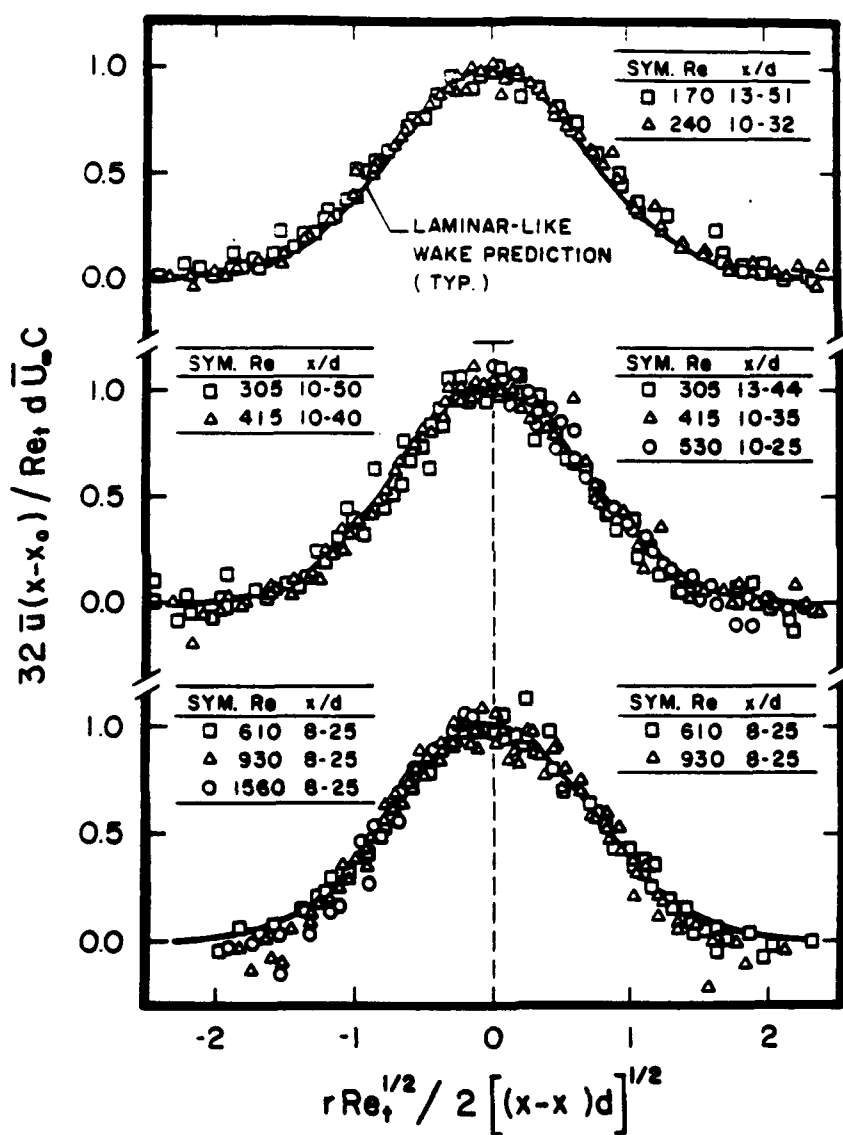


Figure 15. Radial profiles of mean streamwise velocities in wakes in a turbulent environment

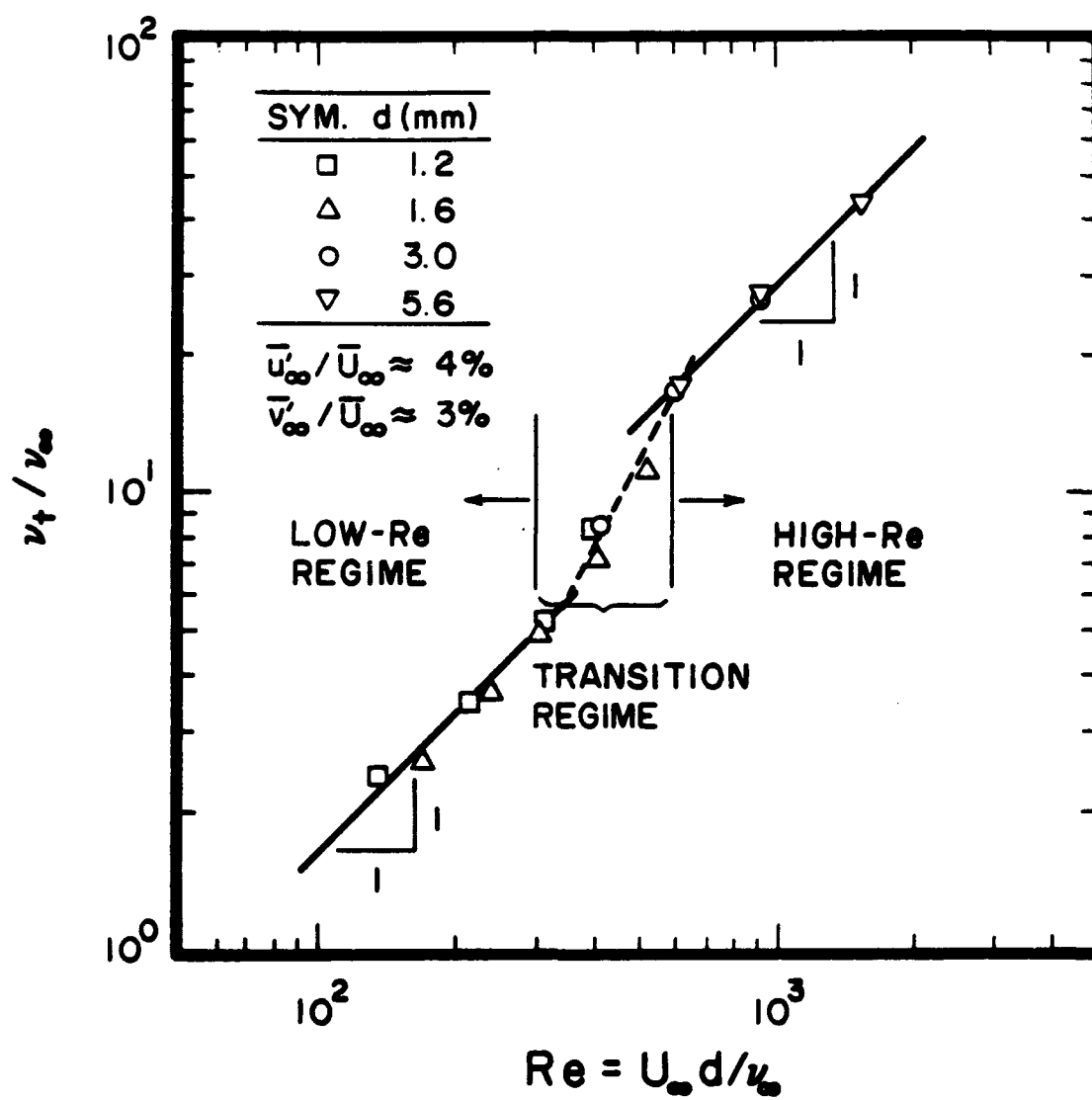


Figure 16. Effective turbulent viscosity for laminar-like wakes in a turbulent environment

quiescent and turbulent environments over the present test range. In particular, integral length scales of the pipe flow are large in comparison to sphere diameters for present conditions, ca. 40 mm, thus, the spheres are locally in a somewhat quasisteady environment. Nevertheless, such conditions are typical of spray environments where drop dimensions generally are much smaller than integral scales (Faeth 1987, 1990).

4.4 Conclusions

Aside from the fact that the onset of eddy shedding always was observed at Re ca. 300, conclusions differed somewhat for quiescent and turbulent environments, as follows:

Quiescent Environment:

1. The wakes exhibited fast decaying ($Re > 300$), turbulent and laminar wake regions, with transition between the turbulent and laminar wake regions at Re_w ca 10.
2. Mean velocities in the turbulent and laminar wake regions scaled according to classical similarity results, even though turbulence intensities along the axis varied in the range 10 - 85%, with turbulence spots extending into the laminar region.
3. The main effect of vortex shedding was to create a fast-decay wake region which deferred the onset of the turbulent wake region.
4. Turbulence levels decayed according to $Re_w^{-7/4}$ as the transition to a laminar wake was approached, which is consistent with theoretical expectations for the final decay period of wake turbulence (Batchelor and Townsend 1948; Phillips 1956; Lee and Tan 1967).

Turbulent Environment:

1. Wakes in this region were always turbulent but exhibited laminar-like similarity scaling of mean velocities with effective turbulent viscosities enhancing mixing rates.
2. Effective turbulent viscosities were constant for particular sphere Reynolds numbers but progressively increased with increasing Re , exhibiting low and high Reynolds number regimes separated by a transition regime for $300 < Re < 600$.
3. The transition regime was associated with the onset of eddy shedding which occurred at Re ca. 300, similar to quiescent environments, with the end of transition associated with the loss of evidence for coherent eddy shedding in the temporal spectra.

The present results are limited because only two ambient conditions, quiescent and an ambient turbulence intensity of ca. 4%, were considered. Thus, behavior at other conditions must be known before the results can be applied to analysis of turbulence generation. Information concerning scalar mixing in sphere wakes at modest Reynolds numbers also is required to understand the scalar turbulent field of dense sprays. Both issues are being addressed during current work in this laboratory.

References

- Batchelor, G. K. and Townsend, A. A. (1948) Decay of turbulence in the final periods. Proc. Roy. Soc. (London) A194, 527-543.
- Carmody, T. (1964) Establishment of the wake behind a disk. J. Basic Engrg. 88, 261-268.
- Chevray, R. (1968) The turbulent wake of a body of revolution. J. Basic Engrg. 90, 275-284.
- Engel, O. G. (1958) Fragmentation of waterdrops in the zone behind an air shock. J. Res. Nat. Bur. Stds. 13, 293-345.
- Faeth, G. M. (1987) Mixing, transport and combustion in sprays. Prog. Energy Combust. Sci. 13, 293-345.
- Faeth, G. M. (1990) Structure and atomization properties of dense turbulent sprays. Twenty-third Symposium (International) on Combustion, The Combustion Institute, Pittsburgh, 1345-1352.
- Hanson, A. R., Domich, E. G. and Adams, H. S. (1963) Shocktube investigation of the breakup of drops by air blasts. Phys. Fluids. 6, 1070-1080.
- Hinze, J. O. (1955) Fundamentals of the hydrodynamic mechanism of splitting in dispersion processes. AIChE J. 1, 289-295.
- Hinze, J. O. (1975) Turbulence, 2nd ed., McGraw-Hill, New York, 496-581.
- Hsiang, L.-P. and Faeth, G. M. (1992) Near-limit drop deformation and secondary breakup. Int. J. Multiphase Flow 18, 635-652.
- Hsiang, L.-P. and Faeth, G. M. (1993) Deformation and secondary breakup of drops. AIAA Paper No. 93-0814.
- Krzczkowski, S. A. (1980) Measurement of liquid droplet disintegration mechanisms. Int. J. Multiphase Flow 6, 227-239.
- Lane, W. R. (1951) Shatter of drops in streams of air. Ind. Engr. Chem. 43, 1312-1317.
- Lee, D. A. and Tan, H. S. (1967) Study of inhomogeneous turbulence. Phys. Fluids 10, 1224-1230.
- Loparev, V. P. (1975) Experimental investigation of the atomization of drops of liquid under conditions of a gradual rise of external forces. Izvestirja Akademii Nauk SSR. Mekhanika Zhidkosti i Gaza 3, 174-178.
- Mizukami, M., Parthasarathy, R. N. and Faeth, G. M. (1992) Particle-generated turbulence in homogeneous dilute dispersed flows. Int. J. Multiphase Flow 18, 397-412.
- Parthasarathy, R. M. (1989) Homogeneous dilute turbulent particle-laden water flows. Ph.D. thesis, The University of Michigan, Ann Arbor, Michigan.

- Parthesarathy, R. M. and Faeth, G. M. (1990a) Turbulence modulation in homogeneous dilute particle-laden flows. J. Fluid Mech. 220, 485-514.
- Parthesarathy, R. M. and Faeth, G. M. (1990b) Turbulent dispersion of particles in self-generated homogeneous turbulence. J. Fluid Mech. 220, 515-537.
- Phillips, O. M. (1956) The final period of decay of non-homogeneous turbulence. Proc. Cambridge Phil. Soc. 52, 135-151.
- Ranger, A. A. and Nicholls, J. A. (1969) The aerodynamic shattering of liquid drops. AIAA J 7, 285-290.
- Reinecke, W. G. and McKay, W. L. (1969) Experiments on waterdrop breakup behind Mach 3 to 12 shocks. Sandia Corp. Rept. SC-CR-70-6063.
- Reinecke, W. G. and Waldman, G. D. (1970) A study of drop breakup behind strong shocks with applications to flight. Avco Rept. AVJD-0110-70-77.
- Rice, S. O. (1954) Mathematical analysis of random noise. in Noise and Stochastic Processes. Dover, New York, 133-294.
- Ruff, G. A., Parthasarathy, R. N. and Faeth, G. M. (1989a) Dense-spray properties: structure and turbulence modulation. Final Report, Grant No. AFOSR-85-0244, University of Michigan, Ann Arbor, Michigan.
- Ruff, G. A., Sagar, A. D. and Faeth, G. M. (1989) Structure and mixing properties of pressure-atomized sprays. AIAA J, 27, 901-908.
- Ruff, G. A., Bernal, L. P. and Faeth, G. M. (1991) Structure of the near-injector region of non-evaporating pressure-atomized sprays. J. Prop. Power 7, 221-230.
- Ruff, G. A., Wu, P.-K., Bernal, L. P. and Faeth, G. M. (1992) Continuous-and dispersed-phase structure of dense nonevaporating pressure-atomized sprays. J. Prop. Power 8, 280-289.
- Schlichting, H. (1977) Boundary Layer Theory, 7th ed., McGraw-Hill, New York, 234-235, 599.
- Simmons, H. C. (1977) The correlation of drop-size distributions in full nozzle sprays. J. Engr. Power 99, 309-319.
- Simpkins, P. G. and Bales, E. J. (1972) Water-drop response to sudden accelerations. J. Fluid Mech 55, 629-639.
- Tan, H. S. and Ling, S. C. (1963) Final stage of decay of grid-produced turbulence. Phys. Fluids 6, 1693-1699.
- Tennekes, H. and Lumley, J. L. (1972) A First Course in Turbulence. MIT Press, Cambridge, Massachusetts, 275-284.
- Uberoi, M. S. and Freymuth, P. (1970) Turbulent energy balance and spectra of the axisymmetric wake. Phys. Fluids 13, 2205-2210.

- White, F. M. (1974) Viscous Fluid Flow, McGraw-Hill, New York.
- Wu, J. S. and Faeth, G. M. (1992a) Sphere wakes in still surroundings at intermediate Reynolds numbers. AIAA J. in press.
- Wu, P. K. and Faeth, G. M. (1992b) Sphere wakes in turbulent surroundings at intermediate Reynolds numbers. AIAA J., submitted.
- Wu, P. K. and Faeth, G. M. (1992c) Aerodynamic effects on primary breakup of turbulent liquids. Atomization and Sprays, submitted.

Appendix A: Faeth (1990)

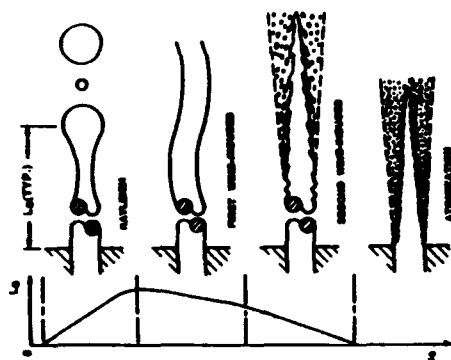


FIG. 1. Spray breakup lengths and regimes for nonturbulent round liquid jets in still gases.

where interphase transport rates are infinitely fast so that both phases have the same velocity and are in thermodynamic equilibrium, mixture fractions where liquid volume fractions become small are roughly an order-of-magnitude larger than those where combustion is complete; therefore, well-atomized sprays have dense-spray regions that are somewhat remote from high-temperature regions where vaporization is significant.⁷ Additionally, jet flows are attractive for studying dense sprays, since they can be described by relatively few parameters. Information on other spray processes and injection systems can be found in Refs. 1-6 and references cited therein.

The following aspects of dense sprays will be addressed: spray breakup regimes; dense-spray structure and its effect on collision, breakup and separated flow; primary breakup at the liquid-surface; and secondary breakup of drops. Generalizations based on available limited information for dense sprays are risky; therefore, the paper concludes with characteristic-time considerations to help order behavior for the many situations that have not been studied.

Spray Breakup Regimes

Description

The first issue concerning dense sprays is to define the topography or spray breakup regime of the flow. Several spray breakup regimes have been identified for nonturbulent liquids in still gases, as follows: nonjetting or drop, stable liquid jet, Rayleigh breakup, first and second wind-induced breakup, and atomization breakup.⁷⁻¹¹ The drop regime involves low flow rates with $We_j < 3-4$, ending when the jet momentum is large enough to overcome surface tension forces at the passage exit.⁷ Stable liquid jets occur for $Oh > 2-4$, where viscous forces are large enough to damp all disturbances that would lead to breakup.⁸ Naturally, neither of these regimes produces dense sprays.

The remaining spray breakup regimes for nonturbulent liquids are illustrated in Fig. 1. With increased flow rates, breakup regimes occur in the following order: Rayleigh, first wind-induced, second wind-induced, and atomization breakup. Rayleigh breakup involves interactions between liquid inertia and surface tension, yielding drop diameters somewhat larger than the injector diameter with jet lengths to breakup increasing with increasing flow rates. The remaining breakup regimes involve gas-phase aerodynamic effects with breakup lengths decreasing with increasing flow rates. First wind-induced breakup is caused by twisting or helical instability of the liquid column as a whole, yielding drops having diameters comparable to the injector

STRUCTURE AND ATOMIZATION PROPERTIES OF DENSE TURBULENT SPRAYS

G. M. FAETH

Department of Aerospace Engineering
The University of Michigan
Ann Arbor, MI 48106-2140, U.S.A.

Aspects of the structure and atomization properties of the near-injector (dense-spray) region of turbulent sprays are reviewed, considering: spray breakup regimes, dense-spray structure, and liquid breakup processes. The discussion is limited to nonvaporizing round pressure-atomized sprays—a fundamental configuration that is representative of dense sprays since they normally occupy the cool portions of combustor sprays where vaporization rates are modest.

Due to the complexity of spray breakup, criteria for breakup regime transitions are still not well developed. More information is particularly needed concerning effects of flow properties at the injector exit, ambient turbulence levels, and high Ohnson numbers where viscous effects become important.

Existing measurements of dense-spray structure are limited to atomization breakup, since most practical applications involve this regime. The dense-spray region for atomization breakup consists of a liquid core (like the potential core of a single-phase jet) surrounded by a multiphase mixing layer that begins right at the injector exit. Recent measurements within the multiphase mixing layer show that the flow is surprisingly dilute and support the classical view of atomization, i.e., primary breakup at the liquid surface followed by secondary breakup of ligaments and large drops with only minor effects of collisions. In contrast, more recent computational studies suggest significant effects of collisions in dense sprays—clearly, this controversy must be resolved. Accepting the classical view, characteristic secondary-breakup and residence times are comparable in dense sprays; therefore, breakup dominates dense sprays much like drop vaporization dominates dilute sprays. Continued primary breakup along the liquid core implies significant separated-flow effects within the multiphase mixing layer, with locally-homogeneous flow only approached at large Weber numbers for sufficiently low Ohnson numbers. Thus, many unresolved problems of separated flow in dilute sprays are relevant to dense sprays, while breakup and modification of turbulence by dispersed phases are particularly important for dense sprays.

Primary and secondary breakup have been widely studied but the dense-spray environment highlights new problems. In particular, more information is needed concerning breakup regime transitions, the temporal evolution and outcome of breakup processes, breakup mechanisms when the liquid core is turbulent, and effects of gas-phase turbulence on breakup.

Introduction

A wide variety of physical phenomena and practical applications have motivated numerous studies of nonvaporizing and combustor turbulent sprays. Much of this work, however, is limited to the dilute-spray region, located at some distance from the injector exit, where both observations and analysis are relatively tractable due to small liquid volume fractions. As a result, many features of dense sprays are reasonably well understood, yet several recent review articles and references cited therein.¹⁻⁷ Thus, attention is turning to the less accessible dense-spray regions near the injector exit, in an effort to better

understand how the characteristics of injectors, injected liquids, and the ambient environment affect the flow properties entering the dilute-spray region. The objective of this paper is to briefly review current understanding of the structure and atomization properties of turbulent dense sprays, and to highlight areas where additional research is needed.

Present considerations will be limited to nonvaporizing round pressure-atomized sprays in still gases. Ignoring evaporation is reasonable, since the dense-spray region of combustor sprays generally involves relatively cool portions of the flow. For example, at the locally-homogeneous-flow (LHFF) limit,

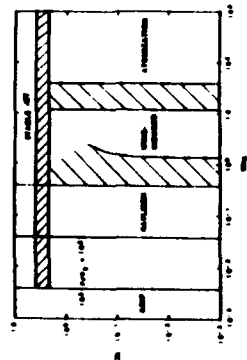


FIG. 2. Spray breakup regime transitions for non-turbulent round liquid jets in still gases. Ranges of transition uncertainties are indicated by crosshatching.

sions to atomization breakup is also relatively broad with Ranz' and Miesse¹⁰ suggesting $We_d = 13$ and 40.

Transitions to the stable jet regime have received little attention, but, all transitions at large Oh probably behave like the Sterling and Sleicher¹² result for wind-induced breakup. Uncertainties in transitions at high Oh are not very important for many liquids at low pressures, e.g., water and kerosene at 30°C have Oh ca. 5×10^{-3} for a 1 mm diameter orifice. However, heavy fuels have higher Oh while Oh becomes large for all liquids at high ambient pressures as the thermodynamic critical point of the liquid surface is approached;¹³ therefore, more study of high Oh transitions is needed. Additionally, both liquid- and gas-phase turbulence affect breakup,^{12,14} and their influence on breakup regime transitions should be quantified.

Dense-Spray Structure

Available Measurements:

Few measurements of the structure of dense sprays are available. In the following, recent measurements of dense-spray structure by Ruff and coworkers¹⁴⁻¹⁶ will be considered in order to provide some background about the nature of the flow. These experiments involved large-scale ($d = 9.5$ and 19.1 mm) water jets in still air with effects of liquid turbulence evaluated by considering non-turbulent slug flow and fully-developed turbulent pipe flow at the jet exit. Effects of separated flow were also studied by comparing measurements with predictions based on the LHF approximation (see Refs. 3, 14 and 15 for computational details).

Liquid volume fractions near the jet exit are unity in Fig. 3, indicating the presence of the liquid core. Reduced liquid volume fractions for fully-developed flow suggest a relatively short liquid core, however, this is not the case; flow visualization showed liquid cores extending well beyond $z/d = 100$ for these measurements.¹⁶ The reason for this behavior is that liquid volume fractions in the range 0.1-1.0 actually correspond to mature fractions in the range 0.98-1.0 due to the large density ratio of the flow. This highlights the fact that the region where the LHF predictions were successful involved disappointingly low levels of misting.

Misting Layer Properties:

Double-flash holograms of the water sprays provided details concerning the structure of the multiphase misting layer.^{15,16} Results for atomization breakup and non-turbulent jet exit conditions at $z/d = 25$ are illustrated in Fig. 4. Findings at other locations were similar.¹⁵ The region near the liquid surface consists of large, irregular, ligament-like elements (large SMD and e_p), while the dilute spray

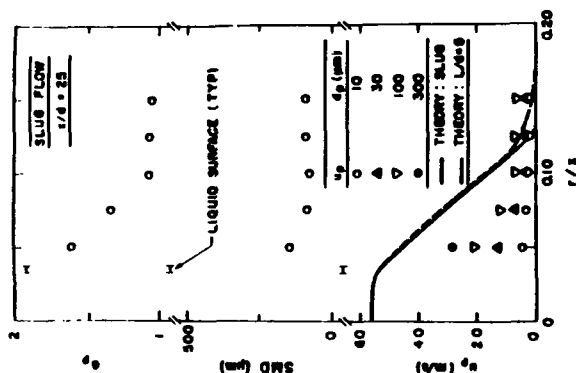


FIG. 4. Dispersed-phase properties for slug flow and atomization breakup at $z/d = 25$. From Ruff et al.¹⁵

region near the edge of the flow involves smaller round drops. This is direct evidence of important effects of secondary breakup near the surface. Additionally, the multiphase misting layer is surprisingly dilute ($\phi_f < 1\%$, implying that collisions between liquid elements are improbable). These findings, as well as consideration of secondary breakup to be discussed later, support the conventional picture of atomization within dense sprays. Breakup of the liquid surface into ligaments and large drops followed by secondary breakup into smaller round drops. This conflicts with recent hypotheses based on computational studies, that small drops are formed at the liquid surface and then collide and coalesce to create larger drops within the multiphase misting layer.¹⁷ Additional measurements are needed to resolve this controversy.

Drop sizes along the liquid surface were larger for turbulent than laminar liquids.¹⁵ Yet in spite of effects of secondary breakup and liquid turbulence, the MMD/SMD ratio was roughly 1.2 everywhere, which agrees with Simmons¹⁸ observations for a wide variety of non-evaporating dilute sprays. Furthermore, drop-size distributions for all conditions also satisfied Simmons¹⁸ universal root-normal distribution for this MMD/SMD ratio.¹⁸ This is helpful since the entire drop size distribution can be related in a simple manner to the SMD. However, an explanation of this behavior and more evidence concerning its generality for dense sprays is needed.

The distributions of drop velocities illustrated in Fig. 4 show that they vary substantially with drop diameter at each point in the flow. Near the liquid core, the largest drops have velocities comparable to liquid injection velocities (ca. 56 m/s); however, velocities decrease with drop size and radial distance. A surprising feature is that gas velocities (which approximate the velocities of the smallest drops)¹⁶ are low and nearly constant across the misting layer. This implies relatively ineffective momentum exchange between the phases since large drops contain most of the momentum and respond slowly to drag forces. The velocity variation with drop size provides direct evidence that the LHF approximation is not suitable, so it is not surprising that the LHF predictions in Fig. 4 are poor. Thus, the success of the LHF approach at large z/d in Fig. 3 occurs because the momentum of the gas and small drops has little influence on flow dynamics at large mature fractions, not because the LHF approximation is correct.

Primary Breakup

Aerodynamic Breakup:

Atomization breakup of non-turbulent liquids involves a stripping mechanism at the liquid surface.

Current estimates of drop sizes from primary breakup are based on theories of aerodynamically-induced wave growth on liquid surfaces, assuming that the mean drop size is proportional to the size of the fastest growing waves, and either ignoring (low Oh limit), or considering (high Oh limit) effects of liquid viscosity on wave growth. Using SMD to represent mean drop diameter for these limits yields:^{18,21}

$$A_1 \text{ SMD } \dot{m}_w / \sigma = 2\pi C_0 \quad (1)$$

$$= 9\pi(10)^{1/3} C_0 (\rho_l / \rho_f)^{1/3} \mu_f \dot{m}_w / \sigma^{2/3}$$

where the larger of the two estimates should be used. Limited measurements in this laboratory suggest $C_0 = 0.4$ and $C_1 = 1.3$. Additionally, Levich²² suggests the presence of a high Oh limit where aerodynamic breakup ends due to viscous damping when $(\rho_l / \rho_f)^{1/3} \mu_f \dot{m}_w / \sigma = 1$.

More study is needed to evaluate Eq. (1) as a means of estimating SMD from primary breakup within dense sprays. Additionally, there are also conceptual problems concerning the mechanism leading to Eq. (1). Aerodynamic breakup theory considers liquid waves which are assumed to separate from the liquid surface as crossstream ligaments and then divide by Rayleigh breakup into drops.²³ Yet, observations of the liquid surface during atomization breakup shows that the ligaments are more aligned with the streamwise direction, somewhat reminiscent of baroclinic vortices emanating from surfaces in single-phase boundary layers.²⁴ Clearly, these observations must be accommodated by any complete theory of primary breakup for non-turbulent liquids.

There are several other open issues with respect to primary breakup of non-turbulent liquids. First of all, the rate of removal of liquid at the surface is needed for any model of the flow. One approach that has been to use LHF analysis to estimate liquid massing at high moisture fractions where LHF predictions are reasonably good. Combusting non-operculated sprays have been treated in this manner with some success but the evaluation of primary breakup was not definitive.²⁵ A second approach has been to use aerodynamic breakup theory to correlate the length of the liquid core, yielding:

$$L_c / d = C_2 (\rho_l / \rho_f)^{1/3} \quad (2)$$

where Chabowski et al.²⁶ find C_2 in the range 7-10 for atomization breakup of pressure-atomized round jets in still gas. Commercial approximations of the core geometry using this length are then used to estimate liquid removal rates. This is plausible for modeling purposes but quantitative evaluation of the method is needed, while effects of liquid turbu-

lence on Eq. (2) have not been resolved. Finally, no information is available concerning drop velocities after primary breakup. Thus, critical aspects of primary breakup for non-turbulent liquids must be resolved before the dense-spray regime can be addressed in a rational manner.

Turbulent Breakup

The much larger drops from primary breakup for turbulent jet exit conditions are due to turbulent distortion of the liquid surface, stabilized by surface tension. In Lee and Spencer²⁷ provide early observations of this breakup mechanism at low ambient pressures. The properties of turbulent breakup can be estimated by considering the momentum required to overcome surface tension forces when forming a drop, using the relationship between velocity fluctuations and eddy size within the inertial region of the turbulence spectrum.²⁷ This yields the following expression for the range of drop sizes that can be formed:¹⁴

$$\rho_f \lambda^3 v'^3 (\rho_l / \lambda)^{3/2} / \sigma \approx 6 C_3 \quad (3)$$

where C_3 is a constant of order unity. The maximum drop size and SMD are assumed to be on the order of the radial turbulent integral scale of the liquid turbulence, thus:

$$\text{SMD} / \lambda = C_3 \quad (4)$$

where C_3 is of order unity and Eq. (4) is appropriate only when Eq. (3) is satisfied for $d_p = \lambda$. Lauder²⁸ finds $\lambda / d = 0.10-0.15$ for turbulent pipe flow while turbulence properties within the liquid core normally don't vary significantly from jet exit conditions. This yields $C_3 = 0.9-1.3$ from the results of Lauder et al.¹⁵ Thus, the turbulent breakup mechanism is consistent with the observations of Lauder et al.¹⁴⁻¹⁶ and deserves additional study as a possible way of estimating other properties of this primary breakup mechanism.

Equations (3) and (4) help put observations of effects of liquid turbulence from large-scale sprays into perspective. In particular, small injector diameters imply relatively small maximum drop sizes from this mechanism so that aerodynamic breakup effects normally dominate primary breakup. Additionally, most practical injectors have small length-to-diameter ratios so that liquid turbulence is not highly developed even when jet Reynolds numbers are high. Thus, turbulent primary breakup is probably not a major feature of most practical dense sprays.

Secondary Breakup

The general importance and relevant mechanisms of secondary breakup will be considered in

the following. Criteria for secondary breakup behind shock waves, and for slower accelerations in free fall, are as follows:²⁹

$$We_{sg} \geq We_{sg}^* = 6.5, We_{sg} \geq We_{sg}^* = 8 / C_D^* \quad (5)$$

Stable large drops in sprays have drag coefficients in the range 0.8-1.2,³⁰ therefore, the two equations yield similar breakup criteria.

Measurements in the water sprays were consistent with Eqs. (5) since only drops near the surface exceeded the criteria.¹⁵ This is generally the case for non-turbulent liquids based on the primary breakup estimates of Eqs. (1). At low Oh, for example, Eqs. (1) imply that the SMD Weber number after primary breakup is $6\pi C_D^* = 8$; therefore, all drops having diameters greater than roughly the SMD, which involves most of the spray liquid, exceed criteria for secondary breakup. Naturally, effects of viscous or turbulent breakup can yield even larger drops with a greater propensity for secondary breakup.

There have been numerous studies of drop breakup, see Refs. 4, 5 and 30-34. Viscous effects inhibit drop breakup for $Oh_p > 2$, but three types of drop breakup have been identified for low Oh_p : deformation, stripping and drop-piercing breakup.³⁵⁻³⁷ Deformation breakup involves distortion of the drop by gas pressure variations, causing simple division into a few large drops or bag-like breakup yielding some large drops accompanied by many very small drops. Stripping breakup is analogous to surface breakup of sprays with the bulk of the drop generating small drops. Drop-piercing breakup occurs at very high relative velocities due to Taylor instability of the windward side of the drop at high accelerations and yields small drops as well.

An illustration of the deformation and stripping regimes, due to Borsoy et al.,³⁸ appears in Fig. 3. The transitions shown reflect regimes that have been observed experimentally and the regimes are probably larger: breakup should occur for $We_{sg} > 6-8$, while transition between deformation and stripping correlates as $We_{sg} / Re_p^{1/2} > 1$.³⁸ Transition to drop-piercing breakup occurs for $We_{sg} > We_{sg}^* = 7000 / C_D^*$ which is well beyond conditions shown in Fig. 3.^{38,39}

Conditions pertinent to dense sprays are also indicated in Fig. 3. The experiments of Ruff et al.¹⁴⁻¹⁶ involve a single trajectory on this plot for non-turbulent and turbulent liquids, with breakup in the deformation and weakly stripping regimes—which was observed. More general limits are shown for aerodynamic breakup of non-turbulent liquids. These ranges were found as follows: the low Oh SMD Weber number is roughly 8 from Eqs. (1), while the universal drop size distribution implies a maximum We_{sg} of 26, after primary breakup, and the

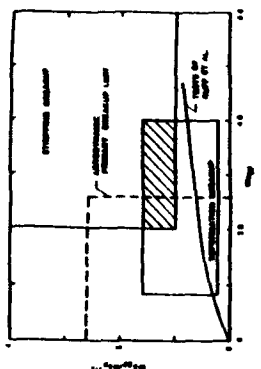


FIG. 3. Drop breakup regime transitions at low Oh_p .

Reynolds numbers of large drops in sprays are 10^2-10^3 , yielding maximum values of $We_{sg} / Re_p^{1/2}$ of roughly 2.6 (with somewhat larger values possible when viscous effects are important). This indicates that secondary breakup in dense sprays is largely due to deformation and weak stripping. While information is available concerning breakup times in these regimes,³³⁻³⁴ outcomes in terms of drop size and velocity distributions are largely unknown. Additionally, turbulent secondary breakup could be a factor for these relatively weak breakup modes. Recent measurements provide evidence for large turbulence intensities in dense sprays so this mechanism should be investigated as well.³⁴

Characteristic Times

Characteristic times are discussed in the following in order to generalize findings concerning secondary breakup and effects of separated flow. Relevant characteristic times are as follows: flow-residence, liquid-core-residence, drop-response and drop-breakup times. The largest drops are of interest, having velocities of roughly u_0 and yielding flow-residence times to reach x of

$$\tau_f = x / u_0 \quad (6)$$

Based on the correlation for L_c from Eq. (2), the liquid-core residence time is

$$\tau_c = L_c / u_0 = C_2 (d / u_0 \rho_f / \rho_l)^{1/3} \quad (7)$$

Drop-response time is defined as $\tau_p = -1/d \, u_p / (du/dt) = -u_p / (d \, u_p / dt)$.¹⁶ Using Eq. (5) to represent the largest stable drop (having relative velocity u_0 in the flow, then yields¹⁶

$$\tau_p = 4 We_{sg}^* \rho_f \sigma / (3 C_D^* \rho_l^2 u_0^2) \quad (8)$$

Finally, drop breakup times for deformation and

stripping can be correlated in a similar manner. Adopting the correlation of Ranzger and Nicholas¹³ for stripping, and considering the maximum stable drop size as before, yields¹⁴

$$\tau_b = C_0 We_d \sigma / (\rho_l u^3) \quad (9)$$

where $C_0 = 4$ is an empirical stripping factor.

A variety of response time ratios can be formed to highlight various properties of dense sprays. First of all, small values of the ratio

$$\tau_b/\tau_p = (3 C_0 C_D)^{1/2} / (4 \rho_l u^3) \quad (10)$$

indicate that breakup times are small in comparison to the time required for drops to approach gas velocities. At atmospheric pressure, τ_b/τ_p is ca. 0.1 so that secondary breakup is relatively fast and its outcome has the greatest influence on spray properties. At high pressures, however, $\tau_b/\tau_p = 1$ and breakup extends over distances comparable to those required for large drops to approach gas velocities; then, drop breakup must be treated like a finite-rate process, analogous to effects of drag and vaporization on drop motion.

Another perspective on secondary breakup can be found from

$$\tau_b/\tau_c = C_0 We_d / (C_0 We_d) \quad (11)$$

which is the ratio of secondary-breakup to liquid-core-residence time. Near the atomization spray breakup limit (Fig. 2), τ_b/τ_c reaches values of 0.1–0.3 which implies that secondary breakup proceeds rather slowly in the multiphase mixing layer (particulate) since new drops are formed all along the liquid core). Thus, for these conditions, secondary breakup tends to control processes in dense sprays, somewhat like drop drag and vaporization tends to control processes in dilute sprays.

Insight concerning separated flow can be obtained from

$$\tau_b/\tau_p = (3 C_0)^{1/2} / (4 We_d \sigma / (\rho_l u^3) d_p^2 / \sigma) \quad (12)$$

which is the ratio of flow-residence time to drop-response time. Large values of τ_b/τ_p correspond to regions where separated flow effects are small. Interpreting τ in Eq. (12) as the distance from breakup implies significant effects of separated flow near the liquid core. Drops near the edge of the flow, however, originate near the injector and exhibit smaller effects of separated flow. These trends correspond to existing observations at atmospheric pressure,^{15,16} while sprays at higher pressure should exhibit smaller effects of separated flow—particularly at large injection velocities.

For a round-jet, most of the liquid enters the flow near the jet exit and large values of the ratio

Acknowledgments

The author's research on sprays has been supported by the Air Force Office of Scientific Research, Grant No. AFOSR-80-0816, and the Office of Naval Research, Grant No. N00014-80-J-1198. The U.S. Government is authorized to reproduce and distribute copies for Governmental purposes notwithstanding any copyright notation thereon.

REFERENCES

1. Law, C. K., *Prog. Energy Comb. Sci.* 9, 169 (1982).
2. SIEGMUND, W. A., *Prog. Energy Comb. Sci.* 9, 291 (1983).
3. FAETH, G. M., *Prog. Energy Comb. Sci.* 13, 284 (1987); *ibid.* 9, 1 (1983); *ibid.* 3, 191 (1977).
4. GIEREN, E., and MURASZEW, A., *The Atomization of Liquid Fuels*, John Wiley & Sons, 1983.
5. CLIFT, R., GACEK, J. R., and WEXLER, M. E., *Bubbles, Drops and Particles*, Academic Press, 1978.
6. LEROUX, A. H., *Gas Turbine Combustion*, p. 371, Hemisphere Publishing, 1983.
7. SCHEELE, G. F., and MEISTER, B. J., *AICHE J.* 14, 9 (1968).
8. RANZ, W. E., *On Sprays and Spraying*, Engineering Research Bulletin No. 63, The Pennsylvania State University, 1966; *ibid.*, Can. J. Chem. Eng. 36, 175 (1958).
9. OHRNBERG, G., *Z. Angew. Math. Mech.* 16, 335 (1936).
10. MIZUSAKI, C. C., *Ind. Eng. Chem.* 47, 1690 (1955).
11. RANZ, W. E., *Atomization and Other Breakup Regimes of a Liquid Jet*, Ph. D. Dissertation No. 1375-T, Princeton University, 1978.
12. STREILING, A. M., and SLICKER, C. A., *J. Fluid Mech.* 68, 477 (1975).
13. HINZE, J. O., *AICHE J.* 1, 299 (1955).
14. RUFF, G. A., SAGAR, A., and FAETH, G. M., *ALAA J.* 27, 549 (1989).

15. RUFF, G. A., BERNAL, L. P., and FAETH, G. M., *ALAA Paper No. 88-0050* (1989); *ibid.*, *J. Prop. Power*, in press.
16. RUFF, G. A., and FAETH, G. M., *ALAA Paper No. 90-0464* (1990).
17. RANZ, W. E., and BACCO, F. V., *Encyclopedia of Fluid Mechanics* (N. P. Cherenin, Ed.), Vol. III, Chapt. 11, 1984.
18. SIMMONS, H. C., *J. Eng. Power* 98, 308 (1977); *ibid.*, 315 (1977).
19. O'Rourke, P. J., and BACCO, F. V., *Inst. Mech. Eng. Pub. ISBN 0859564603*, 101 (1980).
20. LEVICH, V. G., *Physicochemical Hydrodynamics*, Prentice-Hall, pp. 639–646, 1962.
21. MAYER, E., *ARS J.* 31, 1783 (1961).
22. ADLERG, M., *ALAA J.* 6, 1143 (1968).
23. HORT, J. W., and TAYLOR, J. J., *Phys. Fluids* 20, 5253 (1977).
24. LEE, T. W., and FAETH, G. M., *ALAA Paper No. 90-0463* (1990); *ibid.*, *J. Prop. Power*, submitted.
25. CHEN, B., OHMA, Y., CHEN, S.-H., and BACCO, F. V., *SAE Paper No. 890126* (1989).
26. LEE, D. W., and SPENCER, R. C., *NACA Tech. Note No. 424*, 1932; *ibid.*, 454, 1933.
27. HINZE, J. O., *Turbulence*, Chap. 7, McGraw-Hill, 2nd ed., 1975.
28. LAUFER, J., *NACA Tech. Note 2123*, 1950.
29. PRUPACER, H. R., and KLETT, J. D., *Microphysics of Clouds and Precipitation*, p. 123, D. Reidel Publishing, 1978.
30. HANSEN, E. Y., GAUS, G. W., and CHANG, I.-D., *J. Fluid Mech.* 58, 565 (1972).
31. GELFAND, B. E., GIBSON, S. A., and KOCAMMO, S. M., *Inst.-Flz. Zh.* 27, 120 (1974).
32. BOUSOV, A. A., GELFAND, B. E., NATANSON, M. S., and KOSOV, O. M., *Inst.-Flz. Zh.* 40, 64 (1981).
33. RANZ, W. E., and NICHOLS, J. A., *ALAA J.* 7, 255 (1969).
34. WIKER, A., and TAKAYAMA, A., *Rept. Inst. High-Speed Mech.* 53, p. 1, Tohoku University, 1987.
35. PATTENBURY, R. N., and FAETH, G. M., *J. Fluid Mech.* 220, 485 (1990).

Appendix B: Hsiang and Faeth (1992)

involves deflection of the drop into a thin disk normal to the flow direction, followed by deformation of the center of the disk into a thin balloon-like structure extending in the downstream direction, both of which subsequently divide into drops [see Hinze (1955), Hanson *et al.* (1963), Gelfand *et al.* (1974), Krzeczowski (1980), Ranger & Nicholls (1969), Reinecke & McKay (1969), Reinecke & Waldman (1970) and Wierzbna & Takayama (1988) for photographs of all the breakup regimes discussed here]. The shear breakup regime is observed at higher relative velocities: it involves deflection of the periphery of the disk in the downstream direction, rather than the center, and stripping of drops from the periphery of the disk. The transition between the bag and shear breakup regimes involves complex breakup processes, with portions of this regime termed parachute breakup, chaotic breakup, bag-jet breakup, transition breakup etc. (Borisov *et al.* 1981; Krzeczowski 1980); this regime will be denoted the multimode breakup regime in the following. A complex breakup mechanism also has been observed at very large relative velocities, which is called the catastrophic breakup regime (Reinecke & McKay 1969; Reinecke & Waldman 1970). Existing observations of secondary breakup have generally involved liquid/gas density ratios, $\rho_L/\rho_G > 500$ and Reynolds numbers, $Re = \rho_G d_0 u_0/\mu_G > 100$, where d_0 and u_0 denote the original drop diameter and relative velocity and μ_G is the gas viscosity. For these conditions, Hinze (1955) has shown that transitions between breakup regimes largely are functions of the Weber number, $We = \rho_G d_0 u_0^2/\sigma$, and the Ohnesorge number, $Oh = \mu_L/(\rho_L d_0 \sigma)^{1/2}$, where σ = surface tension and μ_L = liquid viscosity, which are measures of the ratios of drag and liquid viscous forces to surface tension forces, respectively. Hinze (1955) found that progressively larger disturbances (i.e. larger We) were required for the onset of breakup as Oh increased, because viscous forces in the liquid tend to inhibit drop deformation (which is the first step in the breakup process) at large Oh . In fact, viscous forces essentially suppressed secondary breakup for the available range of We , for $Oh > 2$ (Hinze 1955). Among others, Lopatov (1975) showed that the properties of the disturbances also affected the onset of breakup, with more slowly applied disturbances requiring larger values of We for breakup at a particular value of Oh ; subsequent considerations will be limited to shock wave disturbances to avoid this complication. Borisov *et al.* (1981) proposed an alternative breakup regime map in terms of We and Re , considering both the bag and shear breakup regimes, which is best suited to conditions where $Oh \leq 1$. Krzeczowski (1980) extended the breakup regime map of Hinze (1955) to locate transitions to the bag, bag-jet, multimode (which Krzeczowski called transition breakup) and shear breakup regimes as a function of We and Oh . Nevertheless, in spite of its importance for initiating breakup, conditions for the onset of drop deformation and the definition of deformation processes have not received much attention.

Another aspect of secondary breakup that has been studied is the time required to complete breakup. Liang *et al.* (1988) summarized past measurements of breakup times, including the findings of Simpkins & Bales (1972) and Ranger & Nicholls (1969) for shear breakup and those of Reinecke & McKay (1969) and Reinecke & Waldman (1970) for catastrophic breakup—all for shock wave disturbances at large ρ_L/ρ_G and low Oh . For these conditions, breakup times could be normalized by a characteristic breakup time, $t^* = d_0(\rho_L/\rho_G)^{1/2}/u_0$, finding that the normalized breakup time does not vary greatly over the large range of We that includes both the shear and catastrophic breakup regimes. However, results near the onset of secondary breakup, within the bag breakup regime, have not been studied very much in spite of the importance of these near-limit conditions to processes within practical sprays (Ruff *et al.* 1992). The deformation properties of drops prior to secondary breakup due to shock wave disturbances have been studied for large ρ_L/ρ_G and $Oh < 0.1$. Wierzbna & Takayama (1988) summarized past work in this area, which included the results of Ranger & Nicholls (1969) and those of Reinecke & McKay (1969) and Reinecke & Waldman (1970) for shear and catastrophic breakup, as well as their own measurements of deformation prior to shear breakup. They found that deformation scales in terms of t^* , although in contrast to breakup times, the behavior of deformation during shear breakup differs somewhat from catastrophic breakup. Additionally, they highlighted problems of interpreting shadowgraph photographs of breakup processes and suggested the use of holography instead. Similar to breakup times, however, drop deformation within the bag and transition breakup regimes have not received much attention.

Finally, due to the problems of observing drops after secondary breakup there is very little information available about the outcome of secondary breakup, even though this information is

NEAR-LIMIT DROP DEFORMATION AND SECONDARY BREAKUP

L. P. HSIANG and G. M. FAETH

Department of Aerospace Engineering, University of Michigan, Ann Arbor, MI 48109-2140, U.S.A.

(Received 29 January 1992; in revised form 11 May 1992)

Abstract—The properties of drop deformation and secondary breakup were observed for shock wave initiated disturbances in air at normal temperature and pressure. Test liquids included water, glycerol solutions, *n*-heptane, ethyl alcohol and mercury to yield Weber numbers (We) of 0.5–1000. Ohnesorge numbers (Oh) of 0.006–4, liquid/gas density ratios of 500–12,000 and Reynolds numbers (Re) of 300–16,000. Measurements included pulsed shadowgraphy and holography to find drop deformation properties prior to breakup, as well as drop size distributions after breakup. Drop deformation and breakup regimes were identified in terms of We and Oh ; regimes at low Oh include no deformation, nonoscillatory deformation, oscillatory deformation, bag breakup, multimode breakup and shear breakup as We is increased. However, most of these regimes occur at higher We when Oh values are increased, with no breakup observed for $Oh > 4$ over the present test range. Unified temporal scaling of deformation and breakup processes was observed in terms of a characteristic breakup time that largely was a function of Oh . Prior to breakup, the drag coefficient evolved from the properties of spheres to those of thin disks as drop deformation progressed. The drop size distribution after breakup satisfied Summerson's universal root normal distribution function for the bag and multimode breakup regimes and could be characterized by the Sauter mean diameter (SMD) alone. Drop sizes after shear breakup, however, did not satisfy this distribution function due to the distorting effect of the core or drop-generating layer. Nevertheless, the SMD after secondary breakup could be correlated in terms of a characteristic liquid boundary layer thickness for all breakup regimes, similar to recent results for non-turbulent primary breakup. Drop properties after secondary breakup suggest that both reduced drop sizes and reduced relative velocities play a role in ending the secondary breakup process.

Key Words: sprays, atomization, drop breakup

1. INTRODUCTION

The secondary breakup of drops is an important multiphase flow process with applications to liquid atomization, dispersed multiphase flow, combustion instability of sprays, heterogeneous detonations of gas/liquid mixtures, the properties of rain, and interactions between high-speed aircraft and raindrops, among others. In particular, recent studies of the structure of dense pressure-atomized sprays [see Ruff *et al.* (1992) and Faeth (1990) and references cited therein] confirm the conventional view of liquid atomization with primary breakup at the liquid surface followed by secondary breakup. It also was found that secondary breakup can control mixing rates of dense sprays in some instances, much like drop vaporization often controls mixing rates of dilute sprays. Finally, recent studies of primary breakup of both nonturbulent and turbulent liquids show that primary breakup intrinsically yields drops that are unstable to near-limit secondary breakup (Wu *et al.* 1991, 1992). Motivated by these observations, the objectives of the present investigation were to study drop deformation and breakup for well-defined shock wave disturbances (yielding a step change in the relative velocity of a drop) at conditions near the onset of secondary breakup. Issues considered include the required flow conditions, dynamics and the outcomes of drop deformation and breakup.

Due to numerous applications, secondary breakup has received significant attention in the past. Giffen & Muraszew (1953) and Hinze (1955) reviewed early work in the field; therefore, the following discussion will be limited to more recent studies. The definition of the onset of breakup, breakup dynamics and the outcome of breakup will be considered, in turn. Most earlier work at least has touched on the definition and conditions for the onset of various breakup regimes. The breakup regime observed at the onset of secondary breakup has been termed bag breakup: it

†To whom correspondence should be addressed.

vital for understanding the structure of dense sprays (Faeth 1990). An exception is some limited results reported by Gelfand *et al.* (1974) for the bag breakup regime. A bimodal distribution was observed with small drops resulting from breakup of the bag and a group of larger drops associated with breakup of the liquid ring at the base of the bag. However, this information is too limited to provide general guidance about drop sizes produced by secondary breakup.

The preceding review indicates that there are several gaps in the literature concerning secondary breakup. In particular, conditions for the onset of various breakup regimes have been defined reasonably well by Krizekowsky (1980) but analogous deformation regimes have not been defined, particularly at high Oh where liquid viscosity effects are important. Breakup times and drop deformation have been studied as well (Ranger & Nicholls 1969; Rennecke & McKay 1969; Rennecke & Waldman 1970), however, available information is limited for the near-limit bag and transition breakup regimes that are important for drop breakup in dense sprays. Finally, measurement problems have limited information about the outcome of secondary breakup in spite of the importance of this breakup property. Thus, the objectives of the present investigation were to extend the earlier work to provide measurements of the onset of various deformation and breakup regimes, the evolution of breakup processes, and the resulting drop sizes after secondary breakup. Phenomenological descriptions of these processes were used to help interpret the data. Measurements emphasized conditions near the onset of breakup where past information is very limited even though this region is particularly important for understanding the structure of dense sprays. The measurements involved pulsed shadowgraph photography and holography, the latter being particularly useful for finding drop sizes after secondary breakup. The study was limited to conditions similar to those treated by Hinze (1955) and Krizekowsky (1980), which are representative of sprays near atmospheric pressure conditions: $\rho_1/\rho_2 > 500$ and $Re > 100$. Shock wave disturbances were considered with water, *n*-heptane, ethyl alcohol, mercury and various glycerol mixtures used as test liquids in order to study effects of liquid phase properties.

The paper begins with a discussion of the experimental methods. Results are then considered, treating breakup regimes, breakup times, drop deformation, drop drag and drop sizes after breakup, in turn.

2. EXPERIMENTAL METHODS

2.1. Apparatus

A shock tube with the driven section open to the atmosphere, similar to Ranger & Nicholls (1969), was used to generate shock wave disturbances. The driver section was pressurized with air and was round with i.d. = 75 mm and a length of 3.1 m. The driven section had a rectangular interior cross section (38 mm wide \times 64 mm high) to facilitate visualization of the flow at the test location. A transition section, with the shock tube diaphragm at its downstream end, provided a gradual evolution from the round driver section to the rectangular driven section. The driven section was 6.7 mm long with the test location 4.0 m from the downstream end. This arrangement provided test times of 17–21 ms in the uniform flow region between the shock wave passing the test location and the subsequent arrival of disturbances from the contact surface and reflections from the ends of the shock tube. Test conditions involved relatively weak shock waves having shock Mach numbers of 1.01–1.24; therefore, thin Mylar film (having thicknesses of 19, 25 and 38 μ m) was used for the diaphragm between the driver and driven sections of the shock tube. The Mylar film diaphragm was ruptured to initiate operation of the shock tube by heating a fine resistance wire mounted on the film; this provided a clean break of the diaphragm that was otherwise problematical due to small pressure differences across the diaphragm because the shock waves were weak.

The strength of the shock waves was monitored by two piezoelectric pressure transducers (PCB Piezotronics Inc., model 101A05) mounted 660 and 310 mm upstream of the test location. The outputs of these transducers were recorded using a digital oscilloscope (LeCroy, model 9400A). The time of passage of the wave between the two transducers provided the shock Mach number (whose properties were checked for consistency using the pressure ratio across the wave). The time required

to break the diaphragm with the heater wire was not very reproducible; therefore, the pressure signals were used to synchronize data accumulation from the experiment.

The drop generator system involved: a vibrating capillary tube, similar to Dabora (1967), to generate a stream of drops; and a drop selection system, similar to Sangiovanni & Kestin (1977), to vary the spacing between drops. The test liquid was placed in a reservoir and pressurized with air so that it flowed to a vibrator chamber and then through a capillary tube (20, 23 or 25 G needles, 12 mm long, depending on the test condition). The upper end of the vibrator chamber was mechanically attached to a speaker (Realistic, model 40-1319) which, in turn, was driven by a signal generator (BK-Precision, model 3020). By varying the liquid flow rate and the frequency of vibration, a uniformly spaced stream of monodisperse drops was generated by Rayleigh breakup. This drop stream passed through 6 mm dia holes in the top and bottom of driven section, crossing the central plane of the driven section at the test location. Quartz windows (25 mm high \times 305 mm long and mounted flush with the inside walls of the driven section) allowed observation of the interaction between the uniform gas flow behind the shock wave and the drop stream.

The separation between drops at the center of the test location due to operation of the vibrating capillary tube alone was 3–4 mm, which was sufficient to allow observation of drop deformation in the early stages of bag and multimode breakup, as well as the shear breakup process, without interactions between drops. However, it was necessary to increase the spacing between drops to observe the later stages and outcomes of bag and multimode breakup. This was accomplished using the approach of Sangiovanni & Kestin (1977), by charging every other drop in the flow and electrostatically deflecting the charged drops out of the drop stream crossing the shock tube. This yielded a drop spacing of roughly 7 mm, which assured the presence of drops in the region of observation when film records were made while minimizing interactions between drops.

2.2. Instrumentation

2.2.1. Pulsed shadowgraphy

Drops were observed in two ways: pulsed shadowgraph photographs and motion pictures to observe the overall dynamics of breakup; and single pulse holography to observe the outcome of breakup. Initial work involved pulsed shadowgraph photography using a Xenon Corp. Micropulser (model 457A, 10 J optical power per pulse with a pulse duration of roughly 1 μ s). The lamp output was collimated and directed through one of the windows at the test location. The image was recorded through the other window using a Graphix camera (4 \times 5" film format, Polaroid Type 55 film) at a magnification of 6:1. The photographs were obtained in a darkened room, varying the time delay between the shock wave passing the downstream pressure transducer and the time of the flash so that various portions of the breakup process could be observed from repeated tests (at least two photographs were obtained for each test condition and delay time).

Pulsed shadowgraph photography was tedious for accumulating data on drop breakup over the wide range of conditions of the present investigation; therefore, the bulk of the results were obtained using motion picture shadowgraphs within a darkened room. This involved using a 20 W copper vapor laser as the light source (Metalaser Technologies, model 2051, 2 mJ per pulse, 30 ns pulse duration) and a 35 mm drum camera (Cordon Inc., model 351 using Agfa 10E75HDNAH film) to record the images at unity magnification. Prior to measurements, the laser was operated in the continuous pulsing mode to reach proper operating temperatures, and the camera drum was brought to proper speed with the camera shutter closed. Laser operation then was terminated briefly, the camera shutter was opened and the shock tube diaphragm was broken. As the shock wave approached the test location, detected by the pressure transducers, the laser was fired as a high frequency burst (controlled by a Hewlett-Packard model 3314 function generator) to capture the breakup process on the film (laser frequency of 6–8 kHz for 20 pictures). The time between film records was known by monitoring the signal generator frequency with a digital oscilloscope. The film records were analyzed using Gould FD 5000 image display as described subsequently. The procedure was to obtain several (5–14) motion picture shadowgraphs for a particular test condition. The data was then grouped to obtain statistically significant results as ensemble averages. The experimental uncertainties of the various measurements will be taken up when the results are discussed.

2.2.2. Holography

The hologram and reconstruction systems used to measure drop properties after breakup were similar to those of Ruff *et al.* (1992). An off-axis arrangement was used with optics providing a 2-3:1 magnification of the hologram image itself over a hologram field that included all the drops generated by secondary breakup. This was coupled with reconstruction optics that allowed drop diameters as small as 25 μm to be measured with 5% accuracy and objects as small as 12-15 μm to be observed. The properties of the reconstructed sprays were analyzed using the Gould FD 5000 image display system with a field of view of 1.7×2.0 mm. Various locations in the hologram camera of the display system could be observed by traversing the hologram in two directions and the video camera of the display system in the third direction.

Drops and other ellipsoidal objects were sized by measuring their maximum and minimum diameters, d_{max} and d_{min} , through the centroid of the image. Assuming ellipsoidal shapes, the diameter, d , of these objects was taken to be the diameter of a sphere having the same volume, $d^3 = d_{\text{max}}^2 d_{\text{min}}$. More irregular objects were sized by finding the area and perimeter of their image and computing the maximum and minimum diameters of an ellipsoid matching these properties; given these parameters, d was found as before. Results at each condition were summed over at least three realizations, considering 150-300 liquid elements, to provide drop size distributions, the mass median diameter (MMD) and the Sauter mean diameter (SMD). Experimental uncertainties generally were dominated by finite sampling limitations because each breakup event only yields a limited number of drops. Within the limitations of the definition of drop sizes, which are difficult to quantify, estimated experimental uncertainties (95% confidence) of the MMD and SMD are <40%. The drop size distributions are presented in terms of cumulative volume percentages. Experimental uncertainties (95% confidence) of the cumulative volume percentages were the same as for the MMD and SMD for values in the range 10-80%—becoming larger outside this range due to sampling limitations at large sizes and resolution limitations at small sizes.

2.3. Test Conditions

The test conditions are summarized in table 1. Test drops of water, *n*-heptane, ethyl alcohol, mercury and various glycerol mixtures were used to provide a wide range of liquid properties. The liquid properties listed in table 1 were obtained from Lange (1952), except for the surface tension of glycerol mixtures which were measured in the same manner as Wu *et al.* (1991). Initial drop diameters were in the range 500-1500 μm , dictated by the need for measurable drop properties after breakup and the difficulties of producing small drops with very viscous liquids. Ranges of other variables are as follows: ρ_l/ρ_g of 580-12,000; Oh of 0.0006-4; We of 0.5-1000; and Re of 300-16,000. Although the full range of Oh was considered for measurements of deformation and breakup regime transitions and dynamics, measurements to find the outcome of breakup were

Table 1. Summary of the test conditions*

Liquid	ρ_l (kg/m ³)	$\mu_l \times 10^3$ (kg/ms)	$\sigma \times 10^3$ (N/m)	d_0 (μm)	Oh	We	Re
Water	997	8.94	70.8	1000	0.0038	0.5-236	340-8250
<i>n</i> -Heptane	683	3.94	20.0	500	0.0036	14-137	720-2270
Ethyl alcohol	800	16.0	24.0	1000	0.011	15-375	1110-6060
Mercury	13,600	15.0	475.0	850	0.00062	10-13	3510-4500
Glycerol (%)							
21	1050	16.0	67.3	1200	0.0071	8-130	1540-6190
42	1105	35.0	65.4	1200	0.0120	8-136	1530-6580
63	1162	108.0	64.8	1200	0.0390	1-129	480-4420
75	1195	356.0	63.8	1200	0.0990	2-128	730-6270
84	1219	1000	63.2	1200	0.260	1-127	500-6210
92	1240	3270	62.5	1200	1.050	1-268	530-8330
97	1253	8350	62.4	1500	1.700	1-205	600-8800
99.5	1260	12,900	62.0	1550	3.850	1-612	630-15760

*Air initially at 98.3 kPa and 298 \pm 3 K in the driven section of the shock tube with shock Mach numbers in the range 1.01-1.24. Properties of the air were taken at normal temperature and pressure: $\rho_0 = 1.18 \text{ kg/m}^3$, $\mu_0 = 18.5 \times 10^{-6} \text{ kg/ms}$.

limited to $\text{Oh} < 0.1$. The We range includes processes from no deformation into the shear breakup regime that are of interest to processes within dense sprays, but does not reach the catastrophic breakup regime studied by Reinecke & McKay (1969) and Reinecke & Waldman (1970). As noted earlier, the Re range of the present experiments is higher than conditions where gas viscosity plays a strong role in drop drag properties; within the present Re range, the drag of spheres only varies in the range 0.6-0.4 (Faeth 1990; White 1974). Shock Mach numbers were relatively low, 1.01-1.24, so that the physical properties within the uniform flow region were not significantly different from in room air.

3. RESULTS

3.1. Deformation and Breakup Regimes

The presentation of results will begin with definition of deformation and breakup regime transitions in order to help organize the remainder of the findings. The deformation and breakup regime map, showing transitions as functions of We and Oh similar to Hinze (1955) and Krzeczowski (1980), is illustrated in figure 1. The present evaluation of the onset of breakup (the transition to the bag breakup regime) is essentially identical to the findings of Hinze (1955) and Krzeczowski (1980) within experimental uncertainties. The present results also agree quite well with the transitions found by Krzeczowski (1980) to shear breakup and multimode breakup (which Krzeczowski called transition breakup). In view of the somewhat subjective identifications of breakup regimes and their transitions, this level of agreement is quite satisfying.

The observations of transitions to nonoscillatory and oscillatory deformation illustrated in figure 1 have not been reported before. The present definition of the transition to the nonoscillatory deformation regime was taken to be the condition where the drop deformed so that the ratio of its maximum (cross stream) dimension to its initial diameter was 1.1, corresponding to a deformation of 10%. Following this transition, there was a range of We at each Oh where the drop decayed back to a spherical shape, much like an overdamped oscillation, yielding nonoscillatory deformation (defined as conditions where the second peak of the diameter fluctuation involved

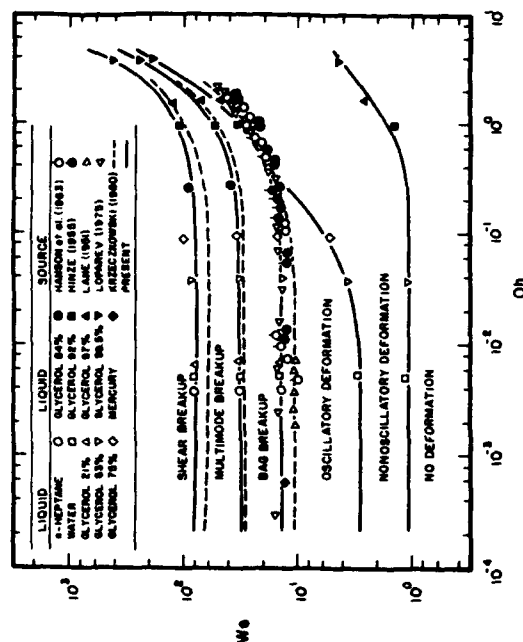


Figure 1. Drop deformation and breakup regime map

deformations < 10%). For $Oh > 0.4$, this regime was ended by the onset of bag breakup, however, for $Oh < 0.4$, there was a range of We where the drop oscillated with progressively decaying ratios of maximum to initial diameters before the bag breakup regime was reached: this regime is denoted the oscillatory deformation regime in figure 1.

The most striking feature of the flow regime map in figure 1 is that progressively higher We are needed for the various transitions as Oh increases. Hinze (1955) and Krzeczowski (1980) also noted this effect for the breakup transitions but the behavior is similar for the deformation transitions as well, with the oscillatory deformation regime disappearing entirely for $Oh > 0.4$ as noted earlier. Hinze (1955) concluded that breakup might no longer be observed for $Oh > 2$; however, it appears that Oh would have to be somewhat greater than 4, the highest value reached during the present investigation, before breakup would be inhibited for $We < 1000$, with somewhat higher values of Oh required to inhibit deformation for $We > 1000$.

Recalling that Oh characterizes the ratio between liquid viscous forces and surface tension forces, the inhibition of deformation and breakup at large Oh clearly is due to increased damping by liquid viscous forces. This slows the deformation process so that drag forces have more time to reduce relative velocities at the point where maximum deformation is reached, and thus the potential for breakup. Another factor is that the final breakup into drops involves Rayleigh type breakup processes which become weak when Oh is large, so that the drops tend to deform into very long cylindrical threads that exhibit little tendency to divide into drops (at least within the deformation regime). This high Oh regime is encountered during spray combustion processes at high pressures, where values of surface tension become small but viscosity remains finite as the drop surface nears its thermodynamic critical point. Thus, the findings illustrated in figure 1 suggest that drops at these conditions would not necessarily shatter due to small surface tension as often thought (Faeth 1990); instead, they would deform or even remain spherical. However, additional study of such high pressure drop processes is needed before definitive conclusions about this behavior can be obtained. In particular, specific drop trajectories across the flow regime map depend on the atomization and mixing properties of the spray, while near-critical drop processes involve much lower values of ρ_l/ρ_g than those considered in figure 1.

All the regime transitions illustrated in figure 1 become relatively independent of liquid viscous forces (or Oh) for $Oh < 0.01$. The We for regime transitions in this low Oh regime are summarized in table 2, considering results from Hinze (1955), Krzeczowski (1980) and the present study. Similar to the regime map itself, the measurements of the various studies agree within experimental uncertainties. The order of the transitions with increasing We is as follows: nonoscillatory deformation, oscillatory deformation, bag breakup, bag-jet breakup [defined as a separate regime by Krzeczowski (1980) but not during the present study], multimode breakup [which involved evolution from center to edge deformation of the drop and is called transition breakup by Krzeczowski (1980)] and finally shear breakup. Catastrophic breakup occurs for $We > 10^4$, which is beyond the present test range.

3.2. Breakup Times

The discussion of deformation and breakup regime transitions highlights the importance of breakup times. In particular, as drop velocity relaxation times and breakup times approach one another, the propensity for drop breakup decreases due to reduction of the relative velocities between the drop and the gas. The present measurements of breakup times, along with earlier

Table 2. Summary of We for the transition to deformation and breakup regimes at $Oh < 0.1$.

Transition to:	Present result	Krzeczowski (1980)	Hinze (1955)
Nonoscillatory deformation	1.1	—	—
Oscillatory deformation	3.0	—	—
Bag breakup	15	10	13
Bag-jet breakup	—	18	—
Multimode breakup*	35	30*	—
Shear breakup	80	63	—

*Called the transition regime by Krzeczowski (1980).

measurements for shock wave disturbances due to Engel (1958), Simpkins & Bales (1972), Ranger & Nicholls (1969), Reinecke & McKay (1969) and Reinecke & Waldman (1970) are plotted as a function of We in figure 2. The breakup times, t_b , in the figure are normalized by the characteristic breakup time for shear breakup defined by Ranger & Nicholls (1969) as follows:

$$t^* = t_b / (\rho_l \mu_g)^{1/2} \mu_g \quad [1]$$

Except for the present results, which are grouped according to Oh , the measurements are for $Oh < 0.1$ and the effects of liquid viscosity are small. Thus, the deformation and breakup regimes at small Oh identified in table 2 are illustrated in the figure for reference purposes (omitting catastrophic etc. breakup regimes at high We , as noted earlier).

A remarkable feature of the breakup time results in figure 2 at $Oh < 0.1$ is that t_b varies very little even though We varies over a large range (roughly 10^0 – 10^4) and a variety of breakup regimes are involved. In fact, the breakup time correlation of Ranger & Nicholls (1969), developed for the shear breakup regime

$$t_b t^* = 5.0 \quad [2]$$

provides a reasonably good correlation of all the measurements illustrated in figure 2 for $Oh < 0.1$. However, when the present results for $Oh > 0.1$ are considered, it is seen that $t_b t^*$ progressively increases with increasing Oh . This reflects the importance of liquid viscosity on breakup, evident from the breakup regime map in figure 1; in particular, large Oh involves the eventual suppression of breakup so that $t_b t^*$ becomes unbounded. An empirical fit of this behavior over the present test range is as follows:

$$t_b t^* = 5.0 (1 - Oh/7); \quad We < 10^4 \quad [3]$$

Equation [3] is seen to provide a reasonable correlation of the present data, however, it is only provisional because it is based on relatively few data with Oh generally < 3.5.

3.3. Drop Deformation

The first stage of drop deformation, in the period where the drop flattens and first reaches a maximum cross stream dimension, was studied due to its influence on drop velocity relaxation and breakup. In particular, the distortion of the drop should affect its drag properties, and thus relative velocities during the breakup process, which undoubtedly plays a role in the onset of breakup. The

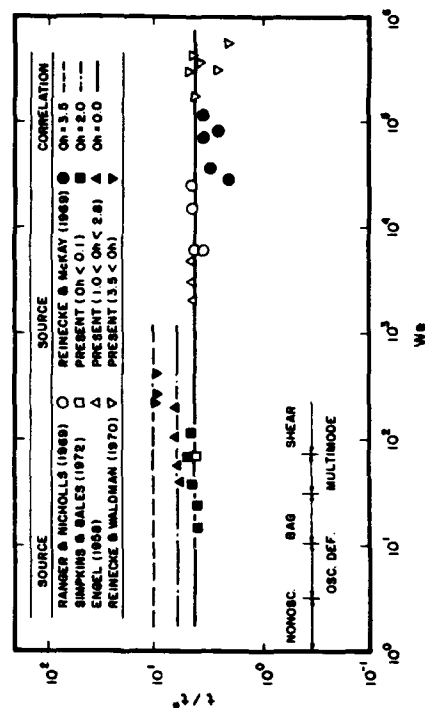


Figure 2. Drop breakup times as a function of We and Oh .

experimental uncertainties (95% confidence) of the present measurements of drop dimensions in this period are estimated to be < 5%.

The present measurements yielded the cross stream diameter, d_c , as a function of time, t , up to the onset of breakup. The results are plotted as the cross stream distortion, $d_c - d_0$, normalized by the maximum cross stream distortion, $d_c - d_0$, in figure 3 (the properties of the maximum distortion will be taken up later). The results of Rieger & Nicholls (1969), Engel (1958) and Wierzbna & Takayama (1988) for shear breakup ($10^{-2} < We < 10^3$) are shown in the figure along with present results for the deformation and bag breakup regimes, to indicate behavior at the limits of the breakup process. All these results are for $Oh < 0.1$, where the effects of liquid viscosity on breakup times are small.

When normalized in the manner of figure 3, drop distortion correlates reasonably well as a linear function of time. The maximum distortion is reached at roughly $t/t^* = 1.6$, or at roughly 30% of the total breakup time. Notably, measurements discussed by Gelfand *et al.* (1974) for a similar range of conditions, and plotted by Wierzbna & Takayama (1988) for the shear breakup regime, exhibit very similar behavior. However, the very high We ($> 10^3$) measurements of Reinecke & Waldman (1970) exhibit somewhat delayed growth to d_{max} . These findings suggest that scaling of drop distortion in the early stages of breakup is relatively universal for $We < 10^3$, which includes the deformation, bag breakup and shear breakup regimes; this is in general agreement with the effects of We and breakup regime on the breakup times discussed in connection with figure 2.

As might be expected, measurements of drop distortion at $Oh > 0.1$, show a progressive delay in the time required for the drop to reach maximum distortion. In fact, this behavior is very similar to the effects of Oh on breakup time, so that results like figure 3 can be obtained in terms of a corrected characteristic breakup time,

$$t^* = t^* (1 - Oh/7), \quad (4)$$

over the present test range ($We < 10^3$, $Oh < 3.5$).

The next parameter of interest is the maximum cross stream diameter of the drop, d_{max} . An approximate expression for the variation of d_{max} with the flow conditions can be obtained for conditions where the effects of liquid viscosity are small, $Oh < 0.1$, by considering the interaction between surface tension and pressure forces when the drop is drawn into a flattened shape. For

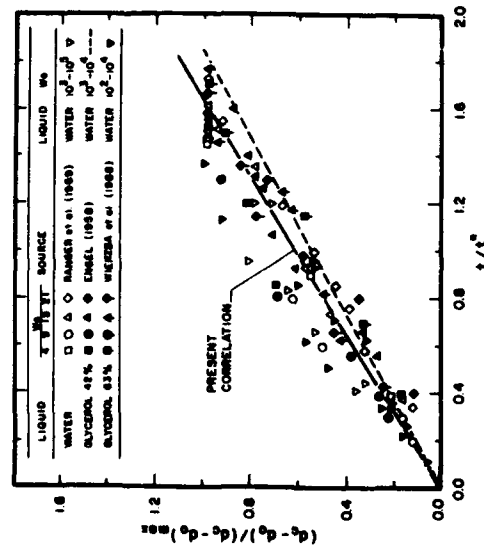


Figure 3. Drop deformation prior to breakup as a function of normalized time.

this treatment, the following assumptions are made: variations in the relative velocity up to the time d_{max} is reached are neglected; the pressure difference between the bulk of the drop liquid and the region near the edge of the drop is assumed to be proportional to the dynamic head of the flow, $\rho_l u_0^2/2$; surface tension forces are assumed to act near the periphery of the deformed (ellipsoidal shaped) drop, along a perimeter of length πd_{max} to resist the pressure forces; and the pressure forces are assumed to act across a peripheral cross sectional area $\pi d_{max} d_{min}$, where d_{min} is the streamwise diameter of the drop along its axis when d_{max} is reached. Equating these forces yields:

$$2\pi d_{max} = C_1 \pi d_{max} d_{min} \rho_l u_0^2 / 2, \quad (5)$$

where C_1 is an empirical coefficient of order of magnitude unity to allow for the effects of the actual pressure distribution and the shape of the drop. During the period of deformation, the total volume of the drop is conserved; thus, assuming that the deformed drop is an ellipsoid about its flow axis, there results

$$d_{min} d_{max}^2 = C_1 d_0^3, \quad (6)$$

where C_1 is an empirical coefficient of order of magnitude unity to allow for departures of the drop from an ellipsoidal shape. Eliminating d_{min} between [5] and [6] then yields

$$d_{max} d_0 = (C_1 C_2)^{1/2} We^{1/2}, \quad (7)$$

Finally, accounting for the fact that $d_{max} d_0$ approaches unity as We becomes small, and fitting the empirical constant using the present measurements, yields

$$d_{max} d_0 = (d_{min} d_0)^{1/2} = 1 + 0.19 We^{1/2}, \quad Oh < 0.1, \quad We < 10^3, \quad (8)$$

where the second part of [8] follows from [5] taking $C_1 = 1$ (which was representative of the present measurements).

Figure 4 is an illustration of the present measurements of $d_{max} d_0$ as a function of We , with Oh as a parameter. The correlating expression of [8] for $Oh \leq 0.1$ also is plotted in the figure. It is evident that [8] provides a reasonable fit of the data, however, it should be noted that [8] is slightly inconsistent with the transition to the nonoscillatory deformation regime of figure 1 because it somewhat overestimates $d_{max} d_0$ near $We = 1$ (by roughly 10%). The effects of increasing Oh can be seen, with $d_{max} d_0$ tending to decrease at a particular We as Oh is increased. Because the deformation motions of the drop cease at the point where d_{max} is reached, this behavior is not thought to be a direct effect of viscous forces on the force balance fixing d_{max} . Instead, the increased time of deformation due to the effects of liquid viscosity is a more probable mechanism. This allows drag forces to act for a longer time before the maximum deformation condition is reached, which tends to reduce the relative velocity, and correspondingly d_{max} through [5] and [6]. This effect also must be responsible for the increased We required for transition to the nonoscillatory deformation

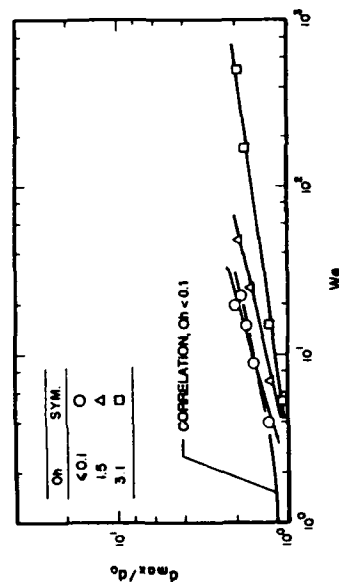


Figure 4. Maximum cross stream diameter prior to breakup as a function of We and Oh .

regime as Oh increases, seen in figure 1. To initiate work toward quantifying this mechanism, the drag properties of drops as they deform will be taken up next.

3.4. Drop Drag

Drop drag properties were found by measuring the motion of the centroid of the drop in the uniform flow field behind the shock wave. This approach is only approximate because it neglects the forces involved as the mass of the drop is redistributed during drop deformation. However, this effect is not expected to be large for the present test conditions because the characteristic velocities in the liquid phase are small. For example, considering either the normal motion of liquid along the axis due to the static pressure increase near the forward stagnation point, or the acceleration of the liquid as the local static pressure decreases in moving toward the edge of the deformed drop, yields the following characteristic liquid phase velocity:

$$u_L = (\rho_G/\rho_L)^{1/2} u_0 \quad [9]$$

For the present conditions u_L is in the range 0.03–0.04, so that the motion of the drop as a whole should dominate the drag properties. Additionally, pressure gradient forces are negligible because the flow behind the shock wave is uniform, and virtual mass and Basset history forces can be neglected because $\rho_L/\rho_G \gg 1$ for the present test conditions (Faeth 1987).

The drop drag coefficient, C_D , was defined in terms of the local relative velocity, u , and cross stream dimension of the drop as follows:

$$C_D = D/(\pi d_c^2 \rho_G u^2/8) \quad [10]$$

where D is the drag force on the drop. Under the present assumptions only the acceleration of the drop must be considered when evaluating the drag force, yielding the following expression for C_D from the measurements of the centroid position, x , as a function of time:

$$C_D = 2\rho_L d_c^3 \dot{x}^2 / [3\rho_G d_c^2 (u_0 - dx/dt)^2] \quad [11]$$

The measurements of C_D primarily were limited by the accuracy of defining centroid motion at small times after passage of the shock wave, to yield experimental uncertainties (95% confidence) < 30%.

The experiments to find C_D involved the initial deformation of the drops up to the time d_{max} was reached. $Oh < 0.1$ and a moderate range of Re (1000–2500), where the effects of Re on the drag of the drops are expected to be small (Faeth 1987). Thus, it was found that C_D largely was a function of the degree of deformation of the drop for the present test conditions. In order to highlight this behavior, the results are plotted in terms of d_c/d_0 in figure 5. Measurements of C_D for solid spheres and thin disks, drawn from White (1974) for the same range of Re as the present tests, also are illustrated in the plot. In spite of the relatively large uncertainties of the measurements, the trend of the data is quite clear; for d_c/d_0 near unity, C_D approximates results for solid spheres and then increases to approach results for thin disks at $d_c/d_0 \approx 2$. Thus, behavior in the period observed appears to be dominated by distortion of the drop, rather than internal circulations which would cause reductions of C_D from values appropriate for solid spheres. This seems reasonable because the characteristic liquid phase velocities are relatively small for the present test conditions, cf. [9].

3.5. Drop Sizes

Measurements of drop sizes after breakup were limited to conditions where $Oh < 0.1$. This was necessary in order to capture the entire drop field after breakup on a single hologram, because larger values of Oh yielded regions containing drops that were too large for the present optical arrangement. The measurements included $We < 10^3$, which corresponds to the bag, transition and shear breakup regimes.

Past work on the structure of dense sprays and processes of primary breakup of nonturbulent and turbulent liquids (Ruff *et al.* 1992; Wu *et al.* 1991, 1992), indicated that local drop size distributions generally satisfied the universal root normal distribution function of Simmons (1977), with $MMD/SMD = 1.2$ [see Beitz (1973) for a discussion of the properties of the root normal distribution function]. This vastly simplifies the presentation of data because the root normal

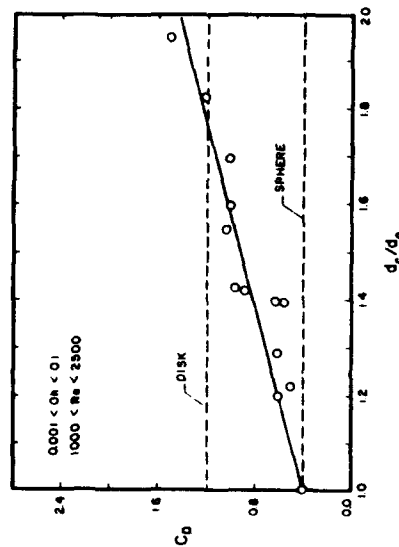


Figure 5. Drop drag coefficient prior to breakup as a function of the normalized cross stream diameter.

distribution only has two moments, and with MMD/SMD a constant, the distribution is entirely specified by the SMD alone. Thus, initial measurements of drop sizes after breakup focused on evaluating the root normal distribution function. This included tests with water, 42 and 63% glycerol mixtures, *n*-heptane and ethyl alcohol for We in the range 15–375.

Typical results of the drop size distribution measurements are illustrated in figure 6 for bag breakup, figure 7 for multimode breakup and figure 8 for shear breakup. The results are plotted in terms of the root normal distribution function, with the function itself illustrated for values of $MMD/SMD = 1.1, 1.2$ and 1.5 . The data are somewhat scattered at large drop sizes because the number of large drops is limited by the breakup of single drops. The results for the bag and multimode breakup regimes (figures 6 and 7) are represented reasonably well by the universal root

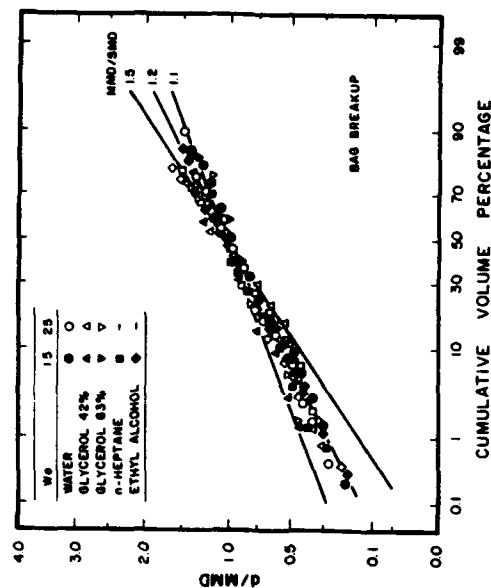


Figure 6. Distribution of drop diameters after bag breakup

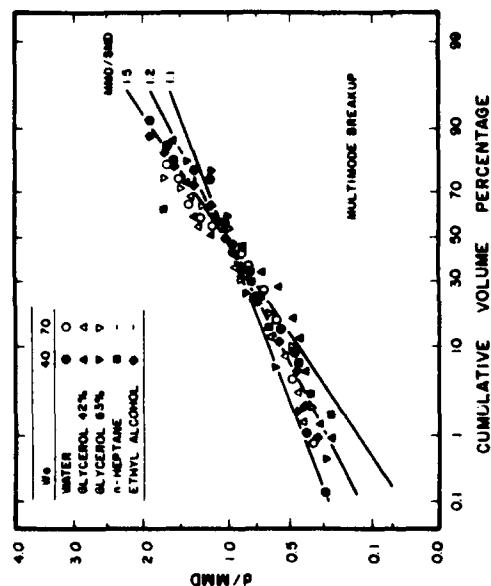


Figure 7. Distribution of drop diameters after multimode breakup

normal distribution function with $MMD/SMD = 1.2$, similar to the findings of Ruff *et al.* (1992) for the near-injector (dense) spray region for pressure atomization and Wu *et al.* (1991, 1992) for primary breakup of nonturbulent and turbulent liquids. In contrast to the present findings, Gelfand *et al.* (1974) observed a bimodal distribution of drop sizes after bag breakup for the two conditions they considered. The reason for this discrepancy is unknown and clearly merits additional study.

The present results yielded bimodal behavior for shear breakup (figure 8) where departure from the root normal drop size distribution for drop sizes greater than the MMD is clearly evident. This behavior was caused by the core (or drop-forming) drop that remained after the stripping of smaller drops from its periphery ceased. Conditions for ending stripping involved a combination of reduced drop sizes and reduced relative velocities so that a description of the behavior was not possible without more information on drop velocities during and after breakup. Results thus far, however, indicate that the universal root normal distribution is only effective for bag and multimode breakup where several large drops form from the ring at the base of the bag, rather than the single core drop of the shear breakup process. This is consistent with observations of Ruff *et al.* (1992) that the universal root normal distribution was effective for dense sprays, including conditions following secondary breakup, because secondary breakup in the bag and multimode regimes dominated their test conditions.

A correlating expression for the SMD after secondary breakup can be obtained by noting the similarity between primary breakup of nonturbulent liquids and shear breakup of drops. In both cases, drops or ligaments are stripped from boundary layers in the liquid phase that form near the liquid surface: on the windward side of waves along the surface for primary breakup of nonturbulent liquids (Wu *et al.* 1991); and on the windward side of the drop for secondary breakup in the shear breakup regime. The configuration for secondary breakup in the shear breakup regime is illustrated in figure 9, where the core (drop-forming) drop is illustrated. It is assumed that the relative velocity at the time of breakup can be represented by the initial relative velocity, u_0 , and that drop sizes after breakup are comparable to the thickness, δ , of the boundary layer as it reaches the stagnation point of the flow. Since this boundary layer develops while moving away from the forward periphery of the drop, the characteristic velocity in the liquid phase is taken to be u_1 from [9]. Additionally, the SMD is dominated by the largest drop sizes in the distribution so that the length of development of the liquid boundary layer is taken to be proportional to d_0 , which should be the condition tending to yield the largest drop sizes. Finally, assuming that the boundary layer is laminar, due to the relatively small values of u_1 and d_0 , there results

$$SMD \cdot d_0 = C_1 (\rho_l / \rho_g)^{1/2} [u_1 (\rho_l d_0 u_0)]^{1/2} \quad (12)$$

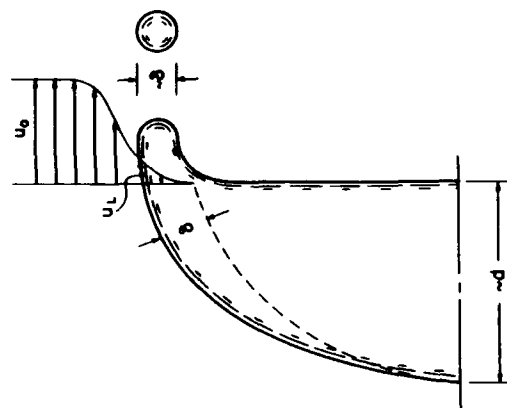


Figure 9. Sketch of the shear breakup process.

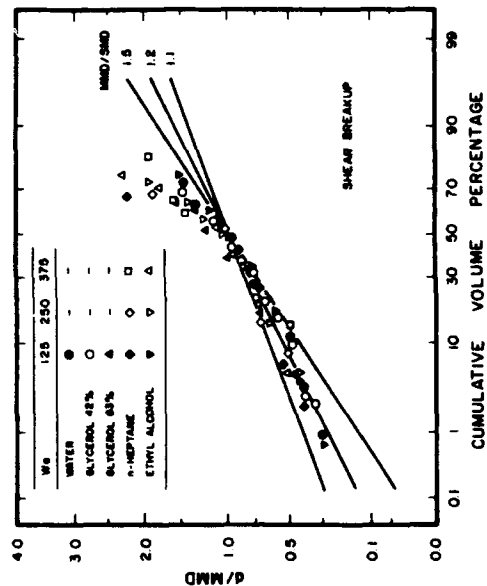


Figure 8. Distribution of drop diameters after shear breakup

where C_s is an empirical constant involving the various proportionality factors. It is convenient to rearrange [12] so that the We based on the SMD is obtained because this helps assess the potential for subsequent breakup of the largest drops in the distribution. Completing this rearrangement yields:

$$\rho_L SMD d_{0,0} \sigma = C_s (\rho_L / \rho_G)^{1/2} [\mu_L / (\rho_L d_{0,0})]^{1/2} We \quad (13)$$

The present measurements of the SMD after secondary breakup are plotted in terms of [13] in figure 10, considering the same liquids as figures 6-8. These results are for $Oh < 0.1$ and $We < 10^4$, including the bag, transition and shear breakup regimes. A correlation of the data according to [13] is also shown in the plot; the power of this correlation is unity within experimental uncertainties, yielding the following empirical fit:

$$\rho_L SMD d_{0,0} \sigma = 6.2 (\rho_L / \rho_G)^{1/2} [\mu_L / (\rho_L d_{0,0})]^{1/2} We \quad (14)$$

The standard deviations of the coefficient and the overall factor on the right-hand side of [14] are 20 and 10%, respectively, with the correlation coefficient of the fit being 0.91. It should be noted, however, that ρ_L / ρ_G does not vary greatly over the present test range and additional measurements are needed to explore density ratio effects.

It is probably fortuitous, and certainly surprising, that a single correlation can express the SMD after bag, multimode and shear breakup. In particular, the three breakup mechanisms appear to be rather different, while the drop size distribution after shear breakup differs from the other two breakup regimes (cf. figures 6-8). On the other hand, similar behavior for the three breakup regimes is consistent with the observation that their breakup times correlate in the same way, as discussed in connection with figure 2. Additionally, the largest drops formed during bag breakup come from the ring at the base of the bag, which has length and velocity scales during its formation that are

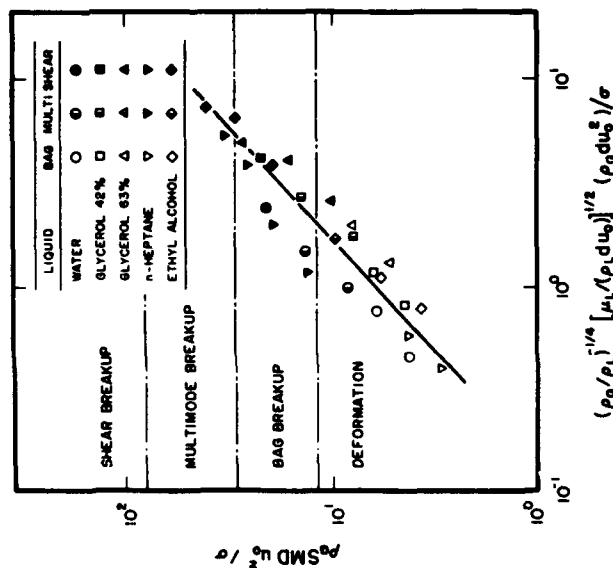


Figure 10 Correlation of the SMD after secondary breakup.

similar to those of shear breakup. This supports the similarity of the SMD after breakup for the bag and shear breakup regimes, with related behavior for the multimode breakup regime that separates them.

Because the largest drops after secondary breakup dominate the SMD, it is of interest to consider their potential for subsequent breakup and the roles that reduced drop sizes and relative velocities play in ending the breakup process. In order to assess the potential for additional deformation and breakup, the regime transitions at low Oh from table 2 have been drawn in figure 10 (interpreting the ordinate as the We of particular drops in the distribution and assuming that u_0 is still representative of the relative velocity). Noting that more than half the mass of the spray involves drop diameters greater than the SMD (recall that typically $MMD/SMD \approx 1.2$), it is clear that a significant fraction of the drops after secondary breakup would be in the deformation and bag breakup regimes if the relative velocities of the large drops still approximated u_0 . For the present test conditions, however, there was no evidence of subsequent breakup of large drops, even though the breakup times of these drops are shorter than the original drop, cf. [1] and [2]. Thus, it is likely that reduction of the relative velocity during breakup is an important factor in stabilizing large drops after secondary breakup, along with the effect of reduced drop diameters. Measurements of drop velocities during and after secondary breakup clearly are needed to better understand how secondary breakup ends; therefore, work along these lines has been initiated in this laboratory.

4. CONCLUSIONS

Drop deformation and secondary breakup after a shock wave initiated disturbance were studied, considering drops of water, *n*-heptane, ethyl alcohol, mercury and various glycerol mixtures in air at normal temperature and pressure (We of 0.5–1000; Oh of 0.0006–4; ρ_L / ρ_G of 580–12,000; and Re of 300–16,000). The major conclusions of the study are as follows:

1. Drop deformation and breakup occurs at $We > 1$, with the following deformation and breakup regimes identified (listed in order of appearance with increasing We at $Oh < 0.1$): no deformation, nonoscillatory deformation, oscillatory deformation, bag breakup, multimode breakup and shear breakup. The We for the onset of deformation and breakup regimes increases with increasing Oh , with no breakup observed over the present test range for $Oh > 4$ due to the stabilizing effect of the liquid viscosity.
2. Unified temporal scaling of deformation and breakup processes was observed in terms of a characteristic breakup time that was nearly independent of We and tended to increase with increasing Oh , cf. [1] and [4].
3. Drop drag coefficients evolved from the properties of spheres to those of thin disks as drop deformations progressed prior to breakup.
4. Drop size distributions after secondary breakup satisfied the universal root normal distribution function (Simmons 1977), with $MMD/SMD \approx 1.2$ for the bag and multimode breakup regimes, similar to recent observations of drop sizes in pressure-atomized sprays and after primary breakup (Ruff *et al.* 1992; Wu *et al.* 1991, 1992), and can be characterized by a single parameter like the SMD. In contrast, drop sizes after shear breakup did not satisfy this distribution function because the largest drops were dominated by the core (drop-forming) drop.
5. Drop sizes after secondary breakup decreased as We increased and could be correlated in a manner similar to recent results for primary breakup of nonvolatile liquids (Wu *et al.* 1991), i.e. in terms of a characteristic liquid boundary layer thickness for all three breakup regimes, cf. [14]. Drop properties after secondary breakup at high We suggest potential for the subsequent breakup of the largest drops in the size distribution if relative velocities did not change during breakup; thus, the fact that the largest drops were observed to be stable suggests that reductions in both drop sizes and relative velocities play a role in ending the secondary breakup process.

Conclusions about the outcome of secondary breakup are limited to conditions where $Oh < 0.1$ and additional study at higher Oh is needed. In addition, practical sprays often involve lower values of ρ_l/ρ_g and Re than the present experiments and the anticipated effects of modifying these variables should be quantified.

Acknowledgements—This research was sponsored by the Air Force Office of Scientific Research, Grant No. 89-0516, under the technical management of J. N. Tishkoff. The authors also would like to thank C. W. Kauffman for the loan of the shock tube facility and advice concerning its operation. The U.S. Government is authorized to reproduce and distribute copies for governmental purposes notwithstanding any copyright notation thereon.

REFERENCES

- BELZ, M. H. 1973 *Statistical Methods in the Process Industries*, pp. 103–104. Wiley, New York.
- BORISOV, A. A., GEL'FAND, B. E., NATANSON, M. S. & KOSOV, O. M. 1981 Droplet breakup regimes and criteria for their existence. *Inzh.-Fiz. Zh.* **40**, 64–70.
- DABOKA, E. K. 1967 Production of monodisperse sprays. *Rev. Scient. Instrum.* **38**, 502–506.
- ENGEL, O. G. 1958 Fragmentation of waterdrops in the zone behind an air shock. *J. Res. Natn. Bur. Stand.* **64**, 245–280.
- FAETH, G. M. 1987 Mixing, transport and combustion in sprays. *Prog. Energy Combust. Sci.* **13**, 293–345.
- FAETH, G. M. 1990 Structure and atomization properties of dense turbulent sprays. In *Proc. 23rd Symp. (Int.) on Combustion*, The Combustion Inst., Pittsburgh, PA, pp. 1345–1352.
- GEL'FAND, B. E., GUBIN, S. A. & KOGARKO, S. M. 1974 Various forms of drop fractionation in shock waves and their special characteristics. *Inzh.-Fiz. Zh.* **27**, 119–126.
- GIFFEN, E. & MURASZEW, A. 1953 *The Atomization of Liquid Fuels*. Chapman & Hall, London.
- HAAS, F. C. 1964 Stability of droplets suddenly exposed to a high velocity gas stream. *AIChE JI* **10**, 920–924.
- HANSON, A. R., DOMICH, E. G. & ADAMS, H. S. 1963 Shock-tube investigation of the breakup of drops by air blasts. *Phys. Fluids* **6**, 1070–1080.
- HASSEL, G. 1972 Untersuchung zur zerstörung von wassertropfen durch aerodynamische krafte. *Forsch. Geb. IngWes.* **38**, 183–192.
- HINZE, J. O. 1955 Fundamentals of the hydrodynamic mechanism of splitting in dispersion processes. *AIChE JI* **1**, 289–295.
- KACZEKOWSKI, S. A. 1980 Measurement of liquid droplet disintegration mechanisms. *Int. J. Multiphase Flow* **6**, 227–239.
- LANE, W. R. 1951 Shatter of drops in streams of air. *Ind. Engng Chem.* **43**, 1312–1317.
- LANGE, N. A. 1952 *Handbook of Chemistry*, 8th edn, pp. 1134 & 1709. Handbook Publishers, Sandusky, OH.
- LIANG, P. Y., EASTES, T. W. & GHARAKHARI, A. 1988 Computer simulations of drop deformation and drop breakup. AIAA paper No. 88-3142.
- LOPAREV, V. P. 1975 Experimental investigation of the atomization of drops of liquid under conditions of a gradual rise of the external forces. *Izv. Akad. Nauk SSSR Mekh. Zhidkosti Gaza* **3**, 174–178.
- RANGER, A. A. & NICHOLLS, J. A. 1969 The aerodynamic shattering of liquid drops. *AIAA JI* **7**, 285–290.
- REINECKE, W. G. & MCKAY, W. L. 1969 Experiments on waterdrop breakup behind Mach 3 to 12 shocks. Sandia Corp. Report SC-CR-70-6063.
- REINECKE, W. G. & WALDMAN, G. D. 1970 A study of drop breakup behind strong shocks with applications to flight. AVCO Report AVSD-0110-70-77.
- RUFF, G. A., WU, P.-K., BERNAL, L. P. & FAETH, G. M. 1992 Continuous- and dispersed-phase structure of dense nonevaporating pressure-atomized sprays. *J. Prop. Power* **8**, 280–289.
- SANGIOVANNI, J. & KESTIN, A. S. 1977 A theoretical and experimental investigation of the ignition of fuel droplets. *Combust. Sci. Technol.* **16**, 59–70.
- STIMMONS, H. C. 1977 The correlation of drop-size distributions in fuel nozzle sprays. *J. Engng Power* **99**, 309–319.
- SHAPKINS, P. G. & BALES, E. J. 1972 Water-drop response to sudden accelerations. *J. Fluid Mech.* **55**, 629–639.
- VOLYNSKII, M. S. & LIPATOV, A. S. 1970 Deformation and disintegration of liquid drops in a gas flow. *Inzh.-Fiz. Zh.* **18**, 838–843.
- WHITE, F. M. 1974 *Viscous Fluid Flow*. McGraw-Hill, New York.
- WIERZBA, A. & TAKAYAMA, K. 1988 Experimental investigation of the aerodynamic breakup of liquid drops. *AIAA JI* **26**, 1329–1335.
- WU, P.-K., RUFF, G. A. & FAETH, G. M. 1991 Primary breakup in liquid/gas mixing layers. *Atomiz. Sprays* **1**, 421–440.
- WU, P.-K., TSENG, L.-K. & FAETH, G. M. 1992 Primary breakup in gas/liquid mixing layers for turbulent liquids. *Atomiz. Sprays*. In press.

Appendix C: Parthesarathy and Faeth (1990a)

Turbulence modulation in homogeneous dilute particle-laden flows

By R. N. PARTHASARATHY† AND G. M. FAETH‡

Department of Aerospace Engineering, The University of Michigan, Ann Arbor,
MI 48106-2140, USA

(Received 25 August 1980)

Continuous-phase properties were studied for homogeneous dilute particle-laden flows caused by nearly monodisperse glass particles falling in a stagnant water bath. Test conditions included 0.5, 1.0 and 2.0 mm diameter particles (yielding particle Reynolds numbers based on terminal velocities of 38, 156 and 545) with particle volume fractions less than 0.01%. Measurements included mean and fluctuating velocities, as well as temporal spectra and spatial correlations of velocity fluctuations in the streamwise and cross-stream directions, using a two-point phase-discriminating laser velocimeter. Flow properties were also analysed using a stochastic method involving linear superposition of randomly-arriving particle velocity fields.

For present test conditions, liquid velocity fluctuations varied solely as a function of the rate of dissipation of particle energy in the liquid. The flows were highly anisotropic with streamwise velocity fluctuations being roughly twice cross-stream velocity fluctuations. Correlation coefficients and temporal spectra were independent of both particle size and the rate of dissipation of particle energy in the liquid. The temporal spectra indicated a large range of frequencies even though particle Reynolds numbers were relatively low, since both mean and fluctuating velocities in the particle wakes contributed to the spectra because particle arrivals were random. The theory predicted many of the features of the flows reasonably well but additional information concerning the mean and turbulent structure of the wakes of freely moving particles having moderate Reynolds numbers in turbulent environments is needed to address deficiencies in predictions of integral scales and streamwise spatial correlations.

1. Introduction

The objective of this investigation was to study turbulence modulation in dispersed multiphase flows, i.e. the direct modification of continuous-phase turbulence properties by transport from the dispersed phase (Al Taweel & Landau 1977). Turbulence modulation is most important in dense sprays and particle-laden flows, however, it is difficult to study in these circumstances owing to the complexities of the flows and limitations of instrumentation. To circumvent these problems a much simpler flow was considered; namely, a homogeneous dilute particle-laden flow generated by a uniform flux of particles moving through a nearly stagnant (in the mean) liquid so that all turbulence properties were due to the relative motion of the particles, i.e. the entire flow field was the result of turbulence modulation phenomenon.

† Present address: Institute of Hydraulic Research, University of Iowa, Iowa City, IO, USA.

‡ Author to whom correspondence should be addressed.

Past studies of turbulence modulation have been reviewed by Owen (1964, 1969), Hinze (1972) and Faeth (1987), while recent work can be found in Michaelides & Stock (1989). Hinze (1972) describes several mechanisms of turbulence modulation, as follows: (i) an effect due to locally increased shear rates in the continuous phase modifying the turbulent energy spectrum of the continuous phase in the wavenumber range corresponding to the distance between elements of the dispersed phase; (ii) effects due to turbulence in the wakes of individual elements of the dispersed phase, modifying the turbulent energy spectrum of the continuous phase in the wavenumber range corresponding to the size of dispersed elements; (iii) the action of groups of particles on the flow pattern of the continuous phase; and (iv) effects due to the volume occupied by the dispersed phase. Owing to the difficulties of making measurements in flows having large particle volume fractions, however, the last mechanism is not considered here, e.g. present particle volume fractions were less than 0.01%. The remaining effects should influence the turbulence energy spectrum in wavenumber ranges corresponding to the size and spacing of the dispersed-phase elements which generally corresponds to the high-wavenumber range for most practical dispersed flows. According to Hinze (1972) modification of the turbulent energy spectrum at high wavenumbers implies greater dissipation rates than a single-phase flow having comparable mean-flow properties. This behaviour is supported by theoretical studies of particle motion in turbulent or turbulent-like flows with small relative velocities at the Stokes limit due to Kuchanov & Levich (1967), Owen (1969) and Al Taweel & Landau (1977).

In contrast, measurements suggest that effects of turbulence modulation are system-dependent and can cause turbulence levels to either increase or decrease. For example, studies reporting reduced turbulence levels attributed to turbulence modulation include: Owen (1969) who found reduced turbulence intensities in particle-laden pipe flows; Shuen *et al.* (1985) who found decreasing turbulence intensities with increasing particle loading in particle-laden turbulent jets; and Solomon *et al.* (1985) who found reduced turbulence levels and greater degrees of anisotropy in the dense region of sprays. On the other hand, studies reporting increased turbulence levels attributed to turbulence modulation include: Kada & Hanratty (1960) and Hino (1963) who found increased turbulence levels in pipe flows of suspensions; Sun & Faeth (1986) and Parthasarathy & Faeth (1987) who found increased turbulence and anisotropy levels in turbulent bubbly and particle-laden jets; and Lance & Bataille (1982) and Lance *et al.* (1980, 1985) who found increased turbulence levels in bubbly grid-generated turbulent flows and bubbly shear flows. Several phenomena are responsible for these differences in shear flows: the presence of the dispersed phase generally modifies mean velocity distributions to some extent, which influences conventional turbulence mechanisms that tend to dominate dispersed multiphase flows that are sufficiently dilute to be amenable to measurements; effects of turbulence modulation are influenced by both particle and turbulence properties which can lead to diverse behaviour even for similar flow configurations; and increased dissipation due to the presence of particles is counteracted by disturbances due to growing particle wakes which supplements turbulence generation by conventional single-phase mechanisms, particularly when the relative velocities of the particles are large.

Problems of interpreting effects of turbulence modulation are minimized in homogeneous flows like those considered by Lance & Bataille (1982) and Lance *et al.* (1985). Two air/water bubbly flow configurations were considered: nearly homogeneous flows downstream of a turbulence-generating grid and shear flows. In

general, continuous-phase turbulence intensities increased with increasing void fractions, with the largest increases observed at low liquid velocities where relative velocities were comparable to liquid velocities. This suggests that increased turbulence production due to the presence of bubble wakes dominated increased dissipation by the bubbles over the range of these experiments. The one-dimensional temporal spectra of streamwise velocity fluctuations were also modified by the presence of bubbles; in particular, the classical $-5/3$ power law for the inertial region of single-phase homogeneous turbulence was modified to a $-3/2$ power when bubbles were present, although temporal spectra were relatively independent of void fractions for the range of these tests. Lance *et al.* (1985) also achieved some success in modifying a second-order turbulence model to treat effects of turbulence modulation on the streamwise variations of the Reynolds stress tensor for the bubbly shear flow; however, these results were not evaluated for the homogeneous bubbly flows. Additionally, effects of turbulent dispersion could not be considered since bubble properties were not measured.

The present study seeks to extend the work of Lance & Bataille (1982) and Lance *et al.* (1985) by considering a homogeneous multiphase flow so that effects of turbulence modulation are highlighted. Rather than contend with the complications of grid-generated turbulence in a flowing continuous phase, however, the present study was limited to a uniform flux of nearly monodisperse spherical glass particles settling in a nearly stagnant (in the mean) water bath. This yields a stationary homogeneous flow where all turbulence properties are due to effects of turbulence modulation. Measurements included particle number fluxes, using Mie scattering from a laser light sheet; and liquid and particle velocities, and liquid temporal spectra and spatial correlations, using a two-point, phase-discriminating laser velocimeter. Stochastic analysis was also undertaken to assist interpretation of the measurements. The present paper is limited to effects of turbulence modulation; results relating to turbulent dispersion are reported in a companion paper (Parthasarathy & Faeth 1990).

Experimental and theoretical methods are described in the next two sections. Measured and predicted results are then presented in §4, considering evaluation of the apparatus, velocity fluctuations, temporal correlations and spatial correlations in turn. Major conclusions of the study are summarized in §5. Additional details and a complete tabulation of data can be found in Parthasarathy (1989).

2. Experimental methods

2.1. Apparatus

Figure 1 is a sketch of the homogeneous particle flow apparatus. The tests were conducted using nearly monodisperse spherical glass particles having nominal diameters of 0.5, 1.0 and 2.0 mm. The flow of particles was controlled by a variable-speed particle feeder (AccuRate, Model 310, having a 25 mm diameter helix for 0.5 mm diameter particles and a 19 mm diameter helix for 1.0 and 2.0 mm diameter particles, with centre rods used in both cases). The particles were dispersed by falling through an array of 9 screens (0.58 mm diameter wire spaced 2.1 mm apart for 0.5 and 1.0 mm diameter particles, and 0.89 mm diameter wire spaced 4.2 mm apart for 2.0 mm diameter particles) with a 190 mm spacing between screens. The particles then fell into a windowed tank (410 × 535 × 910 mm) which was filled with water to a depth of 800 mm. After a deceleration distance of 100–200 mm, the particles reached a steady (in the mean) terminal velocity within the bath. Measurements were

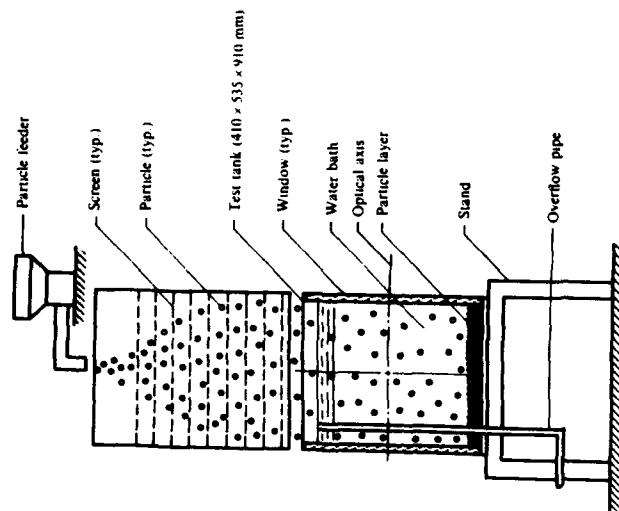


FIGURE 1. Sketch of homogeneous particle flow apparatus.

made near the centre of the tank, roughly at a depth of 400 mm. The particles collected at the bottom of the tank with little rebound upon impact and were removed from time-to-time using a suction system; the maximum depth of collected particles at the bottom of the tank was 100 mm. After collection, the particles were dried and reused since periodic examination showed negligible damage to the particles. Displacement velocities due to collection of particles at the bottom of the tank were less than 0.014 mm/s, which was negligible in comparison to the velocities of interest.

2.2. Instrumentation

Particle number fluxes were measured using a Mie scattering system similar to Sun & Faeth (1986). A small light sheet having a nearly uniform intensity was produced at the measuring volume by passing the beam from a 5 mW He-Ne laser through an aperture. The measuring volume was observed in a horizontal plane, normal to the laser beam, using a photodetector. Particles passing through the measuring volume generated pulses in the detector output which were shaped and recorded by a pulse counter developed in this laboratory. The pulse counter had an adjustable threshold to control spurious background signals. Grazing collisions of particles with the optical measuring volume were recorded so that the region observed had dimensions that were roughly the sum of optical lengths and the particle diameter. The actual

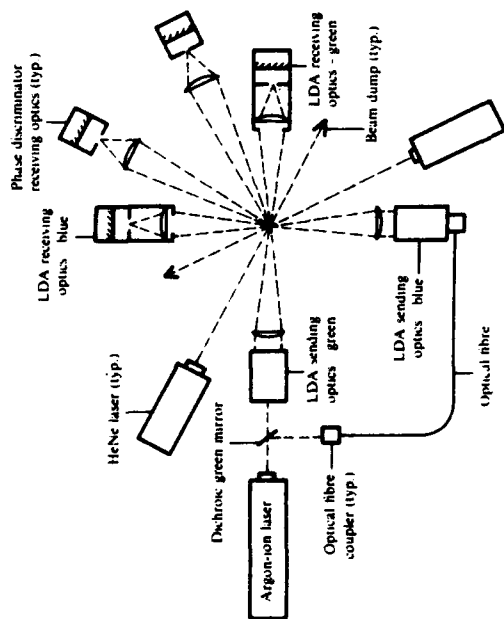


FIGURE 2. Sketch of two-point phase-discriminating laser velocimeter.

area of observation, however, was calibrated by collecting particles for timed intervals. More than 500 particles were counted to find the mean particle number flux. Experimental uncertainties were due to variations of particle diameters within each size group, which influenced the area observed, and finite sampling times: the latter dominated the measurements yielding experimental uncertainties (95% confidence) less than 10% (Parthasarathy 1989).

A two-point, phase-discriminating laser velocimeter (LV) was used to measure mean and fluctuating velocities, and one- and two-point correlations of velocity fluctuations of the liquid, as well as streamwise and cross-stream particle velocities. Figure 2 is a schematic diagram of the LV arrangement. The LV involved one fixed channel, focused at the centre of the tank, and one channel that could be traversed in both the streamwise and cross-stream directions. The two channels were based on the green (514.5 nm) and blue (488 nm) lines of a 2W argon-ion laser operating in the multiline mode. The two laser lines were separated with a dichroic green mirror and the blue line was transmitted to the sending optics of the traversable channel using a fibre-optic cable. Both channels operated in the dual-beam forward-scatter mode and had measuring volumes with diameters of 0.1 mm and lengths of 1.2 mm. Directional bias and ambiguity were eliminated using a 40 MHz Bragg-cell frequency shifter (TSI, Model 918-11) with the output signals downshifted to convenient frequency ranges (0.05–0.1 MHz) for filtering and signal processing. Streamwise and cross-stream velocities were measured by rotating the LV optics accordingly.

One-half gram of titanium dioxide particles in rutile form (nominal diameter of 2.8 μm) were used to seed the bath for the LV measurements. It took about 15 minutes to distribute the seeding particles throughout the bath and 12 hours for them to settle to the bottom. Since the longest test time was roughly 3 hours, settling

of seeding particles did not alter data rate appreciably. This seeding level provided data rates of 2–4 kHz over the test range.

Light scattered by the seeding particles generally yielded lower amplitude signals than light scattered by the glass beads so that simple amplitude-discrimination could be used to detect particle velocity signals. As Matarrese, Tan & Elghobashi (1984) point out, however, particles grazing the LV measuring volume can yield low-amplitude signals which could be misinterpreted as liquid-phase velocity signals; this is a serious problem for the present experiments since relative velocities between the phases were large in comparison to liquid velocities. Thus a phase-discriminating system, illustrated in figure 2, was used on both channels to avoid biasing of liquid velocities due to grazing collisions. The arrangement involved a third beam from a 5 mW He-Ne laser at an angle of 18° from the LV axis which was observed off-axis in the forward-scatter direction at an angle of 32° from the LV axis. This yielded a discriminator measuring volume having a diameter of 0.6 mm and a length of 1.3 mm which enveloped the LV measuring volume. Thus, particles that grazed the measuring volume yielded a scattering signal that was detected by the discriminator system. The data processing system was programmed to eliminate all liquid-phase velocity records where the discriminator signal indicated the presence of a particle near the LV measuring volume. For present conditions, however, the effects of grazing collisions were small since the flows were dilute, e.g. operation with and without the phase discriminators resulted in less than 2% changes of velocity fluctuations.

The time between valid liquid velocity signals was small, *c.* 0.5–1 ms, in comparison to Kolmogorov timescales in the range 66–177 ms and integral timescales in the range 4–7 s; therefore, the analogue outputs of the burst-counter signal processors (TSI Model 980B) were time-averaged, ignoring periods when particles were present, to obtain unbiased time-averaged liquid velocities. The analogue outputs were filtered using Ithaco low-pass filters before the signals were digitized and transferred to a microcomputer for processing. It was found that averaging signals for twenty minutes provided satisfactory values of mean and fluctuating velocities, probability density functions and two-point velocity correlations. One-point temporal spectra were measured over a frequency range of 10^{-4} – 10^3 Hz. These spectra were obtained using three sampling frequencies: 7.5, 50 and 2500 Hz with low-pass filter settings of 4, 25 and 1000 Hz. The spectra were obtained from 4096 points at each sampling frequency, averaging over 80–90 such groups to obtain final results. The spectra at different sampling frequencies overlapped and were matched at the common frequencies before normalizing the total area under the combined spectrum to unity.

Bias errors were small since the flow was homogeneous. Experimental uncertainties (95% confidence) were dominated by finite sampling times and were as follows: mean streamwise and cross-stream velocities, less than 10% and 40%; fluctuating streamwise and cross-stream velocities, less than 14% and 21%; temporal spectra of streamwise and cross-stream velocity fluctuations, less than 35% and 42% for frequencies below 0.01 Hz and less than 16% and 21% for all other frequencies; two-point spatial correlations in the lateral and streamwise directions, less than 29% and 36%; and Reynolds stresses less than 55% (Parthasarathy 1989). These values are high in comparison to typical turbulent flows due to very low liquid velocities (*c.* 10 mm/s) and very high turbulence intensities (in excess of 100%).

Particle diameter (mm)	0.5 (0.043)		1.0 (0.065)		2.0 (0.13)	
	Low	High	Low	High	Low	High
Particle properties						
Terminal velocity (mm/s)		65 (7)		147 (14)		262 (16)
Reynolds number (-)		36 (9)		136 (20)		545 (53)
Drag coefficient (-)		2.06		0.90		0.61
Number flux (1/cm ² /s)	55.4	110.8	3.7	20.9	1.1	3.3
Mean spacing (mm)	10.5	8.2	32.7	18.3	61.8	43.2
Liquid properties						
Rate of dissipation (mm ² /s ⁴)	53.2	0.63	27.3	155.8	61.7	103.5
l_K (mm)	0.33	0.28	0.30	0.25	0.32	0.24
l_K (s)	0.13	0.09	0.18	0.07	0.12	0.07
u_K (mm/s)	2.6	3.1	2.2	3.4	2.7	3.6
$(u^2)^{1/2}$ (mm/s)	3.3	4.7	2.4	3.1	3.7	6.1
$(v^2)^{1/2}$ (mm/s)	1.6	2.7	1.2	2.3	1.7	3.1
w (mm/s)	1.6	3.9	1.0	3.8	3.0	6.0
v (mm/s)	0.7	0.6	1.1	1.6	1.0	0.9

TABLE 1. Representative test conditions. Round glass beads, density of 2450 kg/m³, falling in a stagnant water bath at 296 ± 2 K. Numbers in parentheses denote standard deviations. Particle volume fractions less than 0.01%, displacement velocities less than 0.014 mm/s, direct dissipation by particles less than 4.5%.

2.3. Test conditions

A range of particle number fluxes were considered for each particle size: representative test conditions at the low and high ends of these ranges are summarized in table 1. Measured particle size distributions were approximately Gaussian and had standard deviations of roughly 10% of the nominal particle diameter. Particle drag properties were calibrated by releasing individual particles within the still water bath and measuring their terminal velocities with the LV system. The measured probability density functions (PDFs) of terminal velocities were then compared with predicted PDFs based on the measured size distribution and the standard drag coefficient, C_D , for spheres (Putnam 1961):

$$C_D = 24(1 + \frac{1}{2}Re^{\frac{1}{2}})/Re, \quad (1)$$

where the particle Reynolds number is defined as

$$Re = U_\infty d_p / \nu, \quad (2)$$

and U_∞ is the terminal velocity, d_p the particle diameter and ν the kinematic viscosity of water. Particle Reynolds numbers were 38, 156 and 545 for the 0.5, 1.0 and 2.0 mm diameter particles. Matching predicted and measured mean terminal velocities required corrections to the standard drag coefficient of less than 14%: the resulting corrected drag coefficients and terminal velocities for each particle size appear in table 1. The terminal velocities of particles passing through the dispersing screen, both singly and at test particle fluxes, were not appreciably different from the calibrated terminal velocities.

Mean particle spacings, l_p , were found assuming that particles were falling randomly with a uniform particle number flux \bar{n} , and a mean particle-averaged terminal velocity, \bar{u}_p :

$$l_p = (\bar{u}_p / \bar{n})^{-1}. \quad (3)$$

The resulting particle spacings were in the range 8–62 mm, or 16–33 particle

diameters, yielding particle volume fractions less than 0.01%; therefore, effects of direct particle-to-particle interactions were small.

Within the region where measurements were made, the mean velocities of the particles were constant and were much greater (*c.* 10 times greater) than their velocity fluctuations. Additionally, the particles showed no evidence of rotation as they entered the bath or during their descent in the bath. Then the rate of dissipation of turbulence kinetic energy, ϵ , within the bath can be equated to the rate of production of turbulence by particles assuming that effects of particle velocity fluctuations are small. The rate of production of turbulence is then equal to the rate of loss of the potential energy of the particles as they fall through the bath, yielding

$$\epsilon = \pi \bar{n}^2 g d_p^2 (\rho_p - \rho) / \rho, \quad (4)$$

where g is the acceleration due to gravity, and ρ_p and ρ are the particle and bath densities. Dissipation was used to characterize the measurements since it provides a basis for comparing results for different particle sizes and number fluxes using a single parameter; thus, representative values of ϵ appear in table 1. The corresponding Kolmogorov length, $l_K = (\nu^3/\epsilon)^{1/4}$, time, $t_K = (\nu/\epsilon)^{1/2}$ and velocity $u_K = (\epsilon/\nu)^{1/2}$ scales also appear in the table. Notably, the Kolmogorov lengthscale is comparable to the LV measuring volume and somewhat smaller than the particle diameters. Furthermore, measured liquid streamwise and cross-stream velocity fluctuations, $(u'^2)^{1/2}$ and $(v'^2)^{1/2}$, are comparable to the Kolmogorov velocity scales although the u_K varies to a lesser extent as ϵ is changed. The effect of mean streamwise and cross-stream velocities, \bar{u} and \bar{v} , in the flows, summarized in table 1, will be taken up later.

In a particle-laden flow, the dissipation of turbulence consists of two components: conventional dissipation by the continuous phase; and direct dissipation by interactions between the particles and the continuous phase, the last being the contribution that was ignored when deriving (4) as well as the contribution that is usually considered in turbulence models of the process (Faeth 1987). The relative importance of these two contributions to dissipation can be found by noting that the instantaneous rate of dissipation per particle, ϵ_p , is equal to the product of the drag force and the relative velocity:

$$\epsilon_p = 3\pi\eta d_p(1 + \frac{1}{2}Re^{\frac{1}{2}})u_r^2, \quad (5)$$

where the drag coefficient has been obtained from (1) and u_r is the relative velocity. The time-averaged dissipation per particle is then given by

$$\bar{\epsilon}_p = 3\pi\eta d_p[(1 + \frac{1}{2}Re^{\frac{1}{2}})\bar{u}_r^2 + (1 + 10Re^{\frac{1}{2}}/27)\bar{u}_r'^2], \quad (6)$$

where \bar{u}_r and $\bar{u}_r'^2$ are the mean value and variance of the relative velocity. The first term on the right-hand side of (6) is dissipation due to the mean drag and relative velocity; it is the component of dissipation per particle that is analogous to the production of turbulence considered in (4). The second term on the right-hand side of (6) represents the direct contribution of the particle to the dissipation of turbulence; it is the product of the fluctuating drag force and the fluctuating relative velocity. Parthasarathy (1989) estimates upper bounds for the ratio of the two terms, finding that the second term is generally less than 5% of the first term for present test conditions since $\bar{u}_r'^2/\bar{u}_r^2$ is small. Thus, generation of turbulence by particles, followed by dissipation within the liquid, are the dominant features for present test conditions, while direct dissipation of turbulence by particles is a secondary effect. Furthermore, ignoring the second term when estimating ϵ from (4) is reasonably accurate for present conditions as well.

3. Theoretical methods

3.1. General formulation

Simplified analysis of the flow was undertaken in order to help interpret measurements of liquid-phase properties. Two limiting analyses of the liquid phase were considered: (i) methods used to treat homogeneous turbulent flows with time-averaged governing equations for turbulence quantities, analogous to those considered by Hinze (1975) for isotropic turbulence; and (ii) methods that explicitly consider the properties of the flow field of individual particles, analogous to the approach of Batchelor (1972) for sedimentation processes. Methods used for isotropic turbulence have been applied to grid-generated turbulence where the grid plays a role similar to the particles in the present flows; however, those methods are only applied at some distance from a grid of close-spaced elements where the properties of the near field behind the grid have been lost, yielding a non-stationary decaying isotropic flow. This is not very appealing for the present problem where the flow is stationary and wake sources are present throughout the flow field, i.e. the particles are widely spaced in comparison to their dimensions so that strong interactions between neighbouring wakes do not immediately occur and wakes remain identifiable for some distance before losing their character through interactions with other nearby wakes. Thus, a method that explicitly considers the flow field of the particles, similar to Batchelor (1972), was pursued instead.

The major assumptions of the analysis are: the flow is statistically stationary with a uniform flux of particles and constant liquid properties; particle arrival times at an increment of area are independent of other particle arrival times so that arrival times satisfy Poisson statistics (Rice 1954); the flow was taken to be infinite in extent since the measurements exhibited little effect of bath volume; and the flows are dilute so that the probability of a test point being within a particle is negligibly small. The flow field associated with each particle included the following contributions: the near-field flow around the particle, which was taken to be the potential flow around a sphere since the probability of a point of observation being in the strongly viscous region near the surface is small in dilute flows; and the asymptotic properties of the particle wake. The equations of motion are linear for potential flow, and for asymptotic wake flow; therefore, we can assume that flow properties are the result of a linear superposition of the particle flow fields that have reached the point of observation.

Summing flow properties under these assumptions involves extension of methods used to analyse random noise when effects of noise can be added linearly (Rice 1954). Let the point of observation be the origin of a cylindrical coordinate system with r denoting the streamwise direction and ϕ denoting the radial and azimuthal coordinates. Since wake Reynolds numbers exceed unity for present conditions, effects of wake turbulence can be important (Tennekes & Lumley 1972); therefore, we suppose that arrival of a particle at $x = 0$, r, ϕ and time $t = 0$ produces effects $g(r, \phi, t)$ due to mean properties and $g'(r, \phi, t)$ due to turbulent properties at the point of observation. Then, if the effect of each particle can be added linearly, the total effect due to all particles at time t is:

$$G(t) = \sum_{j=1}^N g(r_j, \phi_j, t-t_{jk}) + g'(r_j, \phi_j, t-t_{jk}), \quad (7)$$

where the position vectors (r_j, ϕ_j) are chosen to collect all particles, and the k th particle at position (r_j, ϕ_j) reaches $x = 0$ at t_{jk} .

Following Rice (1954), Campbell's theorem can be extended to treat random arrivals of particles over a plane to yield the time-averaged effect:

$$\bar{G} = n'' \int_{-\infty}^{\infty} dt \int_0^{\infty} d\phi \int_0^{\infty} g(r, \phi, t) r dr, \quad (8)$$

while the mean-squared fluctuation about the average becomes:

$$G'^2 = n''^2 \int_{-\infty}^{\infty} dt \int_0^{\infty} d\phi \int_0^{\infty} g^2(r, \phi, t) + g'(r, \phi, t) r dr, \quad (9)$$

Rice (1954) also shows that the probability-density function (p.d.f.) of G approaches a normal distribution as $n'' \rightarrow \infty$. For finite n'' , the error in approximating the p.d.f. by the normal distribution is on the order of $G'^2/(G'^2)^2 \sim 1/n''$, which is small for present test conditions.

Temporal correlations and spectra, and spatial correlations, are also of interest since they affect the turbulent dispersion of the particles. Proceeding as before (Rice 1954), the temporal correlation of G with time delay τ , is given by

$$\overline{G'(t)G'(t+\tau)} = n''^2 \int_{-\infty}^{\infty} dt \int_0^{\infty} d\phi \int_0^{\infty} g(r, \phi, t) g(r, \phi, t+\tau) r dr. \quad (10)$$

The temporal spectrum is obtained from the Fourier transform of (10):

$$E_G(f) = 4 \int_{-\infty}^{\infty} \overline{G'(t)G'(t+\tau)} \cos(2\pi f\tau) d\tau, \quad (11)$$

where f denotes frequency. The spatial correlation in the cross-stream direction is most conveniently found in a Cartesian coordinate system with Y and Z denoting coordinates in a cross-stream plane and y the separation distance between points, with no loss of generality since the flow is homogeneous. Then, the spatial correlation of G' in the cross-stream direction is

$$\overline{G'(Y)G'(Y+y)} = n''^2 \int_{-\infty}^{\infty} dt \int_{-\infty}^{\infty} dZ \int_{-\infty}^{\infty} |g(Y, Z, t) g(Y+y, Z, t)| \\ + g'(Y, Z, t) g'(Y+y, Z, t)| dY. \quad (12)$$

In order to find the spatial correlation of G' in the streamwise direction we assume that the particles are moving in the x -direction at their terminal velocities, since particle velocity fluctuations are small in comparison to U_∞ . This implies that effects of turbulent particle dispersion are small, which is only appropriate at the limit of infinitely dilute flow. Thus, the spatial correlation at displacement x is the same as the temporal correlation at delay time τ with $x = t', \tau$, or

$$\overline{G'(X)G'(X+x)} = \overline{G'(t')G'(t'+\tau)}, \quad (13)$$

Several properties of the flow can be inferred immediately from (9) (13) before specifying wake properties and completing the integrations. In particular, since $\epsilon \sim n''$ from (4), effects of dissipation can be summarized as follows for a particular particle size: velocity fluctuations are proportional to $\epsilon^{1/2}$; correlations and temporal spectra are proportional to ϵ ; and correlation coefficients, normalized temporal

spectra, ratios of velocity fluctuations, and temporal and spatial integral scales are all independent of ϵ .

The preceding equations are limited to monodisperse particle flows. However, under the assumption of linear superposition, if $\phi(d_p)$ is a generic property for a particular particle diameter, then the mean value of ϕ becomes

$$\bar{\phi} = \int_0^\infty \phi(d_p) p.d.f.(d_p) dd_p, \quad (14)$$

where the p.d.f. (d_p) was measured as noted earlier.

3.2. Particle flow field and liquid properties

The properties to be found from (8)–(13) can be separated into three components that can be evaluated separately and summed. For a generic property ϕ , this includes the potential flow region, ϕ_{pf} ; the mean properties of the wake, ϕ_{aw} ; and the turbulent properties of the wake, ϕ_{tw} . Potential flow properties were found by assuming that effects of velocity fluctuations in the flow experienced by the particle could be ignored. This is reasonable since the relative turbulence intensities of the particles, which are comparable to $(u')/U_\infty$, are small even though particle diameters are somewhat larger than the Kolmogorov lengthscales. For a sphere moving in a stagnant fluid the potential flow velocities are (Batchelor 1973):

$$u = \left(\frac{1}{2}U_\infty + d_p^2/r_0^2\right)(1 + x^2/r_0^2), \quad (15)$$

$$v = \left(\frac{1}{2}U_\infty - d_p^2 x/r_0^2\right)(1 - x^2/r_0^2), \quad (16)$$

where the centre of the sphere is the instantaneous origin, r_0 is the distance from the point of observation to the centre of the sphere, and x is the streamwise distance from the centre of the sphere. To convert (15) and (16) to a coordinate system fixed at the point of observation, we use the following transformations:

$$x = U_\infty t, \quad r_0^2 = U_\infty^2 t^2 + r^2. \quad (17)$$

The velocities of (15) and (16) decay rapidly with distance from the sphere and are practically zero at $r_0 = 2d_p$; therefore, potential flow calculations were terminated at $r = 2d_p$ and wake properties were used beyond this point. Mean-squared velocity fluctuations for the potential flow region then become:

$$u_{pf}^2 = 0.019u_{\infty}^2 d_p^2/(U_\infty^2 t^2), \quad (18)$$

$$v_{pf}^2 = 0.003u_{\infty}^2 d_p^2/(U_\infty^2 t^2), \quad (19)$$

$$\theta = \left(\frac{1}{2}U_\infty d_p\right)^2. \quad (20)$$

where

The contributions of the potential flow region to velocity fluctuations from (18) and (19) were less than 10% of the contributions of the wakes since the volume of the potential flow region is much smaller than the wake. Thus, the contributions of the potential core were only considered for u'^2 and v'^2 but were ignored for other properties.

Specifying a representative wake is complicated by turbulent dispersion of the freely moving particles and the turbulence of the flow field itself which modifies the structure of the particle wakes from properties found with rigidly-mounted spheres in non-turbulent environments. For lack of an alternative, however, we consider the

limit of an infinitely dilute flow where these disturbances are small and the particle and its wake follow a vortex path. The mean liquid downflow velocity due to particle motion is also negligible at this limit so that velocities outside the wake are negligible. The following discussion will be limited to turbulent wakes. Parthasarathy (1969) presents the formulation for laminar wakes. The mean velocity distributions in turbulent wakes were derived from results appearing in Tennekes & Lumley (1972):

$$u/U_\infty = 2.23(U_\infty l/\theta)^{1/2} \exp(-r^2/2l^2), \quad (21)$$

$$v/U_\infty = 0.74\theta^{1/2}(U_\infty l)^{-1/2} \exp(-r^2/2l^2), \quad (22)$$

$$\text{where} \quad l = 0.47(U_\infty \theta)^{1/2}, \quad (23)$$

and (17) has been used to convert from distance from the sphere to time after arrival of the sphere. Finally, the local wake Reynolds number is

$$Re_l = (U_\infty \theta/\nu)(U_\infty l)^{-1}. \quad (24)$$

From (24) it is evident that Re_l progressively decreases with increasing time, eventually reaching laminar wake conditions if the ambient environment is not turbulent. Equations (21)–(23) are based on similarity assumptions with a constant eddy viscosity over the wake cross-section at asymptotic conditions far from the sphere. In spite of these simplifications, however, (21) provides a reasonable correlation of the existing measurements of Uchiroi & Freymuth (1970) for the wakes of rigidly-mounted spheres in a non-turbulent environment. The values of u and v from (21) and (22) are unbounded at small t but the equations are only used in the present wake region where $t > T_0 = 2d_p/U_\infty$.

Inserting (21)–(23) into (8)–(13) showed that except for \bar{u}_{mw}^2 , the integrals did not converge as $t \rightarrow \infty$. A similar problem is encountered for laminar wake properties so that eventual transition to a laminar wake does not resolve the difficulty. This problem is similar to limit problems encountered for Stokes flow around particles during analysis of sedimentation where resolving the problem benefited from a rigorous knowledge of Stokes flow (Batchelor 1972). In the present case, (21)–(23) are empirical and their relevance to the turbulent environment of the present flows certainly is questionable; therefore, rather pursue the limit problem the present results were found for a finite upper limit of integration, T_1 , assuming that at this point wake properties have lost coherence in the turbulent field. The value of T_1 is specified later to fit measured and predicted velocity fluctuations. The general results are:

$$u_{mw}^2 = 3.34\epsilon(\theta^2 T_1/U_\infty^2)^{1/2}, \quad (25)$$

$$v_{mw}^2 = 0.014\epsilon\theta^2(T_1 - T_0)/(T_0 T_1 U_\infty^2), \quad (26)$$

$$\overline{u'(U_\infty + u + \tau)_{mw}} = 2.23\epsilon(\theta/U_\infty)^{1/2} \int_{T_0}^{T_1} (t + (t + \tau)\theta)^{-1/2} dt, \quad (27)$$

$$\overline{v'(U_\infty + u + \tau)_{mw}} = 0.058\epsilon(\theta/U_\infty)^{1/2} \int_{T_0}^{T_1} (t + (t + \tau)\theta)^{-1/2} dt, \quad (28)$$

$$\overline{u'(U_\infty + u + \tau)_{mw}} = 1.11\epsilon(\theta/U_\infty)^{1/2} \int_{T_0}^{T_1} (t^2 \exp(1.11\theta^2(U_\infty t\theta)^{-1}) dt, \quad (29)$$

where the integrals in (27)–(29) were found numerically after T_i was specified.

Turbulence intensities of wakes are large even near the axis so that the contribution of wake turbulence to (8)–(12) is significant. Wake turbulence properties used during the calculations were taken from Uchiroi & Freymuth (1970) which involved wake Reynolds numbers in the range 4000–150 000. Present wake Reynolds numbers were much lower, with local values in the range 2–500 for the present final selection of T_i , so that computed results can be thought of as an upper bound for effects of wake turbulence on various properties at the limit of low particle number fluxes. Based on numerical integration of the measurements of Uchiroi & Freymuth (1970), we immediately get the following relationships between mean and fluctuating velocities in the wakes:

$$u_{w0}^2/u_{w\infty}^2 = 1.50, \quad v_{w0}^2/u_{w\infty}^2 = 1.15, \quad (30)$$

Uchiroi & Freymuth (1970) found that spectra at various points in the wake were identical at low frequencies when normalized by integral scales, and at high frequencies when normalized by Kolmogorov scales. These spectra were integrated in terms of normalized variables and then matched at intermediate frequencies. This gives the following contribution of wake turbulence to the temporal spectra of streamwise velocity fluctuations

$$E_{w0}/u_{w\infty}^2 = 0.0036 \text{ Hz} \quad (0 < f < 230), \\ = 1.04 \times 10^{-4} f^{-1.39} \quad (230 < f < 2000), \quad (31)$$

where f is the frequency in Hz. The same form was used for the cross-stream temporal spectra, E_{vw} , since the temporal spectra of cross-stream velocity fluctuations were virtually identical to streamwise velocity fluctuations (Uchiroi & Freymuth 1970).

Measurements of lateral spatial correlations in turbulent wakes are not available; therefore, these correlations were calculated based only on mean wake properties. The turbulent contribution to the streamwise spatial correlation was obtained from the temporal correlation as discussed earlier.

4. Results and discussion

4.1. Evaluation of apparatus

Initial experiments dealt with evaluation of the apparatus, considering uniformity of particle number fluxes, homogeneity of liquid flow properties, effects of wave action at the liquid surface, effects of bath size, approach to steady state conditions, mean velocities and Reynolds stresses.

Measurements of particle number fluxes as a function of position are illustrated in figure 3. The 1.0 mm diameter particles are considered at low, medium and high loadings having dissipation rates of 27.3, 68.2 and 155.8 mm²/s². The measurements only extend to the near-wall region on one side due to limitations of traversing the Mie-scattering measuring volume. The particle number fluxes are uniform within experimental uncertainties ($\pm 10\%$) over the middle 300 mm of the bath cross-section. Reduced particle number fluxes in the near-wall region are attributed to the fact that the duct for the particle feed system was 30 mm smaller (in each direction) than the liquid bath. Collection of particles at the bottom of the bath revealed that particle fluxes were uniform in the other direction as well, except within 50 mm of walls.

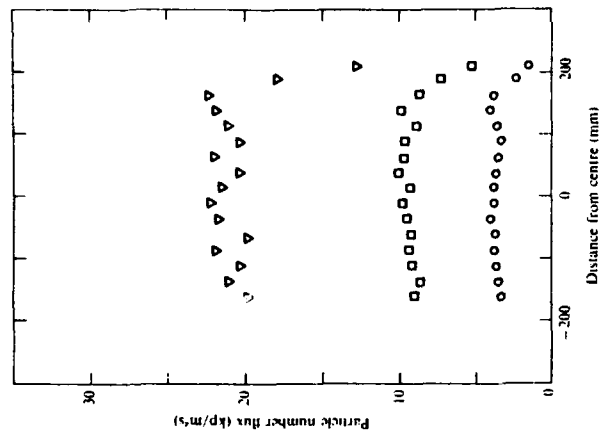


FIGURE 3. Particle number flux distribution for 1 mm diameter particles: O, $\epsilon = 27.3 \text{ mm}^2/\text{s}^2$; □, $68.2 \text{ mm}^2/\text{s}^2$; ▽, $155.8 \text{ mm}^2/\text{s}^2$.

The variation of streamwise liquid velocity fluctuations across the bath are illustrated in figure 4 for the same test conditions as figure 3. Open and shaded symbols represent measurements 100 mm above and below the location of the measuring volume of the fixed LV channel. Similar to the particle number fluxes, the streamwise velocity fluctuations are uniform within experimental uncertainties over the central 300 mm cross-section of the bath. In addition, velocity fluctuations measured at different points in the central region of the bath during the spatial correlation measurements for all three particle sizes also exhibited constant values within experimental uncertainties. Thus, we conclude that liquid properties were homogeneous within the region of measurements for all test conditions.

Effects of surface waves were examined by damping them with a honeycomb at the liquid surface (10 mm cell size, 50 mm thick) with the mean liquid level at the midpoint of the honeycomb. The particles passed through the honeycomb with no difficulty. Virtually no change in streamwise velocity fluctuations was detected with the honeycomb installed; therefore, it was removed for the remainder of the tests for operational convenience.

Disturbances of the uniformity of the particle number fluxes were studied by placing 50 mm wide strips, both one at a time and in pairs adjacent to opposite walls of the bath, with the centres of the strips 50–70 mm from the walls. The effects of these disturbances on streamwise velocity fluctuations at the centre of the bath was

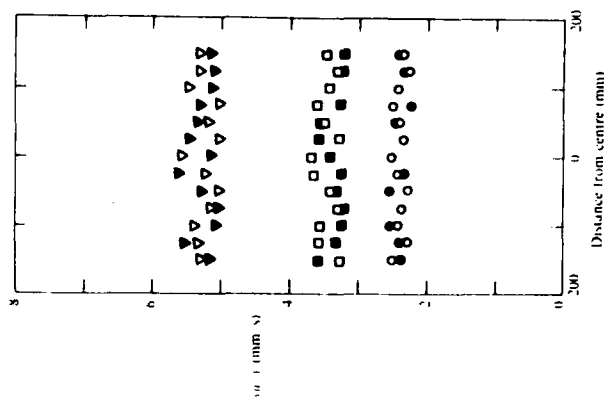


FIGURE 4. Streamwise liquid velocity fluctuation distributions for 1 mm diameter particles: \circ , $u'^2 = 27.3 \text{ mm}^2/\text{s}^2$; \square , $68.2 \text{ mm}^2/\text{s}^2$; \triangle , $155.8 \text{ mm}^2/\text{s}^2$. Open and filled symbols denote positions 100 mm above and below the measuring location, respectively.

generally less than 10%, except for a 15% change with two strips parallel to the 410 mm walls. Such massive uniformities are not likely in view of the measurements illustrated in figure 3; therefore, potential effects of particle flux non-uniformities were well within the experimental uncertainties of the velocity measurements.

Effects of the volume of the liquid bath were studied by placing two boxes constructed of Plexiglas (interior cross-sections of $200 \times 200 \text{ mm}$ and $100 \times 100 \text{ mm}$ and heights of 300 mm) within the bath along the centreline. Streamwise velocity fluctuations were then measured for full liquid heights, as well as half liquid height in the $100 \times 100 \text{ mm}$ box – the last bath volume being $\frac{1}{8}$ of the full bath volume. The smallest bath volume yielded streamwise velocity fluctuations that were only 10% lower than the full bath volume so that it is not likely that present results were influenced to a significant extent by the bath surfaces. This is reasonable since spatial integral scales in the cross-stream and streamwise directions were 15–21 mm and 37–59 mm, which are 5–7 times smaller than the corresponding dimensions in the smallest bath volume that was tested. Test results reported here were obtained in the full-size bath where these ratios are 2–4 times larger.

The approach of the liquid bath to stationary conditions and the capability of the particle feeder to maintain these conditions for test periods of hours were also studied. This was done by ensemble averaging measurements for several tests where

the particle feeder was started and operated for 75 minutes, considering the $100 \times 100 \text{ mm}$ and $200 \times 200 \text{ mm}$ baths as well as the full bath. It was found that streamwise velocity fluctuations at the centre of the baths reached stationary values within five minutes, irrespective of bath size, which supports the idea that the flow was largely controlled by particle motion rather than surface effects. The flows also were stationary within experimental uncertainties once the initial transient period had ended.

Ideally, mean velocities in the bath would be small, however, lower particle number fluxes near the walls induced a large-scale circulation within the bath. Thus, the results summarized in table 1 indicate that $u/(\bar{u}^2)^{1/2}$ was 0–0.5 for the lowest loadings of the 0.5 and 1.0 mm diameter particles, while this ratio varied in the range 0.7–1.0 for the other test conditions. Cross-stream mean velocities, however, were smaller with $v/(\bar{v}^2)^{1/2}$ less than 0.5 for all test conditions. The mean liquid velocities in the bath were small in comparison to particle terminal velocities so that their presence did not affect particle dynamics appreciably. Furthermore, since the flow was homogeneous and stationary, the mean motion did not influence velocity fluctuations, cross-correlations of velocity fluctuations and spatial correlations. However, the presence of a mean velocity did influence the temporal spectra; therefore, a correction was applied to these measurements which will be discussed later.

Ideally, the Reynolds stresses, $\overline{u'v'}$, should be zero for a homogeneous turbulent flow. This property was measured for the 0.5 mm diameter particles for dissipation rates in the range 53.2 – $134.1 \text{ mm}^2/\text{s}^3$, finding $\overline{u'v'}/\bar{u}^2 < 6\%$. Experimental uncertainties were large (55%) for the Reynolds stress measurements due to their small magnitude; therefore, these values are essentially zero within experimental uncertainties.

4.2. Velocity fluctuations

Measured velocity fluctuations in the streamwise and cross-stream directions are plotted as a function of dissipation for all three particle sizes in figure 5. Results for many test conditions other than those summarized in table 1 are plotted so that trends with dissipation and particle size can be seen more clearly.

The measurements for each component of velocity fluctuations illustrated in figure 5 vary solely as a function of dissipation within experimental uncertainties. Thus, effects of variations of particle number flux or spacing are represented by the dissipation through (4) while particle size is a secondary factor over the present test range. The cross-stream velocity fluctuations at the two highest loadings for the 0.5 mm diameter particles are a possible exception to this trend. However, these conditions had the highest particle number densities that were considered and are felt to be less reliable than the rest due to poorer signal-to-noise ratios. In accord with the general expectations from the theory, the ratio of streamwise to cross-stream velocity fluctuations is a constant, roughly 2, independent of test conditions, while both components of the velocity fluctuations are proportional to $\epsilon^{1/2}$. The larger streamwise velocity fluctuations are understandable since liquid motion primarily is caused by particles moving in the streamwise direction. This high level of anisotropy also suggests relatively strong effects of particle wakes; otherwise, the flow would be more isotropic, analogous to conditions somewhat downstream of a turbulence-generating grid.

Predicted velocity fluctuations were found by roughly matching predicted streamwise velocity fluctuations, allowing for both mean and turbulent wake properties, with the measurements. This involved terminating the integration of

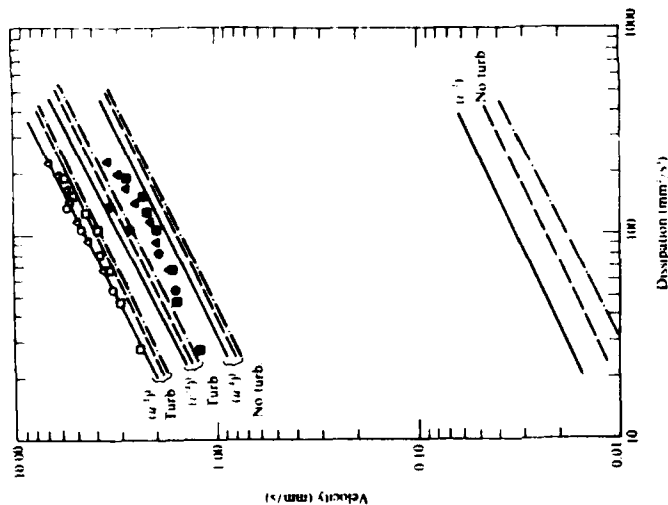


FIGURE 5. Liquid velocity fluctuations. \circ , \bullet , measurements; \square , \triangle , predictions for $d_p = 0.5$ mm; \square , \triangle , measurements; \square , \triangle , predictions for $d_p = 1.0$ mm; \square , \triangle , predictions for $d_p = 2.0$ mm. Open and closed symbols denote streamwise and cross-stream velocity fluctuations, respectively.

wake properties at $x/d_p = U_\infty T_x/d_p = 175$. This choice also seems reasonable on a physical basis. The mean velocity defect on the axis at this location is on the order of 1% of the terminal velocity, and comparable to the streamwise velocity fluctuations, so that it is likely that the coherence of wake properties would be lost in the background turbulence at larger distances. Thus, in a sense, this location is analogous to the location where the flow becomes nearly isotropic downstream of a turbulence-generating grid. Notably, although the fundamental limit problem remains, the sensitivity of predicted velocity fluctuations to the value of T_x is relatively weak, e.g. ignoring the contribution of the potential flow region, velocity fluctuations are proportional to T_x , see (25), (26) and (30).

With this selection of T_x predicted velocity fluctuations, including both mean and fluctuating wake properties, become

$$\frac{u'^2 T_x}{\epsilon^2} \left(\frac{\rho_p}{\rho} - 1 \right) = 46.72 (\theta/d_p)^{1/2}, \quad (32)$$

$$\frac{v'^2 T_x}{\epsilon^2} \left(\frac{\rho_p}{\rho} - 1 \right) = 21.49 (\theta/d_p)^{1/2}. \quad (33)$$

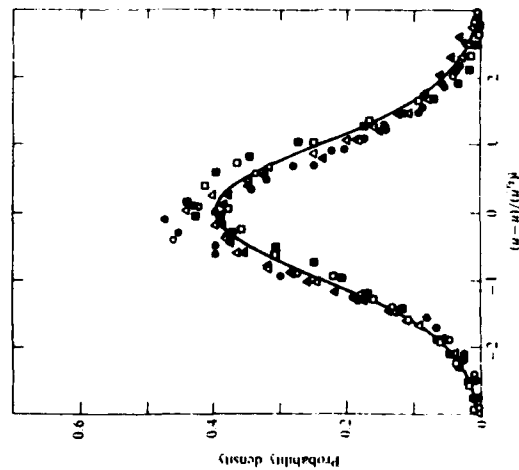


FIGURE 6. Probability density functions of streamwise liquid velocity fluctuations. \square , \triangle , $d_p = 0.5$ mm; \square , \triangle , $d_p = 1.0$ mm; \square , \triangle , $d_p = 2.0$ mm. Open and closed symbols denote streamwise and cross-stream velocity fluctuations, respectively. \cdots , prediction.

A useful alternative formulation can be obtained by introducing expressions for U_∞ and θ in (32) and (33). As noted earlier, mean particle velocities in the bath were essentially the same as terminal velocities in a still environment, yielding

$$U_\infty = (4g d_p (\rho_p/\rho - 1)/(3C_D))^{1/2}. \quad (34)$$

Then substituting (20) for θ and (34) for U_∞ into (32) and (33) yields

$$\frac{u'^2}{\epsilon} \left[\frac{g}{d_p} \left(\frac{\rho_p}{\rho} - 1 \right) \right]^{1/2} = 20.24 \left(\frac{d_p}{\rho} \right)^{1/2}, \quad (35)$$

$$\frac{v'^2}{\epsilon} \left[\frac{g}{d_p} \left(\frac{\rho_p}{\rho} - 1 \right) \right]^{1/2} = 9.31 \left(\frac{d_p}{\rho} \right)^{1/2}. \quad (36)$$

Equations (35) and (36) show that velocity fluctuations vary with particle diameter as $d_p^{1/2}$; this yields roughly a 20% reduction of the velocity fluctuations for a particular value of ϵ as d_p goes from 0.5 to 2.0 mm.

Equations (35) and (36), along with their counterparts when effects of wake turbulence are ignored using the same T_x , are plotted in figure 5. Predictions with and without wake turbulence were considered since present wake Reynolds numbers were low in comparison to those considered by Ubersoi & Freymuth (1970) so that wake turbulence may not be as well-developed for present test conditions. The predictions illustrated in figure 5 suggest that this is not the case. In particular, predictions of cross-stream velocity fluctuations are much smaller than measured cross-stream velocity fluctuations when the contributions of wake turbulence are ignored. This is

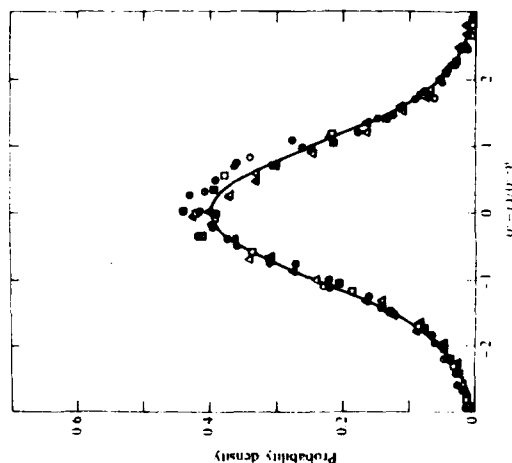


FIGURE 7. Probability density functions of cross-stream liquid velocity fluctuations: see caption of figure 6 for symbols.

not an effect of the selection of T_1 since the prediction of \bar{v}^2 from (26) does not diverge as $T_1 \rightarrow \infty$ and yields essentially the same results as \bar{v}^2 , $T_1/d_p = 175$. Rather, cross-stream mean velocities are much smaller than streamwise mean velocities in wakes, as well as velocity fluctuations in turbulent wakes. On the other hand, the ratio of streamwise-to-cross-stream velocity fluctuations from (35) and (36) is 1.47, which is somewhat less than the value of roughly 2 of the measurements. This might be explained by turbulence levels in particle wakes being lower than the levels found by Uehara & Freymuth (1970) due to the much lower Reynolds numbers of the present particle wakes. Based on these observations, it seems probable that both mean and turbulent wake properties contribute to the turbulence field.

Estimates of velocity fluctuations from (35) and (36) vary with particle diameter as noted earlier. However, this variation is comparable to experimental uncertainties and a similar trend is not seen in the measurements illustrated in figure 5. The degree of development of the turbulence in the wake may also be a factor in the reduced sensitivity of the measurements to particle diameter. In particular, predictions indicate lower levels of turbulent fluctuations with increased particle diameter while larger particles have higher wake Reynolds numbers which should tend to increase wake turbulence levels; therefore, these two effects tend to counteract one another. Additional measurements of turbulent properties in the present Reynolds number range would be helpful in resolving this issue.

The p.d.f.s of streamwise and cross-stream velocity fluctuations are plotted as a function of normalized variables in figures 6 and 7. Within experimental uncertainties, measurements are generally independent of particle size and loading. Predictions based on a Gaussian p.d.f., which is the form expected from the theory,

are also illustrated on each plot. This distribution is in good agreement with the measurements but this is not a strong test of predictions since velocity fluctuations in homogeneous turbulence generally exhibit Gaussian p.d.f.s.

4.3. Temporal spectra

Measured normalized temporal power spectral densities of streamwise and cross-stream velocity fluctuations are plotted as a function of normalized frequency in figures 8 and 9. The integral timescales of streamwise and cross-stream velocity fluctuations, T_u and T_v , used in the normalizations, will be taken up later. The measurements are limited to the lowest loadings of all three particle diameters for the streamwise spectra but just the 0.5 mm diameter particle for the cross-stream spectra. These limitations were necessary in order to select conditions that were not unduly influenced by effects of mean velocities that were mentioned earlier.

Two experimental problems must be considered before discussing the measured temporal spectra: the effect of mean velocities and the effect of step noise. Mean streamwise velocities are generally much larger than mean cross-stream velocities for the conditions plotted in figures 8 and 9; therefore, effects of the latter will be ignored. When there is a mean streamwise velocity, the streamwise temporal correlation measured at a fixed point is $\overline{u(x-u(t+\tau), y, z, t)u(x, y, z, t+\tau)}$ which is actually a two-point, two-time correlation rather than $\overline{u(x, y, z, t)u(x, y, z, t+\tau)}$ which is the temporal correlation that is being sought (Hinze 1975). In order to correct for the effect of the mean velocity, it was assumed that the combined correlation could be decomposed into a product of temporal and spatial correlations:

$$\overline{u(x-u(t+\tau), y, z, t)u(x, y, z, t+\tau)} = \overline{u(x-u(t+\tau), y, z, t)u(x, y, z, t+\tau)/u^2} \quad (37)$$

Equation (37) is not rigorously accurate, however, it is a reasonable approximation for a homogeneous turbulent field. Since the measured spatial correlations in the streamwise direction were unaffected by the mean velocity, $\overline{u(x-u(t+\tau), y, z, t)u(x, y, z, t+\tau)}$ is known from present measurements so that the temporal correlation $\overline{u(x, y, z, t)u(x, y, z, t+\tau)}$ can be calculated from (37). Taking the Fourier transform of this correlation then yields the spectra illustrated in figure 8. The correction for mean velocities was negligible for the lowest loading of the 0.5 mm diameter particles and was relatively small (less than 10%) for the lowest loadings of the other two particle sizes; therefore, only measurements for these conditions are plotted in figure 8.

In order to apply a similar correction for the presence of mean velocities to the temporal correlation of cross-stream velocity fluctuations, the spatial correlation $\overline{v(x-u(t+\tau), y, z, t)v(x, y, z, t+\tau)}$ must be known; unfortunately, this spatial correlation was not measured. However, since the mean velocity correction was small for the temporal correlation of streamwise velocity fluctuations for the lowest loading with the 0.5 mm diameter particles, it was assumed that the correction would be small for the temporal correlation of the cross-stream velocity fluctuations at this condition as well, which are the only measurements plotted in figure 9.

The second problem is that Fourier transformation of the analogue signal of the LV burst processor introduced 'step-noise' caused by the sample-and-hold signals of the processor. Adrian & Yao (1987) have shown that effects of step-noise are observed at frequencies roughly one-tenth of the frequency corresponding to the mean data rate. The characteristics of step-noise are the appearance of a noise band having a constant spectral amplitude followed by a second-order low-pass filter effect

at a slightly higher frequency, i.e. a subsequent decay of the spectra according to f^{-1} . This yields a slight flat spot in the spectra followed by a region where the spectra decrease according to f^{-2} which is noted in figures 8 and 9 for the measurements with the 0.5 mm diameter particles.

The onset of step-noise for present measurements with the 0.5 mm diameter particles corresponds to the estimates of Adrian & Yao (1987). For example, the streamwise spectrum in figure 8 exhibits a change in slope (denoted step-noise in the figure) at $fT_p \approx 10$ which roughly corresponds to one-tenth of the mean data rate (2000 Hz). The onset of step-noise appears at a slightly lower frequency for the cross-stream spectrum in figure 9 which is consistent with the slightly lower data rate of these measurements. Naturally, the portions of the spectra beyond the onset of step-noise are not representative of flow properties and should be ignored; the region is only illustrated in figures 8 and 9 in order to establish that this portion is an artifact of step-noise and not some property of the flow since the predictions also suggested the presence of steps in the streamwise temporal spectra at high frequencies.

A correction for step-noise was made at the same time as the mean velocity corrections for the measurements with the 1.0 and 2.0 mm diameter particles; therefore, the correction is not illustrated for these measurements in figure 8. The correction involves subtracting the step-noise from the spectrum, taking the Fourier transform, and the result to obtain the combined temporal and spatial correlation, applying the mean velocity correction to this correlation, and finally taking the Fourier transform of this correlation to obtain the results illustrated in figure 8.

The differences between the measured temporal spectra of streamwise velocity fluctuations for the three particle diameters illustrated in figure 8 are not significant in comparison to experimental uncertainties. This is consistent with the measurements of streamwise velocity fluctuations, illustrated in figure 4, where it was found that effects of particle diameter are not very important. In addition to differences of particle diameters, the measurements illustrated in figure 8 also have different rates of dissipation; however, it was a general conclusion of the theory that temporal correlations should be independent of the rate of dissipation. Based on these findings, the small effect of particle diameter on the spectra illustrated in figure 8 is quite reasonable.

Perhaps the most surprising feature of the spectra of streamwise velocity fluctuations illustrated in figure 8 is the large range of frequencies in the spectra, even though wake Reynolds numbers are relatively low; and the significant levels of signal energy at very low frequencies, even though the flow field is produced by small high-velocity particles having relatively large interparticle spacings. In fact, based on the theoretical estimates, the measured spectra would have extended over a much larger frequency range if the limitations of step-noise could have been avoided. The reason for this large range of frequencies, as well as the presence of appreciable signal energy at the low frequencies is that the flow includes contributions from both the mean and turbulent velocity fields of the particle wakes while the mean velocities enhance signal energies at low frequencies. Such behaviour is not normally observed in turbulent flows generated by other mechanisms; however, the contributions of mean velocities cannot be separated from the contributions of turbulence in the particle wakes for present flows since particle arrivals are random.

Since predicted temporal spectra were not sensitive to the selection of T_p , a large value was chosen, $x/d_p = l^*/T_p/d_p = 25000$, to cover the complete normalized frequency range of figures 8 and 9. The effect of this selection on

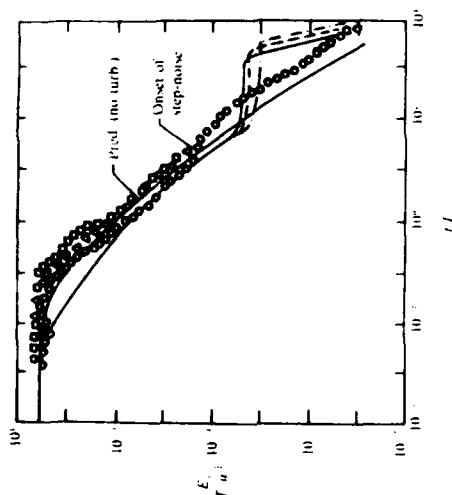


FIGURE 8. Temporal spectral densities of streamwise liquid velocity fluctuations. \bigcirc , $d_p = 0.5$ mm, $\nu = 33.2$ mm²/s²; \square , $d_p = 1.0$ mm, $\nu = 27.3$ mm²/s²; \triangle , $d_p = 2.0$ mm, $\nu = 67.1$ mm²/s². —, prediction.

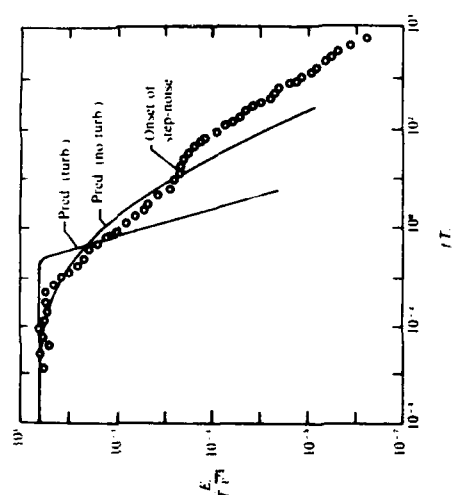


FIGURE 9. Temporal spectral densities of cross-stream liquid velocity fluctuations. \bigcirc , $d_p = 0.5$ mm, $\nu = 33.2$ mm²/s². —, prediction.

predictions of integral scales will be taken up later. Predictions of streamwise temporal spectra considering and ignoring wake turbulence in figure 8 were independent of dissipation rates while predictions ignoring wake turbulence were independent of particle diameter as well. However, predictions considering wake turbulence exhibit somewhat different shapes at high frequencies, reflecting effects of different wake Reynolds numbers for the different sized particles.

Similar to the measurements, predictions of streamwise temporal spectra, both considering and ignoring wake turbulence, exhibit significant signal energy at low frequencies in figure 8; this supports the idea that the low-frequency region is caused by mean velocities in the particle wakes since both predictions include this contribution. Unfortunately, the portion of the spectra that involves the contribution of wake turbulence could not be observed directly due to effects of step-noise. The agreement between predicted and measured temporal spectra of streamwise velocity fluctuations is within the scatter of the data in the region that is not affected by step noise, although quantitative agreement is somewhat better when wake turbulence is ignored. This suggests that the turbulence of the particle wakes may not be developed to the extent observed by Uberti & Freymuth (1970), which would not be surprising since present wake Reynolds numbers are much lower.

Measurements of the temporal spectra of cross-stream velocity fluctuations, illustrated in figure 9, exhibit trends similar to the temporal spectra of streamwise velocity fluctuations: there is significant signal energy at low frequencies and, probably, a large range of frequencies in the spectra if step-noise had not intruded, since both mean and turbulent properties of particle wakes contribute to the spectra. Due to the small magnitude of mean radial velocities in comparison to radial velocity fluctuations in wakes, however, the turbulence contributions to the cross-stream spectra are two orders of magnitude higher than the mean velocity contributions; therefore, the cross-stream spectra provide a more sensitive indication of wake turbulence effects than the streamwise turbulence spectra - analogous to the relative effect of wake turbulence on cross-stream and streamwise velocity fluctuations that was discussed earlier. Thus, the shapes of the predicted spectra with and without wake turbulence differ to a greater extent for the cross-stream velocity fluctuations. The measurements in the step-noise-free portion of the spectrum lie between the two predictions, which suggests a lower degree of development of wake turbulence than observed by Uberti & Freymuth (1970) at higher wake Reynolds numbers. While this is plausible, additional measurements of the properties of turbulent wakes behind spheres at moderate Reynolds numbers would greatly help to resolve the properties of homogeneous particle-laden flows.

4.3. Spatial correlations

The measured spatial correlations of streamwise velocity fluctuations in the cross-stream direction are illustrated in figure 10. Measurements at various particle loadings for the three particle diameters are plotted as a function of cross-stream distance normalized by the cross-stream integral lengthscale, L_{xy} . Consideration of the cross-stream integral lengthscale itself will be taken up later. These measurements were repeated for both positive and negative separation distances to check the symmetry of the correlations. These results are not illustrated to avoid crowding of the figure; however, they showed that the correlations were symmetric within experimental uncertainties.

The spatial correlation measurements for various loadings and particle sizes are essentially the same. This is consistent with the general conclusion of the theory that

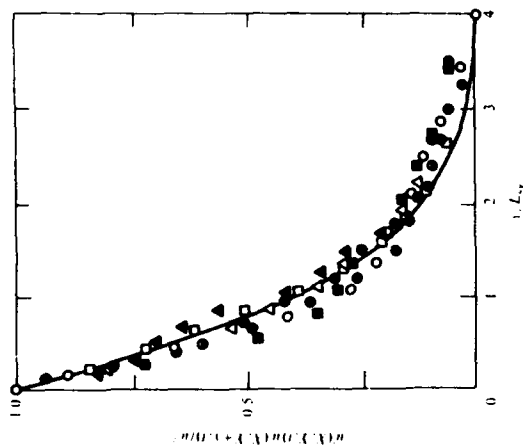


FIG. 10. Spatial correlations of streamwise liquid velocity fluctuations in the cross-stream direction. \square , $d_p = 0.5$ mm, $\epsilon = 53.2$, 106.3 mm²/s²; \circ , $d_p = 1.0$ mm, $\epsilon = 27.3$, 68.2 , 155.8 mm²/s²; \triangle , $d_p = 2.0$ mm, $\epsilon = 67.1$, 193.5 mm²/s²; —, prediction.

correlation coefficients should be independent of the rate of dissipation, and the earlier finding that velocity fluctuations are relatively independent of particle size. The measurements exhibit an exponential-like decay of the correlation with increasing separation distances. This observation is influenced to some extent by experimental problems since effects of step-noise precluded resolving the smallest scales of the flow that would be expected to influence the curvature of the correlation at the smallest separation distances (Hinze 1975).

Predictions of spatial correlations used the same T_i as the temporal spectra. The prediction of the spatial correlation of streamwise velocity fluctuations in the cross-stream direction, illustrated in figure 10, had to be limited to consideration of only mean properties in the particle wakes. To include effects of wake turbulence in these predictions would require measurements of lateral correlations in turbulent wakes and no such measurements have been reported. However, since the measurements emphasize the large-scale features of the flow, which are also emphasized by predictions using only mean wake properties, comparing this prediction with measurements is reasonable. In agreement with the measurements, the prediction indicates that the correlation should be independent of particle loading and size. The quantitative agreement between the predictions and measurements is reasonably good for small separation distances, however, the predictions decay more rapidly than the measurements at large separation distances. Reasons for this behaviour will be considered when integral scales are discussed.

The measured spatial correlations of streamwise velocity fluctuations in the streamwise direction are illustrated in figure 11. Measurements for various particle

	d_p (mm)	0.5	1.0	2.0
T_i (s)				
Measured ^a		6	7	7
Predicted (turb) ^b		10 (21)	10 (21)	12 (21)
Predicted (no turb) ^c		130 (225)	130 (225)	130 (225)
T_i (s)				
Measured ^d		4	0.001	0.001
Predicted (turb) ^b		0.001	0.17	0.17
Predicted (no turb) ^c		0.17		
L_{wv} (mm)				
Measured ^d		17 (2)	13 (2)	21 (3)
Predicted (turb) ^b		2	4	7
Predicted (no turb) ^c				
L_{wv} (mm)				
Measured ^d		59 (2)	59 (6)	57 (2)
Predicted (turb) ^b		70 (710)	140 (1300)	260 (5000)
Predicted (no turb) ^c		850 (9200)	1700 (23700)	2550 (59800)

TABLE 2. Measured and predicted integral timescales and length scales

^a Measured for lowest particle loading only.
^b Predicted assuming $u/d_p = 1$, $T_i/d_p = 175$. Numbers in parentheses are for $T_i/d_p = 27000$.
^c Predicted assuming $u/d_p = 1$, $T_i/d_p = 2730$. Numbers in parentheses are for $T_i/d_p = 25000$.
^d Average value for loading range of table 1. Standard deviation is in parentheses.

4.5. Integral timescales and length scales

Measured and predicted integral time and length scales are summarized in table 2. Integral length scales were measured for the full range of particle loadings; however, integral timescales were only measured for the lowest particle loadings due to uncertainties in correcting for mean velocities noted earlier. The measured integral scales are relatively independent of test conditions. This is remarkable since most experimental variables that might be expected to influence integral scales were varied over a wide range: particle diameters from 0.5 to 2.0 mm, mean particle spacings from 8 to 62 mm, and rates of dissipation from 27 to 194 mm² s⁻². The small effect of dissipation on integral scales is expected from the theory, which implies small effects of particle number flux and spacing through (3) and (4) as well. However, the small effects of particle diameter and spacing is surprising, although effects of these properties also were small for velocity fluctuations, p.d.f.s of velocities, and spatial and temporal correlations.

The ratio between measured streamwise and cross-stream temporal integral scales in table 2 is roughly 1.5; however, the available data base for this ratio is relatively limited. The ratio between streamwise and cross-stream spatial integral scales is roughly 3, which reflects the high level of anisotropy of the present flows. This degree of anisotropy also supports the idea that wake-like properties, rather than loss of wake coherence and approach to isotropic turbulence, are dominant features of the present flows.

Predicted integral scales, considering and ignoring wake turbulence, also are summarized in table 2. T_i was chosen to match measured streamwise velocity fluctuations for baseline predictions, taking $x/d_p = 1$; $T_i/d_p = 175$ and 2730 when wake turbulence was considered and ignored. The sensitivity of predicted integral scales to variations in T_i is also indicated in table 2 by including results for $x/d_p =$

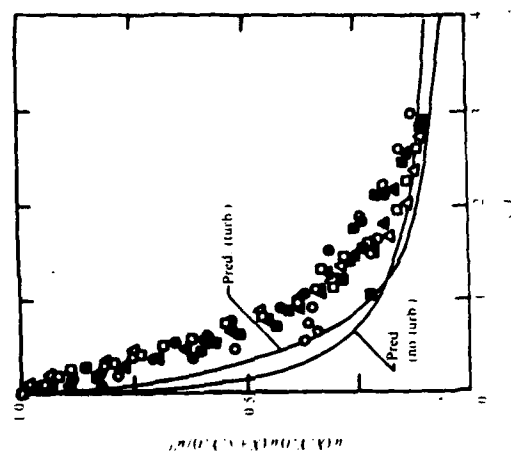


FIGURE 11. Spatial correlations of streamwise liquid velocity fluctuations in the streamwise direction: see caption of figure 10 for symbols.

diameters and loadings are plotted as a function of streamwise separation distance normalized by the streamwise integral lengthscale, L_{wv} . The data scatter of the correlations for the streamwise direction is somewhat greater than the correlations for the cross-stream direction. However, within experimental uncertainties, the correlation is independent of particle loading and size. The reasons for this behaviour are the same as for the lateral correlations.

For correlations in the streamwise direction, spatial correlations needed to compute the contribution of wake turbulence are available; therefore, predictions both considering and ignoring the contribution of wake turbulence are illustrated in figure 11. In agreement with the measurements, both predictions are essentially independent of particle size at x/L_{wv} loading over the present test range. When wake turbulence is ignored, the correlation decreases quite rapidly at small separation distances since the flow is dominated by relatively large length scales associated with the mean velocity profiles of the wake. Considering wake turbulence places a greater degree of the signal energy at the smaller length scales associated with the turbulence; this reduces the rate of decline of the correlation at small separation distances and yields a correspondingly more rapid decrease of the correlation at large separation distances. However, differences between the two predictions are comparable to experimental uncertainties and neither is in particularly good agreement with measurements: the predictions overestimate the initial rate of decrease and exhibit a longer tail than the measurements.

$U_x T_x/d_p = 25000$ which was the value used for temporal spectra and spatial correlations in figures 8, 11.

Predicted integral scales in table 2 are properly independent of the rate of dissipation but are generally unsatisfactory otherwise. A possible exception is T_u considering turbulence, where predicted and measured magnitudes and trends were similar. For the rest T_i is vastly underestimated by predictions, particularly when turbulence is considered. Predictions of T_u and L_{wz} are vastly overestimated when turbulence is ignored and predicted spatial integral scales exhibit variations with particle diameter that are not supported by the measurements. Furthermore, the convergence problem that required an *ad hoc* selection of T_i has a significant impact on predictions of L_{wz} owing to its sensitivity to this choice. Finally, no compromise selection of T_i could be found that provides good predictions of both velocity fluctuations and integral scales.

4.6. Discussion

In spite of numerous simplifications, the theory was helpful for explaining many features of the measurements and the predictions were generally reasonable. However the convergence problem when particle wakes are evaluated, and the relatively poor predictions of integral scales and streamwise spatial correlations, are disconcerting. Two phenomena that may be responsible for these difficulties are discussed in the following: disturbances of wakes due to turbulent dispersion of particles, and the structure of particle wakes in the present turbulent environment.

Recall that predictions were based on particles settling along vertical lines, i.e. effects of turbulent dispersion of particles were ignored. For present experimental conditions, however, turbulent dispersion was significant and cross-stream particle and liquid velocity fluctuations were comparable (Parthasarathy & Faeth 1990). Thus, particle wakes were actually deposited along sinuous paths, affecting the apparent width of the wakes, and augmenting cross-stream velocity fluctuations by placing a component of the mean velocity along the wake axis into a horizontal plane. Since wakes grow relatively slowly in the radial direction, and have small mean radial velocities, these effects can be significant for homogeneous particle-laden flows.

Dye tracks released into the wakes of individual particles were photographed in order to help quantify potential effects of turbulent dispersion of particles. Considering only fresh wakes, with the particle still in view, showed that the projected cross-stream displacements of particles were comparable to characteristic wake radii (based on the mean streamwise velocity being 1.5% of the mean streamwise velocity at the axis), e.g. 2.6 mm for $x/d_p = 175$. This behaviour is consistent with cross-stream liquid and particle velocity fluctuations being comparable. Rough calculations showed that this effect was sufficient to increase predictions of L_{wz} to the range of the measurements and reduce its sensitivity to particle diameter; thus, the effect is significant. Additionally, projected particle tracks were oriented up to 10° from the vertical direction which causes momentum along the wake axis to be deposited into the cross-stream direction; this would tend to reduce potential effects of wake turbulence inferred earlier and modify predictions of cross-stream scales as well. Thus, the nonlinear interaction between turbulent dispersion of particles in the turbulent field that they create must be considered when defining the particle flow field for predictions using the present approach.

Another nonlinear interaction is the effect of the turbulent field generated by the particles on the properties of their wakes. Present predictions were based on the properties of wakes for rigidly-mounted spheres in a non-turbulent environment.

Turbulent dispersion of particles, and the deflection, distortion and improved mixing of wakes in a turbulent environment are likely to modify behaviour from wakes in a non-turbulent environment. In particular, wakes in a turbulent environment should mix more quickly and observe different scaling rules than wakes in non-turbulent environments (Tennekes & Lumley 1972). For example, similarity was assumed to obtain the turbulent wake properties of (21)–(23) with specific results requiring a turbulent viscosity that is constant over the wake cross-section and decreases with increasing streamwise distance. Such scaling is unlikely to be relevant for wakes having modest Reynolds numbers in a turbulent environment and proper scaling might resolve the convergence problem directly. Finally, as mentioned earlier, little is known about the turbulent structure of wakes at the modest Reynolds numbers of present tests, which also affects predictions.

Clearly, further progress concerning turbulence modulation in homogeneous dilute particle-laden flows will require a better understanding of particle wake properties. This includes the structure of turbulent wakes at moderate Reynolds numbers, the structure of wakes in turbulent environments, and the structure of wakes of freely-moving particles undergoing turbulent dispersion.

5. Conclusions

The present investigation considered the continuous-phase properties of homogeneous dilute particle-laden flows. The specific configuration involved nearly monodisperse glass spheres (particle diameters of 0.5, 1.0 and 2.0 mm with corresponding Reynolds numbers of 38, 156 and 545) falling in a water bath. Experimental conditions were as follows: turbulence number fluxes of 1.1–110.8 kpart m²/s, mean particle spacings of 8.2–61.8 mm, rates of dissipation of 27.3–193.5 mm²/s³ and particle volume fractions less than 0.01%. The major observations and conclusions of the study are as follows:

- (i) Velocity fluctuations could be correlated solely as a function of the rate of dissipation of particle energy in the liquid.
- (ii) Streamwise velocity fluctuations were roughly twice cross-stream velocity fluctuations for all test conditions, suggesting a significant influence of the wakes behind individual particles on the properties of the flow.
- (iii) Normalized temporal spectra, spatial correlation coefficients, and temporal and spatial integral scales were relatively independent of both particle size and the rate of dissipation of particle energy in the liquid.
- (iv) Temporal spectra indicated a large range of frequencies even though particle and wake Reynolds numbers were relatively small, since both mean and fluctuating properties of the particle wakes contributed to the spectra because particle arrivals were random.
- (v) An analysis based on linear superposition of undistorted particle wakes in a non-turbulent environment predicted many properties of the flow reasonably well. However, it yielded poor estimates of integral scales and streamwise spatial correlations. These deficiencies are attributed largely to effects of turbulent dispersion of the particles and effects of the ambient turbulence field on the structure of the wakes.
- (vi) Linear superposition of particle wakes in the analysis presented convergence problems, similar to convergence problems encountered during analysis of sedimentation processes. This was resolved by assuming that only the near-field region of the wakes, $x/d_p = T_x U_x/d_p < 175$, would maintain sufficient coherence to

contribute to flow properties as a wake a choice that matched predictions and measurements of streamwise velocity fluctuations. However, a more rational resolution of the convergence problems should be sought.

(vi) Particle-laden flows typically involve turbulent dispersion of particles and particle Reynolds numbers less than 1000 within a turbulent environment; more information is needed concerning the mean and turbulent structure of wakes under these conditions in order to address the difficulties of the present analysis in a rational manner.

The authors wish to thank L. P. Bernal and W. W. Willmarth for helpful discussions during the course of the study. The work was supported by the Air Force Office of Scientific Research, Grant no. AFOSR-85-0244, under the technical management of J. M. Tishkoff. The US Government is authorized to reproduce and distribute copies of this paper for Governmental purposes notwithstanding any copyright notation thereon.

REFERENCES

- ABRAHAM, R. J. & YAO, C. S. 1967 Power spectra of fluid velocities measured by laser Doppler velocimetry. *Exptl Fluids* **5**, 17-28.
- AL-TAWEEK, A. M. & LAMDA, J. 1977 Turbulence modulation in two-phase jets. *Int. J. Multiphase Flow* **3**, 341-351.
- BACHMELOF, G. K. 1972 Sedimentation in a dilute dispersion of spheres. *J. Fluid Mech.* **52**, 245-268.
- BACHMELOF, G. K. 1973 *An Introduction to Fluid Dynamics*, pp. 420-453. Cambridge University Press.
- FARUQ, G. M. 1987 Mixing, transport and combustion in sprays. *Prog. Energy Combust. Sci.* **13**, 293-345.
- HINO, M. 1966 Turbulent flow with suspended particles. *ASME J. Hydrd.* **4**, 161-165.
- HINZE, J. O. 1972 Turbulent fluid and particle interaction. *Prog. Heat Mass Transfer* **6**, 433-452.
- HINZE, J. O. 1975 *Turbulence*. McGraw-Hill.
- KADA, E. J. & HANRATTY, T. J. 1980 Effects of solids on turbulence in a fluid. *AIChE J.* **6**, 624-630.
- KUCHANOV, S. I. & LEVICH, V. G. 1967 Motion of particles suspended in turbulent flow. *Sov. Phys. Dokl.* **12**, 546-548.
- LANER, M. & BATAILLE, J. 1982 Turbulence in the liquid phase of a bubbly air-water flow. *Advances in Two-Phase Flow and Heat Transfer*, vol. 1, pp. 403-427. Martinus Nijhoff.
- LANER, M., MARKE, J. L. & BATAILLE, J. 1985 Homogeneous turbulence in bubbly flows. Publication FEP-29, ASME, 117-124.
- LANER, M., MARKE, J. L., CHARNAY, G. & BATAILLE, J. 1980 Turbulence structure of a concurrent air-water bubbly flow. *STRENGTH/P-8014*. Nuclear Regulatory Commission, Washington, vol. 2, pp. 403-427.
- MICHAELIDES, E. E. & STOW, 1989 *Turbulence modification in dispersed multiphase flows*. FED-vol. 80, ASME, NY.
- MONAGHAN, D., TAN, H. & ELOROBASHI, S. 1984 Two-component LDA measurements in a two-phase turbulent jet. *AIChE J.* **22**, 624-630.
- OWEN, P. R. 1984 Sedimentation of uniform grains in air. *J. Fluid Mech.* **20**, 225-242.
- OWEN, P. R. 1989 Pneumatic transport. *J. Fluid Mech.* **39**, 407-432.
- PARTHASARATHY, R. N. 1989 Homogeneous dilute turbulent particle-laden water flow. PhD thesis, The University of Michigan.
- PARTHASARATHY, R. N. & FARUQ, G. M. 1987 Structure of particle-laden turbulent water jets in still water. *Int. J. Multiphase Flow* **13**, 699-710.
- PARTHASARATHY, R. N. & FARUQ, G. M. 1990 Turbulent dispersion of particles in self-generated homogeneous turbulence. *J. Fluid Mech.* **220**, 515-537.
- PIRATA, A. 1981 Integrable form of droplet drag coefficient. *AIChE J.* **31**, 1467-1468.
- RICE, S. O. 1964 Mathematical analysis of random noise. *Noise and Stochastic Processes*, pp. 133-194. Dover.
- SCHLES, J. S., SOLOMON, A. S. P., ZHANG, Q.-F. & FARUQ, G. M. 1985 Structure of particle-laden jets: measurements and predictions. *AIChE J.* **21**, 1480-1483.
- SCHLES, J. S., SOLOMON, A. S. P., ZHANG, Q.-F. & FARUQ, G. M. 1985 Structure of non-evaporating sprays. II. drop and turbulence properties. *AIChE J.* **23**, 1724-1730.
- SUN, T. Y. & FARUQ, G. M. 1986 Structure of turbulent bubbly jets. II. phase property profiles. *Int. J. Multiphase Flow* **12**, 115-124.
- TESSIER, H. & LEMLEY, J. L. 1972 *A First Course in Turbulence*, pp. 113-124. MIT Press.
- UENO, M. S. & FARMY, P. 1970 Turbulent energy balance and spectra of the axisymmetric wake. *Phys. Fluids* **13**, 2205-2210.

Appendix D: Parthesarathy and Faeth (1990b)

Turbulent dispersion of particles in self-generated homogeneous turbulence

By R. N. PARTHASARATHY† AND G. M. FAETH‡

Department of Aerospace Engineering, The University of Michigan, Ann Arbor,
MI 48106-2140, USA

(Received 6 October 1979)

Turbulent dispersion of particles in their self-generated homogeneous turbulent field was studied both experimentally and theoretically. Measurements involved nearly monodisperse spherical glass particles (nominal diameters of 0.5, 1.0 and 2.0 mm) falling with uniform particle number fluxes in a nearly stagnant water bath. Particle Reynolds numbers based on terminal velocities were 38, 156 and 545 for the three particle sizes. The flows were dilute with particle volume fractions less than 0.01%. Measurements included particle motion calibrations, using motion-picture shadowgraphs; and streamwise and cross-stream mean and fluctuating particle velocities, using a phase-discriminating laser velocimeter. Liquid-phase properties were known from earlier work. Particle properties were predicted based on random-walk calculations using statistical time-series methods to simulate liquid velocities along the particle path.

Calibrations showed that particle drag properties were within 14% of estimates based on the standard drag correlation for spheres; however, the particles (particularly the 1.0 and 2.0 mm diameter particles) exhibited self-induced lateral motion even in motionless liquid due to eddy-shedding and irregularities of shape. Particle velocity fluctuations were primarily a function of the rate of dissipation of kinetic energy in the liquid since this variable controls liquid velocity fluctuations. Streamwise particle velocity fluctuations were much larger than cross-stream particle velocity fluctuations (2.5:1) largely due to varying terminal velocities caused by particle size variations. Cross-stream particle and liquid velocity fluctuations were comparable owing to the combined effects of turbulent dispersion and self-induced motion. Predicted mean and fluctuating particle velocities were in reasonably good agreement with the measurements after accounting for effects of particle size variations and self-induced motion. However, the theory must be extended to treat self-induced motion and to account for observations that this motion was affected by the turbulent environment.

1. Introduction

The objective of this investigation was to study the turbulent dispersion of particles moving in their self-generated homogeneous turbulent field. This process is important in dispersed multiphase flows when direct modification of continuous phase turbulence properties by transport from the dispersed phase, called turbulence modulation by Al Taweel & Landau (1977), is significant. Such conditions are encountered in the dense regions of sprays as well as in dilute dispersed flows when mean velocity gradients are small, e.g. the flow field within liquid- or particle-

† Present address: Institute of Hydraulic Research, University of Iowa, Iowa City, IO, USA.
‡ Author to whom correspondence should be addressed.

containing rocket engines as well as in natural phenomena like rainstorms. The study involved a homogeneous dilute particle-laden flow generated by a uniform flux of particles settling under the force of gravity in a nearly stagnant (in the mean) liquid bath. A companion study considered the continuous-phase properties of these flows (Parthasarathy & Faeth 1980); the emphasis of the present study was to investigate the dispersed-phase properties both theoretically and experimentally.

Early studies of the turbulent dispersion of particles concentrated on the small-Eulerian limit where the relative velocities between the phases are small and particle mixing can be approximated by single-phase scalar mixing through the locally-homogeneous-flow approximation, see Faeth (1987) for a review of past work along these lines. The locally-homogeneous-flow approximation is of limited value, however, since most practical dispersed multiphase flows involve significant relative velocities between the phases and dispersed-phase elements do not remain associated with particular fluid elements. This phenomenon was recognized by Yudine (1959) and (Sanady (1963) and is called the 'crossing trajectories' effect, i.e. dispersed-phase elements and fluid elements follow different trajectories and only interact for a time. Katz (1966) and Meek & Jones (1973) report early applications of these ideas to the study of the dispersion of heavy particles in the atmosphere. Other work, at the Stokes limit for particle motion and with various approximations for the continuous phase of simple turbulent flows, includes Reeks (1977, 1980), Pismen & Nir (1978), Nir & Pismen (1979), Goussbet, Berlemont & Pivart (1984), Desjonquieres *et al.* (1986) and Maxey (1987). All these studies find significant effects of finite relative velocities between the phases.

Most practical dispersed flows, as well as past experiments, involve dispersed-phase Reynolds numbers beyond the Stokes limit. Numerous measurements of continuous- and dispersed-phase properties have been reported for sprays and other turbulent shear flows, see Faeth (1987) for a summary of recent work; however, homogeneous flows involve fewer complications for the interpretation of turbulent dispersion phenomena and will be emphasized here. Snyder & Lumley (1971) completed measurements of turbulent dispersion of single particles in the isotropic decaying turbulent flow downstream of a grid; this study has served as a primary source of data for developing models of the process. Wells & Stock (1983) studied turbulent particle dispersion in a similar arrangement, using charged particles in an electric field so that effects of relative velocities (crossing trajectories) could be separated from particle inertia; they found that inertia influenced particle velocity fluctuations but concluded that particle dispersion was primarily influenced by crossing trajectories for their test conditions. Ferguson & Stock (1986) also studied particle dispersion in grid-generated turbulence, further highlighting effects of crossing trajectories. Taken together, these results demonstrate the importance of both particle and continuous-phase properties on turbulent dispersion; therefore, the process does not lend itself to empirical correlation and must be understood at a fundamental level before reliable estimates of turbulent dispersion can be achieved.

Numerous models of turbulent dispersion in dilute dispersed flows have appeared but recent work has emphasized stochastic simulations as a way of providing for the nonlinear interactions between the phases in a relatively fundamental way. This involves random-walk calculations of dispersed-phase trajectories coupled with a simulation of the properties of the continuous-phase. Methods involving turbulence modelling concepts have been widely reported and have exhibited capabilities to match existing measurements for simple shear flows (Crowe 1982; Faeth 1987). However, the *ad hoc* features of these models are not very satisfying and recent work

has sought more fundamental methods. Maxey (1987) and Picart, Berlemont & Goussier (1986) describe representative work along these lines for dilute isotropic turbulent flows. Maxey (1987) computes the motion of particles at the Stokes limit in a constant density flow generated as a finite series of randomly selected Fourier modes following Kraichnan (1970). This is a reasonable approximation that is much simpler than direct numerical simulation of turbulence. However, extending this approach to practical shear flows will require substantial advances of computer capabilities. The approach of Picart *et al.* (1986) is somewhat more general and involves approximate simulation of turbulence properties only along the particle trajectory, yielding good predictions of the Snyder & Lumley (1971) measurements. This approach is closely related to well-developed methods of statistical time-series simulations described by Box & Jenkins (1976), although Picart *et al.* (1986) do not note this analogy.

The objective of the present investigation is to consider turbulent particle dispersion in homogeneous turbulent fields generated solely by particle motion through a nearly stagnant (in the mean) liquid bath. Unlike grid-generated isotropic turbulence, this flow is formally stationary and exhibits levels of anisotropy that are typical of dispersed multiphase flows (Faeth 1987). Measurements of liquid-phase properties of these flows have been reported by Parthasarathy & Faeth (1980); the present study completes the description of these flows by providing measurements of dispersed-phase properties. Finally, flow properties are predicted along the lines of Picart *et al.* (1986) except that methodology from statistical time-series simulations is adopted in order to take advantage of past work in this field (Box & Jenkins 1976).

Experimental and theoretical methods are described in the next two sections. Measured and predicted results are then presented in §4, considering mean and fluctuating particle velocities, particle velocity probability density functions (p.d.f.s) and the sensitivity of predictions to variations of parameters in the formulation. In turn, major conclusions of the study are summarized in §5. Additional details and a complete tabulation of data can be found in Parthasarathy (1989).

2. Experimental methods

2.1. Apparatus

The experimental apparatus and its evaluation are described by Parthasarathy & Faeth (1990) and will be considered only briefly here. The flow was generated by a variable-speed particle feeder which delivered particles to an array of screens to provide a uniform particle flux. The particles then fell into a windowed tank (410 × 535 × 910 mm) filled with water to a depth of 800 mm. The particles reached terminal velocities within 100–200 mm of the liquid surface while measurements were made at the centre of the tank. The particles collected naturally at the bottom of the tank, inducing a negligible displacement velocity of the liquid (less than 0.014 mm/s), and were removed from time to time using a suction system.

Tests to evaluate the uniformity of the flow, effects of tank volume and the time required to achieve stationary conditions are described by Parthasarathy & Faeth (1990). The central region of the tank (300 × 200 mm cross-section for a range of heights extending ±100 mm from the measuring location) had particle number fluxes and liquid velocity fluctuations that were uniform while Reynolds stresses were essentially zero, within experimental uncertainties (10% for fluxes and velocity fluctuations, 50% for Reynolds stresses). Effects of stabilizing waves at the liquid surface with a honeycomb were negligible while reducing the bath volume by a factor

of 32, using Plexiglas partitions and reducing liquid depths, also caused less than a 10% variation of liquid velocity fluctuations. Thus, the arrangement provided a homogeneous flow with relatively little effect of the bath surfaces on flow properties.

2.2. Instrumentation

Streamwise and cross-stream mean and fluctuating particle velocities were measured using the phase-discriminating laser velocimeter (LV) described by Parthasarathy & Faeth (1990). This involved a fixed LV channel, based on the 514.5 nm line of a 2 W argon-ion laser, operating in the dual-beam forward-scatter mode. Directional bias and ambiguity were eliminated using a 40 MHz Bragg-cell frequency-shifter with the output signal downshifted to convenient frequency ranges for filtering and signal processing. Streamwise and cross-stream velocities were measured by rotating the LV optics accordingly. A beam spacer provided an initial 9 mm beam spacing while the receiving optics were shifted to 45° from the forward-scatter direction to minimize problems of large pedestal signals from the particles. This yielded a fringe spacing of 14.3 µm and an optical measuring volume that was 300 µm in diameter and 300 µm long (the actual measuring volume was increased from this size by the particle dimensions since grazing collisions were recorded). The LV signals were interpreted using a burst-counter signal processor (TSI Model 1860B).

The phase discrimination system involved a third beam from a 5 mW He-Ne laser (at an angle of 18° from the LV axis), which enveloped the LV measuring volume, and collection optics set off-axis (at an angle of 32° from the LV axis). The region viewed by the discriminator (0.6 mm diameter and 1.3 mm long) surrounded the LV measuring volume. Particle velocity measurements were made with the water unseeded and the detector operated at low gain which only responded to large-amplitude signals from particles. Thus, the discriminator system was only used to validate the presence of a particle when the signal was recorded. Operation was confirmed by ending the flow of particles which invariably caused the data rate of the LV processor to return to zero. Particle arrival rates were low (10–80 per hour). Number averages of mean and fluctuating velocities were obtained over 200–500 particles.

Parthasarathy (1989) evaluated the experimental uncertainties (95% confidence) of these measurements, as follows: mean streamwise particle velocities: less than 6%; mean cross-stream particle velocities: less than 41%; fluctuating streamwise particle velocities: less than 11%; and fluctuating cross-stream particle velocities: less than 16%. These uncertainties were largely dominated by finite sampling times.

2.3. Particle properties

2.3.1. Particle size

Glass particles having nominal diameters of 0.5, 1.0 and 2.0 mm, and a density of 2450 kg/m³, were used for the tests. The size distributions of the 0.5 and 1.0 mm diameter particles were measured under a microscope with experimental uncertainties (95% confidence) of less than 10% near maximum probability conditions; the size distribution of the 2.0 mm diameter particles was measured using a vernier calliper with experimental uncertainties (95% confidence) of less than 5% near the maximum probability condition. The resulting p.d.f.s of particle diameter are plotted as a function of normalized diameters in figure 1. The measurements for the three particle sizes follow Gaussian distributions within experimental uncertainties. Standard deviations are roughly 10% of the nominal diameter of the particles; actual values of the standard deviations will be taken up later.

Predictions of the p.d.f.s of terminal velocities were also undertaken as the first step in developing the analysis of particle velocities in the homogeneous turbulent flow. These predictions were based on the measured p.d.f.s of particle diameter, illustrated in figure 1, assuming spherical particles at the terminal velocity condition in a quiescent liquid. Under these conditions the terminal velocity, U_t , of a particle having a diameter d_p is as follows:

$$U_t = (4g d_p^2 (\rho_p - \rho) / (3C_D \rho))^{\frac{1}{2}} \quad (1)$$

where g is the acceleration due to gravity, ρ_p and ρ are the particle and liquid densities, and C_D is the drag coefficient. C_D was found from the standard drag curve for spheres (Putnam 1961)

$$C_D = 24(1 + 1.4Re^{\frac{1}{4}})/Re, \quad (2)$$

where the particle Reynolds number is defined as follows:

$$Re = U_t d_p / \nu, \quad (3)$$

and ν is the kinematic viscosity of the liquid. Equation (2) is limited to $Re < 1000$ which is satisfactory for present test conditions.

The calibration was completed by matching the predicted and measured most probable terminal velocity by multiplying the standard drag correlation of (2) by a fixed constant for each nominal particle size as follows: 1.14 for the 0.5 and 2.0 mm diameter particles, and 1.00 for the 1 mm diameter particles. These corrections are surprisingly small in view of the ellipticities of some of the particles and anticipated uncertainties of the standard drag correlation (Cift, Grace & Weber 1978).

The predicted and measured p.d.f.s of the normalized terminal velocities for the three particle sizes are illustrated in figure 2 (normalization parameters will be taken up later). After the minor corrections of the drag coefficients that were just noted, the comparison between predictions and measurements is quite good. This implies that particle diameter variations are responsible for most of the variance of the terminal velocities of the particles. Since the corrections of the standard drag correlation were small, and the p.d.f.s of terminal velocities were reasonably good based on the corrected drag expression, this expression was used for all subsequent calculations of particle drag.

2.3.3. Self-induced motion

It was found that particles dropped individually into a still bath did not fall straight; instead, there was cross-stream motion which increased with increasing particle diameter. This behaviour was calibrated since self-induced motion influences particle velocity fluctuations and affects the interpretation of turbulent dispersion results.

Measurements of self-induced motion with the LV were not possible since sampling rates were too low; therefore, these velocities were measured from shadowgraph motion pictures of individual particles falling in a still bath. The single-particle feeder, without the glass tube, was used to release individual particles into the bath. A shadowgraph motion picture of the falling individual particles, having a field view of 250 mm, was obtained with a Redlake LAXAM camera using Kodak Tri-X Reversal film (ASA 400). The film was projected frame-by-frame on a screen having a grid so that particle tracks could be followed and recorded. The particle displacement tracks were differentiated numerically to find particle velocities using a central-difference scheme. Mean and fluctuating streamline and cross-stream particle velocities were calculated by averaging over 50 particle paths. Uncertainties

Turbulent dispersion of particles

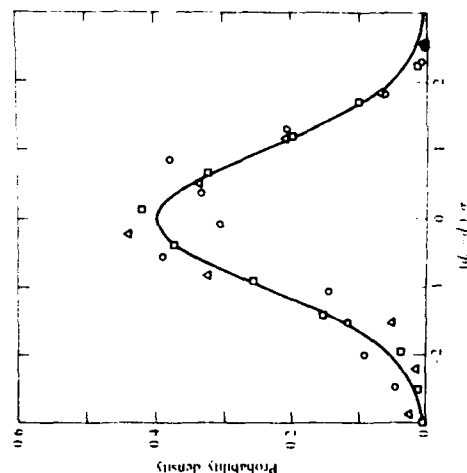


FIGURE 1. Probability density functions of particle diameters: \square $d_p = 0.5$ mm, \circ $d_p = 1.0$ mm, \triangle $d_p = 2.0$ mm. — Gaussian distribution.

These measurements also showed that the particles were not all spherical. The degree of ellipticity (ratio of the major to the minor diameter) increased with increasing nominal particle diameter, as follows: 20% of the 0.5 mm diameter particles were ellipsoids with a mean ellipticity of 1.05; 40% of the 1.0 mm diameter particles were ellipsoids with a mean ellipticity of 1.45; and 65.5% of the 2.0 mm diameter particles were ellipsoids with a mean ellipticity of 1.25.

2.3.2. Particle drag

The drag coefficients of the particles were calibrated by measuring the terminal velocities of individual particles settling in a motionless bath with the LV. A single-particle feeder described by Parthasarathy (1989) was used for these tests: it delivered particles to a glass tube (4 mm inner diameter) that ended 150 mm above the LV measuring volume. The time intervals between particles were in the range 20–500 s. It was necessary to aim the particles with the glass tube to get adequate velocity samples in a reasonable length of time; however, calculations showed that the particles reached their terminal velocities within 60 mm of the point of release so that the particle feeder did not affect terminal velocities. Liquid velocity measurements also showed that disturbances of the bath due to previous particles were small for the separation times between particles used for these measurements.

The LV system was similar to the arrangement described for particle velocity measurements in the homogeneous turbulent flow, however, a large-diameter aperture (2 mm) was used on the detector to increase signal rates. The results were summarized as p.d.f.s of particle velocities for the three particle sizes. The uncertainties of these measurements were less than 9% near the maximum probability condition, largely governed by the number of samples.

Turbulent dispersion of particles

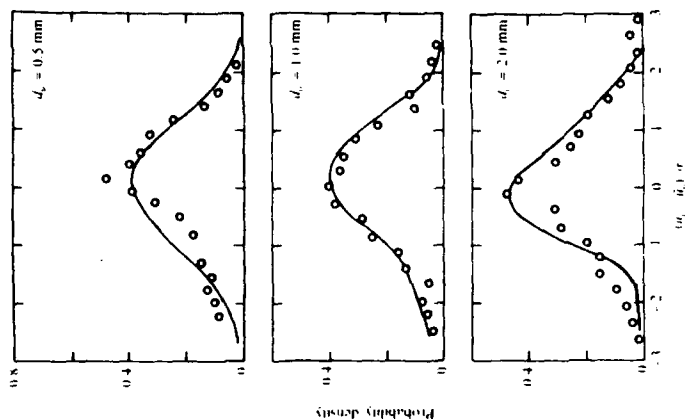


FIGURE 2. Probability density functions of terminal velocities. O, data; ●, predictions.

(95% confidence) of these measurements were largely governed by sampling limitations and were less than 1.5% for mean streamwise velocities and less than 30% for velocity fluctuations.

The mean and fluctuating particle velocities due to self-induced motion are summarized in table 1 for the three particle sizes. The mean terminal velocities from these particle track measurements agreed with the LV measurements made during the particle drag calibrations within the experimental uncertainties of each (10%). The particle velocity fluctuations due to self-induced motion, summarized in table 1, represent variations along particular particle paths so that effects of terminal velocity changes due to diameter variations within a particular size group are small. The streamwise velocity fluctuations due to self-induced motion for the 0.5, 1.0 and 2.0 mm diameter particles are 2.8, 0.96 and 0.19% of the mean terminal velocities; in comparison, the apparent streamwise velocity fluctuations due to size variations are 10.8, 9.5 and 6.1% for the same three particle sizes. Thus, particle velocity fluctuations in the streamwise direction were dominated by effects of particle size variations and turbulent dispersion while effects of self-induced particle motion were small for this component of velocity. The self-induced cross-stream particle velocity

Particle diameter (mm)	0.5 ^a	1.0 ^b	2.0 ^b
\bar{u}_p (mm/s)	71	137	270
$(\bar{u}_p^2)^{1/2}$ (mm/s)	2.0	1.5	0.5
$(\bar{u}_p^2)^{1/2}$ (mm/s)	1.1	5.6	13.1

^a Measurements based on individual particles dropped near the water surface.

^b Measurements based on individual particles dropped through the dispersing screen arrangement.

TABLE 1. Summary of self-induced particle motion properties

fluctuations, however, are significant particularly for the 1.0 and 2.0 mm diameter particles where particle Reynolds numbers exceed 150. Two factors probably contributed to this behaviour: unsteady lateral forces on the particles due to eddy shedding at higher terminal particle Reynolds number (Nakamura 1976; Viets 1971), and effects of increased ellipticity with increasing particle size.

In view of the combined effects of streamwise particle velocity fluctuations caused by size variations and cross-stream particle velocity fluctuations caused by self-induced motion, observations of cross-stream particle velocity fluctuations for the 0.5 mm diameter particles provide the best indication of effects of turbulent dispersion for the present test conditions. Results for the larger particle sizes will still be considered, however, since it is of interest to study whether the turbulent field of the particle-laden flow induces self-induced motion, which is large for these particle sizes.

Measurements were also undertaken to determine whether the dispersing screens induced any cross-stream motion of the particles. This was a concern since the impact of the particles on the screens could cause the particles to spin, generating Magnus forces which would deflect the particles in the cross-stream direction. This effect was studied by dropping particles individually through the dispersing screen arrangement and measuring particle velocities using shadowgraph motion pictures. Result: of these experiments for the 2.0 mm diameter particles are also summarized in table 1. The measurements of mean and fluctuating velocities of the particles passing through the screen arrangement are seen to be almost the same as for single particles dropped directly into the bath; therefore, the dispersing screen did not modify particle properties appreciably.

2.4. Test conditions

A range of particle number fluxes were considered for each particle size: representative test conditions at the low and high ends of these ranges are summarized in table 2. Particle properties are emphasized in table 2; additional information about liquid-phase properties can be found in Parthasarathy & Faeth (1980) for the same test conditions. The properties of the particle size and terminal velocity distributions that were discussed earlier are summarized at the top of the table. Mean streamwise particle velocities within the particle-generated turbulent field of the bath, \bar{u}_p , were the same as terminal velocities in a still liquid, within experimental uncertainties.

Mean particle spacings, l_p , were found by assuming that particles were falling randomly with a uniform particle number flux, \bar{n} , at the mean particle terminal velocity, yielding

$$l_p = (\bar{u}_p / \bar{n})^{1/3} \quad (4)$$

Particle diameter (mm)	0.5 (0.045)		1.0 (0.085)		2.0 (0.15)	
	Low	High	Low	High	Low	High
Particle properties						
Terminal velocity (mm/s)	65 (5)		147 (14)		262 (16)	
Reynolds number (-)	36		156		345	
Number flux (kg/m ² s)	55.4	110.8	3.7	20.9	1.1	3.3
Mean spacing (mm)	10.5	8.2	32.7	18.3	61.8	43.2
u_p (mm/s)	66.8	71.5	144.2	139.0	265.0	265.0
$(u_p^2)_{\text{av}}$ (mm ² /s)	11.0	12.1	17.0	21.9	19.0	20.5
$(u_p^2)_{\text{av}}$ (mm ² /s)	2.7	4.4	2.5	7.4	7.8	9.8
Liquid properties						
Rate of dissipation (mm ² /s ²)	53.2	106.3	27.3	155.8	61.7	193.5
ϵ (mm/s)	1.6	3.9	1.0	3.8	3.0	6.0
ϵ (mm/s)	0.7	0.6	1.1	1.6	1.0	0.9
$(\epsilon^2)_{\text{av}}$ (mm/s)	3.3	4.7	2.4	5.1	3.7	6.1
$(\epsilon^2)_{\text{av}}$ (mm/s)	1.6	2.7	1.2	2.3	1.7	3.1

TABLE 2. Representative test conditions. Round glass beads, density of 2530 kg/m³ falling in a stagnant water bath at 29.5 ± 2 K. Numbers in parentheses denote standard deviations. Particle volume fractions less than 0.01%, displacement velocities less than 0.014 mm/s, direct dissipation by particles less than 4.5%.

The resulting particle spacings were in the range 8–62 mm, or 16–33 particle diameters, yielding particle volume fractions less than 0.01%, therefore, effects of direct particle-to-particle interactions and collisions were negligible. Apparent streamwise particle velocity fluctuations, $(u_p^2)_{\text{av}}$, were much larger than cross-stream particle velocity fluctuations, $(v_p^2)_{\text{av}}$, owing to variations of terminal velocities caused by size variations, as noted earlier.

Following Parthasarathy & Faeth (1980), the rate of dissipation of turbulence kinetic energy within the bath, ϵ , was used to characterize bath operating conditions for various particle sizes and number fluxes. ϵ was found by noting that mean particle velocities were constant and were much greater than particle velocity fluctuations (the ratio of $(v_p^2)_{\text{av}}/\bar{u}_p$ is most representative since effects of particle size variations are small for cross-stream velocity fluctuations). Then the rate of production of turbulence kinetic energy in the bath is equal to the rate of loss of potential energy of the particles as they fall through the bath, which in turn is equal to the rate of dissipation, i.e.

$$\epsilon = \pi \bar{u}_p^2 g d_p^3 (\rho_p - \rho) / (6\rho). \quad (5)$$

Parthasarathy (1969) shows that direct dissipation by particles is small, less than 5%, so that dissipation primarily occurs within the particle wakes.

The particle flows generated mean streamwise and cross-stream velocities, \bar{u} and \bar{v} , in the bath, as discussed by Parthasarathy & Faeth (1980); however, these velocities are small in comparison to the terminal velocities of the particles and they had little effect on particle motion. Streamwise and cross-stream liquid velocity fluctuations, $(u^2)_{\text{av}}$ and $(v^2)_{\text{av}}$, were largely functions of ϵ for present test conditions, with particle sizes and number fluxes being secondary factors (Parthasarathy & Faeth 1980). Particle and liquid velocity functions in the cross-stream direction are comparable so that effects of turbulent dispersion were significant for present test conditions.

3. Theoretical methods

3.1. Particle motion

The predictions of particle-phase properties involved computations of particle motion in the random velocity field of the continuous phase and are analogous to random walk calculations. A sufficient number of particle trajectories, allowing for the variation of particle size within a particular nominal particle size, were computed to obtain statistically significant results.

Computation of particle motion generally followed an approach used earlier for particle-laden jets (Parthasarathy & Faeth 1987). Since particle volume fractions were small, the flow was assumed to be dilute and effects of nearby particles on interphase momentum transport, as well as particle collisions, were neglected. The particles were assumed to be small in comparison to the smallest scales of the turbulence. This is marginal since Kolmogorov length scales are in the range 240–380 μm which is somewhat smaller than the particle diameters. Nevertheless, this approximation is reasonable since the turbulent dispersion of particles is dominated by the large-scale energy-containing features of the flow while the terminal velocities of particles in the turbulent environment were not very different from a still liquid. The particles were assumed to be spherical with p.d.'s of particle diameter taken from figure 1; this is justified by the reasonable estimates of particle terminal velocity distributions using this approach, illustrated in figure 2. Effects of Magnus forces were neglected based on observations during calibration of self-induced motion discussed earlier. Since the flows were homogeneous, Saffman lift forces were neglected while effects of static pressure gradients can be neglected with little error since bath velocities are small in comparison to particle velocities.

Under these assumptions, particle motion can be found using the formulation of Odar & Hamilton (1964), reviewed by Clift *et al.* (1978), as follows:

$$dx_{pi}/dt = u_{pi}, \quad (6)$$

$$(\rho_p/p + \Delta_A/2) du_{pi}/dt = g(\rho_p/p - 1)\delta_{ii} - 3C_D u_{pi} u_{pi}/(4d_p) - \Delta_H(81\nu/\pi d_p^3) \int_{t_0}^t (t-\xi)^{-1/2} (du_{pi}/d\xi) d\xi, \quad (7)$$

where x_{pi} and u_{pi} are the particle position and relative velocity in a Cartesian reference frame with $i = 1$ denoting the vertical direction, t is time, t_0 is the time of the start of motion, δ_{ii} is the Kronecker delta function and Δ_A and Δ_H are parameters which account for effects of particle acceleration. The terms on the left-hand side of (7) represent the acceleration of the particle and its virtual mass; the terms on the right-hand side represent buoyancy, drag and Basset history forces.

The parameters Δ_A and Δ_H were empirically correlated by Odar & Hamilton (1964), as follows:

$$\Delta_A = 2.1 - 0.123M_A/(1 + 0.12M_A^2), \quad (8)$$

$$\Delta_H = 0.48 + 0.52M_A^2/(1 + M_A^2), \quad (9)$$

where M_A is the particle acceleration modulus

$$M_A = (du_i/dt) d_p/\nu^2. \quad (10)$$

The values of Δ_A and Δ_H vary in the ranges 1.0–2.1 and 1.00–0.48, the former values being the correct limit of (7) at the Basset-Boussinesq-Oseen (B-B-O) limit of the formulation (Clift *et al.* 1978). The drag coefficient was found from (2) as noted

earlier, this is reasonable based on the terminal velocity predictions of figure 2 and the fact that liquid velocity fluctuations are small in comparison to particle terminal velocities, i.e. relative turbulent intensities are small. Naturally, use of the Okubo & Hamilton (1964) correction factors in a turbulent environment is speculative. However, evaluation of the sensitivity of the predictions to these parameters, to be taken up later, shows that their effect is small for present test conditions in any event.

3.2 Statistical simulation

Statistical simulation of particle trajectories was based on statistical time series simulation techniques adapted from Box & Jenkins (1976). The statistical simulation of the velocity field of the continuous phase can be designed to satisfy any number of the properties of the continuous phase: mean velocities, velocity fluctuations, Lagrangian time correlations, instantaneous conservation of mass, higher-order correlations, etc. However, priorities must be set since computational requirements increase as the number of properties in the flow to be simulated increase. Based on the results of earlier simulations to predict the turbulent dispersion of particles (Faeth 1967), mean and fluctuating velocities and Lagrangian time correlations of velocity fluctuations appear to be sufficient to treat turbulent particle dispersion. Therefore, present simulations were designed to reproduce these properties.

The properties of the liquid velocity field were taken from Parthasarathy & Faeth (1980) at the appropriate test conditions. The present flows are homogeneous so that cross-correlations like $\overline{u_i u_j}$ are small while mean liquid velocities are also small and do not affect particle velocity fluctuations; therefore only liquid velocity fluctuations must be simulated and velocity components can be assumed to be statistically independent. However, liquid velocity fluctuations are not isotropic (see table 2) with streamwise velocity fluctuations being roughly twice cross-stream velocity fluctuations (both components of which are equal). Finally, measurements showed that liquid velocity fluctuations satisfied Gaussian p.d.f.s (Parthasarathy & Faeth 1980).

To illustrate the approach used to simulate liquid velocities along a particle path, consider a simulation using equal timesteps, Δt , that has proceeded $i-1 > p > 0$ timesteps. The value of any component of the liquid velocity fluctuations at the location of the particle at the end of the next timestep, say u_i (where u can be any velocity component and i denotes the timestep) is found from the following autoregressive process (Box & Jenkins 1976):

$$u_i = \sum_{j=p}^{i-1} A_{ij} u_j + a_i \quad (1 \leq p \leq i-1). \quad (11)$$

In (11) the A_{ij} are weighting factors so that correlations at various times can be satisfied, a_i is an uncorrelated random variable having a Gaussian p.d.f. chosen so that the p.d.f. of u_i is satisfied, and p is selected to eliminate points having small correlation coefficients with respect to the point i . The A_{ij} are related to correlations of liquid velocity fluctuations through the Yule-Walker equations, as follows (Box & Jenkins 1976):

$$\overline{u_i u_k} = \sum_{j=p}^{i-1} A_{ij} \overline{u_j u_k} + \overline{a_i u_k} \quad (k = p, \dots, i-1). \quad (12)$$

The first moment of a_i is zero while the second moment is found from the following expression

$$\overline{a_i^2} = \overline{u_i^2} - \sum_{j=p}^{i-1} A_{ij} \overline{u_j u_i}. \quad (13)$$

Given the correlations $\overline{u_i u_j}$, etc. (12) is a positive-definite linear system of equations which can be readily solved using Cholesky factorization. The a_i^2 can then be found from (13) since all quantities on the right-hand side of this equation are known.

For present flows, it will be shown that the correlations are roughly exponential; then, Box & Jenkins (1976) show that (12) can be reduced to a Markov process where only a single previous timestep must be considered to find a_i as follows:

$$a_i = A_{i,i-1} a_{i-1} + a_i \quad (14)$$

where $A_{i,i-1}$ is the correlation $\overline{u_i u_{i-1}}$. Then a_i is found from a Gaussian distribution with a zero mean value and a variance from (13) as follows:

$$\overline{a_i^2} = (1 - A_{i,i-1}^2) \overline{a_i^2}. \quad (15)$$

At this limit, the simulation becomes a Uhlenbeck-Ornstein (OU) process, which has been used in past studies of turbulent dispersion of fluid particles (Durbin 1980; Anand & Pope 1985; Sawford & Hunt 1986).

The simulation begins with a random selection of the components of the velocity fluctuations at the initial condition, u_0 , satisfying Gaussian p.d.f.s having the measured variances and degree of anisotropy. $\overline{a_i^2}$ can then be found from (15). A random selection of a_i from its p.d.f. then yields u_i from (14). After repeating this process to find all three velocity components, the motion of the particle in this velocity field is computed by integrating (6) and (7) to find particle properties at Δt . The calculation continues in this manner for additional increments of time until particle properties become statistically stationary. For present computations, 5000 trajectories of this type were considered to find final results, with the sizes of the 5000 particles distributed according to the particle size distributions illustrated in figure 1.

Liquid velocity fluctuations were known directly from the measurements of Parthasarathy & Faeth (1980). Thus, the key to simulating particle trajectories is knowledge of the Lagrangian correlations, $A_{i,i-1}$. Fortunately, although Taylor's hypothesis is not appropriate to relate temporal and spatial variations of turbulence properties at a fixed point, since mean liquid velocities were small, it could be applied to obtain correlations along a particular path, since the relative velocities of the particles were large in comparison to velocity fluctuations. Thus, knowledge of spatial and temporal correlations in the streamwise direction from Parthasarathy & Faeth (1980) allowed the $A_{i,i-1}$ to be estimated and showed that departures from Taylor's hypothesis were small. In particular, the Lagrangian correlation of streamwise liquid velocity fluctuations along a particle path was obtained from the measured streamwise correlation of liquid velocity fluctuations, as follows:

$$\overline{u_{L,i} u_{L,i-1}} \approx \overline{u_L(x+U_z(i-1)\Delta t, t) u_L(x+U_z(i-1)\Delta t, t)} = \overline{u_L(x, t) u_L(x+U_z \Delta t, t)}, \quad (16)$$

where x and u_L are the streamwise direction and liquid velocity. The correlation coefficients needed to find the correlations of (16) are plotted as a function of $\Delta t/\tau_L$, where τ_L is the Lagrangian integral timescale, in figure 3. The measurements of Parthasarathy & Faeth (1980) at the low and high loadings of the three particle sizes, as well as the exponential approximation, $\exp(-\Delta t/\tau_L)$, are shown on the figure. The exponential approximation is seen to provide a reasonably good fit of the measurements within experimental uncertainties (estimated to be less than 36%). Naturally, this comes about largely due to the inability of the measurements to resolve the shortest length-scales of the flow owing to problems of step-noise, where the correlation departs from exponential behaviour (Parthasarathy & Faeth 1980).

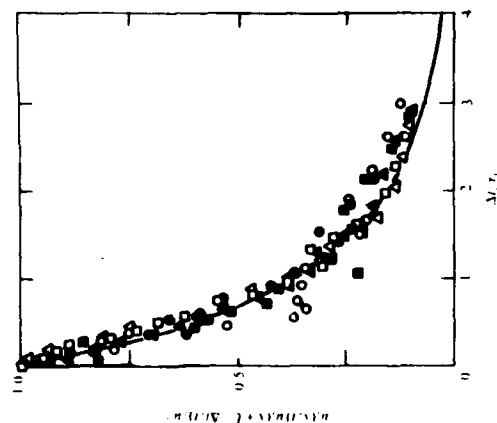


FIGURE 3. Lagrangian temporal correlations of streamwise liquid velocity fluctuations along a particle path. $d_p = 0.5$ mm: \square , low and high loadings; $d_p = 1.0$ mm: \circ , low and high loadings; $d_p = 2.0$ mm: \triangle , low and high loadings; —, $\exp(-\Delta t/\tau_L)$ approximation.

However, particle motion is primarily influenced by liquid motions having large scales so that this deficiency is not a major problem for present purposes. Based on the results of Parthasarathy & Faeth (1990) the values of τ_L are 0.91, 0.40 and 0.22 s for the 0.5, 1.0 and 2.0 mm diameter particles.

The simulation requires knowledge of the Lagrangian correlations of cross-stream liquid velocities as well. Unfortunately, spatial correlations of cross-stream liquid velocities in the streamwise direction were not measured by Parthasarathy & Faeth (1990), therefore, they were assumed to vary in the same manner as the spatial correlations of liquid streamwise velocities for lack of an alternative. The output of the stochastic simulation consisted of particle properties like u_p , v_p , u_p^2 and v_p^2 — the latter two being direct measures of the effects of turbulent particle dispersion.

4. Results and discussion

4.1. Velocities

Measured and predicted particle properties included mean and fluctuating velocities and velocity probability density functions. These results are considered in the following, concluding with a study of the sensitivity of the predictions to parameters of the formulation.

Measurements of mean streamwise and fluctuating streamwise and cross-stream particle velocities are illustrated in figure 4. The velocities are plotted as a function of the rate of dissipation, which is the main variable controlling liquid velocity fluctuations (Parthasarathy & Faeth 1990), for the 0.5, 1.0 and 2.0 mm diameter

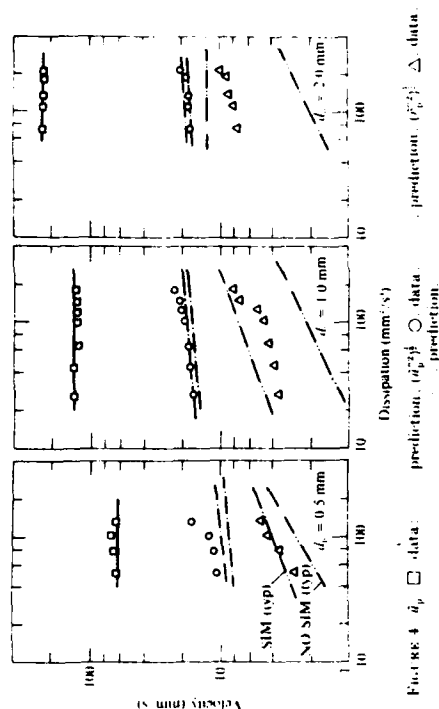


FIGURE 4. u_p , \square , data; \circ , prediction; \triangle , data; \square , prediction.

particles. A range of particle loadings (or values of ϵ) are considered, rather than just the loadings for each particle size summarized in table 2, so that the trends of the measurements can be observed more readily.

Measurements of mean particle velocities illustrated in figure 4 do not exhibit any systematic variation with dissipation and are identical to the terminal velocities of the particles within experimental uncertainties (see table 2). In contrast, evidence for changes of mean particle velocities in particle-generated flows or homogeneous turbulent fields is provided by the theoretical studies of Batchelor (1972) and Maxey (1987). Batchelor (1972) considers the sedimentation of particles having Reynolds numbers in the Stokes regime, finding that settling velocities decrease as the particle volume fractions increase. Aside from the fact that present particle Reynolds numbers are greater than 38, which is well beyond the Stokes regime so that the applicability of these results is questionable, present particle volume fractions are also low, less than 0.01%, so that changes estimated from Batchelor's findings are less than 0.1% and are not significant in comparison to experimental uncertainties. Maxey (1987) considers dilute particle flows in a homogeneous turbulent field, also at Stokes limit. He finds that settling velocities should increase in the presence of turbulence, however, the effect becomes relatively small when the ratio of the mean particle velocity to the continuous-phase velocity fluctuations exceeds 2. For present test conditions, this ratio is in the range 13–71 so that changes in settling velocities due to this mechanism should be small as well.

Thus, due to small particle volume fractions, and large settling velocities in comparison to levels of turbulent fluctuations, it is not surprising that there was little difference between settling velocities in turbulent and non-turbulent environments for the present test conditions. However, additional evaluation of factors influencing settling velocities beyond the Stokes regime would be desirable. Furthermore, the picture could change at higher particle loadings than those considered here. For example, liquid velocity fluctuations are proportional to $\epsilon^{1/2}$ (Parthasarathy & Faeth 1990) so that large particle loadings could yield velocity fluctuations comparable to

Particle diameter (mm)	0.5		1.0		2.0	
	Low	High	Low	High	Low	High
Particle loading	0.6	0.4	0.6	0.3	0.4	0.1
$(\bar{u}^2_p/\bar{u}^2_b)$	2.0	1.4	5.9	2.8	4.3	2.6
$(\bar{u}^2_p/\bar{u}^2_b)$	3.3	2.6	7.1	4.3	5.1	3.4
$(\bar{u}^2_p/\bar{u}^2_b)$	0.7	0.4	4.7	2.4	7.9	4.4
$(\bar{u}^2_p/\bar{u}^2_b)$	1.7	1.6	2.1	3.2	4.6	3.2

TABLE 3. Ratios of particle/liquid velocity fluctuations

settling velocities. Particle concentrations at such conditions would be very high, however, more like fluidized bed processes, so that such flows would not be dilute and extrapolation of present results to these conditions would be very questionable. Nevertheless, the evolution between the present dilute particle flows and fluidized bed conditions has interesting implications for a better understanding of both flows and merits further study.

The particle velocity fluctuations illustrated in figure 4 are influenced by several phenomena, as follows: self-induced particle motion, apparent streamwise velocity fluctuations due to the variation of terminal velocities over the size range of the present experiments and turbulent dispersion of the particles. Results summarized in table 3 help provide some insight into the relative importance of these phenomena for present test conditions. This table is a summary of the ratios of particle velocity fluctuations normalized by the corresponding component of both liquid velocity fluctuations. Test conditions include low and high loadings for all three particle sizes. Streamwise and cross-stream velocity fluctuations are considered for self-induced motion (\bar{u}^2_{ps}) and (\bar{v}^2_{ps}) (obtained by calibration) and motion within the bath itself, (\bar{u}^2_p) and (\bar{v}^2_p) . However, only the streamwise apparent velocity fluctuations due to particle size variations (\bar{u}^2_{pa}) (obtained by calibration) have been considered since this is the only velocity component that is relevant for this effect.

Comparing the velocity fluctuation ratios listed in table 3 for self-induced motion and terminal velocity variations with those measured in the bath provides a relative measure of the importance of these effects in comparison with turbulent dispersion. It is seen that streamwise velocity fluctuations due to self-induced motion are small while apparent fluctuations due to terminal velocity variations are comparable to those measured in the bath; therefore, streamwise particle velocity fluctuations are dominated by effects of terminal velocity variations due to variations of particle diameter for present test conditions and relatively little can be learned about turbulent dispersion from this velocity component. A possible exception is the highest loading with the 0.5 mm diameter particles where effects of terminal velocity variations are roughly half the velocity fluctuation levels observed in the bath; nevertheless, reduced sensitivity due to direct effects of turbulent dispersion still makes this condition marginal for definitive conclusions. The results for cross-stream velocity fluctuations suggest that effects of self-induced motion are relatively small in comparison to turbulent dispersion for the 0.5 mm diameter particles; therefore, this condition provides a reasonable indication of effects of turbulent dispersion. In contrast, cross-stream velocity fluctuations due to self-induced particle motion are generally larger than those observed in the bath for the 1.0 and 2.0 mm diameter particles so that these test conditions are of questionable value for gaining information about turbulent dispersion. A curious phenomena is that cross-stream

velocity fluctuations observed in the bath for the larger sizes are smaller than those observed during the calibration tests for self-induced particle motion in still liquids. This suggests that the turbulent field of the bath is interfering with eddy-shedding that is thought to cause this behaviour. Additional study of this effect under more controlled conditions would be desirable.

The previous considerations imply that turbulent dispersion is the dominant process causing particle velocity fluctuations only for the cross-stream velocity fluctuations with the 0.5 mm diameter particles for present test conditions. In this case, the ratio of particle to liquid cross-stream velocity fluctuations are in the range 1.6-1.7 (see table 3) which implies that particle velocity variations is subtracted from the similarly, if the contribution of terminal velocity variations is subtracted from the streamwise velocity fluctuations measured in the bath the result still yields particle streamwise velocity fluctuations greater than the liquid streamwise velocity fluctuations for the 0.5 mm diameter particles. This occurs since particle response varies over the spectra of the continuous-phase velocity fluctuations and depending upon the energy content of the range of frequencies where the response is greatest the particle fluctuations can be greater or smaller than a single measure of liquid-phase velocity fluctuations such as the root-mean squared velocity fluctuation. The results also suggest that turbulent dispersion is very effective in the homogeneous turbulence field generated by the particles themselves. This behaviour is caused by the large frequency range of the continuous-phase velocity fluctuations since both mean and turbulent wake properties contribute to the spectra, see Parthasarathy & Faeth (1980). With such a large range of frequencies available, the probability that the particles will encounter a range of frequencies where their response is high is enhanced, enhancing effects of turbulent dispersion as well. In particular, particle response tends to be highest (approaching unity) at low frequencies (Al Tawel & Landau 1977). Thus, the high signal energy content at low frequencies due to effects of mean wake velocities is probably a significant factor in the good turbulent dispersion properties of present homogeneous particle-laden flows.

Combining an efficient mechanism of turbulent dispersion with effects of self-induced motion and variations of terminal velocities, generally yields particle velocity fluctuations that are greater than liquid velocity fluctuations (as much as 5.5 times greater) over the present test range. Thus, when considering effects of turbulent dispersion, intuitive ideas that particles will have some difficulty in responding to liquid-phase fluctuations owing to their inertia, and will necessarily mix more slowly than an infinitely small particle as a result, should be accepted with caution.

Effects of loading (dissipation) on particle velocity fluctuations can be seen best in figure 4. Streamwise particle velocity fluctuations are large, and do not vary very much with dissipation, since they are dominated by variations of terminal velocities over the present test range (the highest loading for the 0.5 mm diameter particles exhibits a greater effect but measurements are also least accurate at this condition since particle concentrations are greatest). In contrast, cross-stream particle velocity fluctuations are significantly increased with increasing rates of dissipation for all particle sizes. As just discussed, this increase can be attributed to effects of turbulent dispersion for the 0.5 mm diameter particles. In fact, noting that the ratio of $(\bar{v}^2_p)/(\bar{u}^2_p)$ is roughly constant, indicating similar particle response to cross-stream liquid velocity fluctuations over the present test range (see table 3), this increase simply follows the λ variation of liquid velocity fluctuations. Surprisingly, the cross-stream particle velocity fluctuations also exhibit significant increases with increasing

dissipation for the 1.0 and 2.0 mm diameter particles even though these results should be dominated by self-induced lateral motion of the particles (see table 3). This suggests that eddy-shedding mechanisms leading to self-induced lateral motion in still liquids may be less effective in turbulent environments so that effects of turbulent dispersion are greater than might be anticipated from the results summarized in table 3.

Predictions based on the present stochastic analysis of the particle phase are also illustrated in figure 4. Recall that these predictions are based on the measured turbulence properties of the liquid phase and that effects of particle size variations are considered, however effects of self-induced motion of the particles have been ignored since no information is available concerning the fluctuating forces on the particles due to irregular particle shapes and eddy shedding. In an effort to provide some indication of potential effects of self-induced particle motion, predictions are shown where mean-squared particle velocity fluctuations from the particle trajectory simulations and the self-induced motion are $\bar{u}_p^2 = \bar{u}_{pred}^2 + \bar{u}_{pi}^2$, etc. These predictions are denoted SIM to indicate that 'self-induced motion' has been considered. The baseline predictions without consideration of self-induced motion are denoted by NO SIM.

Mean velocity predictions are in excellent agreement with measurements in figure 4. This is not a very critical test of predictions, however, since the predictions largely reflect the correct calibration of particle drag properties which was discussed earlier. The new features that the simulations include is the increase of mean particle drag properties by turbulent fluctuations, i.e. computing particle drag using average liquid phase properties is not correct since drag is not a linear function of the relative velocity for Reynolds number greater than unity (Faeth 1987); and the biasing of particle motion by interactions with the turbulent field analogous to the properties investigated by Maxey (1987). These factors are considered by the simulations because drag is based on instantaneous relative velocities and the turbulent field is simulated through second-order correlations. Nevertheless, neither effect influences mean particle velocities significantly for present test conditions since mean particle velocities are much greater than liquid velocity fluctuations, the relative turbulence intensities never exceeded 8% so that biasing of drag is small while the turbulent interaction effect is not likely to be significant based on the results of Maxey (1987) discussed earlier.

Predicted streamwise particle velocity fluctuations in figure 4 generally agree with measurements within experimental uncertainties. In this case, the fluctuations are dominated by the effects of variations of terminal velocities and effects of self-induced motion are small (see table 3). Nevertheless, it is encouraging that the relatively small increase of particle velocity fluctuations due to increased turbulent dispersion with increasing dissipation is represented quite well by the predictions. The comparison between predicted and measured cross-stream velocity fluctuations in figure 4 is hampered by effects of self-induced particle motion. However, this effect is modest for the 0.5 mm diameter particles and the baseline predictions (NO SIM) are reasonably good while the present *ad hoc* correction for self-induced particle motion yields results (SIM) that are in excellent agreement with measurements. This suggests that the most important properties of the turbulent field have been considered and that effects of turbulence on particle drag are modest. The last observation is reasonable since the relative velocities of the particles are large in comparison to liquid phase velocity fluctuations, i.e. relative turbulence intensities are small as noted earlier. Predictions ignoring self-induced motion show

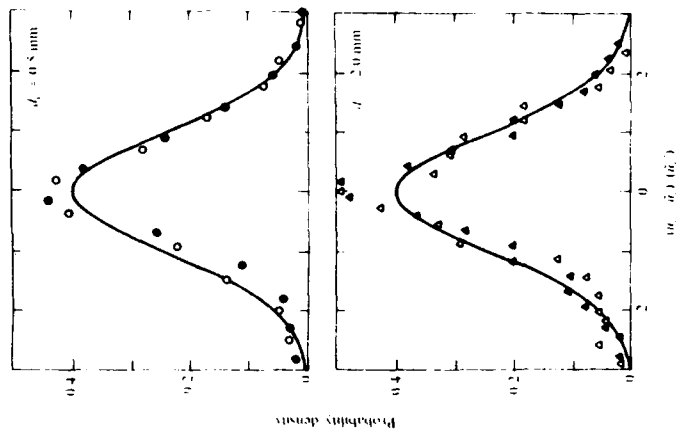


FIGURE 5. Probability density functions of streamwise particle velocity fluctuations, $d_p = 0.5$ mm (○), low and high loadings; $d_p = 2.0$ mm (△), low and high loadings; —, prediction.

a progressive reduction of cross-stream particle velocity fluctuations with increasing particle diameter at the same value of ϵ . This behaviour follows since liquid velocity fluctuations only depend on ϵ for present test conditions (Parthasarathy & Faeth 1980) while increased particle diameter reduces the response of the particles to liquid velocity fluctuations. Effects of self-induced motion tend to overwhelm this trend, however, so that predictions ignoring self-induced motion are much smaller than the measurements for the 1.0 and 2.0 mm diameter particles while including the self-induced motion causes cross-stream particle velocity fluctuations to be overestimated. This highlights the need to develop a rational method of including the self-induced forces on the particles in particle trajectory calculations. As noted earlier, the results suggest that the turbulent flow field may be modifying eddy-shedding mechanisms responsible for self-induced particle motion as well.

4.2. Probability density functions

The probability density functions of streamwise particle velocity fluctuations are plotted as a function of normalized variables in figure 5. Measurements for the different loadings of the 0.5 and 2.0 mm diameter particles appear on the plots. These

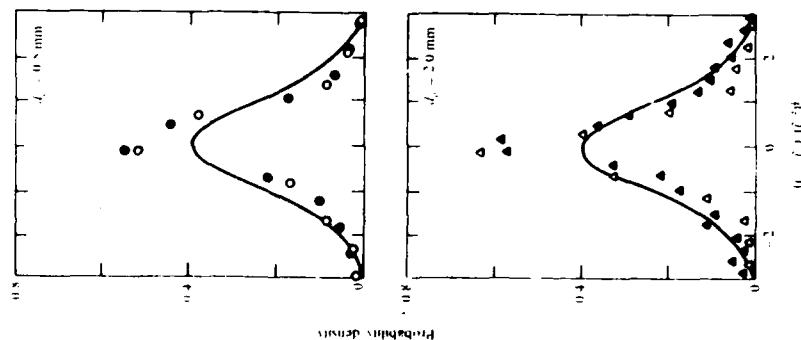


FIGURE 6. Probability density functions of cross-stream particle velocity fluctuations. Identification of symbols the same as figure 3.

measurements are not significantly different from the particle drag calibrations, since particle velocity fluctuations in the streamwise direction are dominated by terminal velocity variations. Thus, predictions both considering and ignoring self-induced motion are very nearly the same and are in reasonably good agreement with the measurements, particularly since the results are normalized. The predictions essentially yield Gaussian probability density functions.

The probability density functions of cross-stream particle velocity fluctuations are illustrated in figure 6. The method of plotting and test conditions are the same as figure 3. Owing to the method of normalization, results for the 0.5 mm diameter particles (which are dominated by effects of turbulent dispersion) are essentially the

Input parameter (100% change)	Change of output parameter (%)			
	u_0	$(\sigma_{u_x}^2)^{1/2}$	$(\sigma_{u_y}^2)^{1/2}$	$(\sigma_{u_z}^2)^{1/2}$
$(\sigma_{u_x}^2)^{1/2}$	~ 0	20 to 24	~ 0	~ 0
$(\sigma_{u_y}^2)^{1/2}$	~ 0	~ 0	98 to 100	~ 0
τ_0	~ 0	0 to 4	~ 0	~ 0
τ_0	-32 to -39	-28 to -32	~ 0	~ 0

TABLE 4. Results of sensitivity study of particle properties. These results were similar for the 0.5 and 2.0 mm diameter particles over the present range of particle loadings; therefore, only the range of output changes are shown. Use of standard values or $\Delta u_0 = 0$ resulted in negligible changes of predictions.

same as results for larger particles (which are dominated by effects of self-induced particle motion). Similarly, the various predictions are nearly the same and all of the predictions approximate Gaussian probability density functions. The flatness factors of the measured probability density functions of the cross-stream velocity fluctuations are 4.7 and 5.3 for the low and high loadings of the 0.5 mm particles, and 6.3 and 3.5 for the low and high loadings of the 2 mm particles. Thus, these measurements depart from a Gaussian distribution which would have a flatness factor of 3. A possible reason for this behaviour is that self-induced motion may inhibit Gaussian behaviour, but more study is needed to understand the effects of self-induced particle motion on particle motion before any firm conclusions can be drawn.

4.3. Sensitivity study

The numerical simulations of particle motion required the prescription of a number of parameters subject to significant uncertainties, as follows: the liquid velocity fluctuations, the Lagrangian integral timescale, the particle drag coefficient, and the virtual mass and Basset history force parameters of (8) and (9). In order to better understand the nature and limitations of the numerical simulation, the sensitivity of predictions to variations of these parameters was studied.

Results of the sensitivity study appear in table 4 where changes in output parameters for 100% changes in input parameters are summarized. Effects of particle size variations were considered during these computations but not effects of self-induced particle motion. These results were similar for all three particle sizes over the range of loadings considered during this investigation; therefore, only the range of output variable changes are shown. Predicted mean streamwise particle velocities were only sensitive to estimates of particle drag coefficients, where 100% changes of τ_0 yielded 30–40% changes of the particle mean velocity. This behaviour is expected since terminal velocities of the particles were not influenced strongly by the bath turbulence and are proportional to $\tau_0^{1/2}$, see (1).

Predicted streamwise particle velocity fluctuations were primarily influenced by changes of the drag coefficient and streamwise liquid velocity fluctuations. The effect of drag coefficient is the same as for mean particle velocities – for the same reasons. The effect of a 100% increase of liquid velocity fluctuations on streamwise particle velocity fluctuations was only 20–24%; this follows since streamwise particle velocity fluctuations were dominated by variations of particle terminal velocities due to size variations for present test conditions. The small effect of cross-stream liquid velocity fluctuations on streamwise particle velocity fluctuations occurs since this variable primarily influences streamwise properties by modifying particle drag

coefficients, therefore, its effect is not large since particle terminal velocities are much greater than liquid velocity fluctuations for present test conditions. The insensitivity to variations of the Lagrangian integral timescale, T_L , follows since this variable is most closely associated with effects of turbulent dispersion that are small for this component of velocity.

Predicted cross-stream particle velocity fluctuations were really only influenced by variations of cross-stream liquid velocity fluctuations, where the changes of the output have a one-to-one correspondence with changes of the input. This highlights the strong interaction between the particles and the turbulence of the liquid phase for present test conditions, causing very effective turbulent dispersion, i.e. cross-stream particle velocity fluctuations are greater than liquid velocity fluctuations in the cross-stream direction. The insensitivity to streamwise liquid velocity fluctuations follows for the same reasons that cross-stream liquid velocity fluctuations had little effect on streamwise particle velocity fluctuations. The insensitivity to both τ_L and C_D are probably related. The effective turbulent dispersion for present conditions implies that particles have sufficiently high drag to respond quite closely to the lateral liquid velocity fluctuations; therefore, additional time to respond is not needed while increasing the drag coefficient only serves to reduce already small relative velocities in the cross-stream direction.

Finally, effects of using either of the standard values Δx and Δy or setting these parameters equal to zero was small. This follows since mean particle velocities are not influenced by particle size variations, and particle response in the cross-stream direction is very high and is relatively insensitive to parameters that influence particle drag properties.

5. Conclusions

The present investigation considered the turbulent dispersion of particles in their self-generated homogeneous turbulent field. The specific configuration involved nearly monodisperse glass spheres (particle diameters of 0.5, 1.0 and 2.0 mm with corresponding Reynolds number of 38, 156 and 545) falling with constant particle number fluxes in a water bath under dilute conditions (particle volume fractions less than 0.01%). The major observations and conclusions of the study are as follows:

- (i) Present particles exhibited drag coefficients that were within 14% of the standard drag curve for spheres, in spite of some ellipticity of their shapes. However, individual particles falling in motionless water exhibited self-induced motion, particularly in the lateral direction. Self-induced motion increased with increasing particle size due to both eddy-shedding at large particle Reynolds numbers as well as increased ellipticity of the larger particles.
- (ii) Mean particle velocities were independent of dissipation and approached the terminal velocity of the particles in a still liquid since liquid volume fractions were small and particle settling velocities were large in comparison to liquid velocity fluctuations.
- (iii) Particle velocity fluctuations exceeded liquid velocity fluctuations for all test conditions. Large streamwise particle velocity fluctuations were dominated by smallest particle size differences resulting in variations of terminal velocities. Cross-stream velocity fluctuations were due to turbulent dispersion, which is effective in this flow since integral scales are relatively large, enhanced by effects of self-induced motion for the larger particles. However, effects of self-induced motion were smaller in the particle-generated turbulent field than in still liquids, suggesting that

turbulence may interfere with eddy-shedding mechanisms thought to be responsible for this behaviour.

(iv) Stochastic simulation of particle motion, allowing for probability density functions of liquid velocity fluctuations and Lagrangian temporal correlations yielded encouraging results. This indicates that use of statistical time-series techniques to simulate liquid-phase properties provides a useful simplification to treat turbulent dispersion since it eliminates many of the *ad hoc* features of earlier simplified methods while avoiding the extensive computations needed for full numerical simulation of the flow.

The authors wish to thank L. P. Bernal and W. W. Willmarth for helpful discussions during the course of the study. The work was supported by the Air Force Office of Scientific Research, Grant no. AFOSR-85-0244, under the technical management of J. M. Tishkoff. The US Government is authorized to reproduce and distribute copies of this paper for Governmental purposes notwithstanding any copyright notation thereon.

REFERENCES

- AL-TAWEL, A. M. & LAMDAI, J. 1977 Turbulence modulation in two-phase jets. *Int. J. Multiphase Flow* **3**, 341-351.
- ANAND, M. A. & POPE, S. B. 1985 Diffusion behind a line source in grid turbulence. *Fourth Symposium on Turbulent Shear Flows*, pp. 17-11-17-17.
- BATCHELOR, G. K. 1972 Sedimentation in a dilute dispersion of spheres. *J. Fluid Mech.* **52**, 245-268.
- BOA, G. E. P. & JENKINS, G. M. 1976 *Time Series Analysis*, rev. edn, pp. 47-84. Holden Day.
- CLIFT, R., GRACE, J. R. & WEWER, M. E. 1978 *Bubbles, Drops and Particles*, pp. 266-268. 298-302. Academic.
- CROWE, C. T. 1982 Review - numerical models for dilute gas particle flows. *J. Fluids Engng* **104**, 297-303.
- CASANOVY, G. T. 1983 Turbulent diffusion of heavy particles in the atmosphere. *J. Atmos. Sci.* **20**, 201-208.
- DESJOURS, P., GODESBET, G., BERLEMONT, A. & PICART, A. 1986 Dispersion of discrete particles by continuous turbulent motions: new results and discussions. *Phys. Fluids* **29**, 2147-2151.
- DUBUIS, P. A. 1980 A random flight model of inhomogeneous turbulent dispersion. *Phys. Fluids* **23**, 2151-2153.
- FAGRO, G. M. 1987 Mixing, transport and combustion in sprays. *Prog. Energy Combust. Sci.* **13**, 293-345.
- FERGUSON, J. R. & STOK, D. E. 1986 Particle dispersion in decaying isotropic homogeneous turbulence. *Gia-Sidd Flows* (ed. J. Jurewicz), pp. 9-14. ASME.
- GODESBET, G., BERLEMONT, A. & PICART, A. 1984 Dispersion of discrete particles by continuous turbulent motions. Extensive discussion of the Tchen's theory using a two-parameter family of Lagrangian correlation functions. *Phys. Fluids* **27**, 827-837.
- KATZ, E. J. 1986 Atmospheric diffusion of settling particles with sluggish response. *J. Atmos. Sci.* **23**, 159-168.
- KRACHMAN, R. H. 1970 Diffusion by a random velocity field. *Phys. Fluids* **13**, 22-31.
- MAKEY, M. R. 1987 The gravitational settling of aerosol particles in homogeneous turbulence and random flow fields. *J. Fluid Mech.* **174**, 441-465.
- MEER, C. C. & JONES, B. G. 1973 Studies of the behavior of heavy particles in a turbulent fluid flow. *J. Atmos. Sci.* **30**, 238-244.
- NAKAMURA, I. 1978 Steady wake behind a sphere. *Phys. Fluids* **19**, 5-8.

- NOR, A. & PISSEY, I. M. 1979 The effect of a steady drift on the dispersion of a particle in a turbulent fluid. *J. Fluid Mech.* **94**, 369-381.
- OSER, F. & HANFMAN, W. S. 1964 Force on a sphere accelerating in a viscous fluid. *J. Fluid Mech.* **18**, 302-314.
- PARTHASARATHY, R. N. 1969 Homogeneous dilute turbulent particle-laden water flows. PhD thesis, The University of Michigan.
- PARTHASARATHY, R. N. & FASTER, G. M. 1967 Structure of particle-laden turbulent water jets in still water. *Ind. J. Multiphase Flow* **13**, 699-716.
- PARTHASARATHY, R. N. & FASTER, G. M. 1980 Turbulence modulation in homogeneous dilute particle-laden flows. *J. Fluid Mech.* **220**, 485-514.
- POHRT, A., BERGMIST, A. & GUNESBERG, G. 1986 Modelling and predicting turbulence fields and dispersion of discrete particles transported by turbulent flows. *Int. J. Multiphase Flow* **12**, 537-561.
- PISSEY, I. M. & NOR, A. 1978 On the motion of suspended particles in stationary homogeneous turbulence. *J. Fluid Mech.* **84**, 193-206.
- PITTSAM, A. 1961 Integrable form of drag coefficient. *Am. Rocket Soc. J.* **31**, 1467-1468.
- REEKS, M. W. 1977 On the dispersion of small particles suspended in an isotropic turbulent fluid. *J. Fluid Mech.* **83**, 529-546.
- REEKS, M. W. 1980 Eulerian direct interaction applied to the statistical motion of particles in a turbulent fluid. *J. Fluid Mech.* **97**, 569-586.
- SAWYER, R. L. & HINCH, J. C. R. 1986 Effects of turbulence structure, molecular diffusion and source size on scalar fluctuations in homogeneous turbulence. *J. Fluid Mech.* **165**, 373-400.
- SNYDER, W. H. & LAUREN, J. L. 1971 Some measurements of particle velocity auto-correlation functions in a turbulent flow. *J. Fluid Mech.* **48**, 41-71.
- VAN DER HOF, H. 1971 Accelerating sphere wake interaction. *HTA J.* **9**, 2087-2089.
- WELLS, M. R. & STOKES, D. E. 1983 The effects of crossing trajectories on the dispersion of particles in turbulent flow. *J. Fluid Mech.* **136**, 31-62.
- YUEN, M. J. 1959 Physical considerations on heavy particle diffusion. *Adv. Geophysics* **6**, 185-191.

Appendix E: Mizukami (1992)

PARTICLE-GENERATED TURBULENCE IN HOMOGENEOUS DILUTE DISPERSED FLOWS

M. MIZUKAMI,† R. N. PARTHASARATHY, and G. M. FAETH

Department of Aerospace Engineering, University of Michigan, Ann Arbor, MI 48109-2140, U.S.A.

(Received 6 June 1991; in revised form 15 December 1991)

Abstract—Homogeneous turbulence generated by uniform fluxes of round glass beads (0.5–1.0 and 2.0 mm dia) falling through stagnant (in the mean) air was studied for particle Reynolds numbers in the range 100–400 and particle volume fractions <0.004%. Moments, probability density functions, spatial correlations and temporal spectra of air velocity fluctuations were measured using two-point phase-discriminating laser velocimetry. Predictions based on a simplified stochastic analysis, involving linear superposition of randomly-arriving particle velocity fields, were used to help interpret the measurements. Guided by the theory, correlations of turbulence properties were achieved for both the present particle air and earlier particle water measurements. Turbulence intensities (referenced to mean particle relative velocities) and integral scales are functions of the rate of dissipation of particle mechanical energy and particle drag properties; however, normalized probability density functions, spatial correlations and temporal spectra are largely independent of particle properties.

Key words dispersed flow, turbulence generation, homogeneous turbulence

1. INTRODUCTION

The objective of this investigation was to study the influence of turbulence/dispersed-phase interactions on the continuous-phase turbulence properties of dispersed multiphase flows. These interactions are important in either dense or homogeneous dispersed flows—homogeneous dilute dispersed flows were studied because they are more tractable for measurements. Experimental conditions involved uniform fluxes of particles falling in nearly stagnant (in the mean) air, in order to supplement earlier findings for similar particle/water flows (Parthasarathy & Faeth 1990). A simplified model of the flow, developed by Parthasarathy & Faeth (1990), was used to help interpret and correlate both sets of measurements.

Turbulence modulation and generation are two important turbulence/dispersed-phase interactions that affect continuous-phase turbulence properties in dispersed multiphase flows (Huang 1972). Turbulence modulation is an interaction between continuous- and dispersed-phase velocity fluctuations which supplements conventional damping of continuous-phase turbulence (Al Tawell & Landau 1977); it is most important when relative turbulence intensities (continuous-phase r.m.s. velocity fluctuations normalized by the mean relative velocity between the phases) are large, and the dispersed-phase is responsive to continuous-phase velocity fluctuations. This mechanism is often included in turbulence models that allow for the effects of separated flow, where it appears as a damping term when the governing equation for continuous-phase turbulence kinetic energy is derived. However, methods of modeling turbulence modulation have not been definitively assessed because the phenomenon is most important for dense dispersed flows within the Stokes drag regime where accurate measurements are problematical (Faeth 1987).

Turbulence generation involves perturbation of the continuous-phase flow by the wakes of individual dispersed-phase elements. Turbulence generation in dispersed flows is somewhat similar to the action of turbulence-generating grids; however, there are significant differences between the properties of the two flows because dispersed-phase elements are distributed throughout the flow and their arrival at any point is random. Turbulence generation is most important when velocity defects within the wakes of dispersed-phase elements are large in comparison to background continuous-phase velocity fluctuations, which requires large relative velocities between the phases

and correspondingly low relative turbulence intensities. Additionally, the effects of turbulence generation are most significant in nearly homogeneous flows where other sources of turbulence production are weak. Thus turbulence generation in practical multiphase flows, evidenced by increased anisotropy and turbulence levels in comparison to corresponding single-phase flows, has been observed in the near-axis regions of turbulent bubbly and particle-laden jets (Sun & Faeth 1986; Parthasarathy & Faeth 1987). Similar flow conditions exist within the near-injector (dense-spray) region of sprays, the spray-containing region of large liquid rocket engines, and heavy rainstorms, among others. Motivated by these applications, the present investigation concentrates on the properties of turbulence generation.

Past experimental investigations of turbulence generation have considered homogeneous dilute dispersed flows (Lance & Bataille 1982; Lance *et al.* 1980, 1985; Parthasarathy & Faeth 1990). Lance and coworkers studied homogeneous air/water bubbly flows downstream of a turbulence-generating grid. The effects of turbulence generation were observed as a progressive increase in continuous-phase turbulence levels with increasing void fractions, with the increase being most evident when relative velocities were comparable to liquid velocities. These results are valuable because most practical multiphase flows involve turbulence generation by the dispersed phase as well as other forms of turbulence production in the continuous phase. However, the results are difficult to interpret, due to the combined effects of bubble- and grid-generated turbulence.

Earlier work in this laboratory considered flows where turbulence generation was the dominant mechanism of turbulence production (Parthasarathy & Faeth 1990). The experimental conditions consisted of a uniform number fluxes of nearly monodisperse round glass beads falling at their terminal velocities in stagnant (in the mean) water. The flows were dilute (particle volume fractions <0.01%) and the effects of turbulence modulation were small (relative turbulence intensities <10%). Measurements included phase velocities and the probability density functions, temporal spectra and spatial correlations of liquid velocity fluctuations. Liquid-phase properties also were analyzed using a simplified stochastic method that involved linear superposition of randomly-arriving particle velocity fields. It was found that continuous-phase turbulence levels were largely controlled by the rate of dissipation of particle energy in the liquid. In contrast to grid-generated turbulence far from the source, where the turbulence is nearly isotropic, streamwise velocity fluctuations were nearly twice the cross-stream velocity fluctuations, which suggested a significant direct contribution of particle wakes to the observed properties of the continuous phase. The temporal spectra also supported this view: they exhibited a large range of scales even though particle Reynolds numbers were low (<10³), and they decayed at slower rates than conventional turbulence with increasing frequency. These features agreed with predictions based on superposition of the mean velocity profiles of randomly-arriving particle wakes. However, while the theory assisted interpretation of flow properties, quantitative predictions of integral scales and spatial correlations were not very satisfactory and there were convergence problems similar to those encountered when sedimentation is treated using stochastic methods (Batchelor 1972). Thus, generalization of the particle/water results to other flow conditions is questionable due to a limited range of experimental conditions and uncertainties of the theory.

The objective of the present investigation was to extend the particle/water study to particle/air flows. The primary motivation for this step is that rates of dissipation of particle energy in air are orders of magnitude larger than for particles in water at similar conditions so that effects of this important parameter can be resolved. Particle/air flows also reduce complications due to turbulent dispersion of particles because the particle response is smaller in air than in water. Other aspects of the present study are similar to Parthasarathy & Faeth (1990); in particular, particle Reynolds numbers for both studies were <10³ because this range is typical of drops in sprays and rainstorms (Faeth 1987; Humphreys 1964).

The paper begins with a description of the experimental and theoretical methods. Measured and predicted results are then considered, treating evaluation of the apparatus, velocity fluctuations, spatial correlations and temporal spectra in turn. Additional details about the experimental and theoretical methods can be found in Parthasarathy (1989) and Parthasarathy & Faeth (1990).

† Present address: *Propulsion Systems Division, NASA Lewis Research Center, Cleveland, Ohio, U.S.A.; † Institute of Hydrologic Research, University of Iowa, Iowa City, Iowa, U.S.A.

2 EXPERIMENTAL METHODS

2.1 Apparatus

Figure 1 is a sketch of the particle/air flow apparatus. The tests were conducted using nearly monodisperse spherical glass particles having nominal diameters of 0.5, 1.0 and 2.0 mm. The flow of particles was controlled by a variable-speed particle feeder, whose feed rate was calibrated by collecting particles for timed intervals. The particles were dispersed by falling through an array of six screens (0.89 mm dia and spaced 4.2 mm apart) with a 190 mm spacing between screens. The particles then fell into a windowed test chamber (410 × 335 × 910 mm), where the measurements were made. The particles were collected, with little rebound, at the bottom of the tank and removed periodically so that their maximum depth was 100 mm. Displacement velocities due to the collection of particles at the bottom of the tank were negligible, < 0.02 mm/s.

The free fall distance of the particles between the last screen and the region where measurements were made was 1200 mm, which was not sufficient for the particles to reach their terminal velocities. However, the rate of increase of particle velocities within the region of observations was small (15–35% m or 2–4% streamwise integral length scale) so that the flow was nearly homogeneous in the streamwise direction. Air velocities within the flow were small (ca. 10 mm/s); therefore, drafts and natural convection disturbances were controlled by closing all joints with tape and covering the exterior surfaces of the apparatus with styrofoam insulation (not shown in figure 1) except for small openings needed for optical access.

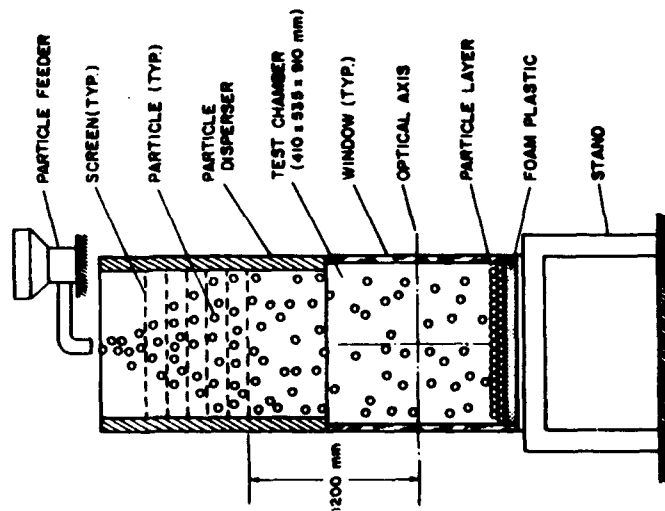


Figure 1. Sketch of homogeneous particle/air flow apparatus.

2.2 Instrumentation

Measurements involved particle number fluxes, particle velocities and continuous-phase flow properties. Particle number fluxes were measured by collecting particles in the containers for timed intervals at the bottom of the test chamber. Experimental uncertainties of these measurements were dominated by finite sampling times which were selected to keep uncertainties (95% confidence) < 10%.

Particle velocities were measured by particle tracking, which differed from Parthasarathy & Faeth (1990). This involved illuminating the central region of the test tank with a light sheet (100 mm high and 25 mm thick) from a stroboscopic light source having a flash time of 1 μ s and operating at frequencies 500–1000 Hz. The particle tracks were recorded with an open camera lens at a magnification of 0.7. Particle velocities were in the range 3000–6000 mm/s so that the light sheet essentially stopped the motion of the particles and yielded tracks having 10–20 images on the film. Velocities were found from the known flashing rate and the spacing between particle images on the film. Experimental uncertainties were dominated by sampling limitations over the size range of the particles; they are estimated to be < 5% (95% confidence).

A two-point, phase-discriminating laser velocimeter (LV), with one fixed channel at the center of the test chamber and a second channel that could be traversed in the streamwise and cross-stream directions, was used to measure air velocities. Discrimination to remove velocity signals due to particles followed Modarress *et al.* (1984), while the arrangement was identical to that of Parthasarathy & Faeth (1990) (which should be consulted for details). The air was seeded with oil drops (nominal diameter of 1 μ m using a TSI model 9306 atomizer) to provide data rates of 5–10 kHz.

The time between valid air velocity signals was small, 100–200 μ s, in comparison to Kolmogorov time scales of 11–32 ms and integral time scales of 1.8–5.8 s; therefore, the low-pass filtered analog outputs of the burst-counter signal processor were time-averaged, ignoring periods when particles were present, to find unbiased time-averaged gas velocities. Signals were collected in bursts of 16–32 K elements, for total sampling times on the order of 5 min, in order to achieve stationary values with acceptable uncertainties. One-point temporal spectra were measured over a frequency range of 10^{-1} – 10^4 Hz using several subfrequency intervals (including appropriately longer sampling times to resolve low frequencies) to provide reasonable dynamic ranges, as discussed by Parthasarathy & Faeth (1990).

Kolmogorov length scales were 0.44–0.74 mm, which were comparable to the dimensions of the measuring volumes, and the flows were homogeneous; therefore, gradient bias errors were small. Experimental uncertainties (95% confidence) were as follows: mean streamwise and cross-stream velocities, < 10% and < 40%; fluctuating streamwise and cross-stream velocities, < 15% and < 20%; spatial correlations in the streamwise and cross-stream directions, < 15% and < 30%; and streamwise and cross-stream temporal spectra, < 30% and < 40% for frequencies < 0.01 Hz and < 15% and < 25% for all other frequencies (except for the effects of step noise at the highest frequencies which will be discussed later). The present experimental uncertainties are similar to uncertainties for the particle/water flows. They are high in comparison to measurements in typical turbulent flows, however, due to the relatively low flow velocities (ca. 10 mm/s) and very high turbulence intensities (generally in excess of 100%) of the homogeneous dilute dispersed flows.

2.3 Test conditions

Properties of the 0.5, 1.0 and 2.0 mm dia particles are summarized in table 1. Particle size distributions were measured by Parthasarathy & Faeth (1990); they were roughly Gaussian and had standard deviations of approx. 10% of the nominal particle diameter. Particle velocities in the region of the measurements were independent of particle number fluxes, however, they were lower than terminal velocities due to the limited available distance between the lowest screen and the test chamber. Particle Reynolds numbers were in the range 116–780, which is comparable to the range considered during the particle/water measurements. Rates of particle acceleration in the region of the measurements were used to evaluate particle drag. Similar to the earlier particle/water

Since particle velocities in the measuring region are known, however, it is more accurate to estimate the rate of turbulence generation as the rate of loss of potential energy of the particles as they fall through the bath, minus their rate of increase of kinetic energy, as follows:

$$\epsilon = n\pi^2 d^3 g (\rho_p - \rho) - \rho_p U dU/dx / (6\rho) \quad (6)$$

where g is the acceleration of gravity, ρ_p and ρ are the particle and air densities and x is distance in the vertical (streamwise) direction. Due to the much lower density of air than water, rates of dissipation for the particle/air flows in table 2 are 10^3 – 10^4 times larger than the earlier particle/water experiments. This was the main reason for the present interest in the particle/air flows because ϵ tends to dominate the flow properties.

The Kolmogorov length, $l_k = (\nu^3/\epsilon)^{1/4}$, time, $t_k = (\nu/\epsilon)^{1/2}$, and velocity $u_k = (\nu\epsilon)^{1/4}$, scales also appear in table 2. The Kolmogorov length scales are comparable to the LV measuring volume and are somewhat smaller than the particle diameters. Measured air streamwise and cross-stream velocity fluctuations, $(\bar{u}^2)^{1/2}$ and $(\bar{v}^2)^{1/2}$, are comparable to the Kolmogorov velocity scales although u_k changes at a lower rate as ϵ is changed (similar to the particle/water flows, velocity fluctuations are proportional to $\epsilon^{1/3}$, while u_k is proportional to $\epsilon^{1/4}$). Mean velocities in the streamwise and cross-stream directions, \bar{u} and \bar{v} , are comparable to velocity fluctuations. This behavior is similar to the particle/water experiments and is due to bulk motions caused by reduced particle fluxes near the surfaces of the particle distribution system and the walls of the test chamber. These mean motions preclude measurements of true temporal spectra at all but the lowest particle loadings, where mean velocities are relatively small, but they do not affect the other measurements. Measured integral length scales, based on two-point correlations of streamwise velocity fluctuations in the streamwise and cross-stream directions, L_{11} and L_{22} , are roughly twice those measured during the particle/water experiments. However, these length scales are still an order of magnitude smaller than the corresponding dimensions of the test chamber so that the surfaces of the apparatus has little effect on the continuous-phase turbulence properties. Temporal integral scales of velocity fluctuations in the streamwise and cross-stream directions, T_1 and T_2 , are roughly two orders of magnitude smaller than sampling times so that the large-scale features of the flow are easily resolved.

In particle-laden flows, dissipation of turbulence consists of conventional dissipation by the continuous phase and turbulence modulation, i.e. direct dissipation by interactions between particle and continuous-phase velocity fluctuations. Parthasarathy & Faeth (1990) show that the fraction of dissipation due to turbulence modulation is proportional to \bar{D}^2/U^2 , where \bar{D}^2 is the variance of the relative velocity between the phases. As noted earlier, particle velocity fluctuations were small for the present conditions so that $\bar{D}^2 \sim \bar{u}^2$ and the turbulence modulation portion of dissipation is proportional to the square of the relative turbulence intensity. For the present particle/air test conditions, the relative turbulence intensities were in the range 10^{-1} – 10^0 so that the effects of turbulence modulation were small, i.e. dissipation primarily occurred by processes within the continuous phase, similar to single-phase turbulent flows.

3. THEORETICAL METHODS

3.1. Velocity fluctuations

The simplified analysis described by Parthasarathy & Faeth (1990) was used to help interpret and correlate the measurements. A stochastic method is used that explicitly considers the effects of individual particle flow fields, analogous to the approach of Batchelor (1972) for sedimentation processes. The major assumptions of the analysis are as follows: the flows are statistically stationary with uniform particle fluxes and constant continuous-phase properties; particle arrival times at an increment of area satisfy Poisson statistics, i.e. they are independent of other particle arrival times (Rice 1954); the flows are infinite in extent because the measurements were relatively independent of test chamber volume (Parthasarathy & Faeth 1990); the flows are dilute so that the probability of a test point being within a particle is negligibly small; similarly, the contribution of flow properties immediately around a particle is ignored because it is small (<10%) in comparison to the contributions of particle wakes due to much

Table 1. Particle properties

	0.5	1.0	2.0
Nominal diameter (mm)	0.043	0.083	0.17
Diameter standard deviation (mm)	3360	4970	5640
Relative velocity (mm/s)	116	344	780
Reynolds number	1.03	0.64	0.47
Drag coefficient	0.18	0.28	0.48
Wake momentum diameter (mm)	0.18	0.28	0.48
Round glass beads, of density 2450 kg/m ³ , falling in stagnant air at 298 ± 2 K. Air properties: density = 1.17 kg/m ³ , kinematic viscosity = 15.7 × 10 ⁻⁶ m ² /s.			

measurements, drag coefficients agreed within 15% of estimates based on the standard drag coefficient, C_D , for spheres (Putnam 1961):

$$C_D = 24(1 + Re^{1/2})/Re \quad (1)$$

where the particle Reynolds number is defined as

$$Re = U'd/\nu \quad (2)$$

and U' is the local mean relative velocity, d is the nominal particle diameter and ν is the kinematic viscosity of air. These conditions yield wake momentum diameters, θ , defined as

$$\theta = (C_D d^2/8)^{1/2} \quad (3)$$

in the range 0.18–0.48 mm.

A range of particle number fluxes, n , for each particle size was considered for measurements of velocity fluctuations. The extremes of these conditions and a typical mid-range condition are summarized in table 2. Mean particle spacings, l_p , were found assuming that the particles were falling randomly with a uniform particle number flux and relative velocity, as follows:

$$l_p = (U'n)^{-1/2} \quad (4)$$

The resulting particle spacings were in the range 31–218 mm, or 62–116 particle diameters, yielding particle volume fractions $< 0.0004\%$.

Particle velocity fluctuations could not be measured accurately, however, estimates indicated that they were negligible due to modest air velocity fluctuations and poor particle response to air motion. Based on the particle/water study, the particle dispersing system did not introduce significant particle rotation. For such conditions, the rate of dissipation of turbulence kinetic energy within the measuring region, ϵ , can be equated to the rate of generation of turbulence by particles. The rate of generation of turbulence is equal to the rate of loss of particle mechanical energy as they fall through the bath, i.e.

$$\epsilon = n\pi^2 d^2 C_D U^2/8 \quad (5)$$

Table 2. Summary of test condition*

	$d = 0.55$ mm				$d = 1.0$ mm				$d = 2.0$ mm			
	Loading	Low	Medium	High	Low	Medium	High	Low	Medium	High	Low	High
n (particles/m ³)	174	58.4	110.8	3.7	9.2	20.9	0.54	1.10	3.30	119.6	172.5	119.6
l_p (mm)	57.8	39.3	31.2	110.4	81.5	62.0	218.0	133.0	98.000	98.000	133.0	98.000
θ (mm)	20.400	64.900	26.300	65.300	148.300	16.300	0.74	0.62	0.47	0.47	0.62	0.47
l_k (mm)	0.70	0.52	0.44	0.65	0.52	0.42	0.74	0.62	0.47	0.47	0.62	0.47
u_k (mm/s)	29	16	11	25	16	11	32	23	13	13	23	13
\bar{u} (mm/s)	24	32	39	28	32	40	11.8	13.0	22.6	22.6	13.0	22.6
$(\bar{u}^2)^{1/2}$ (mm/s)	8.6	20.4	—	9.7	17.2	29.0	11.8	13.0	22.6	22.6	13.0	22.6
$(\bar{v}^2)^{1/2}$ (mm/s)	8.8	13.5	18.5	2.4	6.0	12.1	8.4	7.9	13.0	13.0	7.9	13.0
d (mm)	6.4	55.4	—	0.5	22.6	69.4	1.5	1.2	47.9	47.9	1.2	47.9
\bar{u} (mm/s)	2.8	8.6	8.9	0.9	2.6	6.4	1.7	1.1	2.8	2.8	1.1	2.8
L_{11} (mm)	117	98	—	123	97	—	143	176	—	—	143	176
L_{22} (mm)	48.1	38.2	—	12.5	20.0	—	24.9	23.2	—	—	24.9	23.2
T_1 (s)	1.8	—	—	2.6	—	—	5.8	—	—	—	5.8	—
T_2 (s)	3.2	—	—	3.4	—	—	—	—	—	—	—	—

*Particle volume fractions $< 0.0004\%$, direct dissipation by particles $< 1\%$.

larger wake volumes (Parthasarathy & Faeth 1990); and because the equations of motion are linear for asymptotic wakes, flow properties are taken to be the result of a linear superposition of particle flow fields that have reached the point of observation. The last assumption implies that the flow is sufficiently dilute so that distortion of each wake by other wakes can be ignored. This is questionable because velocity fluctuations were always present at the measuring volume, however, the approach was still pursued because it was helpful for the particle/water flows (Parthasarathy & Faeth 1990).

Summing flow properties under these assumptions is an extension of methods used to analyze random noise (Rice 1954). Let the point of observation be the origin of a cylindrical coordinate system with x being the streamwise direction and r and ϕ the radial and azimuthal coordinates. Considering the potential effects of wake unsteadiness or turbulence, the arrival of a particle at $x=0$, r , ϕ and time $t=0$ can produce effects $g(r, \phi, t)$ and $g'(r, \phi, t)$ at the point of observation due to the mean and turbulent wake properties. Following Rice (1954), Campbell's theorem can be extended to treat random arrivals of particles over a plane as a summation of effects of individual particles (Parthasarathy & Faeth 1990). This yields the time-averaged effect

$$\bar{G} = n^{-1} \int_{-\infty}^{\infty} dt \int_{-\infty}^{\infty} d\phi \int_0^{\infty} g(r, \phi, t) r dr; \quad [7]$$

and the mean-squared fluctuation about the average,

$$\bar{G}^2 = n^{-1} \int_{-\infty}^{\infty} dt \int_{-\infty}^{\infty} d\phi \int_0^{\infty} [g^2(r, \phi, t) + g'(r, \phi, t)^2] r dr. \quad [8]$$

Equations [7] and [8] are for monodisperse particle flows. Under the assumption of linear superposition, however, if $\phi(d)$ is generic property for a particular particle diameter, then the mean value of ϕ becomes

$$\bar{\phi} = \int_0^{\infty} \phi(d) \text{PDF}(d) dd, \quad [9]$$

where PDF(d) is the probability density function of particle diameter.

A difficulty in applying [7]–[9] to find the present flow properties involves proper estimates of the particle effects, g and g' . In particular, particle Reynolds numbers are modest, in the range 38–80 for the combined particle/water and air measurements, and the particle wakes are within their self-generated turbulent field. There is no existing information concerning wake properties under these conditions and approximations must be made. Since wake Reynolds numbers are greater than unity in the region of interest, effects of turbulence in the asymptotic wake region cannot be ruled out (Tennekes & Lumley 1972). Therefore, integrations to find velocity fluctuations from [7]–[9] used mean velocity distributions for turbulent wakes from Tennekes & Lumley (1972) and wake turbulence properties from Uberoi & Freymuth (1970) in the integrations to find velocity fluctuations from [8] and [9], see Parthasarathy & Faeth (1990) for the specific formulas.

A second problem encountered with integrations of [7]–[9], when using effects estimated from particle wakes, is that the integrals do not converge as $r \rightarrow \infty$. A similar difficulty is encountered for Stokes flow around particles during analysis of sedimentation, however, this can be resolved based on rigorous knowledge of Stokes flow (Batchelor 1972). Since information on wake properties in the present Reynolds number regime is empirical, and is questionable for the reasons noted earlier, a similar attack on the convergence problem would be premature. Instead, the integrations are terminated at $x/d = 175$, which yields estimates of velocity fluctuations that are in reasonably good agreement with the measurements. Additionally, mean velocity defects in the wakes are comparable to levels of ambient velocity fluctuations at this location, suggesting that identifiable wake properties are lost in the background turbulent field in the region where the integrations are terminated. Finally, divergence of velocity fluctuations is relatively slow, proportional to $(x/d)^{1/2}$; therefore, the exact selection of the value of x/d where integrations are ended is not very crucial.

Using turbulent asymptotic wake properties, and terminating integrations at $x/d = 175$, yields the following expressions for the relative turbulence intensities in the streamwise and cross-stream directions (Parthasarathy & Faeth 1990):

$$(\bar{u}')^{1/2}/U = C_u [d(\theta/d)^{1/2}/U]^{1/2} \quad [10]$$

and

$$(\bar{v}')^{1/2}/U = C_v [d(\theta/d)^{1/2}/U]^{1/2}, \quad [11]$$

where $C_u = 6.84$ and $C_v = 4.63$. Using $C_u = C_v/2 = 3.42$, however, provides a better fit of the measurements, as will be discussed later. The parameter $d(\theta/d)^{1/2}/U$ on the right-hand sides (r.h.s.) of [10] and [11] appears later and will be called the dissipation factor for convenience.

3.2. Correlations and spectra

Expressions for correlations and spectra from the simplified theory can be found in Parthasarathy & Faeth (1990). However, while the theory yielded reasonable estimates of velocity fluctuations, predictions of two-point spatial correlations and integral length scales were not very satisfactory. This was attributed to uncertainties about wake properties within the Reynolds number range and ambient turbulence levels of the present dispersed flow. In particular, the ambient flow was shown to deflect and distort the trajectory of the wake axis, which is likely to have a significant effect on spatial correlations and integral scales even though velocity scales might be influenced only to a modest degree. In view of these observations, an alternative empirical approach was used to treat correlations, spectra and integral scales. First of all, a direct result of the simplified theory (which agrees with experimental observations), is that correlation coefficients and normalized spectra should be independent of properties like n' and ϵ . Additionally, particle size and Reynolds number did not have a significant effect on correlations and spectra so that assuming universal forms of these functions (determined by the measurements) seems reasonable. As a result, only generalized relationships for integral scales must be found.

Spatial integral scales are assumed to be proportional to dissipation length scales represented in the usual manner, i.e. $\sim k^{-1/2} \epsilon$, based on dimensional considerations, where k is the turbulence kinetic energy. For the present dispersed flows, streamwise and cross-stream velocity fluctuations scale in the same manner from [10] and [11], orthogonal cross-stream velocity fluctuations are the same because the flows are homogeneous and no change in the degree of anisotropy of the flows was observed over the test range. This implies that integral scales, L_u and L_v , should vary in the following manner:

$$L_{u,v}/U^3 = C_{u,v} [d(\theta/d)^{1/2}/U]^{1/2}, \quad [12]$$

where $i = u$ or v . The coefficients of proportionality, $C_{u,v}$, are found by fitting the particle/water and air measurements. Additionally, the measurements do not confirm the $3/2$ power of the dissipation factor on the r.h.s. of [12] so this power was considered to be an empirical parameter as well.

Temporal integral scales are correlated by assuming that they were related to spatial integral scales and velocity fluctuations, i.e. $T_i \sim L_{u,v}/(\bar{u}')^{1/2}$ based on dimensional considerations, where $i = u$ or v . Then, the expressions for the $L_{u,v}$ and $(\bar{u}')^{1/2}$ from [10] and [12] yield the following correlating expressions for the temporal integral scales:

$$T_{i,v}/U^3 = C_{Ti} [d(\theta/d)^{1/2}/U]^{1/2}, \quad [13]$$

where C_{Ti} is an empirical coefficient and $i = u$ or v . The C_{Ti} are found by correlating the measurements. Additionally, the measurements yield a power other than unity for the dissipation factor appearing on the r.h.s. of [13], as discussed later.

4. RESULTS AND DISCUSSION

4.1. Evaluation of apparatus

Apparatus evaluation during the particle/water study had shown that the apparatus was sufficiently large that wall effects had little influence on flow properties, e.g. reducing the test

chamber volume by a factor of 32 had negligible effect on the measurements (Parthasarathy & Faeth 1990). Thus, the present apparatus evaluation concentrated on establishing whether the flow was homogeneous because changes had been made in the particle distribution system.

The uniformity of particle number fluxes was tested by measuring the distribution of n^* over the bottom of the chamber. Except for the region within 50 mm of the walls of the test chamber, the standard deviations of particle number fluxes at various positions were < 6% of the mean feed rate. This value was within experimental uncertainties so that n^* was adequately uniform within the region of the present measurements. The spatial variation of r.m.s. streamwise velocity fluctuations was measured over the central portion of the test chamber (± 120 mm in the cross-stream direction and ± 180 mm in the streamwise direction). The mean variations of velocity fluctuations over this region, from point-to-point and from test-to-test, were the same (< 10%). Thus, the velocity field within the region of the measurements also was homogeneous within experimental uncertainties.

4.2. Velocity fluctuations

The probability density functions of velocity fluctuations were Gaussian, similar to the particle/water observations (Parthasarathy & Faeth 1990); therefore, only the moments of the distribution are considered in the following. Measured relative turbulence intensities in the streamwise and cross-stream directions for both the particle-air and water tests are illustrated in figure 2. The measurements are plotted according to the predictions of [10] and [11] with predictions based on the "best fit" results ($C_s = 6.84$ and $C_v = C_s/2$) also shown on the plots.

Several properties of the measured velocity fluctuations in figure 2 agree with predictions and suggest that the wakes of individual particles make a significant contribution to continuous-phase properties. First of all, the degree of anisotropy is roughly 2, which is more representative of turbulent shear flows like particle wakes than the isotropic turbulence observed far from turbulence-generating grids (Hinze 1975). Next, for a given particle size and ambient fluid,

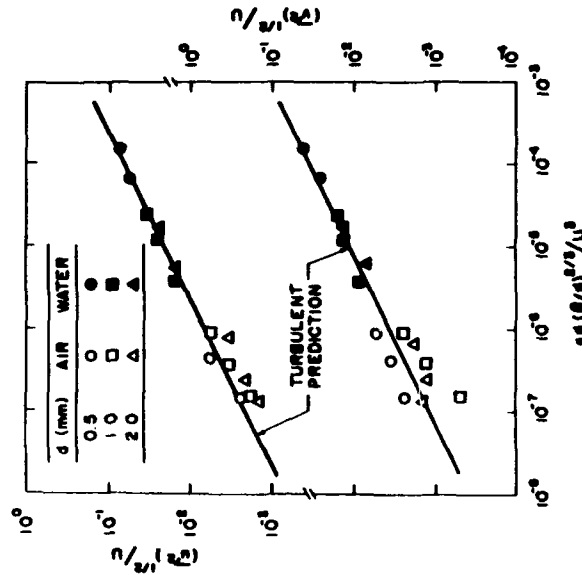


Figure 2. Streamwise and cross-stream r.m.s. velocity fluctuations.

velocity fluctuations are proportional to $d^{1/3}$, and thus $d^{1/3}$ through [5] and [6] which agree with theoretical predictions based on the summation of individual particle wake properties from [8]. Finally, the relative turbulence intensities correlate quite well as functions of the dissipation factor. In particular, the streamwise relative turbulence intensities agree with predictions based on turbulent wake properties for a reasonable integration limit $x/d = 175$, as discussed earlier. The corresponding predictions of cross-stream relative turbulence intensity are not as satisfactory, however, yielding an anisotropy of 1.5 rather than the measured value of 2.

The range of the correlations of relative turbulence intensities illustrated in figure 2 is relatively broad: relative turbulence intensities of 10^{-1} – 10^{-1} , dissipation factors of 10^{-1} – 10^{-1} and particle Reynolds numbers of 38–780. Applying the correlations outside the range of the measurements, however, is questionable. First of all, conditions at higher relative turbulence intensities involve greater degrees of turbulence modulation than present test conditions so that increased dissipation by direct interaction between the particles and the continuous-phase turbulence might modify flow properties. Next, lower values of the dissipation factor than the present test range imply low levels of relative turbulence intensities, tending to reduce distortion and mixing rates of particle wakes by the ambient flow, with corresponding changes of continuous-phase turbulence properties. Finally, particle Reynolds numbers outside the present range should also modify wake properties. Lower Reynolds numbers approach sedimentation conditions that involve greater effects of the flow field around the particle in comparison to the wakes, and might better be treated using the approach of Batchelor (1972). Higher Reynolds numbers would yield more fully developed turbulent wakes, closer to the measurements of Uberoi & Freymuth (1970), and modify continuous-phase turbulence properties accordingly.

4.3. Spatial correlations

Measured two-point correlation coefficients of streamwise velocity fluctuations in the cross-stream and streamwise directions are illustrated in figures 3 and 4 for both the particle/air and water flows. In each case, the measurements are plotted as a function of streamwise or cross-stream distance, x and y , normalized by the corresponding integral length scale. The measurements are

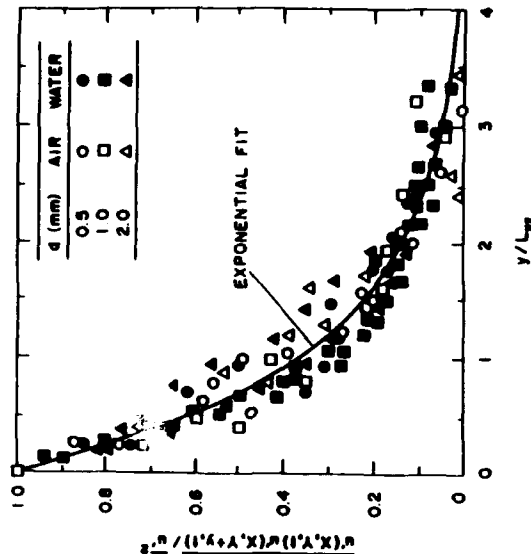


Figure 3. Spatial correlations of streamwise velocity fluctuations in the cross-stream direction for low and medium loadings.

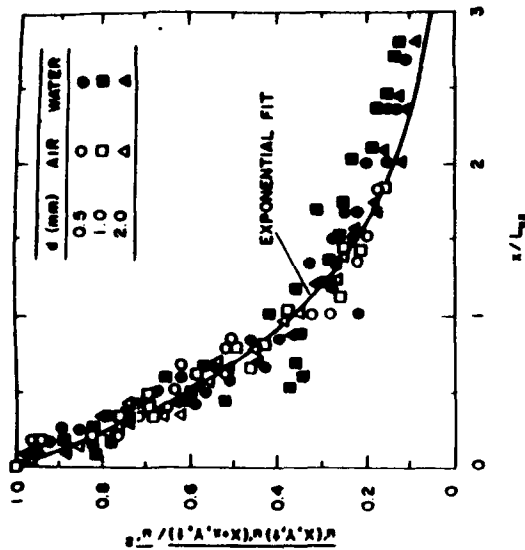


Figure 4 Spatial correlation of streamwise velocity fluctuations in the streamwise direction for low and medium loadings

identified only according to particle size and continuous-phase fluid because particle number fluxes did not noticeably affect the correlations. Results only are shown for a single displacement direction, however, the correlations were symmetric within experimental uncertainties.

Ratios of Kolmogorov to integral length scales for the present dispersed flows are < 0.03 , and the Kolmogorov length scales are somewhat smaller than the LV measuring volumes; therefore, small-scale features near the origin are not captured by the results illustrated in figures 3 and 4. Consistent with theory, the variation of correlation coefficients with normalized distance is independent of dissipation rate and the ambient fluid. The correlations are also independent of particle size. As noted earlier, predictions of correlations based on the velocity profiles of wakes were not very satisfactory, probably due to increased mixing rates and distortion of the wakes by continuous-phase turbulence. However, simple exponential functions, $\exp(-x/L_w)$ and $\exp(-x/L_{w,1})$, are seen to provide reasonably good fits of the somewhat scattered data. An exception involves large separation distances for the correlation in the streamwise direction, where measured values are consistently higher than the exponential fits. Similar long tails of correlations in the streamwise direction were found from the predictions even though the predicted shapes of the correlations were not very satisfactory (Parthasarathy & Faezi 1990). This suggests that the streamwise tails of the correlations are caused by the relatively large aspect ratios of wakes, analogous to the observed large levels of anisotropy.

Measured integral length scales in the streamwise and cross-stream directions for both the particle air and water flows, are illustrated in figure 5. The dimensionless length scales are plotted as a function of the dissipation factor, as suggested by [12]. The following empirical fits of the measurements also are shown on the plots:

$$L_w \epsilon / U^3 = C_w [\epsilon d(\theta) / U^3]^{1/3} \quad [14]$$

where $\epsilon = \gamma$ and x and $C_w = 1.4$ and $C_{w,1} = 5.4$. Equations [14] provide a reasonable fit of the integral length scale measurements. The main exception involves L_w for the present particle/air measurements, where there is significant scatter about the fitted curve. However, these conditions also

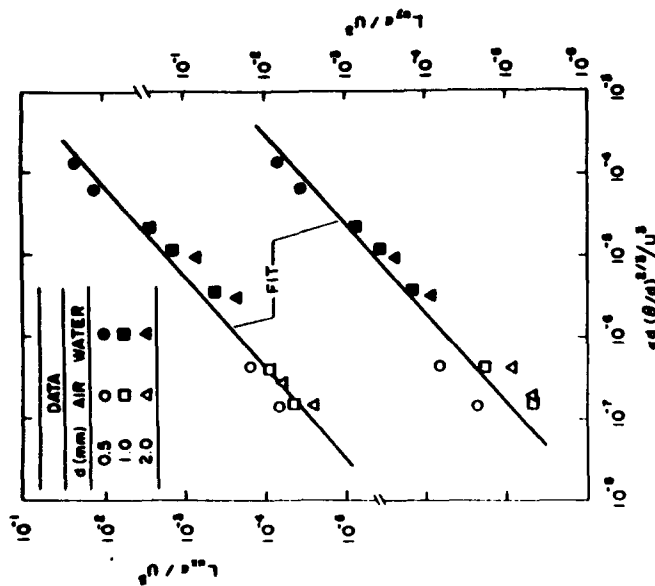


Figure 5 Streamwise and cross-stream spatial integral scales

exhibit relatively large scatter for $(\epsilon^{-1/3})^{1/3}$ in figure 2, so that measurement difficulties due to the smaller value of cross-stream than streamwise velocity fluctuations may be the source of the problem. Additionally, some systematic effects of particle size can be seen, with results for the smallest and largest particles tending to be consistently above and below the fitted line, respectively. However, the degree of these variations is not significant in comparison to the experimental uncertainties of the measurements.

An interesting feature of the measurements in figure 5 is that the dimensionless length scales increase according to the 0.9 power of the dissipation factor. This is substantially lower than the 3/2 power estimate of [12], which was based on the correspondence between integral and dissipation length scales. An explanation of the reduced effect of the dissipation factor on integral length scales is that high values of the dissipation factor imply large relative turbulence intensities within the flow (see figure 2). This tends to increase mixing rates and distortion of the wakes, and reduces the streamwise distance to the point where the velocity defect within the wakes becomes comparable to ambient velocity fluctuations. These effects should tend to reduce integral length scales, with corresponding reductions in the rate of increase of the length scales with increasing dissipation factor.

The integral length scales exhibit significant anisotropy, with $L_w/L_{w,1}$ roughly 3.9 over the range of the measurements, which is typical of shear flows like wakes (Hinze 1975). Additionally, the fitted correlations for the length scales of [14] have a relatively weak dependence on ϵ and U . The particle property dependence is roughly proportional to $dC_p^{1/3}$, which has not been varied to a great degree over the experiments (only a standard deviation of roughly one-third from the mean value of this parameter). This accounts for the modest changes of integral length scales over the present range of test conditions.

The relatively large range of length scales of the continuous phase, in spite of relatively low particle Reynolds numbers, is an interesting feature of the present flows (Parthasarathy & Faeth 1990). This can be quantified from [14] and the expression for the Kolmogorov length scale, as follows:

$$L_{\eta}/l_p = C_{\eta}(U^3/\nu)^{1/4}[d(\theta/d)^{1/2}]^{1/4}U^{1/8} \quad (15)$$

For both the particle/air and water flows, L_{η}/l_p is in the range 150–300, with L_{η}/l_p proportionately smaller according to the integral length scale anisotropy ratio. This relatively large range of length scales, in spite of low particle and wake Reynolds numbers, is caused by the contribution of mean velocities in particle wakes to flow properties because particle arrivals are random. Equation [15] implies that the length scale ratio increases with increasing U , ϵ and d ; however, the rates of increase are relatively weak so that variations of L_{η}/l_p are not large over the range of the particle/air and water experiments.

4.4. Temporal spectra

Measured temporal power spectral densities of streamwise and cross-stream velocity fluctuations, $E_u(f)$ and $E_v(f)$, are plotted as a function of frequency, f , in figures 6 and 7. The spectra and the frequencies have been normalized by the corresponding velocity fluctuations and temporal integral scales. The measurements are for particle air flows and are limited to the lowest loadings for each particle size so that effects of mean velocities are small. Conditions at the onset of step noise due to the sample-and-hold signals of the LV processor are marked on the plots, based on estimates from Adrian & Yao (1987); measurements at higher frequencies should be ignored. Predicted spectra, ignoring contributions of wake turbulence that primarily appear beyond the step-noise limit, also are shown on the plots. Similar results for the particle/water flows can be found in Parthasarathy & Faeth (1990); however, measurements and predictions for the particle/water and air flows are nearly the same.

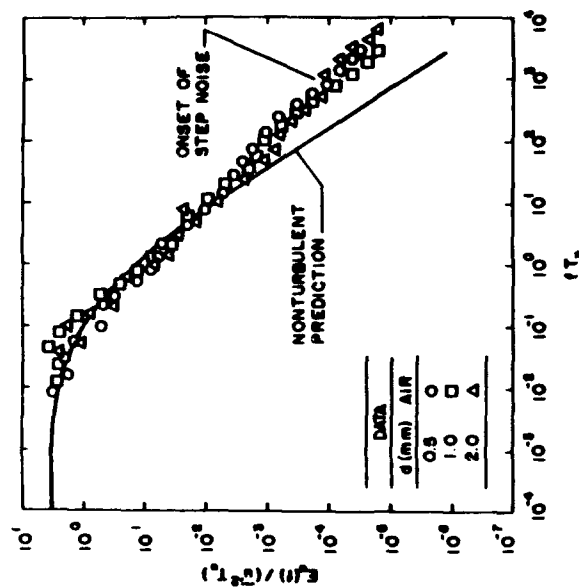


Figure 6. Temporal power spectral densities of streamwise velocity fluctuations.

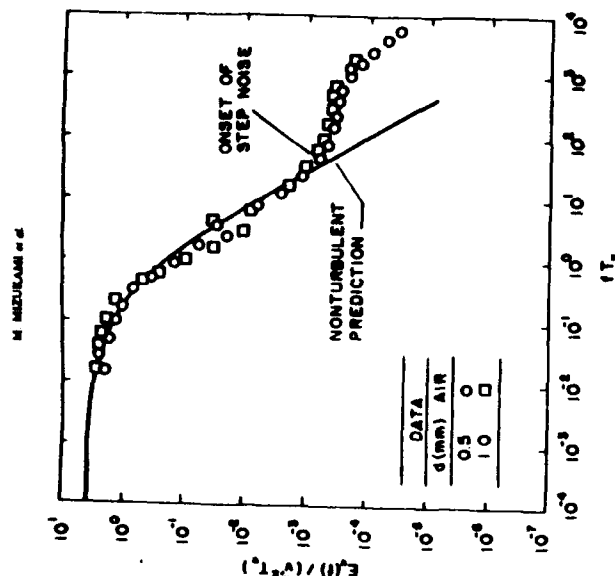


Figure 7. Temporal power spectra of cross-stream velocity fluctuations.

Effects of particle size and loading on the measured temporal spectra are small in comparison to experimental uncertainties. Dimensionless frequencies corresponding to the Kolmogorov microscale regime— $f T_c = T_c/l_p$ and $f T_c = T_c/l_p$ —are in the range 60–180; unfortunately, measurements are not available in this region due to the intrusion of step noise. The spectra decay for dimensionless frequencies in the range 10^{-2} – 10^0 . As noted earlier, the relatively large range of time scales for low wake Reynolds numbers is probably due to contributions from mean velocities in particle wakes. This view is supported by the properties of the inertial-like regions and spectral decay. Rather than decaying according to $f^{-1.5}$, typical of conventional turbulence, E_u decays according to $f^{-1.1}$ and E_v according to $f^{-1.5}$. The predictions based on mean velocity profiles in turbulent wakes, illustrated in figures 6 and 7, agree quite well with these trends. Even use of mean velocity profiles for laminar wakes yields similar behavior (Parthasarathy & Faeth 1990). This lack of sensitivity to the shape of mean velocity profiles in the wakes suggests that effects of distortion of the wakes by ambient turbulence may not have a large influence on normalized spectra in the range of frequencies that could be resolved. Additionally, direct contributions of wake turbulence, if present, only appear for dimensionless frequencies beyond the step noise limit, as noted earlier. Taken together, the properties of the temporal spectra appear to be largely governed by mean velocities in randomly-arriving particle wakes.

Measured temporal integral scales of streamwise and cross-stream velocity fluctuations are illustrated in figure 8 for both the particle/air and water flows. The dimensionless time scales are plotted as a function of the dissipation factor, as suggested by [13]. The following empirical fit of the measurements also is shown on the plot:

$$T_c/U^3 = C_T[d(\theta/d)^{1/2}]^{1/4}U^{1/8} \quad (16)$$

where $i = u$ and v and $C_T = C_T = 2.5$. The temporal integral scale measurements illustrated in figure 8 are limited and scattered, however, [16] provides a reasonable fit of the data. In this case, no particular trend with respect to particle size is observed. Similar to the correlation of length scales, the power of the dissipation factor is smaller than estimates based on the correspondence

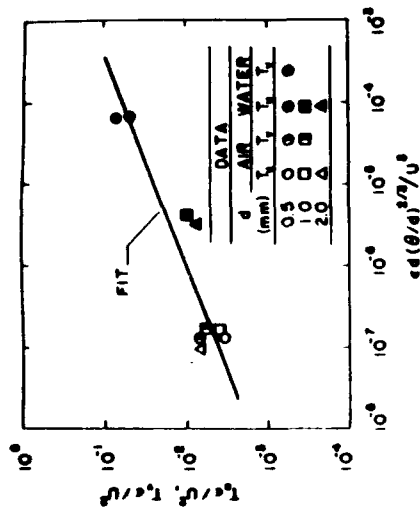


Figure 8. Temporal integral scales of streamwise and cross-stream velocity fluctuations.

between integral and dissipation length scales: 0.4 in [16] as opposed to 1.0 in [13]. Reasons for this behavior are analogous to those discussed in connection with the length scales.

The ratios, T_{ϵ}/τ_k and T_{ϵ}/τ_k were discussed earlier. Based on [16], and the expression for the Kolmogorov time scale, the functional forms of these ratios are as follows:

$$T_{\epsilon}/\tau_k = C_1 (U^3/\epsilon)^{1/3} \tau_k (\theta/d)^{2/3} / U^3 \quad (17)$$

Similar to the length scale ratios of [15], the time scale ratio increases with U , ϵ and d , but the rates of increase are relatively weak so that the variation of T_{ϵ}/τ_k is not large over the range of the particle/air and water experiments.

5. CONCLUSIONS

The present investigation considered the properties of particle-generated turbulence in the continuous phase of homogeneous dilute particle-laden flows. The specific configurations involved nearly monodisperse glass spheres falling in stagnant air, to supplement earlier findings for particles falling in stagnant water. The combined data base involved the following conditions: particle Reynolds numbers of 38–780; particle number fluxes of 0.54–110.8 kpart/m² s; mean particle spacings of 8.2–218 mm; rates of dissipation of 27–148,300 mm²/s²; particle volume fractions <0.01%; and relative turbulence intensities of 10^{-3} – 10^{-1} . The major observations and conclusions of the study are as follows:

- Relative turbulence intensities and integral scales could be correlated as functions of the dissipation factor $[\epsilon d (\theta/d)^{2/3} / U^3]$. However, use of these correlations outside the present test range is not recommended: higher relative turbulence intensities would involve significant effects of turbulence modulation; lower relative turbulence intensities would reduce turbulent distortion of particle wakes; and particle wake properties vary with Reynolds number—all potentially modifying flow properties from the present findings.
- A number of features of particle-generated turbulence are similar to other homogeneous turbulent flows; in particular, the probability density functions of velocity fluctuations approximate Gaussian functions, and the large-scale features of spatial correlation coefficients and normalized temporal spectra are relatively independent of flow conditions when plotted in terms of normalized distances and frequencies.

(c) However, a number of features of particle-generated turbulence are distinctly different from other turbulent flows, probably due to contributions from mean velocities in randomly-arriving particle wakes; for example, the degree of anisotropy of the flow is usually large $[(\bar{u}^2)^{1/2} = 2(\bar{v}^2)^{1/2}]$; length scales correlate with wake properties and are essentially independent of the mean spacing between particles, and streamwise temporal spectra decay proportional to $f^{-1.1}$ rather than $f^{-1.3}$.

(d) A simplified model, based on linear superposition of randomly-arriving particle velocity fields, was helpful for interpreting and correlating many features of the flow. However, more information on the character of particle wakes at modest Reynolds numbers in turbulent environments is needed for quantitative assessment of this approach and a better understanding of the mechanisms controlling continuous-phase turbulence properties in these flows.

Acknowledgments—This investigation was supported by the Air Force Office of Scientific Research, Grant No. AFOSR-89-0516, under the technical management of J. M. Tishkoff. The U.S. Government is authorized to reproduce and distribute copies of this paper for governmental purposes notwithstanding any copyright notation thereon.

REFERENCES

- ADRIAN, R. J. & YAO, C. S. 1987 Power spectra of fluid velocities measured by laser Doppler velocimetry. *Exps Fluids* **5**, 17–28.
- AL TAWEL, A. M. & LANDAU, J. 1977 Turbulence modulation in two-phase jets. *Int. J. Multiphase Flow* **3**, 341–351.
- BATCHELOR, G. K. 1972 Sedimentation in a dilute dispersion of spheres. *J. Fluid Mech.* **52**, 245–268.
- FARH, G. M. 1987 Mixing, transport and combustion in sprays. *Prog. Energy Combust Sci* **13**, 293–345.
- HINZE, J. O. 1972 Turbulent fluid and particle interaction. *Prog. Heat Mass Transfer* **6**, 433–452.
- HINZE, J. O. 1975 *Turbulence*, pp. 556–565. McGraw-Hill, New York.
- HUMPHREYS, W. J. 1964 *Physics of the Air*, pp. 279–281. Dover, New York.
- LANCE, M. & BATAILLE, J. 1983 Turbulence in the liquid phase of a bubbly air–water flow. *Advances in Two-phase Flow & Heat Transfer*, Vol. 1, pp. 403–427. Martinus Nijhoff, The Hague.
- LANCE, M., MARIE, J. L., CHARNAY, G. & BATAILLE, J. 1980 Turbulence structure of occurrent air–water bubbly flow. NUREG/CP-0014, Vol. 2, pp. 403–427. Nuclear Regulatory Commission, Washington, DC.
- LANCE, M., MARIE, J. L. & BATAILLE, J. 1985 Homogeneous turbulence in bubbly flow. Publications FEP-29, pp. 117–124. ASME, New York.
- MODARRES, D., TAN, H. & ELCHOWASHI, S. 1984 Two-component LDA measurements in a two-phase turbulent jet. *AIChE J.* **22**, 624–630.
- PARTHASARATHY, R. N. 1989 Homogeneous dilute turbulent particle-laden water flow. Ph.D. Thesis, Univ. of Michigan, Ann Arbor.
- PARTHASARATHY, R. N. & FARH, G. M. 1987 Structure of particle-laden turbulent water jets in still water. *Int. J. Multiphase Flow* **13**, 699–716.
- PARTHASARATHY, R. N. & FARH, G. M. 1990 Turbulence modulation in homogeneous particle-laden flows; *ibid.* Turbulent dispersion of particles in self-generated homogeneous turbulence. *J. Fluid Mech.* **220**, 485–537.
- PUTNAM, A. 1961 Integrable form of droplet drag coefficient. *Am. Rocket Soc. J.* **31**, 1467–1468.
- RICE, S. O. 1954 Mathematical analysis of random noise. In *Noise and Stochastic Processes*, pp. 133–294. Dover, New York.
- SUN, T.-Y. & FARH, G. M. 1986 Structure of turbulent bubbly jets—II. Phase property profiles. *Int. J. Multiphase Flow* **12**, 115–124.
- TENNEKES, H. & LUMLEY, J. L. 1972 *A First Course in Turbulence*, pp. 113–124. MIT Press, Cambridge, MA.
- UMOTO, M. S. & FARVATH, P. 1970 Turbulent energy balance and spectra of the axisymmetric wake. *Phys. Fluids* **13**, 2205–2210.

Appendix F: Wu and Faeth (1992)

SPHERE WAKES IN STILL SURROUNDINGS

AT-INTERMEDIATE REYNOLDS NUMBERS

by

J.-S. Wu* and G. M. Faeth†
Department of Aerospace Engineering
The University of Michigan
Ann Arbor, Michigan

The wakes of spheres in a still environment were studied for sphere Reynolds numbers, Re , in the range 30-4000. The experiments consisted of towed spheres in quiescent baths of glycerin and water mixtures. Measurements included dye traces illuminated by a laser light sheet for visualization and laser velocimetry for streamwise velocities. The recirculation region on the downstream side of the sphere was stable and symmetric for $Re < 200$, stable and unsymmetric for $200 \leq Re < 280$, and unstable with vortex shedding for $Re \geq 280$. Three wake regions were identified: a fast-decay region that only was observed when vortex shedding was present, followed in succession by turbulent and laminar wake regions. Vortex shedding increased the distance to the onset of the turbulent wake region by an order of magnitude due to the presence of the fast-decay wake region. Mean velocities within the turbulent and laminar wake regions scaled according to classical similarity theories, with transition between these regions at conditions where their estimates of mean streamwise velocities along the axis were the same: this occurred at a local wake Reynolds number, $Re_w \approx 10$. Within the turbulent wake region, turbulence intensities along the axis were roughly 85% for $Re_w > 70$; however, as the onset of the laminar wake region was approached, turbulence intensities along the axis were proportional to $Re_w^{7/4}$, which is consistent with scaling proposed earlier for the final decay period of axisymmetric wakes.

* Graduate Assistant, Department of Aerospace Engineering.

† Professor, Department of Aerospace Engineering, Fellow AIAA.

Nomenclature

a	= velocity decay exponent in fast-decay wake region
C	= constant for final decay period, Eq. (11)
C_D	= drag coefficient
d	= sphere diameter
l	= characteristic wake width, Eq. (3)
l_t	= scaled characteristic wake width, Eq. (9)
r	= radial distance
R	= sphere radius
Re	= sphere Reynolds number, $d U_\infty / \nu$
Re_w	= local wake Reynolds number, $\bar{u} d / \nu$
t	= time
\bar{u}	= mean streamwise velocity
\bar{u}'	= r.m.s. streamwise velocity fluctuation
U_s	= streamwise sphere velocity
$(U_0)_t$	= velocity scale for turbulent wake region
x	= streamwise distance from center of sphere
ν	= kinematic viscosity
θ	= initial momentum thickness of wake, Eq. (1)
θ'	= wake separation angle

Subscripts

c	= centerline value
cm	= uncorrected centerline value
tr	= transition from turbulent to laminar wake
o	= virtual origin condition
∞	= ambient condition

Introduction

The flow associated with spheres has attracted attention due to numerous applications, e.g., dispersed particle-laden flows, sprays and rainstorms, among others. Recent work on the production of turbulence by dispersed phases,^{1,2} however, has shown the need for more information about the structure of sphere wakes at the intermediate sphere Reynolds numbers ($10 < Re < 10^3$) that are often encountered for drops and particles in sprays and other dispersed flows. Particularly important issues are the effects of turbulence and vortex shedding from the sphere and on wake structure, and the range of conditions where such effects are observed. Motivated by these observations, the objective of the present investigation was to measure flow properties near spheres at intermediate Reynolds numbers, with particular emphasis on properties within the wake.

Early studies of the flow associated with spheres at intermediate Reynolds numbers are discussed in the extensive series of review articles by Torobin and Gauvin,³ and references cited therein. Initial work emphasized drag and flow properties near the sphere, with later experimental and computational work along these lines reported by Pruppacher et al.,⁴ Rimon and Cheng⁵ and Roos and Willmarth.⁶ Subsequently, several studies focussed on the near wake of the sphere, including the nature of the recirculation zone behind the sphere and the characteristics of vortex shedding from this region.⁷⁻¹⁶ These results established that a recirculation zone begins to form at a Re of roughly ten, that this zone grows in size as the Re increases, and that vortex shedding from the sphere into the wake begins at roughly $Re = 300$ and continues to affect near-wake properties at higher values of Re in the intermediate Reynolds number regime. Within the intermediate Reynolds number regime, the configuration of vortices shed from the sphere involves closed-end double-helix vortex tubes unwinding from a cylindrical vortex sheet around the periphery of the sphere, giving the appearance of a vortex street passing into the sphere wake when viewed in cross-section.^{15,16} These results were obtained from flow

visualization, however, so there is little quantitative information available about the effect vortex shedding on wake properties.

Existing quantitative information about sphere wakes largely is limited to the turbulent wake, see Refs. 17-22 and references cited therein. This involves measurements in the wakes of various axisymmetric objects far enough downstream so that wake properties did not exhibit periodic behavior associated with vortex shedding and were controlled by the drag rather than the shape of the object. These measurements generally were completed for object (sphere) Reynolds numbers on the order of 10^4 or greater, with local wake Reynolds numbers on the order of 10^2 or greater. Thus, the properties of wakes for intermediate Reynolds numbers, or even whether turbulent wakes are present for such conditions, are unknown in spite of the importance of this Reynolds number range for dispersed multiphase flows.^{1,2}

The present investigation was undertaken to provide new information about the structure of the flow near and in the wakes of spheres at intermediate sphere Reynolds numbers. This included visualization of the flow near the spheres to provide information about the recirculation zone and vortex shedding into the wake, measurements of mean streamwise velocities both near the spheres and in their wakes, and measurements of r.m.s. velocity fluctuations along the flow axis with velocity measurements extending to conditions where the wakes were laminar. The experiments involved spheres towed through quiescent water and glycerol mixtures to achieve sphere Reynolds numbers in the range 30-4000. Within both the turbulent and laminar portions of the wakes, velocity measurements were compared with classical similarity correlations as well as correlations of turbulence properties in wakes,¹⁸⁻²⁷ in order to help define conditions for the transition between these regimes and the scaling of turbulence properties at intermediate wake Reynolds numbers.

The paper begins with a description of experimental methods and test conditions, and a summary of mean velocity scaling from similarity theories. Flow visualization is then used to assess experimental conditions and to identify the major features of the flow near the spheres, including conditions for the onset of vortex shedding. The paper concludes with discussion of the velocity measurements, considering flow near the spheres, along the axis and in the turbulent and laminar wake regions, in turn.

Experimental Methods

Apparatus

A sketch of the test apparatus appears in Fig. 1. The experiment involved traversing a sphere through a still liquid bath and observing flow properties at the center of the bath. The liquid bath was filled to a depth of 875 mm within a windowed tank ($415 \times 535 \times 910$ mm). The sides and bottom of the tank were covered with insulation (not shown in Fig. 1) to minimize natural convection disturbances, except for small openings where optical access was needed. The bath liquid was either water or a glycerol mixture so that a range of sphere Reynolds numbers could be considered using a sphere of fixed size and a modest range of velocities to control spatial resolution requirements and uncertainties of velocity measurements.

The test sphere was a 10 mm diameter plastic ball (polished polycarb ball, $\pm 50 \mu\text{m}$ radius tolerance, sphericity within $50 \mu\text{m}$, surface roughness less than $16 \mu\text{m}$). The sphere was mounted on a 125 μm diameter stainless steel wire which passed horizontally through its center and sealed with epoxy. The wire was mounted in tension between two struts that could be traversed down the corners of the tank. Tests with no sphere present showed that disturbances from the wire support system were negligible in comparison to background disturbances in the bath over the region where measurements were made. Additionally, the

arrangement was sufficiently rigid so that sphere vibrations during a traverse could not be detected.

The traversing system involved a counterbalanced mounting plate, which could move along a linear bearing system, to support the struts. The motion of the plate was controlled by a stepping motor driven linear positioner (Daedal, Model 008-2686 single-axis positioner). The positioner was programmed so that it accelerated to the appropriate sphere velocity (147-476 mm/s) in the first 150 mm of travel, just prior to entering the bath. The test velocity was maintained for the next 700 mm (300 mm beyond the measuring station) before decelerating to a stop at the bottom of the tank in the last 150 mm of travel. The arrangement provided test sphere velocities with an accuracy of 1%, with velocity variations within this range for the constant speed portion of the traverse.

Instrumentation

Flow Visualization

Light sheet illuminated dye traces were used to observe the recirculation region behind the sphere and the vortex shedding process, similar to past work. This was done by painting a liquid soluble dye (Higgins drawing ink no. 4085) near the forward stagnation point of the sphere and photographing the dye trace after illumination by a vertical light sheet passing through the axis of the flow. The light sheet was formed by focussing the 488 nm line of an argon-ion laser with a spherical lens to yield a waist diameter of 200 μm , and then spreading the beam with a cylindrical lens to illuminate a 300 mm section along the axis of motion. The resulting dye pattern was photographed using an SLR camera (3200 ASA black and white film) with exposure times of 1-4 ms to stop the motion of the fluid (the sphere displacement generally was less than 1 mm during the time of exposure).

Laser Velocimetry

The laser velocimeter was identical to the fixed channel arrangement used by Parthasarathy and Faeth¹ and will be described only briefly. A dual-beam forward-scatter configuration was used, based on the 488 nm line (100-200 mW) of an argon-ion laser. The measuring volume had a diameter and length of 0.1 and 1.2 mm. Directional bias and ambiguity were eliminated using a Bragg-cell frequency shifter. The bath liquid was seeded with titanium dioxide particles (2.8 μ m nominal diameter) to provide data rates in the range 0.5-2 kHz. The velocities were found from the low-pass filtered analog output of a burst-counter signal processor, using a 12 bit a/d converter operating at a constant sampling frequency (1-4 kHz). The data for each traverse were stored in a 120 k buffer memory and then transferred to a laboratory computer for processing and storage.

The laser velocimeter measuring location was fixed; therefore, the trajectory of the sphere was traversed to observe various points in the flow. The streamwise traverse was carried out by the motion of the sphere itself, with distances known from the position indicator of the linear positioner after finding the position of the measuring volume of the laser velocimeter by aligning it with the center of the sphere. Positioning accuracy in the streamwise direction was controlled primarily by uncertainties of locating the center of the sphere at the measuring volume and the time between samples, yielding an uncertainty of 0.4 mm. Crossstream traverses were carried out by moving the wire support points with a manual traversing system attached to the struts, yielding a positioning accuracy of 0.2 mm. The overall alignment was checked periodically by observing the position of the sphere relative to fixed reference points using a cathetometer.

Measurements were carried out by ensemble averaging results from 20-120 traverses at a particular radial position and sphere Reynolds number. The number of traverses was selected to control the experimental uncertainties and were large in regions

where effects of vortex shedding were important (due to large traverse-to-traverse variations of flow properties) and when r.m.s. velocity fluctuations were sought. This approach was tractable for present measurements because operation of the traversing system was computer controlled, allowing a traverse to be completed and data recorded, the sphere to be returned to its original position, and the next traverse to be initiated after bath disturbances from the sphere motion were sufficiently decayed (specified to be $\bar{u}'/U_s < 0.5\%$). Reestablishing a quiescent bath normally required a 4-8 minute separation between traverses.

Experimental uncertainties varied with sphere Reynolds number and position in the wake, with measurements in the far wake terminated when background disturbances became significant in comparison to wake velocities. For data reported here, uncertainties (95% confidence) of mean streamwise velocities were less than 13%, and those of r.m.s. stream-wise velocity fluctuations were less than 25%. All measurements were repeatable within these ranges over a period of testing of several months. These uncertainties are high in comparison to conventional laser velocimeter measurements due to the relatively low velocities and the ensemble averaging technique of the present tests.

Test Conditions

Test conditions are summarized in Table 1. A single 10 mm diameter sphere was used over a relatively narrow range of sphere velocities; therefore, Reynolds numbers mainly were varied by using either water or glycerol solutions ranging up to 81% glycerin by mass. The densities and viscosities of the test liquids were measured periodically during testing with a hydrometer and a Cannon/Fenske viscometer. The kinematic viscosities of the bath liquid varied in the range 1.02-42.0 mm²/s. Effects of bath temperature changes on kinematic viscosities were compensated by adjusting the sphere velocity to obtain the desired sphere Reynolds number.

Drag coefficients for the various sphere Reynolds numbers generally were computed from correlations due to Punam²⁸ and Kilren et al.²⁹ The one exception was $Re = 280$, which was at the onset of vortex shedding where existing drag correlations were suspect; therefore, C_D at this condition was found from the measured velocity defect in the wake. Values of the initial momentum thickness of the wakes then were computed as follows:²¹

$$\theta = (C_D d^2/8)^{1/2} \quad (1)$$

The last column in Table 1 is $(U_0)_c$, which is a velocity scale for the turbulent portion of the wake that will be considered later.

Wake Similarity

Turbulent Wake

The results of classical similarity analysis of wake properties are helpful for interpreting the measurements and identifying turbulent and laminar wake regimes. It is well known that mean velocity distributions in high Reynolds number axisymmetric turbulent wakes, far from the drag-producing object, correlate reasonably well with results of similarity analysis based on a constant eddy viscosity over the wake cross section, in spite of the crudeness of these approximations, see Uberoi and Freymuth¹⁹ and references cited therein. Based on results appearing in Tennekes and Lumley,²¹ this yields the following expression for streamwise mean velocities:¹

$$\bar{u}/U_s = 2.23 ((x-x_0)/\theta)^{-2/3} \exp(-r^2/2\theta^2) \quad (2)$$

where the characteristic width of the wake is given by

$$\theta/\theta = 0.47 ((x-x_0)/\theta)^{1/3} \quad (3)$$

and x_0 is the virtual origin of the flow. The local wake Reynolds number based on the centerline velocity and characteristic wake width then becomes:

$$Re_w = \theta \bar{u}_c/\nu = 1.048 (\theta U_s/\nu)((x-x_0)/\theta)^{1/3} \quad (4)$$

The similarity results of Eqs. (2)-(4) yield $\bar{u}_c \sim (x-x_0)^{-2/3}$, $\theta \sim (x-x_0)^{1/3}$ and $Re_w \sim (x-x_0)^{1/3}$ in fully-developed turbulent wakes far from the source — the last implying eventual transition to a laminar wake as Re_w becomes small if the surroundings are quiescent.²¹

Laminar Wake

Laminar wake regions also were observed during the experiments. Streamwise mean velocities in this region are given by classical similarity analysis, as follows:²³

$$\bar{u}/U_s = (\theta^2 U_s / 4\nu (x-x_0)) \exp(-r^2/2\theta^2) \quad (5)$$

where

$$\theta/\theta = (2\nu (x-x_0) / \theta^2 U_s)^{1/2} \quad (6)$$

From Eqs. (5) and (6), the local wake Reynolds number based on the centerline velocity and characteristic width in the laminar wake regime becomes:

$$Re_w = \theta \bar{u}_c / \nu = \theta^2 (U_s^3 / 8\nu^3 (x-x_0))^{1/2} \quad (7)$$

The mean velocity, \bar{u} , has been used in Eqs. (5)-(7) even though an average normally has no relevance for a steady laminar flow. This was done because present values of u were obtained as ensemble averages which were influenced to some extent by background disturbances in the bath due to the low velocities in the laminar wake region.

The classical similarity results of Eqs. (5)-(7) yield $\bar{u}_c \sim (x-x_0)^{-1}$, $\theta \sim (x-x_0)^{1/2}$ and $Re_w \sim (x-x_0)^{-1/2}$ in the fully developed laminar wake region. Thus, the similarity theories imply that the rates of decay of the velocity and wake Reynolds number, and the rate of growth of the width of the wake, are larger for laminar than turbulent wakes.

Results and Discussion

Flow Visualization

Flow visualization is considered during most investigations of the flow near spheres and other axisymmetric bodies at intermediate Reynolds numbers.⁷⁻¹⁶ Similar observations were made during the present investigation to verify flow behavior in the present test apparatus and to visualize the flow in wake after vortex shedding had begun.

Photographs of the light-sheet illuminated dye traces for sphere Reynolds numbers in the range 40-280 appear in Fig. 2. This range is representative of conditions where vortex shedding is not present, $Re \leq 240$, up to conditions where vortex shedding just begins, $Re \approx 280$. In the region where they overlap ($Re < 200$) present observations are very similar to those of Nakamura⁵ for freely falling spheres, except for minor effects due to different methods of introducing the dye. This suggests that the present horizontal wire support did not have a significant effect on flow properties near the sphere. For $20 \leq Re < 200$ (the former being the lowest value considered) a stable and symmetric recirculation zone is attached to the downstream side of the sphere, with the size of the recirculation zone progressively increasing as Re increases. Throughout this region, dye traces leaving the downstream end of the recirculation zone were smooth and gave little evidence of unsteady or turbulent-like behavior over the region where they could be seen. For $200 \leq Re \leq 240$, the recirculation zone still remained attached and stable, however, it generally was no longer symmetric. Additionally, the dye trace leaving the recirculation zone was still released along the axis and was only slightly more irregular than for $Re < 200$. As is evident from Fig. 2, however, behavior changed significantly at $Re = 280$ where vortex shedding began. Typical of behavior at higher Re , where effects of vortex shedding on wake properties were very significant, the recirculation zone was very unsymmetric and the dye trace leaves the recirculation zone near its edge. The properties of vortex shedding will be discussed later in more detail, based on visualizations extending farther into the wake.

A more quantitative assessment of the flow properties near the sphere for both wire mounted and freely falling spheres can be obtained from the results illustrated in Fig. 3. This is a plot of the half angle between the attachment points of the recirculation zone, θ' , as a function of sphere Reynolds number for conditions where the recirculation zone was stable and symmetric ($Re < 200$). Results for freely falling spheres from Ref. 5 are shown on the plot along with present measurements. Present measurements are in good agreement with those of Nakamura,⁵ except at $Re = 20$ where the different methods of introducing the dye probably is a factor. The earlier results of Taneda (cited in Ref. 5) also disagree with other measurements in this region because they were affected by drift of the aluminum particles he used to visualize the flow at low Re , as discussed by Nakamura.⁵

As noted earlier, the wake flow transitioned at $Re \approx 280$ so that the recirculation zone was no longer stable and vortex shedding began. This observation is in good agreement with results for freely falling spheres, suggesting small effects of the wire support on the vortex shedding process, e.g., Magarvey and MacLachy⁸ and Goldberg and Florsheim¹⁰ report $Re = 300$ and 270, respectively, for this transition for freely falling spheres.

Light-sheet illuminated dye traces, extending roughly fifteen sphere diameters into the wake, are illustrated in Fig. 4 for Re in the range 400-4000 where vortex shedding was present. While these dye traces are representative, there is significant variation from one traverse to the next due to the unsteady behavior of the vortex shedding process. Not surprisingly, increasing sphere Reynolds numbers yield dye traces having finer scaled features. Nevertheless, the large-scale back and forth distortion of the dye traces is consistent with the double helix vortex tube structure thought to represent the vortex shedding process,¹⁶ even at the highest sphere Reynolds number illustrated in Fig. 4. Additionally, the vortex-like (swirling) features seen near the outer boundary of the dye

traces (particularly at $Re = 700, 960$ and 2000) are suggestive of behavior near nodal points of the double helix structure.¹⁶ Comparing the traces near the end of the recirculation zone in the presence and absence of vortex shedding (cf. Figs 2 and 4) it is evident that vortex shedding has a significant effect on wake properties; subsequent results will show that this involves the appearance of a fast-decay wake region and delay of the onset of the turbulent wake region.

Flow Near Sphere

Measurements of complete streamwise velocity distributions near the sphere were limited to conditions where effects of vortex shedding were either weak ($Re = 280$) or absent ($Re < 280$). This was necessary because unsteady effects due to strong vortex shedding, particularly at off-axis positions, required excessive numbers of traverses to obtain statistically significant mean velocities.

Present measurements of mean streamwise velocities near the sphere are plotted as a function of radial distance in Fig. 5. Results are shown at $Re = 90, 170$ and 280 for $x/d = -1.5, -0.8, 0.75, 1.0$ and 2.0 (negative values of x/d implying planes in front of the sphere). The velocity disturbance in at $x/d = -1.5$ is relatively small, with maximum values at the axis less than 5% of the sphere velocity. At $x/d = -0.8$, however, values of \bar{u}/U_s reach 30% at the axis with the velocity disturbance extending to $r/R = 2$ due to acceleration of the flow over the front of the sphere. Effects of Re on \bar{u}/U_s are more prominent behind the sphere, with higher values of Re yielding higher values of \bar{u}/U_s near the axis. Values of \bar{u}/U_s greater than unity are observed in this region due to backflow toward the rear stagnation point of the sphere in the recirculation zone, see Fig. 2. There is a consistent trend that the maximum streamwise velocity is slightly off axis at $x/d = 0.75$, and 1.0 ; this is reasonable due to deceleration of the backflow as it approaches the rear stagnation point at $x/d = 0.5$. For $x/d \leq 1$, the flow width is roughly $r/R = 1.5$ but by $x/d = 2$ the width has

increased to roughly $r/R = 2$ as the radial growth of the wake begins; limited observations indicated that these dimensions were relatively independent of the presence or absence of vortex shedding.

Mean Velocities at Wake Axis

Streamwise mean velocities along the wake axis are illustrated in Fig. 6 for conditions where vortex shedding has a strong effect on mean velocities ($Re = 400, 960$ and 4000) and in Fig. 7 for conditions where effects of vortex shedding are either weak ($Re = 280$) or absent ($Re = 35, 60, 90$ and 170). The results are plotted as a function of x/θ , (or $(x-x_0)/\theta$ with $x_0/\theta = 1$ as described later) so that they can be related to the similarity expressions for turbulent and laminar wakes, Eqs. (2) and (5). The measurements on the plots begin relatively close to the rear stagnation point of the sphere, x/θ or $(x-x_0)/\theta$ of roughly two or x/d in the range $0.5-1.0$. The measurements are ended when wake velocities are too low in comparison to background disturbances to maintain the experimental uncertainties specified earlier.

The first feature evident from the results illustrated in Figs. 6 and 7 is the increase of velocity with increasing distance very near the sphere. This behavior is caused by stagnation of the backflow along the axis of the recirculation zone as the sphere is approached. The maximum velocity along the axis, however, is reached relatively close to the sphere, at $(x-x_0)/\theta$ of $4-6$ or $x/d = 1.4 \pm 0.2$, with the maximum tending to approach the sphere as the recirculation zone becomes smaller as Re decreases.

When vortex shedding is present, $Re \geq 280$, mean velocities along the axis initially exhibit a more rapid decay than farther into the wake (cf. Figs. 6 and 7). The rate of decay in this region tends to decrease as Re decreases toward the onset of vortex shedding. For

example, if $\bar{u}/U_s \sim x^{-a}$ in the fast-decay wake region, maximum values of a are 1.8, 1.7, 1.6 and 1.2 for $Re = 4000, 960, 400$ and 280 , respectively. Thus, the strength of the vorticity being shed from the sphere affects the enhancement of near-wake mixing rates. Velocities in the fast decay wake also exhibited large variations from one traverse to the next so that numerous traverses were required to obtain mean velocities with reasonable experimental uncertainties in this region. This behavior probably was caused by random orientation of the double helix vortex structure in the circumferential direction and variations of the phase of vortex shedding at the point where measurements were made.

The end of the fast decay wake, and regions behaving like turbulent and laminar wakes, were identified using the classical similarity expressions of Eqs. (2) and (5). It was found that laminar wake behavior was in good agreement with Eq. (5), after choosing $x_0/\theta = 1$; therefore, these correlations are entered directly for Re in the range 35-280 where laminar wakes were observed (Fig. 7). Additionally, the turbulent portions of the wakes were in fair agreement with Eq. (2) using the same value of x_0/θ when eddy shedding was absent but the plots were offset when eddy shedding was present due to the influence of the fast-decaying wake region on the virtual origin. Thus, in order to display conditions for transition between various wake regimes, with no change of virtual origin, a generalized correlation for the turbulent wake region was developed from Eqs. (2) and (3) as follows:

$$\bar{u}/U_s = (U_0)_t/U_s ((x-x_0)/\theta)^{-2/3} \exp(-x^2/2\theta^2) \quad (8)$$

where

$$\theta_t/\theta = (U_s/2(U_0)_t)^{1/2} ((x-x_0)/\theta)^{1/3} \quad (9)$$

The values of the parameter $(U_0)_t/U_s$ were selected to provide the turbulent wake fits illustrated in Figs. 6 and 7; the values used are summarized in Table 1 for each Re considered. The parameter $(U_0)_t/U_s = 2.23$ for exact agreement with Eq. (2); present measurements agree with this estimate for $Re \leq 400$, with an average value and standard

deviation of 2.2 and 0.3 over this Reynolds number range. Results at $Re = 960$ and 4000 exhibit lower values of $(U_0)_t/U_s$, near unity, which are consistent with the value of 0.9 found for the measurements of Uberoi and Freymuth¹⁹ for the turbulent wake of a sphere at $Re = 8600$. Naturally, scaling at high Re is normally handled by changing the location of the virtual origin instead of the present approach.

The results plotted in Fig. 6 indicate that the turbulent wake region is reached for $x/\theta = 200$ for $Re \geq 960$, which corresponds to x/d in the range 40-50; this is comparable to other observations of the onset of fully-developed turbulent wake properties for spheres and other blunt objects for $Re > 1000$ (which involve vortex shedding from the object).¹⁷⁻¹⁹ In contrast, when vortex shedding is absent, Fig. 7 for $Re \leq 170$, the onset of the turbulent wake region is reached at $(x-x_0)/\theta \leq 4$, which corresponds to $x/d \leq 1.7-2.5$; this is comparable to Chevray's²⁰ observation of a rapidly developing turbulent wake behind a slender spheroid at $Re = 458,000$ (based on the body diameter) for conditions where vortex shedding also is absent. Chevray²⁰ also points out that his behavior agrees with Townsend's³⁰ prediction that the self-preserving turbulent wake should develop rapidly if production of turbulence within the separation region is small, i.e., stronger turbulence production in the presence of vortex shedding both enhances mixing rates in the fast-decaying wake and causes the onset of the turbulent wake region to be deferred. Conditions at $Re = 400$ and 280 (Figs. 6 and 7) represent intermediate behavior as the onset of vortex shedding is approached; at $Re = 400$, onset of the turbulent wake region occurs near $x/\theta = 300$ or $x/d = 80$ while at $Re = 280$, onset occurs near $x/\theta = 20$ or $x/d = 5$. It is not surprising that x/d for onset of the turbulent wake becomes smaller as the onset of vortex shedding is approached; however, additional study is needed to establish that different relative rates of decay of vortices shed from the sphere and development of turbulence yield a maximum in the streamwise distance required to develop a turbulent wake structure for $Re < 10^3$.

For $Re \leq 280$, the measurements extended far enough so that a laminar wake region scaling according to Eq. (5) was reached (see Fig. 7). It is seen that the transition from turbulent to laminar wake behavior occurs where the two similarity expressions for \bar{u}_c/U_s cross: Eq. (2) for the turbulent wake because $(U_0)/U_s \approx 2.23$ for this range of Re and Eq. (5) for the laminar wake. Thus, an expression for the transition condition can be obtained by equating Eqs. (2) and (5) to yield:

$$(x-x_0)_T/\theta = 1.41 \times 10^{-3} (\theta U_s/\nu)^3 \quad (10)$$

where this expression only has been established for $Re < 400$. Substituting Eq. (10) into either Eq. (4) or Eq. (7) yields a wake Reynolds number at transition from the turbulent to laminar wake regimes of $Re_{WT} \approx 9.4$. Tennekes and Lumley²¹ note that this transition should take place for Re_{WT} on the order of unity. This is not in disagreement with present findings in view of the somewhat arbitrary selection of velocity and length scales in the definition of Re_W and the range of $(x-x_0)/\theta$ required to complete transition from turbulent to laminar wake behavior.

Turbulent Wake Region

The scaling of streamwise mean velocities along the axis in the turbulent wake region, and the agreement with the correlations of Eqs. (2) and (8), is evident from the results plotted in Figs. 6 and 7. Thus, only the radial scaling of mean streamwise velocities in the turbulent wake, and the variation of turbulence intensities along the axis, will be considered in the following.

The radial profiles of mean streamwise velocities in the turbulent wake region are illustrated in Fig. 8. In addition to present measurements, results from Uberoi and Freymuth¹⁹ for a sphere having a $Re = 8600$ and Chevray²⁰ for a slender body having a Re

$= 458,000$ (which involve conditions where vortex shedding is present and absent, respectively) are shown on the plots. Variations of the virtual origin are handled by scaling in terms of $(U_0)/U_s$ through Eqs. (8) and (9) as before. The value of $(U_0)/U_s = 0.9$ for the measurements of Uberoi and Freymuth,¹⁹ which is comparable to present results when effects of vortex shedding are strong, as noted earlier. The value of $(U_0)/U_s = 3.0$ for the measurements of Chevray,²⁰ the higher value being typical of present measurements when vortex shedding is either absent or weak, see Table 1.

All the results illustrated in Fig. 8 are seen to be reasonably correlated with each other and with the Gaussian velocity distribution function found from simplified similarity theory for the self-preserving turbulent wake.²¹ Present measurements are identified by x/d but they extend over the full range where \bar{u}_c/U_s agrees with turbulent wake scaling in Fig. 7. Thus, results illustrated in Fig. 8 extend from $Re_W > 90$ for measurements from Refs. 19 and 20 down to $Re_W = 10$ near transition to laminar wake behavior for the present measurements, with effects of vortex shedding both present and absent. Clearly, mean velocity distributions within turbulent wakes generally are independent of these factors, upon appropriate definition of a virtual origin or a velocity scale like (U_0) .

The relative insensitivity of mean velocities within turbulent wakes to the specific properties of the turbulence are highlighted by considering streamwise r.m.s. velocity fluctuations along the axis. These results are plotted in terms of the turbulence intensity at the axis, $(\bar{u}'/\bar{u})_c$, as a function of x/d in Fig. 9. The measurements of Uberoi and Freymuth¹⁹ are shown in the figure, along with present measurements for Re in the range 280-4000 (present measurements were not feasible at lower values of Re because excessive numbers of transverse were required to establish reliable values of \bar{u}'_c due to low signal-to-noise ratios). Results for the full range of x/d for the measurements are illustrated with the portion in the turbulent wake region (or the fully-developed turbulent wake region

identified in Ref. 19) denoted by darkened symbols. These results have not been corrected for background disturbances due to uncertainties about these effects in the strongly directed near-wake region. Outside this region, the corrections are small except for the latter parts of the wakes for $Re \leq 960$: corrected results for the turbulent wakes will be considered subsequently

Present measurements of (\bar{u}/\bar{u}_c) within the turbulent wake region at $Re = 4000$ are in reasonably good agreement with Uberoi and Freymuth¹⁹ in Fig. 9: turbulent intensities are nearly constant at roughly 85% and the onset of this regime is in the range $x/d = 40-60$. Thus, within this regime, $\bar{u}_c \sim (x-x_0)^{-2/3}$ from Eq. (2) as observed during a number of past studies. For $Re \leq 960$, however, turbulence intensities in the turbulent wake region progressively decrease with decreasing Re ; nevertheless, even though these turbulence intensities are low in comparison to the standards of high Reynolds number turbulent wakes, they are still comparable to values found in the actively turbulent flows, e.g., near the axis of turbulent jets and pipe flows.^{21,22} Additionally, at these lower Reynolds numbers, there is a tendency for the turbulence intensity to decrease with increasing distance: this is particularly evident beyond the initial development region for $Re = 280$ (i.e., $x/d \geq 40$) where present measurements captured an extended turbulent wake region. Such behavior is expected as the turbulent wake decays toward transition to the laminar wake region and will be considered in more detail later.

Effects of vortex shedding on turbulence intensities in the near wake region also can be seen from the results plotted in Fig. 9. For present measurements at $Re = 4000$, the turbulence intensity reaches a peak near $x/d = 10$, due to strong effects of vortex shedding, and then decreases as the vortex pattern decays; subsequently, the development of wake turbulence causes the turbulence intensity to increase again and finally become nearly constant in the self-preserving wake region (this latter portion corresponding to behavior

seen by Uberoi and Freymuth¹⁹ at comparable Re). With strong effects of vortex shedding at low Re , e.g., $Re = 960$ and 400 , the peak in turbulence intensity due to vortex shedding still is evident near the sphere, however, the intensity subsequently decays monotonically to conditions in the turbulent wake region. For $Re = 400$, the maximum turbulence intensity due to vortex shedding is largest in comparison to values in the turbulent wake region, roughly 2.5 times larger; thus, the greater decay required to reach turbulent wake conditions probably accounts for the larger x/d required to reach self-preserving turbulent wake conditions, as noted earlier. Finally, when vortex shedding is weak, $Re = 280$, there is no peak in the turbulence intensity prior to the turbulent wake region and the onset of this region (with respect to the mean velocity distribution) occurs close to the sphere; however, turbulence still develops near the sphere, reaching a maximum intensity near $x/d = 40$, which is representative of the development region for high Reynolds number turbulent wakes.¹⁹

The character of the decay of turbulence during approach to transition from turbulent to laminar wake behavior (with respect to mean velocities) is illustrated in Fig. 10. Present data on this figure has been corrected for ambient disturbances in the usual manner, i.e., $\bar{u}_c'^2 = \bar{u}_{cm}'^2 - \bar{u}_\infty'^2$, where $\bar{u}_{cm}'^2$ is the initial measured value and $\bar{u}_\infty'^2$ is the both disturbance level prior to traversing the sphere. The results involve turbulence intensity at the wake axis plotted as a function of the local wake Reynolds number. The findings of Carmody¹⁷ and Uberoi and Freymuth¹⁹ at high wake Reynolds numbers are shown on the plot along with present results at moderate wake Reynolds numbers. These measurements involve fully-developed turbulent wake conditions observed at $x/d \geq 40$ for Uberoi and Freymuth¹⁹ and present tests, and at $x/d = 15$ for the high Reynolds number results of Carmody.¹⁷

Taken together, the results illustrated in Fig. 10 suggest a reasonable correlation of wake turbulence properties in terms of the wake Reynolds number. For $Re_w > 70$, turbulence intensities along the axis are nearly constant with \bar{u}'/\bar{u}_c in the range 0.85-0.92. At lower wake Reynolds numbers, however, turbulence intensities rapidly decrease (in terms of Re_w) in the final decay period as conditions for transition to a laminar wake are approached. Several proposals for the decay of turbulence energy in the final decay period have been made;²⁴⁻²⁷ present results are in reasonable agreement with estimates for axisymmetric wakes,^{25,27} where $\bar{u}'^2 \sim r^{-5/2}$. Noting that $x \sim U_\infty t$ for the fully developed turbulent wake region ($x/d \geq 40$) then yields the following relationship between turbulence intensity and local wake Reynolds number, using Eqs. (2) and (4):

$$(\bar{u}'/\bar{u})_c = C Re_w^{7/4} \quad (11)$$

The best fit of present data ($10 < Re_w < 30$) yields $C = 1.3 \times 10^{-3}$ with a standard derivation of 4×10^{-4} .

The best fit correlation of Eq. (11) is plotted in Fig. 10, where it is seen to provide a reasonable fit of present measurements for various values of Re and $10 \leq Re_w \leq 30$. If the same decay law was adopted from the laminar wake region, Eqs. (5) and (7) yield $(\bar{u})_c \sim Re_w^{1/2}$, which implies a much slower decay rate in terms of Re_w for laminar than turbulent wakes. Unfortunately, experimental evaluation of the transition of velocity fluctuations from turbulent to laminar wake behavior was not possible due to limitations of experimental uncertainties. Finally, the alternative final decay behavior proposed by Tan and Ling,²⁶ $\bar{u}'^2 \sim r^{-2}$, yields $(\bar{u}'/\bar{u})_c \sim Re_w^0$ and Re_w in the laminar and turbulent wake regions, the latter yielding a much slower rate of decay than present observations.

Laminar Wake Region

In view of the relatively large velocity fluctuations in the region after transition to laminar wake behavior seen in Fig. 9, and the relatively slow decay rates of turbulence in the laminar wake region discussed in connection with Fig. 10, it is useful to conclude by considering mean velocity distributions in the laminar wake region. The scaling of mean velocities along the axis in the laminar wake region, and its agreement with the correlation of Eq. (5) for all the present data, is evident from the results plotted in Fig. 7. Thus, only radial profiles of mean streamwise velocities will be considered in the following.

The radial profiles of mean streamwise velocities in the laminar wake region are illustrated in Fig. 11. Results are shown for $Re = 90, 170$ and 280 for x/d in the range 50-120, plotted according to the similarity relationships of Eqs. (5) and (6) with $x_0/\theta = 1$. The measurements do not extend to the edge of the flow because low velocities in this region precluded results within the experimental uncertainties specified earlier for a reasonable number of traverses. Over the range considered, however, the measurements agree with Eqs. (5) and (6) within experimental uncertainties in spite of the relatively high turbulence levels and the slow rate of decay of turbulence. An explanation for this behavior is that turbulence in the final decay period is not connected over the flow cross-section similar to high Reynolds number turbulent wakes; instead, it involves noninteracting localized regions of decaying turbulence (called turbulence spots, stratified turbulence or dilute vortex streaks).²⁴⁻²⁷ The absence of connectedness prevents mixing (entrainment or engulfment of ambient fluid) by large-scale turbulence structures that extend over a significant portion of the flow width, characteristic of high Reynolds number turbulent wakes; then, overall mixing is dominated by laminar viscous effects so that mean velocity distributions adjust accordingly with the decaying turbulence spots only mildly affecting flow properties.

Conclusions

The major conclusions of the study are as follows:

- 1) The properties of the recirculation zone on the downstream side of the sphere were similar to earlier observations:⁷⁻¹⁶ the recirculation zone was stable and symmetric for $Re \leq 200$, stable and unsymmetric for $200 < Re < 280$, and unstable with vortex shedding present for $Re \geq 280$.
- 2) The wakes exhibited three regions: a fast-decay wake region near the sphere that only was observed when vortex shedding was present, followed in succession by turbulent and laminar wake regions.
- 3) Mean velocities within the turbulent wake region scaled according to similarity predictions for self-preserving turbulent wakes, Eqs. (2), (3) or (8), (9), even though turbulence intensities along the axis varied in the range 10-85% and vortex shedding was present or absent. The main effect of vortex shedding on the turbulent wake region was to defer its onset, by an order of magnitude, due to the presence of the fast-decay wake region.
- 4) Transition from the turbulent to the laminar wake regime occurred where similarity estimates of mean streamwise velocities along the axes for laminar and turbulent wakes were the same, Eq. (10). This corresponded to local wake Reynolds numbers on the order of ten.
- 5) Within the fully-developed turbulent wake region ($x/d \geq 40$), $(\bar{u}/\bar{u}_c) = 85\%$ for $Re_w > 70$, typical of high Reynolds number axisymmetric wakes; however, as conditions for transition to laminar wakes were approached, $(\bar{u}/\bar{u}_c) \sim Re_w^{-7/4}$, which is consistent with the final decay period of turbulence in axisymmetric wakes.^{25,27}
- 6) Even though velocity fluctuations in the laminar wake region were significant, mean velocity distributions scaled according to laminar similarity predictions, Eqs. (6) and (7). This is plausible because turbulence in the final decay period involves isolated turbulent spots so that overall mixing is not controlled by the connected large-scale

structures found in turbulent wakes; instead, mixing is dominated by laminar viscous effects and mean velocity distributions adjust accordingly.

Acknowledgements

This research was sponsored by the Air Force Office of Scientific Research, Air Force Systems Command, USAF, under Grant AFOSR-89-0516. The U.S. Government is authorized to reproduce and distribute reprints for Governmental purposes notwithstanding any copyright notation thereon.

References

- ¹Parthasarathy, R.N. and Faeth, G.M. (1990) "Turbulence Modulation in Homogeneous Dilute Particle-Laden Flows," *Journal Fluid Mech.* 220, 1990, pp. 485-514.
- ²Mizukami, M., Parthasarathy, R.N. and Faeth, G.M., "Particle-Generated Turbulence in Homogeneous Dilute Dispersed Flows," *Int. J. Multiphase Flow*, in press.
- ³Torobin, L.B. and Gauvin, W.H., "Fundamental Aspects of Solids-Gas Flow, Part I: Introductory Concepts and Idealized Sphere Motion in Viscous Regime," *The Canadian Journal of Chemical Engineering*, Vol. 37, No. 4, August 1959, pp. 129-141; also "Part II: The Sphere Wake in Steady Laminar Fluids," Vol. 37, No. 5, October 1959, pp. 167-176; also, "Part V: The Effects of Fluid Turbulence on the Particle Drag Coefficient," Vol. 38, No. 6, December 1960, pp. 189-200.
- ⁴Pruppacher, H.R., LeClair, B.P. and Hamielec, A.E., "Some Relations Between Drag and Flow Pattern of Viscous Flow Past a Sphere and a Cylinder at Low and Intermediate Reynolds Numbers," *Journal of Fluid Mechanics*, Vol. 44, Part 4, 1970, pp. 781-790.
- ⁵Rimon, Y. and Cheng, S.I., "Numerical Solution of a Uniform Flow Over a Sphere at Intermediate Reynolds Numbers," *Physics of Fluids*, Vol. 12, No. 5, May 1969, pp. 949-959.
- ⁶Roos, F.W. and Willmarth, W.W., "Some Experimental Results on Sphere and Disk Drag," *AIAA Journal*, Vol. 9, No. 2, February 1971, pp. 285-291.
- ⁷Magarvey, R.H. and Bishop, R.L., "Wakes in Liquid-Liquid Systems," *Physics of Fluids*, Vol. 4, No. 7, July 1961, pp. 800-805.
- ⁸Magarvey, R.H. and MacLachy, C.S., "Vortices in Sphere Wakes," *Canadian Journal of Physics*, Vol. 43, September 1965, pp. 1649-1656.

²⁵Phillips, O. M., "The Final Period of Decay of Non-Homogeneous Turbulence," Proc. Cambridge Phil. Soc., Vol. 52, 1956, pp. 135-151.

²⁶Tan, H. S. and Ling, S. C., "Final Stage of Decay of Grid-Produced Turbulence," Physics of Fluids, Vol. 6, No. 12, December 1963, pp. 1693-1699.

²⁷Lee, D. A. and Tan, H. S., "Study of Inhomogeneous Turbulence," Physics of Fluids, Vol. 10, No. 6, June 1967, pp. 1224-1230.

²⁸Putnam, A., "Integrable Form of Droplet Drag Coefficient," ARS Journal, Vol. 31, 1961, pp. 1467-1468.

²⁹Kürten, H., Raasch, J. and Rumpf, H., "Beschleunigung eines Kugelförmigen Feststoffteilchens im Strömungsfeld konstanter Geschwindigkeit," Chem.-Ing.-Tech., Vol. 38, No. 9, January 1966, pp. 941-948.

³⁰Townsend, A. A., The Structure of Turbulent Shear Flow, The Cambridge University Press, Cambridge, 1956.

⁹Willmarth, W. W., Hawk, N. E. and Harvey, R. L., "Steady and Unsteady Motions and Wakes of Freely Falling Disks," Physics of Fluids, Vol. 7, No. 2, February 1964, pp. 197-208.

¹⁰Goldberg, A. and Florsheim, B. H., "Transition and Strouhal Number for the Incompressible Wake of Various Bodies," Physics of Fluids, Vol. 9, No. 1, January 1966, pp. 45-50.

¹¹List, R. and Hand, M. J., "Wakes of Freely Falling Water Drops," Physics of Fluids, Vol. 14, No. 8, August 1971, pp. 1648-1655.

¹²Viets, H., "Accelerating Sphere-Wake Interaction," AIAA Journal, Vol. 9, No. 10, October 1971, pp. 2087-2089.

¹³Calvert, J. R., "Some Experiments on Flow Past a Sphere," Aeronautical Journal, Vol. 76, April 1972, pp. 248-250.

¹⁴Achenbach, E., "Vortex Shedding from Spheres," Journal of Fluid Mechanics, Vol. 62, Part 2, 1974, pp. 209-221.

¹⁵Nakamura, I., "Steady Wake Behind a Sphere," Physics of Fluids, Vol. 19, No. 1, January 1976, pp. 5-8.

¹⁶Pao, H.-P. and Kao, T. K., "Vortex Structure in the Wake of a Sphere," Physics of Fluids, Vol. 20, No. 2, February 1977, pp. 187-191.

¹⁷Carmody, T., "Establishment of the Wake Behind a Disk," Journal of Basic Engineering, Vol. 87, No. 4, December 1964, pp. 869-883.

¹⁸Hwang, N. H. C. and Baldwin, L. V., "Decay of Turbulence in Axisymmetric Wakes," Journal of Basic Engineering, Vol. 88, No. 1, March 1966, pp. 261-268.

¹⁹Uberoi, M. S. and Freymuth, P., "Turbulent Energy Balance and Spectra of the Axisymmetric Wake," Physics of Fluids, Vol. 13, No. 9, September 1970, pp. 2205-2210.

²⁰Chevray, R., "The Turbulent Wake of a Body of Revolution," Journal of Basic Engineering, Vol. 90, No. 2, June 1968, pp. 275-284.

²¹Tennekes, H. and Lumley, J. L., A First Course in Turbulence, MIT Press, Cambridge, Massachusetts, 1972, pp. 113-124.

²²Hinze, J. O., Turbulence, 2nd ed., McGraw-Hill, New York, 1975, pp. 496-581.

²³Schlichting, H., Boundary Layer Theory, 7th ed., McGraw-Hill, New York, 1977, pp. 234-235 and 599.

²⁴Batchelor, G. K. and Townsend, A. A., "Decay of Turbulence in the Final Period," Proc. Roy. Soc. (London), Vol. A194, 1948, pp. 527-543.

Table 1 Test Conditions^a

Re (-)	Glycerin Concentration ^b	ν (mm ² /s)	U_s (mm/s)	C_D (-)	θ (mm)	$(U_0)/U_s^{\dagger}$
35	81	42.0	147	1.91 ^c	4.88	1.9
60	81	42.0	252	1.42 ^c	4.22	2.0
90	81	37.8-41.0	340-369	1.16 ^c	3.81	2.3
170	76	24.0-28.0	408-476	0.86 ^c	3.29	2.6
280	62	10.1-11.7	283-328	0.59 ^d	2.72	2.4
400	62	10.2	408	0.603 ^e	2.75	2.0
960	50	4.8	461	0.430 ^e	2.32	0.9
4000	0	1.02	408	0.381 ^e	2.18	0.8

^aSphere diameter of 10 mm; bath temperature variation less than 0.5 K during tests; $\bar{u}/U_s < 0.5\%$ before tests.

^bPercent glycerin in water by mass

^c $C_D = 24(1 + Re^{2/3})/Re$, from Putnam, 28

^dDefined from measured radial mean velocity distribution.

^e $C_D = 0.28 + 6/Re^{1/2} + 21/Re$, from Kürten et al. 29

^fBased on a fixed virtual origin at $x_0/\theta = 1$.

List of Figures

- Fig. 1 Sketch of the experimental apparatus.
- Fig. 2 Visualization of near wakes for intermediate Reynolds numbers ($Re = 40$ -280).
- Fig. 3 Variation of the wake separation angle with Reynolds number.
- Fig. 4 Visualization of near wakes for intermediate Reynolds numbers ($Re = 400$ -4000).
- Fig. 5 Mean streamwise velocity distributions near the sphere ($Re = 90$ -280).
- Fig. 6 Mean streamwise velocities along the wake axis ($Re = 400$ -4000).
- Fig. 7 Mean streamwise velocities along the wake axis ($Re = 35$ -280).
- Fig. 8 Correlation of radial profiles of mean streamwise velocities in the turbulent wake region.
- Fig. 9 Streamwise r.m.s. velocity fluctuations along the wake axis ($Re = 280$ -8600).
- Fig. 10 Streamwise turbulence intensities along the axis as a function of wake Reynolds number in the turbulent wake region ($Re = 280$ -71000).
- Fig. 11 Correlation of radial profiles of mean streamwise velocities in the laminar wake region ($Re = 90$ -280).

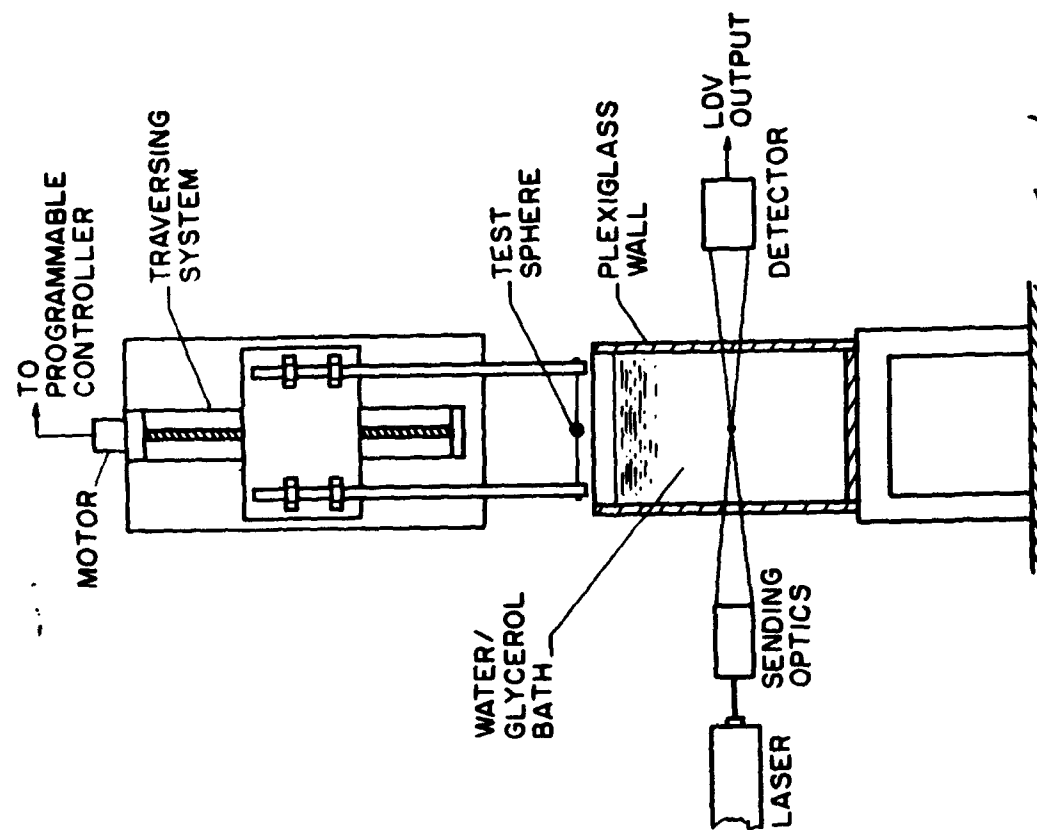
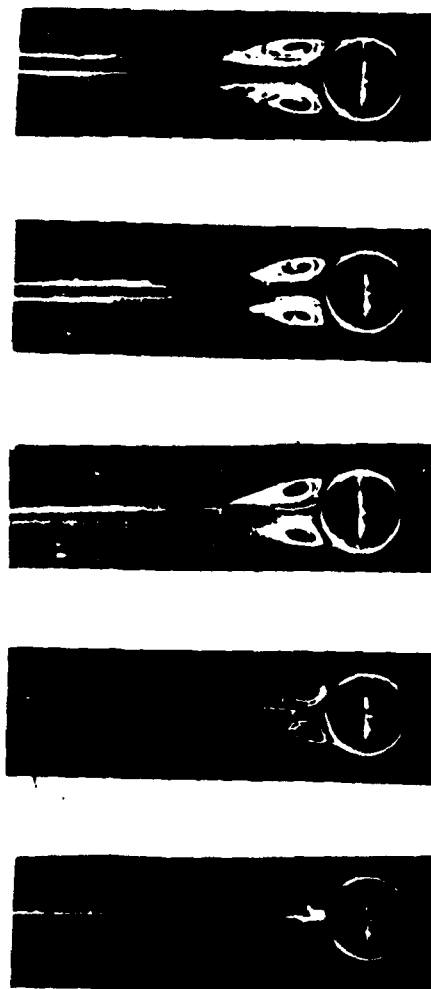
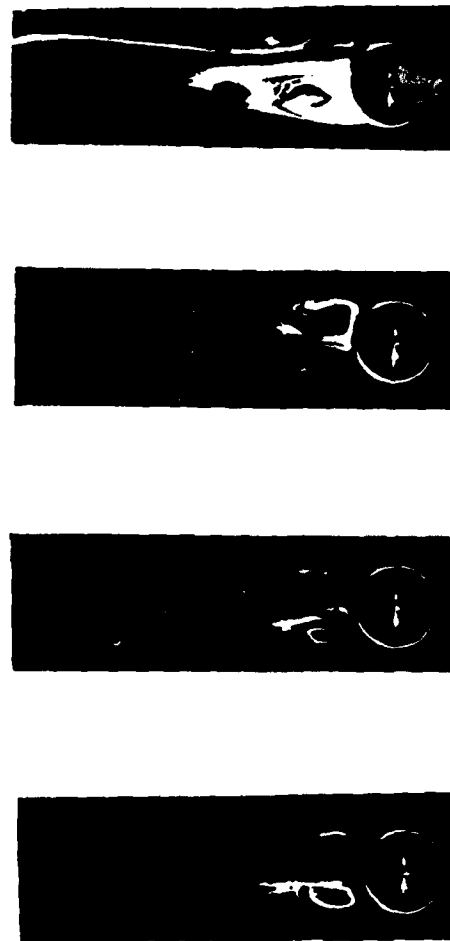


Fig. 1



Re = 40 Re = 60 Re = 90 Re = 120



Re = 200 Re = 220 Re = 240 Re = 280

FIG. 2

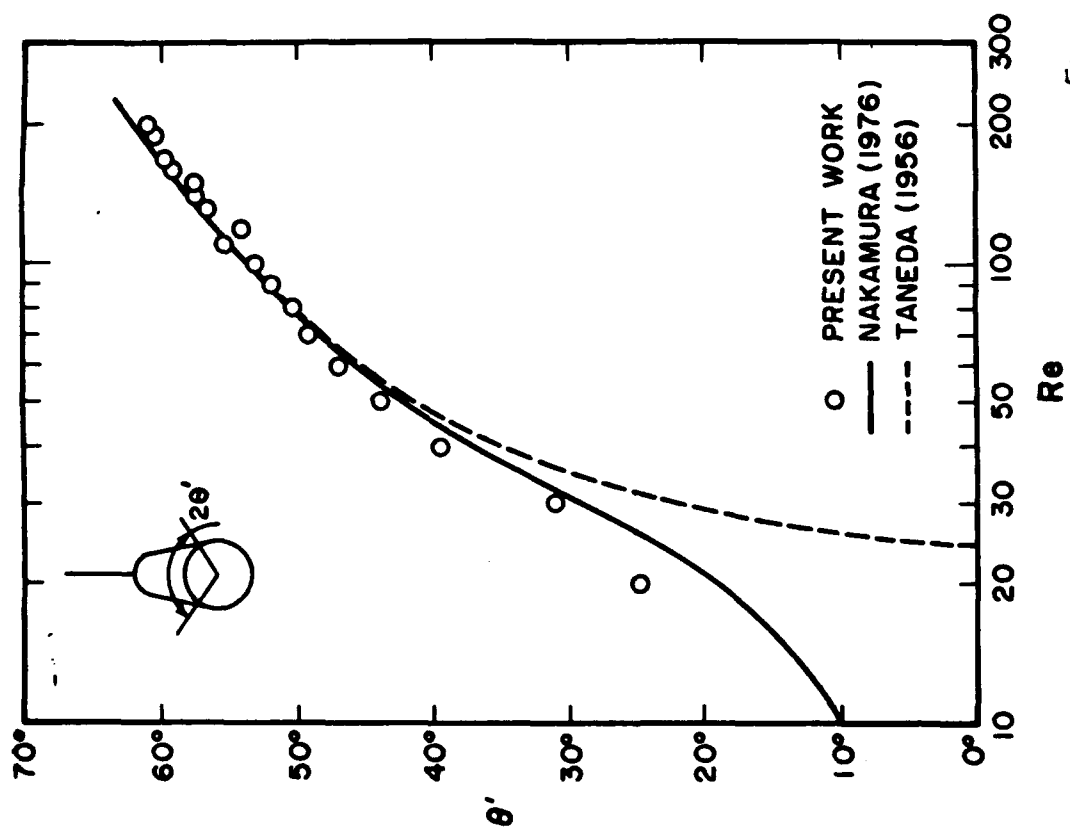


Fig. 3



$Re = 4000$



$Re = 2000$



$Re = 960$



$Re = 700$



$Re = 400$

FIG. 4

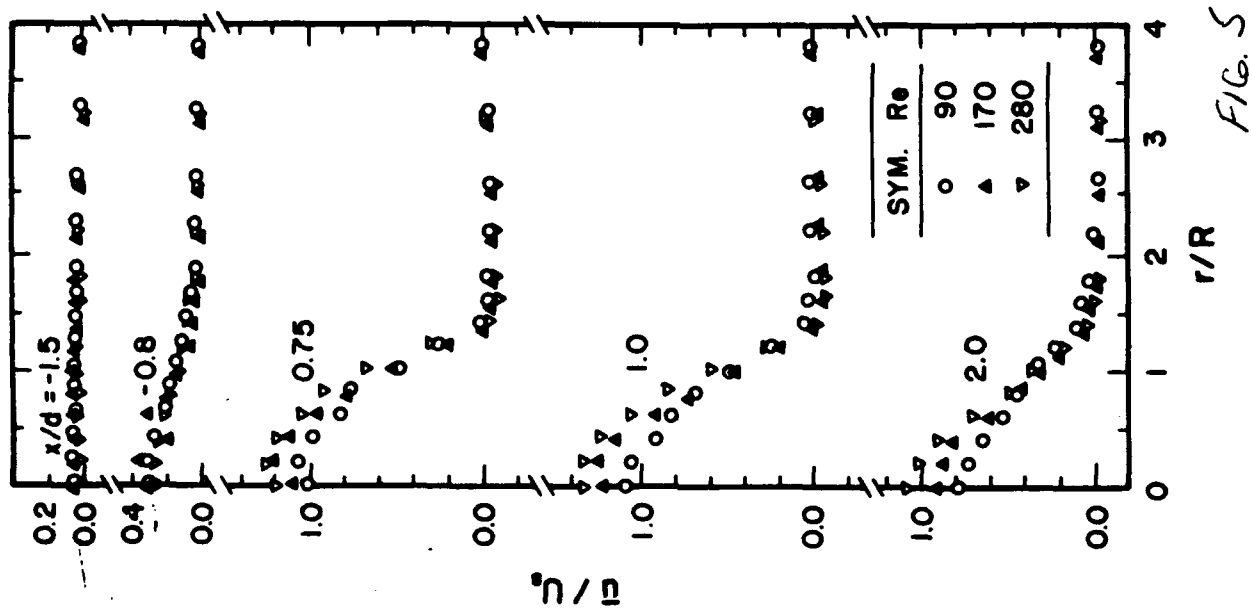


FIG. 5

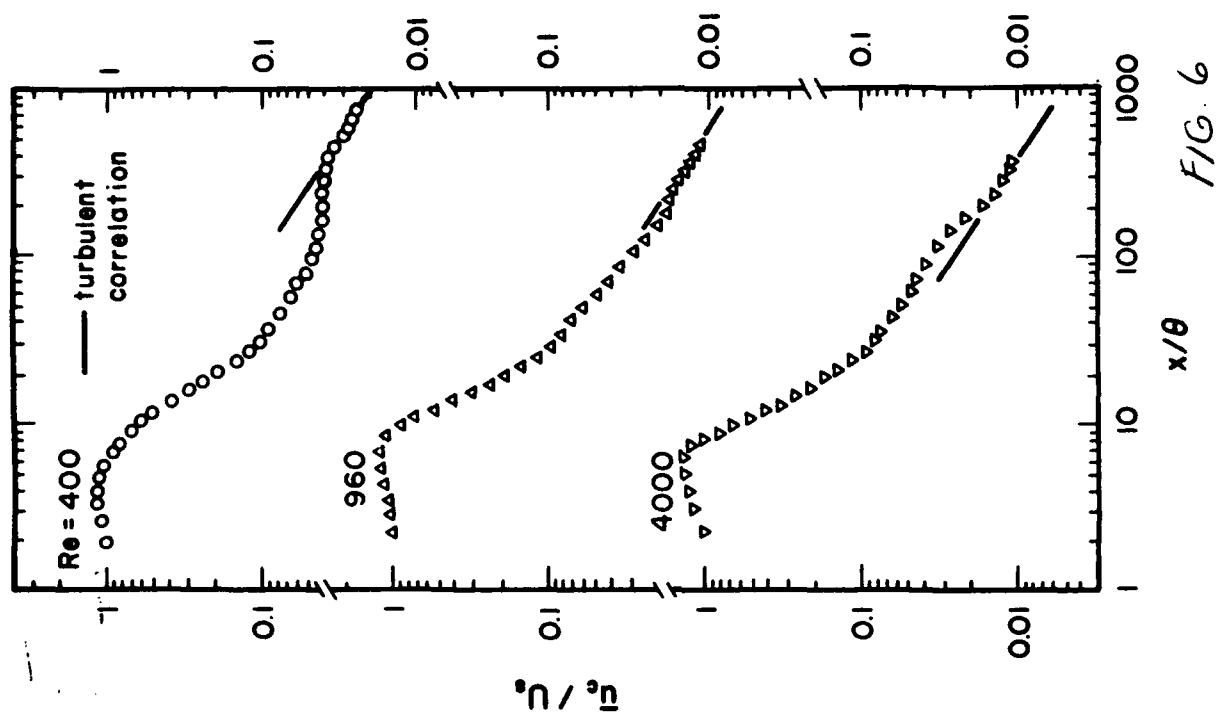
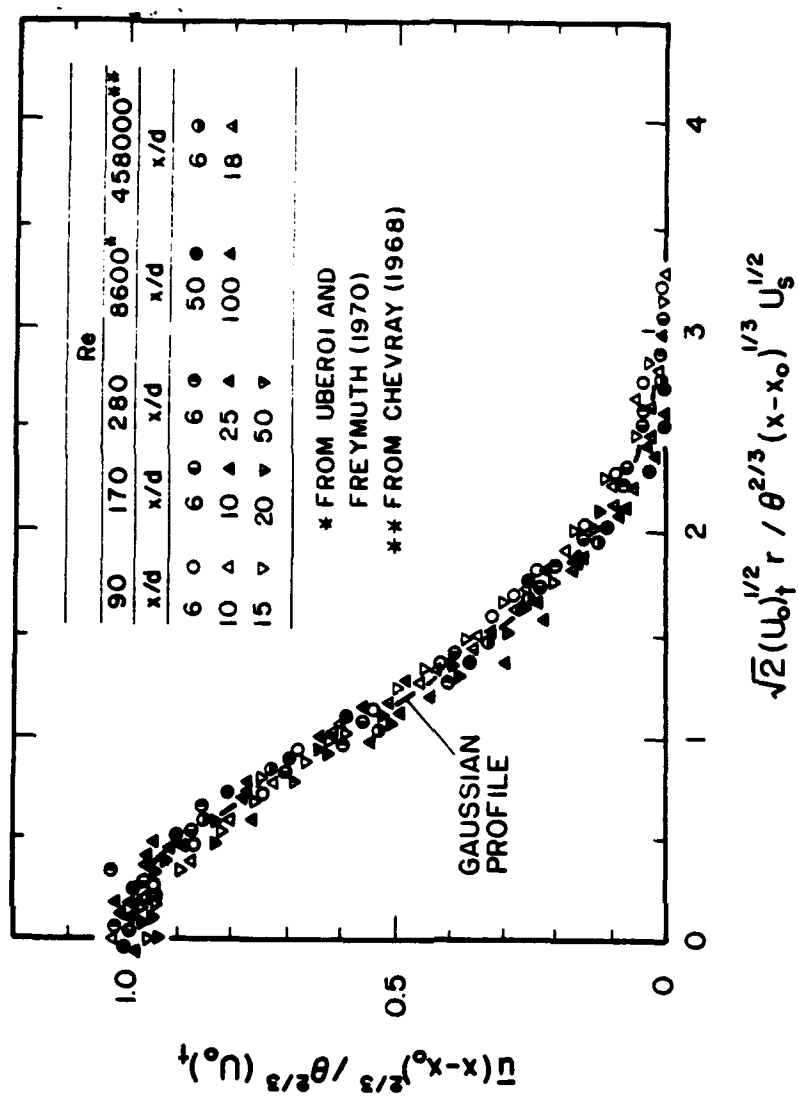
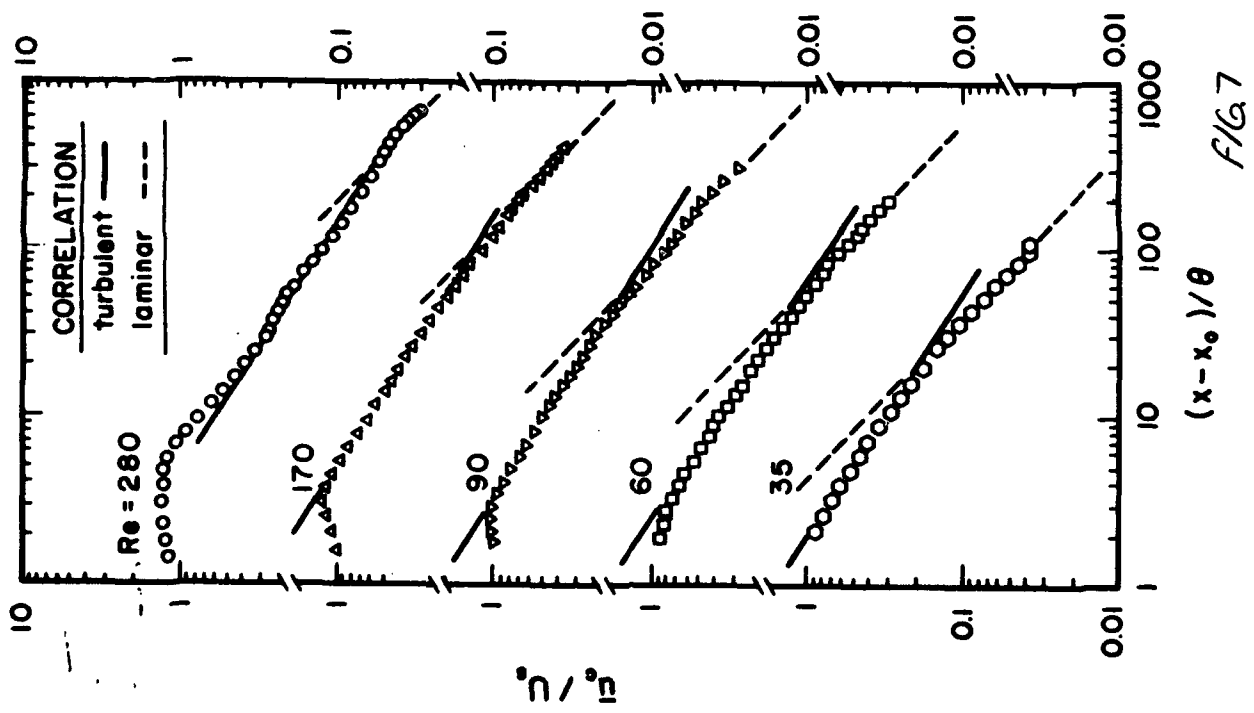


FIG. 6



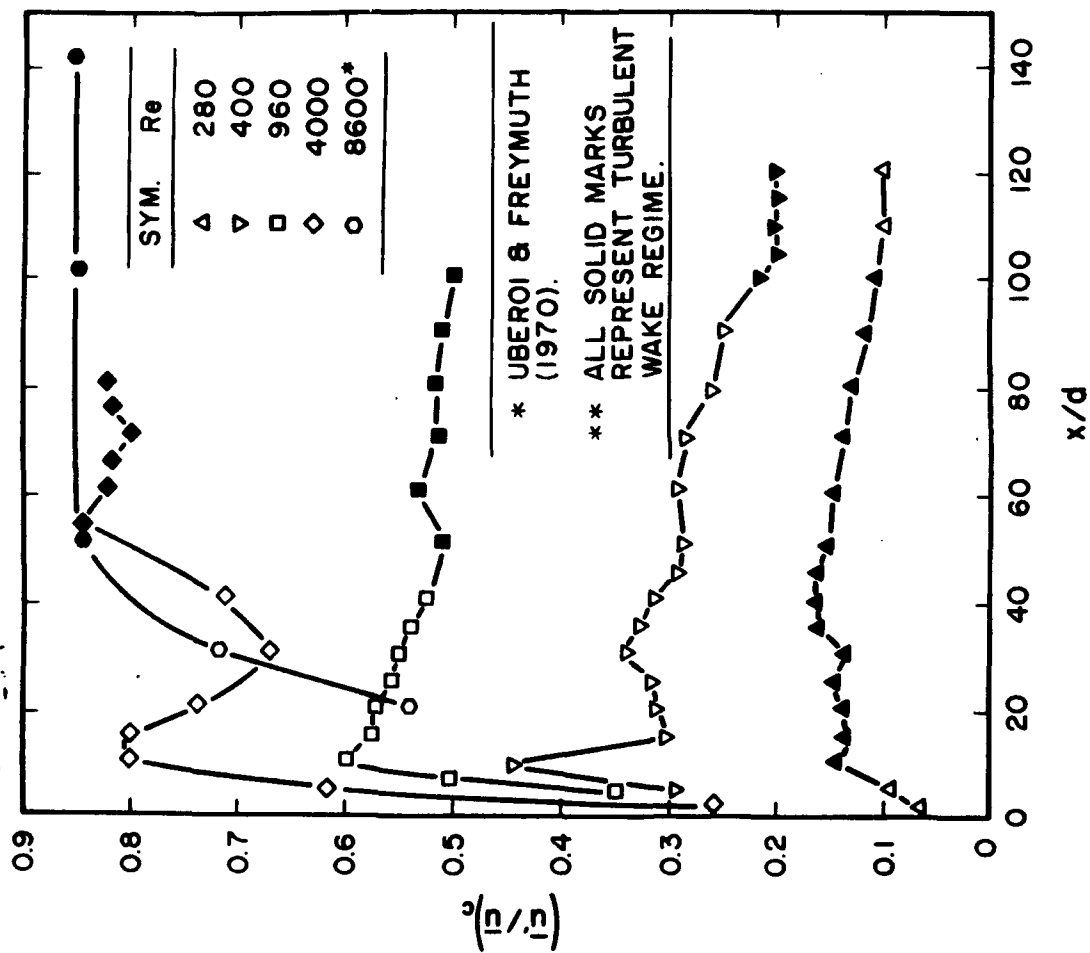


FIG. 9

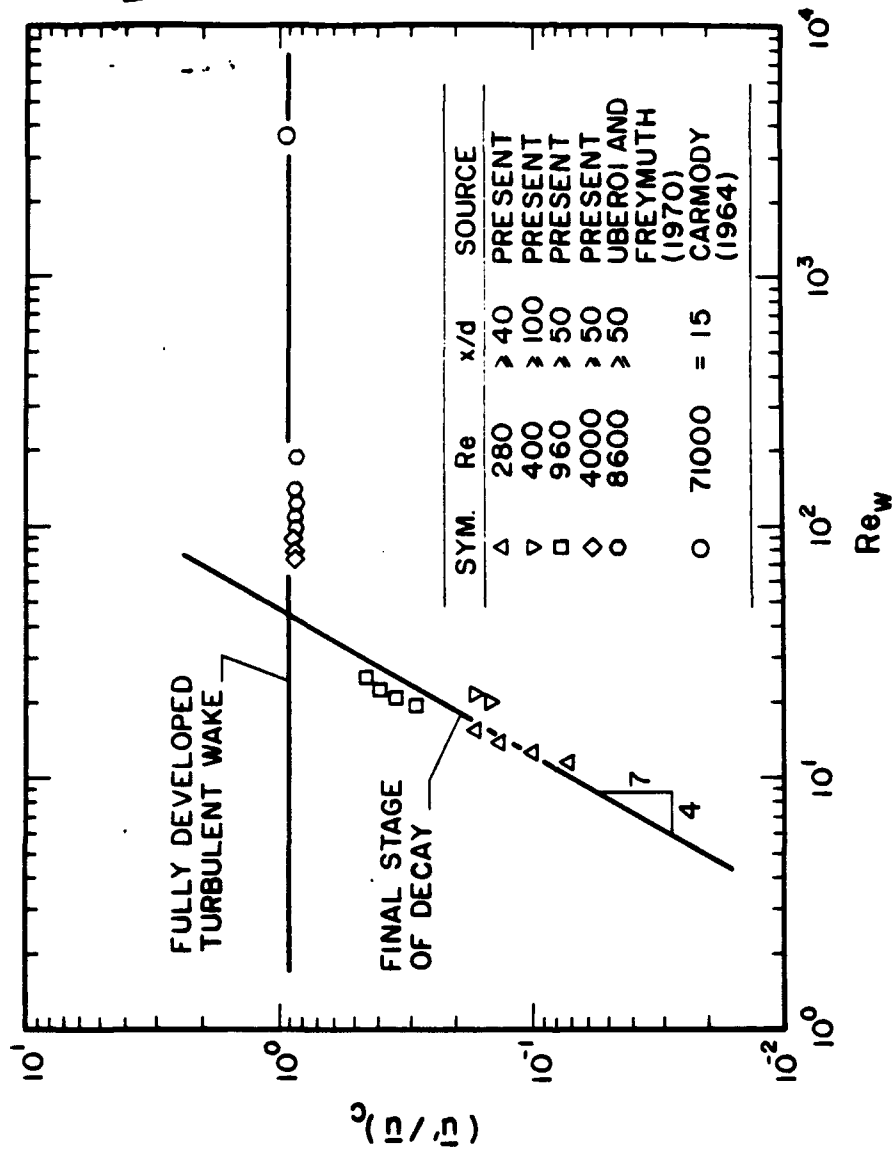


FIG. 10

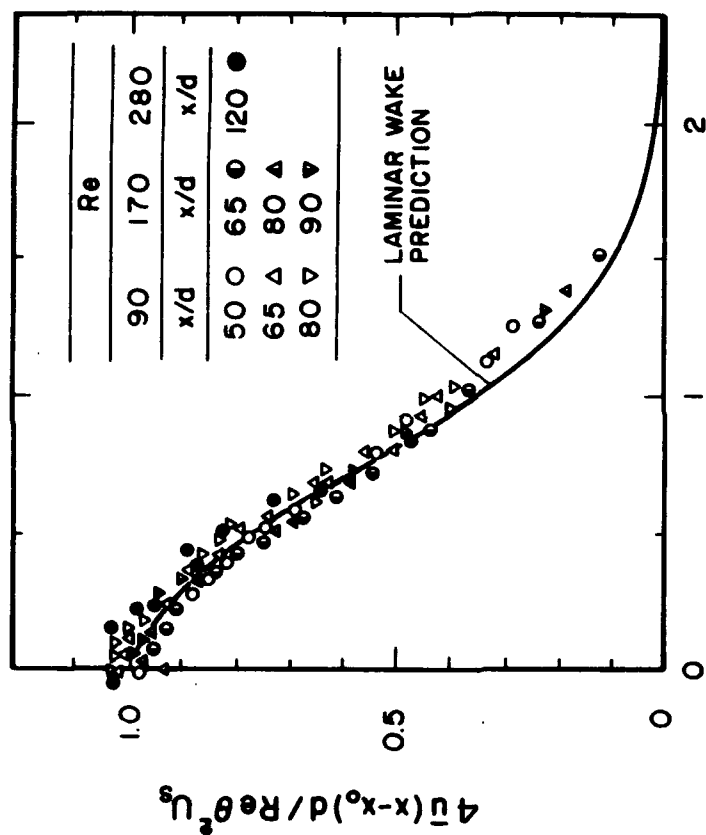


FIG. 11